The elastic properties and the crystal chemistry of carbonates in the deep Earth

DISSERTATION

zur Erlangung des akademischen Grades einer Doktorin

der Naturwissenschaften (Dr. rer. nat.)

in der Bayreuther Graduiertenschule für Mathematik und Naturwissenschaften (BayNAT)

der Universität Bayreuth

vorgelegt von

Stella Chariton

aus *Thessaloniki (Griechenland)*

Bayreuth, 2019

This doctoral thesis was prepared at the Bavarian Research Institute of Experimental Geochemistry and Geophysics at the University of Bayreuth from 10/2015 until 02/2019 and was supervised by Prof. Dr. Leonid Dubrovinsky and PD Dr. Catherine McCammon.

This is a full reprint of the thesis submitted to obtain the academic degree of Doctor of Natural Sciences (Dr. rer. nat.) and approved by the Bayreuth Graduate School of Mathematical and Natural Sciences (BayNAT) of the University of Bayreuth.

Date of submission: 25.02.2019

Date of defense: 18.04.2019

Acting director: Prof. Dr. Dirk Schüler

Doctoral committee:

Prof. Dr. Leonid Dubrovinsky (reviewer)
Prof. Dr. Daniel Frost (reviewer)
PD Dr. Catherine McCammon (chairwoman)
Dr. Thomas Meier

Ἄνευ αἰτίου οὐδέν ἔστιν

(Nothing happens without a reason)

Aristotle
384-322 BC

Zusammenfassung

Die vorliegende kumulative Dissertation beschreibt eine experimentelle Untersuchung der elastischen Eigenschaften und Kristallchemie von rhombohedrischen Karbonaten bei für den Erdmantel relevanten Druck- und Temperaturbedingungen. Ziel dieser Arbeit ist es, das Stabilitätsfeld für einige Endglieder der Kalzitgruppe ($FeCO_3$, $MnCO_3$, $CoCO_3$, $ZnCO_3$, $NiCO_3$), sowie für Fe-Magnesit-Zusammensetzungen $(Fe,Mg)CO_3$ zu untersuchen, um kristallchemische Gesetzmäßigkeiten zu erforschen und deren Hochdruckpolymorphe unter extremen Bedingungen zu beschreiben. Zusätzlich wurde die seismische Nachweisbarkeit von Fe-haltigen Karbonaten im Erdmantel untersucht, in dem die Schallgeschwindigkeiten dieser Minerale mit den Geschwindigkeitsprofilen des Mantels verglichen wurden. Vorrangig wurden für diese Arbeit laser-geheizte Diamantstempelzellen verwendet, um die hohen Druck- und Temperaturbedingungen des Erdmantels zu generieren. Phasen und Strukturen, sowie in situ Charakterisierungen von neuen Verbindungen, wurden mithilfe von Röntgenbeugung an Pulvern und Einkristallen bestimmt. Zusätzlich wurden molekulare Vibrationsmoden anhand von Ramanspektroskopie und akustische Geschwindigkeiten durch nukleare inelastische Streuung gemessen.

Die Zustandsgleichungen synthetischer Einkristalle der Zusammensetzungen Siderit ($FeCO_3$), Ferromagnesit [$(Mg_{0.74}Fe_{0.26})CO_3$], Rhodochrosit ($MnCO_3$), Spherocobalit ($CoCO_3$), Gaspeit ($NiCO_3$) und Smithsonit ($ZnCO_3$) wurden durch statische Kompression bei Raumtemperatur bestimmt. Alle oben genannten Karbonate bleiben in der Kalzit-Struktur ($R\overline{3}c$) bis mindestens 44 GPa bei Raumtemperatur stabil. Bei diesem Druck findet eine Strukturumwandlung von $MnCO_3$ zu der triklinen $MnCO_3$-II ($P\overline{1}$) Phase statt. Der Fe^{2+}-Spinübergang in Fe-haltigen Karbonaten führt außerdem zu einer drastischen Reduktion des Volumens. Obwohl sich der elektronische Zustand von Fe verändert, können Siderit und Ferromagnesit bis 70 GPa und Raumtemperatur immer noch der $R\overline{3}c$ Struktur zugeordnet werden. $CoCO_3$, $NiCO_3$ und $ZnCO_3$ sind in der Kalzit-Struktur bis mindestens 56, 82 und 110 GPa stabil. Die kompressionsabhängige Verformung der Polyeder wird für alle Proben beschrieben und miteinander verglichen. Nachdem die Proben mit dem Laser auf relevante Druck- und Temperaturbedingungen gebracht wurden, konnten mehrere dichtere Karbonatpolymorphe und Zersetzungsprodukte festgestellt werden. $MnCO_3$ unterläuft einer komplexen chemischen Veränderung mit der Entstehung von CO_4-polymerisierten Einheiten (MnC_2O_5, $Mn_4C_4O_{13}$) und der Zersetzung in verschiedene Mn-haltige Oxide (Mn_3O_4, Mn_5O_7, $pv - Mn_2O_3$, $\delta - Mn_2O_3$), vergleichbar mit dem Phasendiagramm von $FeCO_3$ und Fe-haltigen Karbonaten. Zusätzlich zu zuvor beschriebenen Strukturen mit tetraedrisch koordiniertem C wird die viel diskutierte Struktur von Magnesit-II beschrieben, die aus {C_3O_9}$^{6-}$-Karbonatringen aufgebaut ist.

Konkret wird $Fe_{0.4}Mg_{2.6}C_3O_9$ ($C2/m$) nach der Laserheizung bei 2500 K bei 95 GPa gebildet. $NiCO_3$, $ZnCO_3$ und $CoCO_3$ formen unter einem Druck von 100 GPa und einer Temperatur von 2500 K keine Tetrakarbonatstrukturen. Stattdessen durchlaufen sie thermische Zersetzungsprozesse und bilden Oxide (NiO, CoO, Co_4O_5) oder neue Karbonate ($ZnCO_3$-II). Diese Dissertation demonstriert sowohl den komplexen Charakter einiger Übergangsmetall-Karbonate, als auch die Stabilisierung von Karbonaten mit kleineren Kationen im Erdinneren, was einen großen Einfluss auf den tiefen Kohlenstoffzyklus hat.

Natürliche Proben, besonders solche aus dem tiefen Erdmantel, die Anhaltspunkte über den tiefen Kohlenstoffzyklus mit sich tragen, wurden zwar gefunden, sind aber extrem selten. Deswegen werden Szenarien für die Nachweisbarkeit von Karbonaten durch geophysikalische Methoden diskutiert. Die Wellengeschwindigkeiten von Fe-haltigen Karbonaten werden mithilfe von nuklearer inelastischer Streuung bis ~70 GPa bestimmt und die Vorzüge dieser Methode hervorgehoben. Mg-reichere Proben, in diesem Fall $(Mg_{0.74}Fe_{0.26})CO_3$, haben bis zu ~19% schnellere Wellengeschwindigkeiten als das reine Fe-Endglied. Zusätzlich ist eine signifikante Zunahme der Geschwindigkeiten nach dem Fe^{2+}-Spinübergang sichtbar. Eine deutliche Abnahme der Geschwindigkeiten wurde nach dem Laserheizen der $FeCO_3$-Probe bei Drücken des tiefen Erdmantels festgestellt, was mit der thermischen Zersetzung von Siderit zu einer oder mehreren Phasen in Verbindung gebracht werden kann. Wenn man den jährlichen Kohlenstofffluß, die Auflösung von seismischen Abbildungsmethoden und Phasenstabilitätsdiagramme berücksichtigt, kann darauf geschlossen werden, dass bis zu 22 Gew.% CO_2 in subduzierenden Platten vorhanden sein muss, um 1% Abnahme in den Scherwellengeschwindigkeiten im Vergleich zu nicht-karbonathaltigen Lithologien in der Übergangszone und dem unteren Erdmantel zu erklären. Es existieren heutzutage Subduktionszonen, besonders in Zentralamerika, die einen so hohen Anteil an CO_2 beinhalten und welche bis in den tiefen Erdmantel subduziert werden. Diese oder ähnliche Regionen sind von großer Bedeutung, wenn man in der Zukunft geophysikalische Untersuchungen durchführen möchte, die Karbonate in der tiefen Erde erforschen wollen.

Summary

The present cumulative thesis describes an experimental investigation of the elastic properties and crystal chemistry of rhombohedral carbonates at pressures and temperatures relevant to the Earth's mantle. The goal of the thesis is to investigate the high-pressure behavior and determine the stability fields of several endmember minerals that represent the calcite group ($FeCO_3$, $MnCO_3$, $CoCO_3$, $ZnCO_3$, $NiCO_3$), as well as ferromagnesian [$(Fe,Mg)CO_3$] compositions, in order to determine crystallochemical regularities and describe high pressure polymorphs and dissociation products at extreme conditions. In addition, the seismic detectability of Fe-bearing carbonates in the Earth's mantle is explored by deriving sound velocities and comparing them to the velocity profiles of the bulk mantle. The main tools used in these studies are: laser-heated diamond anvil cells for generating the high pressures and temperatures that exist in the Earth's mantle; powder and single-crystal X-ray diffraction for phase identification, structure solution and refinements, and in situ characterization of the chemical compositions of novel compounds; Raman spectroscopy for the investigation of the molecular vibrational modes; and nuclear inelastic scattering for the determination of acoustic velocities.

The equations of state of synthetic single crystals of siderite ($FeCO_3$), ferromagnesite [$(Mg_{0.74}Fe_{0.26})CO_3$], rhodochrosite ($MnCO_3$), spherocobaltite ($CoCO_3$), gaspeite ($NiCO_3$), and smithsonite ($ZnCO_3$) were obtained during cold compression. All of the above carbonates remain stable in the calcite-type structure ($R\bar{3}c$) up to at least 44 GPa at room temperature. At this pressure, $MnCO_3$ undergoes a structural transformation to the triclinic $MnCO_3$-II ($P\bar{1}$) phase, while Fe-bearing carbonates experience a sudden volume collapse induced by Fe^{2+} spin crossover. Despite the Fe electronic change, siderite and ferromagnesite remain calcite-structured upon compression at ambient temperatures. Similarly, $CoCO_3$, $NiCO_3$ and $ZnCO_3$ are stable in the calcite-type structure at least up to 56, 82 and 110 GPa, respectively. The evolution of polyhedral distortions during compression is described for all samples and comparisons among them are discussed. After laser heating at pressures and temperatures relevant to the Earth's mantle, several denser carbonate polymorphs and dissociation products are observed. $MnCO_3$ displays complex chemistry with formation of CO_4 polymerized units (MnC_2O_5, $Mn_4C_4O_{13}$) and dissociation to various Mn-oxides (Mn_3O_4, Mn_5O_7, $pv - Mn_2O_3$, $\delta - Mn_2O_3$), which makes it comparable to the phase stability diagram of $FeCO_3$ and Fe-bearing carbonates. In addition to the previously reported structures with tetrahedrally-coordinated C, the much-debated crystal structure of magnesite-II, which is based on $\{C_3O_9\}^{6-}$ carbonate rings, is presented here. More concretely, $Fe_{0.4}Mg_{2.6}C_3O_9$ ($C2/m$) formed after laser heating at 2500 K and 95 GPa. The $NiCO_3$, $ZnCO_3$ and $CoCO_3$ do not form tetracarbonate structures upon

compression and after high-temperature treatment up to about 100 GPa and 2500 K. Instead, they either thermally dissociate with formation of oxides (like NiO, CoO, Co_4O_5) or they transform to new carbonates ($ZnCO_3$-II in particular). The thesis demonstrates the complex character that some transition-metals carbonates have compared to others, as well as the significance of small size cations in stabilizing carbonates in the Earth's interior, which in turn has important implications for the deep carbon cycle.

Natural samples that carry evidence of the deep carbon cycle, particularly from the lower mantle, have been discovered, but they are extremely rare. Therefore, scenarios for the detectability of carbonates from geophysical methods are discussed. The sound velocities of Fe-bearing carbonates were derived up to ~70 GPa using the nuclear inelastic scattering technique and the merits of the method are highlighted. More Mg-rich samples, in this case $(Mg_{0.74}Fe_{0.26})CO_3$, have ~ 19 % higher sound velocity than the pure end-member Fe composition. In addition, a significant velocity increase is observed following the Fe^{2+} spin transition. A dramatic velocity drop is observed after laser heating of $FeCO_3$ at lower mantle conditions, which is associated with the thermal decomposition of siderite to another phase(s). Taking into account factors that include annual carbon flux, resolution of seismic imaging methods, and phase stability diagrams, it is concluded that nearly 22 wt% of CO_2 must be present in the subducting slab in order to show a 1% shear wave velocity decrease compared to non-carbonated lithologies at transition zone to lower mantle boundary depths. A few subduction trenches exist today that contain such a high amount of CO_2, mostly located in Central America, and they are all well-known examples of subducting slabs that penetrate into the lower mantle. These or similar regions are of high interest for possible future geophysical surveys looking for carbonates in the deep Earth.

Acknowledgements

Table of Contents

Chapter 1

Introduction

"All chemical elements are special, but some are more special than others. Of the 88 naturally occurring, long-lived elements on Earth, carbon stands alone. As the basis of all biomolecules, no other element contributes so centrally to the wellbeing and sustainability of life on Earth, including our human species."

R. Hazen & C.M. Schiffries, 2013
Carbon in Earth, Reviews in Mineralogy and Geochemistry

1.1. Carbon through space and time

Next to hydrogen, helium and oxygen, carbon is the most abundant element in the universe and plays an important role in the chemical evolution of galaxies, stars, planets and life. It is generally accepted that carbon genesis is connected with the slow ending of a star's life [1, 2]. Following the Big Bang substantial amounts of He, H and a little bit of Li were created, while all other elements were formed by nucleosynthesis in stars [3]. Nuclear fusion powers a star for most of its life. Initially, the energy is generated by the deuterium (D + ^{1}H → ^{3}He) and lithium (^{7}Li + ^{1}H → ^{4}He) burning at the core of the main-sequence star. When the star runs out of hydrogen to fuse in its core, it begins to collapse until the central temperature rises to 10^8 K [4]. At this temperature and density, alpha particles can fuse fast enough to produce significant amounts of carbon and restore thermodynamic equilibrium in the core through helium

burning (also known as the triple-alpha process) (Figure 1). During this process ^{12}C is formed. With further increases of temperature and density, fusion processes produce further nuclides. Often, and depending on their mass evolution, stars death is characterized by supernova explosions that disperse the newly formed elements into the solar nebula, which in turn condense into polyatomic compounds that formed the cosmic dust [5].
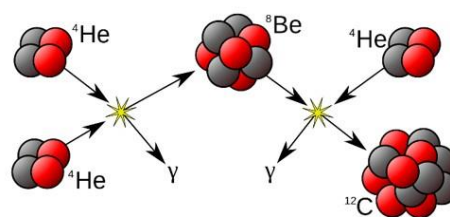
Figure 1. The triple-alpha process.

Accretion of cosmic particles in protoplanetary disks formed small chondrules or large planetisimals. It is suggested that the terrestrial carbon might have been supplied by various cosmochemical reservoirs, such as the protostellar nebula, the comets and the meteorites [2, 5]. On the basis of their isotopic signatures, terrestrial volatiles are thought to have derived from carbonaceous
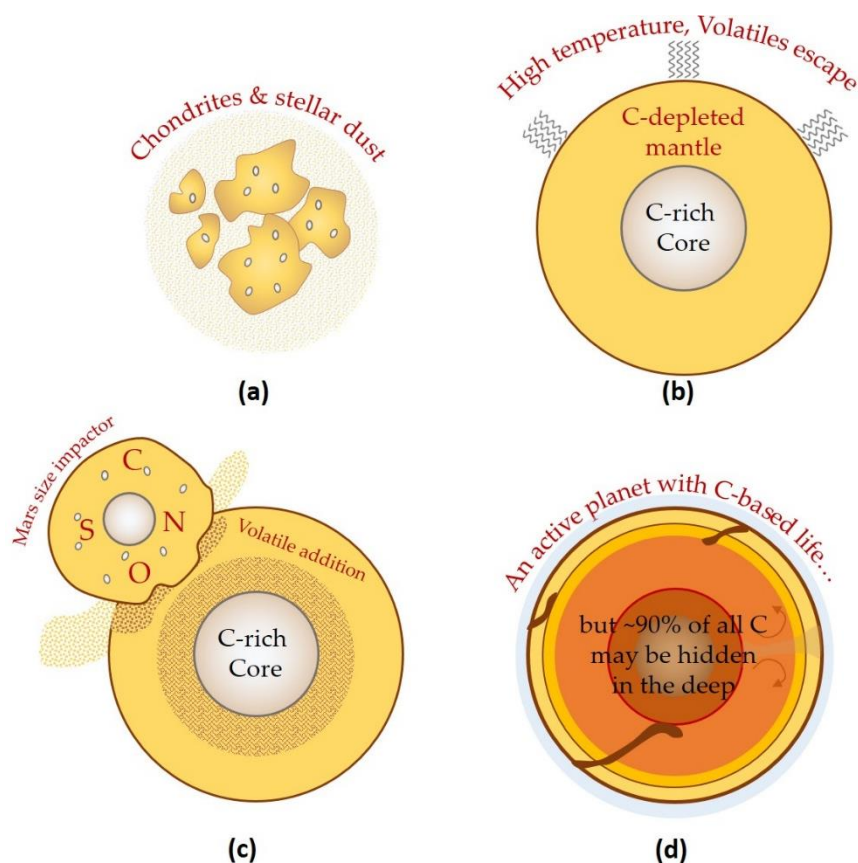
Figure 2. Cartoon illustrating the major events in Earth's history and describe the main model in which most of the carbon is in the core. **a)** Cosmic material accretes to form the Earth. **b)** Any carbon left on earth mainly resides in the core, leaving a C-depleted mantle. Carbon that was incorporated in volatiles escape the planet due to their low condensation temperatures. **c)** A Mars size impactor delivers volatile elements (C-O-H-N-S) on Earth and forms the Moon. **d)** Today, carbon is the basis of life on the surface of the earth, but actually ~90% of all carbon on Earth may be in the mantle and core.

chondrites, while the isotopic compositions of non-volatile major and trace elements suggest that enstatite chondrite–like materials are the primary building blocks of Earth [2, 6, 7]. This has cause many difficulties in reconstructing a model for the primordial Earth and study its evolution to the modern days (Figure 2). However, it is generally accepted that the early Earth was largely depleted in carbon [6-8]. During the first stages of accretion and core formation, gaseous C-bearing phases must have escaped the Earth due to their low condensation temperatures [9] (Figure 2a, b). On the other hand, carbon incorporated in solid phases, such as carbides or as elemental carbon (graphite/diamond) may have been partitioned into the Earth's core, leaving back a C-depleted mantle (Figure 2b). This scenario is supported by experimental and theoretical works that demonstrate the high solubility of C in liquid iron [e.g. 6-8, 10] and the existence of graphite and cohenite (Fe,Ni)$_3$C in iron meteorites [11]. These evidences additionally suggest that carbon could account for the density deficit of the Earth's core along with other light elements [e.g. 8, 12]. It was repeatedly suggested by many authors that frequent and violent collisions with other planetary bodies during the Earth's early history delivered carbon and other volatile elements that make our planet habitable today [e.g. 7, 13]. One of these collisions resulted in the formation of the Moon (Figure 2c).

Since that time, our planet has matured and carbon has play a protagonist role in several phases of the Earth's evolution (Figure 2d). For example, it is possible that carbon may have aided the formation of the liquid-outer and solid-inner layers of the core through solidification of iron carbides as the Earth was cooling down. This in turn led to the generation of the Earth's magnetic field by the geodynamo [14]. In addition, carbon is a key component of all known life on Earth. Without CO$_2$ the life of photosynthetic organisms and animals would have been impossible. Even though it seems that carbon's strongest participation is on our planet's surface, in reality the largest carbon reservoir is located in the Earth's deep interior [6]. However, many open questions remain as to how the deep carbon influences the geological processes inside Earth. With respect to these questions, the deep carbon science emerged to explore the quantities, movements, forms, and origins of carbon on Earth.

1.2. Carbonate mineralogy and the carbon cycle

1.2.1. Carbonate mineralogy and formation (important concepts)

The International Mineralogical Association (IMA) recognizes more than 380 carbon-bearing minerals; among those are native carbon polymorphs, carbides, carbonates, organic compounds and many others. However, nearly 300 out of the total discovered species are carbonate minerals. Those are the minerals that incorporate the carbonate ion CO_3^{2-}. Carbonate rock-forming minerals in massive

sedimentary and metamorphic formations account for at least 90% of the crustal carbon [15]. Carbonates classification at ambient conditions is usually done with respect to their crystal structure (Figure 3). The calcite –type structure describes rhombohedral carbonates that crystallize in the $R\overline{3}c$ space group (Figure 3a). Calcite-type carbonates usually incorporate divalent earth-alkaline or transition metal cations that have atomic radius smaller than Ca^{2+} (1.00 Å). These cations occupy octahedral sites and are coordinated by oxygens, while the CO_3^{2-} units form planar equilateral triangles. The topology of calcite-type carbonates is similar to that of NaCl, however the orientation of the CO_3^{2-} units are 180° out of phase in successive layers, thus doubling the repeat distance along the c-axis relative to the NaCl analog. Common mineral examples in this group are calcite ($CaCO_3$), magnesite ($MgCO_3$), siderite ($FeCO_3$), rhodochrosite ($MnCO_3$), otavite ($CdCO_3$) smithsonite ($ZnCO_3$), spherocobaltite ($CoCO_3$) and gaspeite ($NiCO_3$). However,
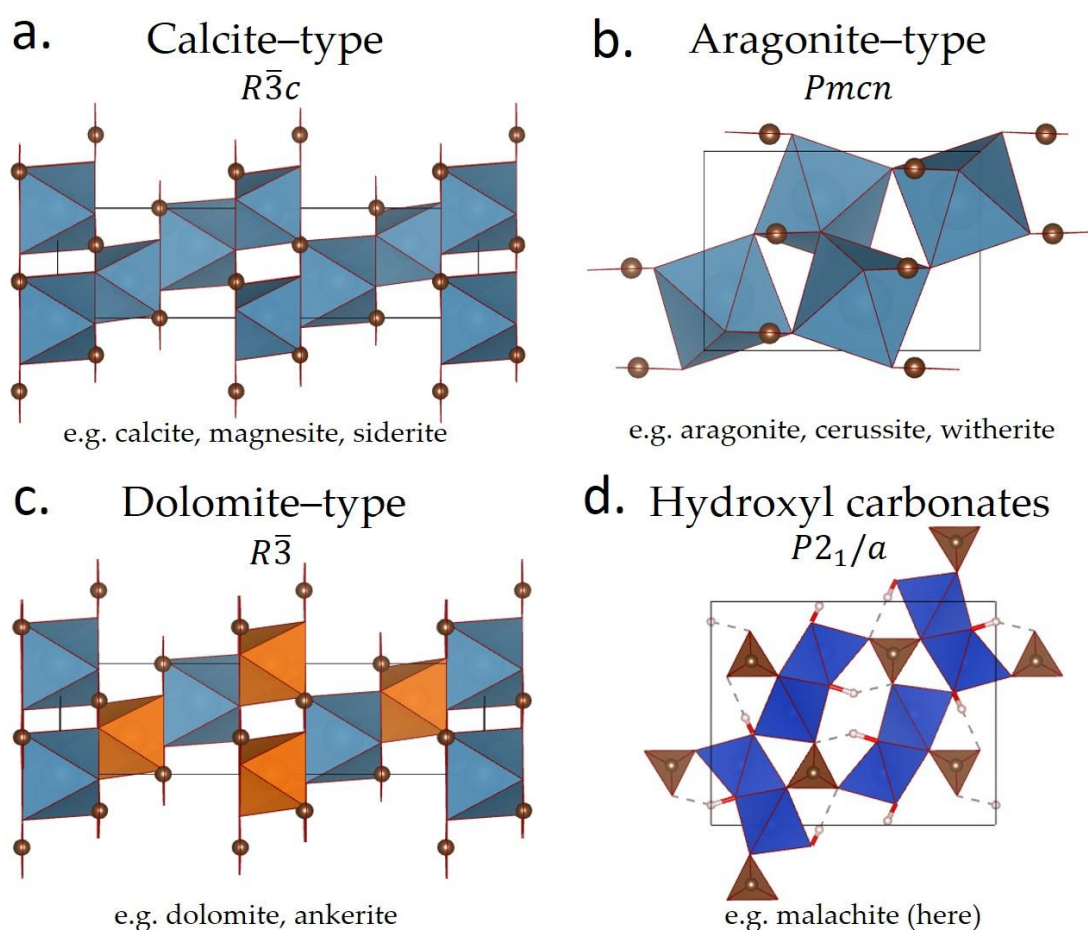
Figure 3. Classification of carbonates with respect to their crystal structures. Four major categories are underlined: **a)** the calcite-type, which contains rhombohedral carbonates crystallizing in the $R\overline{3}c$ space group **b)** the aragonite-type, which includes orthorhombic carbonates that crystallize in the $Pmcn$ space group, **c)** dolomite-type carbonates, which consists of rhombohedral carbonates with more than one metal cations (e.g. dolomite has both Ca and Mg) arranged in a specific order within the lattice and **d)** carbonates that incorporate the hydroxyl group or halogens and crystallize in the monoclinic system (space groups may vary in this case).

very rarely these minerals occur as pure end-members in nature. The aragonite-type structure carbonates includes orthorhombic carbonates that crystallize in the Pmcn space group (Figure 3b). This type of structure prevails for carbonates that contain a metal cation of the same size or bigger than Ca^{2+} (1.00 Å). The divalent metal cations are 9-coordinated by oxygens forming tricapped trigonal prisms. Common mineral representatives of this group are aragonite (denser form of $CaCO_3$), cerussite ($PbCO_3$), witherite ($BaCO_3$), and strontianite ($SrCO_3$). The dolomite-type-structure group includes a series of rhombohedral carbonates that are indexed in the $\overline{R3}$ space group (Figure 3c). The topology of the dolomite structure is identical to the calcite structure. However, in dolomite-type at least two metal cations (usually a combination between Ca and Mg, Fe, Mn or Zn) occupy alternate layers perpendicular to the c-axis (see alternations of blue and orange octahedra in Figure 3c). Famous representatives of this group are dolomite [$CaMg(CO_3)_2$], ankerite [$CaFe(CO_3)_2$] and kutnohorite [$CaMn(CO_3)_2$]. Note how deviations from the chemical composition of the dolomite mineral establish new minerals. This is due to the substantial substitution of Mg by 3d transitional metals, in particular Fe^{2+} and Mn^{2+} in different geological environments. For example, in natural ferroan dolomites, Fe substitutes for Mg up to an Fe/(Fe+Mg) ratio of 0.2 [16]. Finally, a major carbonate category is the hydrous carbonates, which incorporate the OH^- group and crystallize in the monoclinic system (Figure 3d). The type of metal cations present in the structure can vary a lot, while usually they occupy octahedral crystallographic sites. In this category belong "bizarre" carbonate minerals with mixed anionic groups, such as mixtures of carbonates with silicates, phosphates, sulfates or containing uranyl, arsenate or halogen ionic groups. The most typical mineral examples of this group are malachite [$Cu_2CO_3(OH)_2$] and azurite [$Cu_3(CO_3)_2(OH)_2$].

The genesis processes of carbonate minerals and rocks may vary, but they all require somehow a water (rain, ocean…etc) and a CO_2 (usually in the atmosphere) source. Limestone, for example, is the most famous example of a carbonate rock and its formation relates to the sedimentation processes in the oceans, while it can have both biogenic and abiogenic character (Figure 4a). During this chemical process, carbon dioxide from the atmosphere (or other sources) is dissolved in seawater and reacts to form carbonic acid (H_2CO_3), which is unstable (in seawater) and thus releases first one H^+ to form the bicarbonate anionic group (HCO_3^-) and later the second H^+ in formation of the carbonate ion (CO_3^{2-}). The latter combines with Ca^{2+} (or other divalent cations dissolved in the seawater) and forms calcite ($CaCO_3$). Bivalves, corals, foraminifera and other sea-organisms benefit from this chemistry, too. The slow precipitation of calcium carbonate along with the deposition of skeletal fragments of marine organisms create the typical layered formation of limestones (Figure 5a, b). In the meantime, the weathering

processes of surface rocks promote the calcification processes in the oceans (Figure 4b) through the Urey reactions:

$$CaSiO_3 + 2\ CO_2 + H_2O \rightarrow Ca^{2+} + 2\ HCO_3^- + SiO_2 \qquad (Eq.\ 1)$$

$$CaCO_3 + CO_2 + H_2O \leftrightarrow Ca^{2+} + 2\ HCO_3^- \qquad (Eq.\ 2)$$
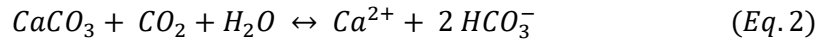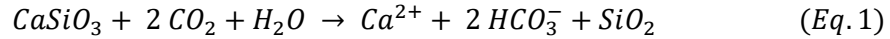
In these reactions, CO_2 dissolved in meteoric water forms carbonic acid that weathers Ca-bearing silicate rocks and carbonates on the surface of the Earth and releases Ca^{2+} ions and HCO_3^- that are in turn carried by the river networks into the oceans. In similar way, CO_2-enriched meteoric or underground water cycling in ore deposits zones leads to formation of many secondary carbonates that have rarer occurrence than calcite, such as $MnCO_3$ (Figure 5d). In other cases, meteoric or ocean water enriched in HCO_3^- can navigate in fractured plutonic rocks and react with the silicate minerals, leading in the formation of large-scale
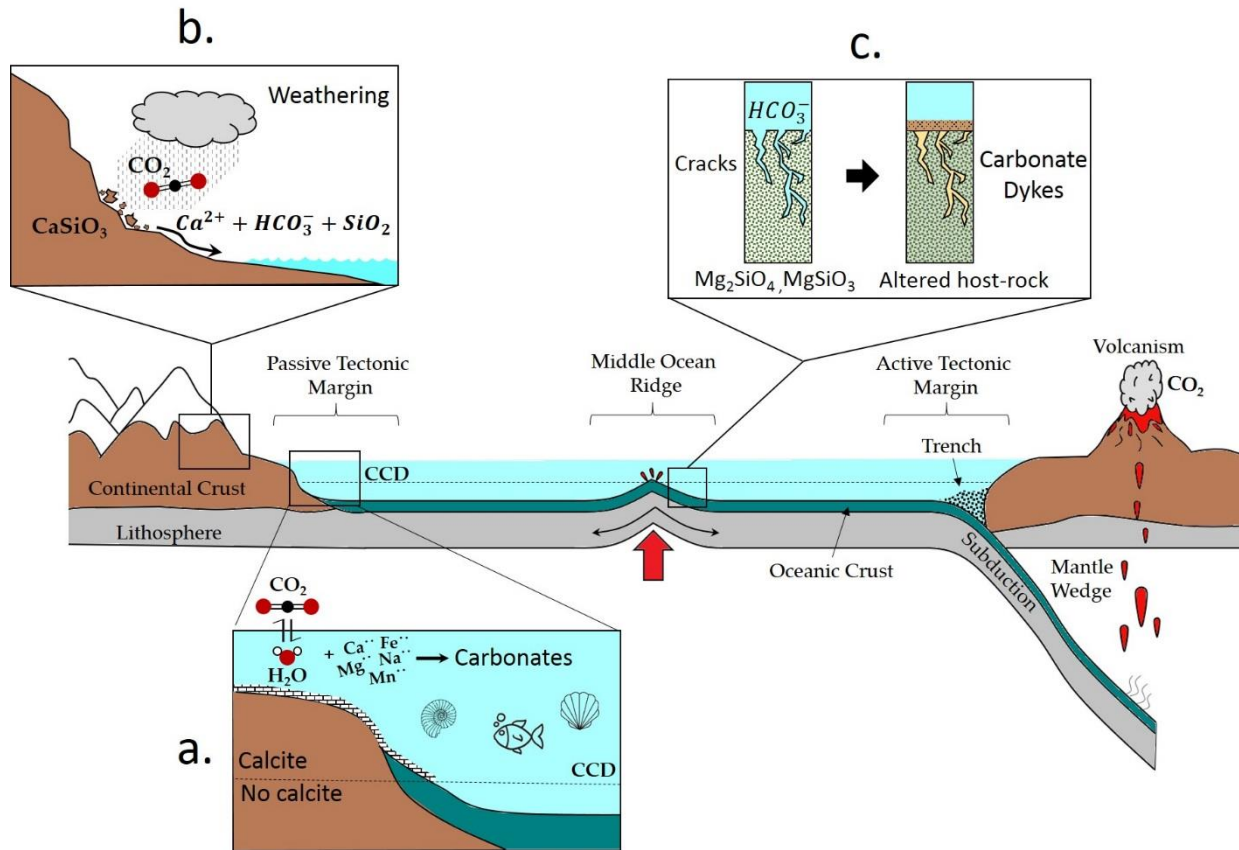
Figure 4. Explanatory sketch of important geotectonic settings and of the various reactions that lead to carbonate formation and finally to its subduction in the deep Earth. **a)** Carbonate rocks, such as limestones, form in the bottom of the ocean as a result of biogenic and abiogenic procedures. The calcite compensation depth (CCD) is strongly affecting the composition of carbonate rocks that form below it and, thus controls the chemistry of the subducted carbonates. **b)** Other carbonate minerals form due to weathering processes of surface rocks. In addition, the products of weathering reactions are washed into the ocean, which in turn promotes the calcification process. Similar to the latter procedure, **c)** some carbonates form in expense of other mineral. For example, cracks developed in peridotitic and pyroxenitic rocks, due to plate tectonics, allow seawater to alter them and form magnesite dykes.

carbonate vein networks (Figure 4c). Such is the case for example, of the carbonated peridotites often found in ophiolitic series or in deep-drilling cores of the ocean floor (Figure 5c).

Although the sedimentation rates of carbonates, and in particular calcite, in active and passive tectonic margins are very high, limestone cannot always precipitate over the whole ocean floor. Calcite formation is restricted above the "calcite compensation depth" (CCD); this is the depth in the oceans below which $CaCO_3$ becomes soluble in water and therefore no calcite is preserved. The CCD level varies from one ocean to another, but also over geologic time [17]. For example, the CCD level is placed today at about 4500 and 5000 m below the sea surface in the Pacific and the Atlantic oceans, respectively. However, due to increase concentration of CO_2 (i.e. increased volcanism) and the higher water temperatures during the Cretaceous period (i.e. 66-145 Mya), the CCD is believed that was located at shallower depths [18]. The dissolution of calcite into seawater begins before the CCD level is reached, and thus rocks from this depth range (i.e. $CaCO_3$ dissolution start depth to actual CCD depth) are often characterized by high Fe and Mn contents [17-19]. Below the CCD level, clay and radiolarite (Si-rich rock composed of radiolarians remains) formations dominate the ocean floor (Figure 5e). It is clear, that the position of the CCD level close to the subduction zones is very crucial for the type (and chemistry) of sediments that contribute to the deep carbon cycle [20, 21].

1.2.2. The deep carbon cycle (fluxes and budgets)

All the following are carbon-source representatives in a subduction zone: carbonate rocks (mainly limestone and dolomite that gradually become enriched in Fe and Mn with increasing ocean depth), carbonated mafic to ultra-mafic plutonic rocks within the oceanic crust (e.g. carbonated peridotites/dunites/eclogites containing mostly magnesite), seawater (enriched in CO_2 or HCO_3^-), elemental carbon (graphite) and hydrocarbons (e.g. CH_4, petroleum), other organic carbon (e.g. oxalates), the deep biosphere and others. From all the above, carbonates are believed to be the major carriers of carbon into the deep Earth [22]. On the contrary, carbon returns to the Earth's surface/atmosphere through the following mechanisms: volcanism (mainly CO_2 degassing in arc, back-arc, ocean-island or middle-ocean-rift volcanoes), and diffusion venting. However, the most effective way for carbon outgassing is via volcanoes, such as the Mount Etna, which currently accounts for ~10 % of the global CO_2 emissions (Figure 5f) [23]. In addition, carbon can be "trapped" (i.e. never return in the atmosphere) in the following settings: the deep Earth (upper/lower mantle and core in the form of diamonds, fluids, carbonate melts, solid carbonates and carbides), and the lithosphere and crust (recycled C-bearing material that was never exhumed on the surface). Carbon ingassing into the mantle through subduction,

cycling within the Earth and outgassing in the atmosphere, a process known as the "deep carbon cycle",
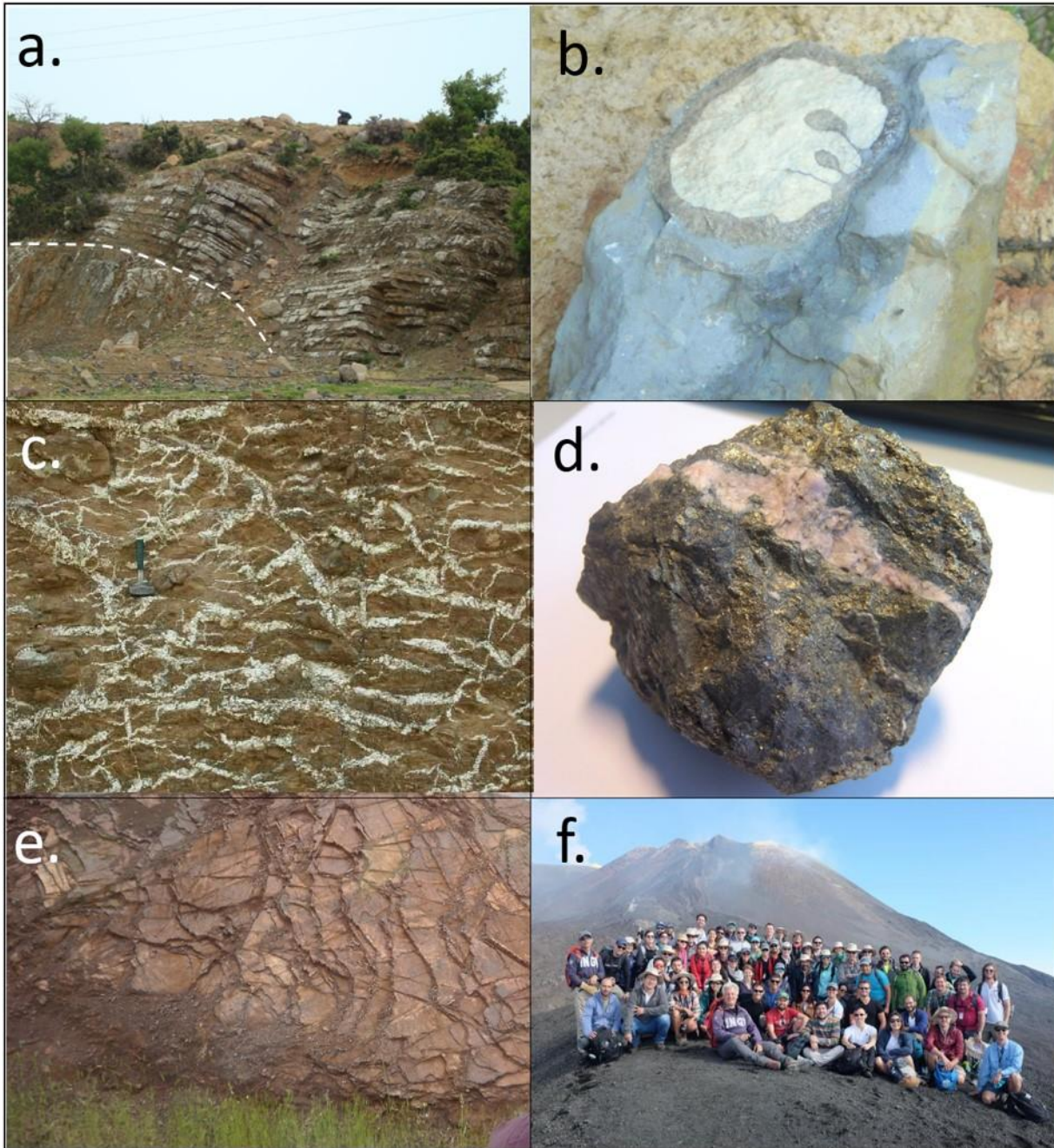
Figure 5. Selected representative photographs of carbonate systems and others. **a)** The characteristic layered structure of a limestone intruded by an andesitic dyke forming a Skarn zone (Sounio, Greece). **b)** Sampling a fossiliferous limestone that contains a hippurite fossil, characteristic of the upper Cretaceous period (Chaeronea, Greece). **c)** Excavation site of a magnesite ore deposit, showing the complex framework of magnesite dykes inside its highly altered peridotitic host-rock (Gerakini, Greece). **d)** Sampling a galena-pyrite-sphalerite hydrothermal ore deposit, where rhodochrosite is a vein-filling material (Stratoni, Greece). **e)** A radiolarite formation found on top of an ophiolitic series, indicating sedimentation at ultra-deep ocean environments, where calcite cannot form anymore (Pindos, Greece). **f)** The Mount Etna is degassing great amounts of CO_2 in the background during the 3rd early career workshop organised by the Deep Carbon Observatory (photo credit ®DCO – Sicily, Italy).

is a very complex procedure that requires the expertise of many different scientific disciplines. In this framework, global research programs, such as the Deep Carbon Observatory (DCO), were launched that are dedicated to the intensive and versatile studies of carbon's role in and on the Earth.

One of the most important challenges in the deep-carbon-cycle research is the quantification of carbon fluxes and reservoirs (i.e. what goes in, what goes out and what stays). This has been proved to be a very difficult task [e.g. 6, 22, 24-27]. Two studies have been by far the most popular on this field, namely by Dasgupta and Hirschmann (2010) [22] and a reevaluated version by Kelemen and Manning (2015) [24] (Figure 6, Table 1). Such studies are based on large databases that include characterized rock-samples and inclusions from multiple locations on Earth and datasets from monitored volcanic emissions globally, while they also incorporate results from experimental studies and *ab initio* calculations (e.g. phase relations, melting curves, elements partitioning etc.…). Their goal is to describe the expected upper and lower C concentration limits in various geotectonic settings.

Dasgupta and Hirschmann (2010) suggested that 90 % of the Earth's carbon has segregated into the mantle and core (Figure 6a). More concretely, the authors proposed that the modern mantle and core have a total carbon budget of 80-1250 and 2000-8000 Pt, respectively. In addition, they estimated that every year 54-88 Mt of carbon are introduced to the deep Earth in subduction zones [6], but only 31.2-46 Mt return to the atmosphere. The study concluded that 20-70 % of the original carbon input to subduction zones is returned to the atmosphere leading to the carbon "paradox" (i.e. where is the rest of the subducted carbon if not recycled?). Although other studies recognize the carbon paradox, they disagree
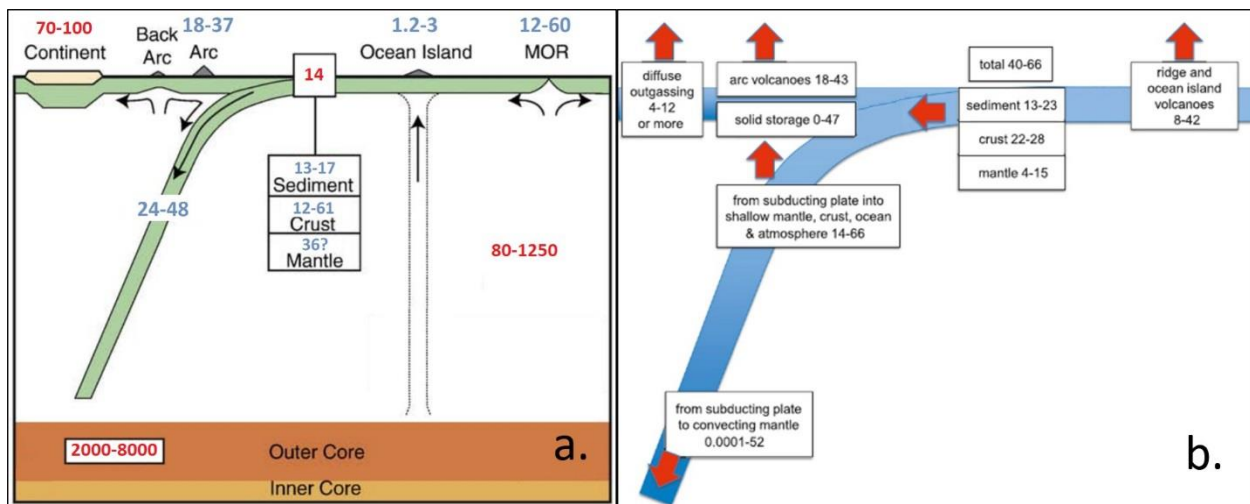
Figure 6. Estimations of the major fluxes of carbon according to **a)** Dasgupta and Hirschmann (2010) [22] and **b)** Kelemen & Manning (2015) [24]. All the shown values refer to Mt of C per year (x10^{12} g of C/yr) except for the red text in **a)** which are the total C budget in Pt (x10^{21} g of C).

Table 1. *Simplified summary of the carbon annual fluxes and total reservoirs reported in [22] and [24].*

	Dasgupta & Hirschmann (2010)	Kelemen & Manning (2015)
Input (Mt of C/yr)		
Subducted material (sediments, crust & lithosphere)	61(?)–114(?) [22] 54-88 [6]*	40-66
Output (Mt of C/yr)		
Volcanoes (arc, back-arc, ocean-ridge and island)	31.2-46	26-85
Diffuse outgassing	N/A	4-12
Reservoirs		
Budget in continental crust *(Pt of C)*	70-100	N/A
Trapped in the lithosphere & crust while trying to escape *(Mt of C/yr)*	N/A	0-47
Subducted into convecting mantle *(Mt of C/yr)*	**24-48**	**0.0001-52**
Budget in the mantle *(Pt of C)*	800-1250	N/A
Budget in the core *(Pt of C)*	2000-8000	N/A

*(?) stands for uncertain values; * authors revised values; N/A = not available*

on the percentage of carbon that is outgassed (40% in [26], 18-70% in [27]). However, recently Kelemen and Manning (2015) presented reevaluated carbon fluxes values taking into account new estimates of carbon concentration in subducting mantle peridotites, the carbonate solubility in aqueous fluids and the diapirism of carbonated metasediments (Figure 6b). The authors proposed that 40-66 Mt of carbon goes down via subduction zones every year, but most of it ends up coming back to the atmosphere. However, a substantial amount of C (14-66 Mt of C/yr) [24] is "trapped" while trying to escape the subduction slab through the mantle wedge and the overlying crustal lithologies (Figure 4). Therefore, the authors concluded that a scenario where little carbon resides in the convecting mantle (0.0001-52 Mt of C/yr) is plausible. However, they do argue that many uncertainties exist in these calculations and that future data on C-bearing minerals in eclogite facies and mantle wedge lithologies would be extremely valuable.

Carbon fluxes probably could have been different in previous geological periods. This is due to variations in seawater temperature, the atmospheric pCO_2 over periods of increased/decreased volcanic activity, subduction rates, sedimentation rates, ocean depth, water turbulence, life evolution and others (Figure 7) [28, 29]. For example, it is well known that there was an extraordinary active volcanism during the Cretaceous period that lead to increased CO_2 atmospheric content (intense greenhouse effects) and

thus, extremely high sedimentation rates (nearly 1.5 times faster than today) that lead in the formation of huge oceanic plateaus [30]. Another example is the shift from formation of shelf carbonates to deposition of pelagic carbonates in deep oceans due to the Mid Mesozoic revolution (i.e. predators with perfected body-mechanisms feed on more shells) (Figure 7d-e) [28]. The latter must have been a turning point in the nature of carbon subduction (from periodic fluxes to steady state) [24].
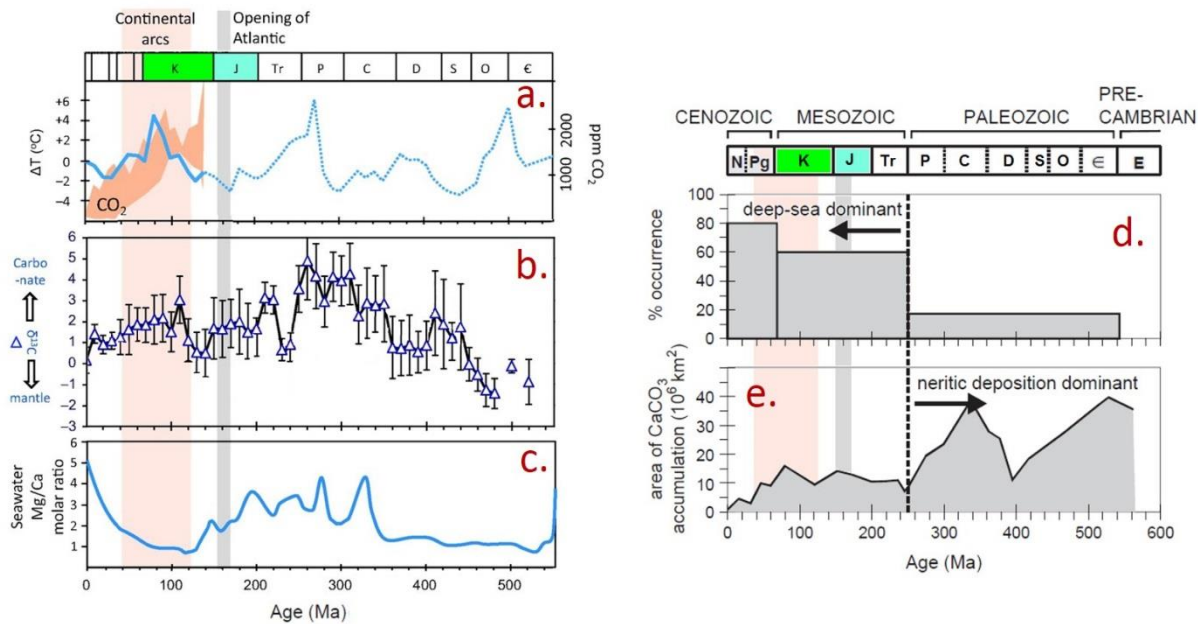
Figure 7. Changes **a)** in tropical sea surface temperatures and the atmospheric pCO_2 since the Cambrian and Cretaceous periods, **b)** seawater carbon isotopic compositions inferred from carbonates, and **c)** seawater Mg/Ca molar ratio can affect the deep carbon cycle during Earth's history. The **d)** percent occurrence of carbonates in ophiolite complexes, and **e)** the changes in the total area of platform (shallow water) carbonates indicate the mid-Mesozoic shift from formation of shelf carbonates to deposition of pelagic carbonates in deep ocean. Grey and orange shaded areas point at the approximate time of the Atlantic Ocean opening and period of enhanced continental activity, respectively. Figures **a-c** and **d-e** are slightly modified after [28] and [29], respectively.

1.3. Carbonates in the mantle

1.3.1. Natural evidences

Over the years, several discoveries of mineral inclusions and xenoliths have provided evidences of the deep carbon cycle. It is known that when carbonate sedimentary rocks are subjected to relative high pressures and temperatures they are metamorphosed (e.g. limestone recrystallization forms marble). Becker and Altherr (1992) reported one of the first evidence of marble formation from sediments

recycled in sublithospheric depths in the western Alps [31]. The authors suggested that these carbonate rock formations are the result of subducted carbonate sediments in upper-mantle depths, where they equilibrated and later exhumed to the surface. More recently, similar discoveries were made in the central Asian orogenic belt [32]. In this case, petrological and geochemical analysis of carbonatitic xenoliths in basalts (Figure 8) suggested that sedimentary limestone can be subducted to at least >120 km

Figure 8. Carbonatitic xenolith exhibits a sharp boundary with the host basalt. Adapted from [32].

depth, while their composition was found to be only slightly different from the mother carbonate rock.

The great majority of natural evidences supporting the deep carbon cycle comes from diamonds and their mineral inclusions. However, it is impressive how rarely such evidences come in the hands of a researcher. Diamonds crystallize at depths at least greater than 120 km. They are commonly found in cratonic areas worldwide and are normally hosted in volcanic rocks, known as kimberlites (and lamproites). A great part of the carried diamonds is destroyed (graphitized) if the upwelling of the kimberlitic body is not fast enough. The median concentration of diamonds in economic kimberlite deposits is about 17 ppb, while the average concentration in noneconomic kimberlites is negligible (0-2 ppb) [33]. Only 1 % of all mined diamonds come from sublithosheric depths, mainly from 250-450 km or even less from the 600-800 km window. Diamonds associated with lower-mantle-depth origins arrive in the surface carrying all signs of their torturous travel. As much as aesthetically poor such diamonds appear, the information they carry is of tremendous value for geoscientists; this is our only direct window into the deep Earth.

The Juina kimberlitic complex (Brazil) has offered some of the most precious samples in the deep carbon research [34-40]. The great diversity of mineral inclusions found in diamonds of this complex, have led scientists to believe that the Juina kimberlites may be sampling material from depths below 1,700km. In reality, several populations of diamonds exist in the region, originating from different kimberlitic bodies, but they are all washed away together in nearby river networks (i.e. alluvial deposits). Some diamond populations carry an upper mantle signature, while others originated from lower mantle depths; the latter being the dominant subgroup [37]. Carbonate mineral inclusions have been reported enclosed in Juina lower mantle diamonds, the most popular example of which is illustrated in Figure 9a [39]. An Fe-magnesite and a dolomite phase coexist with sodium phosphate phases, while the pores indicate the presence of fluid(s) phase(s) as well. The most important characteristic of this section is the sharp euhedral angles, which implies that inclusion and host have the "negative" morphology that is common in
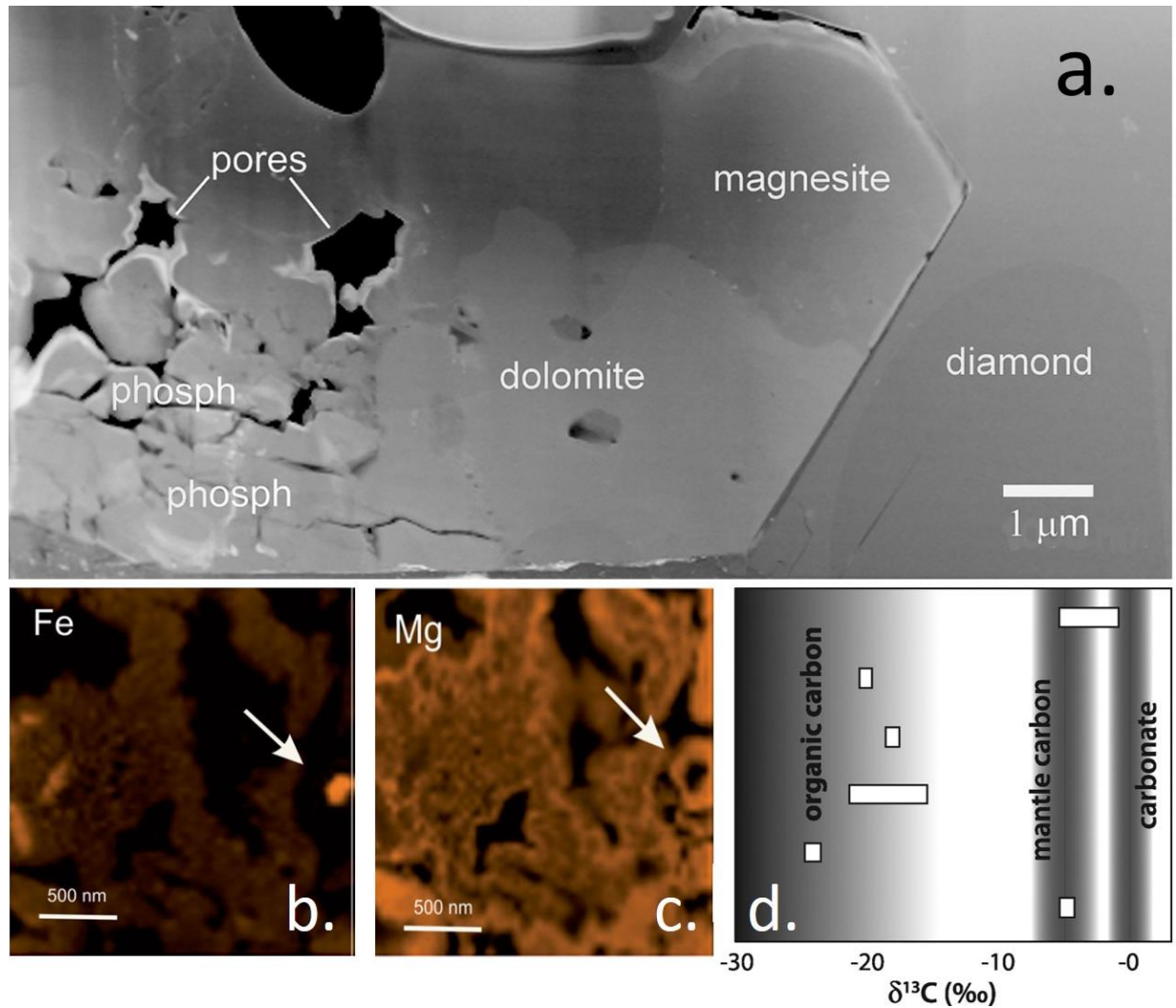
Figure 9. a) Dolomite, magnesite and phosphate mineral inclusions in a Juina diamond, as reported by [39]. The euhedral faces of the inclusion suggest that the carbonates and the host diamond are syngenetic. **b,c)** Elemental map showing the spherical inclusions of wüstite (core) and periclase (rim) in a dolomite matrix as described by [38]. d) Carbon isotopic compositions of Juina diamonds investigated in [35]. Note the great population of diamonds that carry organic carbon signatures from surface or near-surface origin (biogenic or abiogenic carbon), but also diamonds that have characteristic mantle and carbonate isotopic signatures.

syngenetic (i.e. formed together, at the same time) mineral inclusions in diamond. Ca–Mg–Fe-carbonates have been found in several Juina diamonds, but they occur mainly as micro-inclusions, thus making their chemical analysis difficult [37]. However, it is common that some carbonates have up to 3% Na_2O content or even Na_2CO_3 minerals crystallize [7, 11]. It was also found that the pores of some dolomitic inclusions contained euhedral shaped wüstite and periclase nano-inclusions, which suggest formation at lower mantle conditions (Figure 9b,c) [38, 41]. The carbon isotopic signatures (expressed as $\delta^{13}C$ ‰) of these diamonds suggest that surface sediments are transported in the lower mantle via subduction (Figure 9d)

[35, 39, 42, 43] and they provide the carbon for the diamond formation through redox melting and freezing reactions [34, 44, 45].

1.3.2. Carbonates, diamonds and the oxidation state of the mantle

The mantle is estimated to contain few hundreds of ppm by weight of carbon [46]. Carbon in the mantle is stored largely in accessory phases, such as elemental carbon, carbonates, carbides and fluid components (e.g. CO_2, CH_4) [47] due to its low solubility in mantle minerals [48]. Under the shallow oceanic upper mantle, carbonate is the stable crystalline C-bearing phase [47]. However, its chemistry may vary as we move to greater depths. More concretely, at shallow depths (<90 km) the stable crystalline carbonate is generally Ca-rich (dolomitic composition) [49]. At greater depths, the very strong partitioning of Ca in silicates suggests that magnesite or better say Fe-bearing magnesite is the stable carbonate in the presence of silicates in the Earth's lower mantle [50].

The presence of carbonate in mantle lithologies has a tremendous influence in partial melting in the mantle. However, not all the mantle domains may be favorable for storage of carbon in the form of carbonates. The very shallow part of the oceanic mantle are considered too hot to allow stability of crystalline carbonate and thus carbon would dissolve in melts or fluids [51]. On the other hand, the deeper part of the mantle can be too reduced to favor stable carbonates and thus carbon shall adopt a more reduced form, such as diamond. As we previously reviewed, diamonds are indeed often hosts of carbon in the mantle [42]. However, the recent suggestions that the Earth's lower mantle is saturated with metallic iron and that the Fe–Ni metal saturation may occur as shallow as the shallow upper mantle question the mutual stability of metal and reduced carbon in the Earth's mantle [52].

Experiments have shown that carbonate melts are unstable when infiltrating the ambient mantle and are soon reduced to diamond or graphite (Figure 10), which is immobile and its effect on melting relations in the mantle would be minimal [34, 44, 45, 47]. This process is known as "redox freezing" and leads to diamond-enriched domains in which the Fe^0, resulting from Fe^{2+} disproportionation in perovskites and garnets, is consumed, but the Fe^{3+} is preserved. More concretely, carbonate melts are generated when the carbonate-bearing subducting slab (carbonates in oceanic crust and sediments) deflects into the transition zone above the 660-km discontinuity or when stagnating in the lower mantle. On a local scale, oxidized carbonatite melt migrating into the mantle will consume metal (Fe^0) to first form iron carbide in an intermittent stage, and then further oxidize the Fe and Ni contained in the carbide to leave a mantle domain that contains all iron as Fe^{2+} and Fe^{3+} in silicates (e.g. bridgmanite) and ferropericlase and all carbon as diamond [44]. Owing to its low viscosity and high wetting properties, any excess
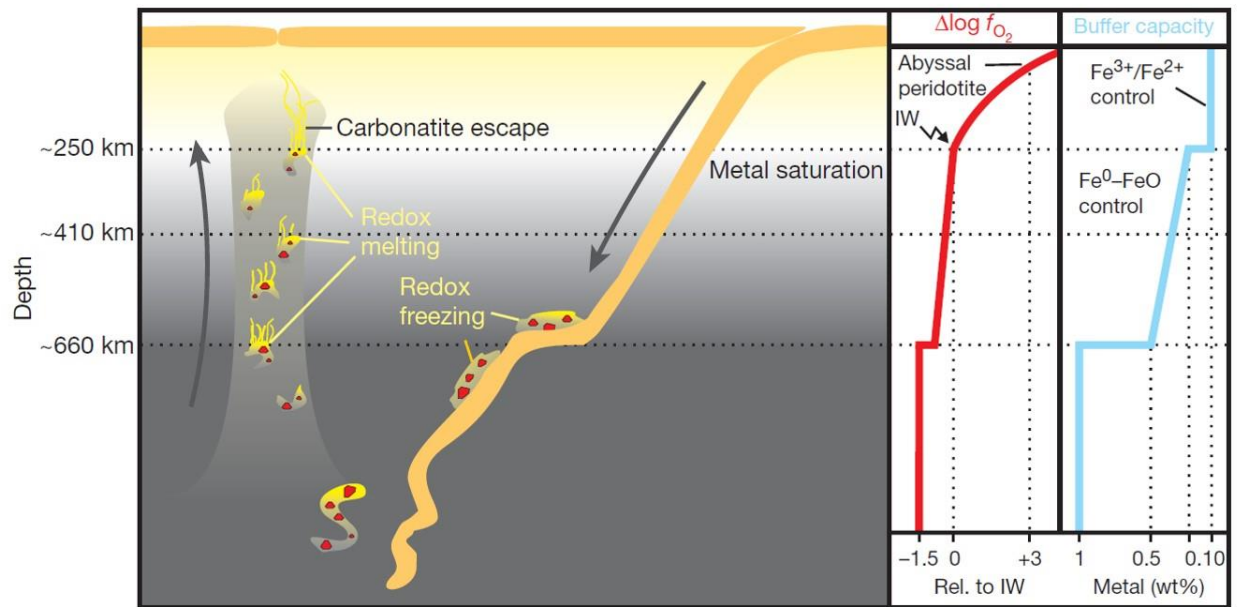
Figure 10. Carbonatitic redox freezing and redox melting caused by redox capacity changes in Earth's mantle. Main panel, cartoon illustrating a possible sequence of redox freezing and redox melting events driven by oxidation state contrasts between subducted lithosphere and ambient asthenospheric mantle. Right, potential mantle f_{O_2} (red line) and redox buffer capacity (blue line) as function of depth. Adapted from [44].

carbonatite not consumed by redox reactions would percolate upwards along grain boundaries and exhaust further (Fe,Ni)-metal and carbide until complete redox freezing (immobilization due to reduction of CO_2 to C^0) is achieved. This presumably very efficient process will eventually exhaust all buffering metal and carbide through precipitation of diamond, and result in a metal-free mantle domain where diamonds coexists with Fe^{3+}-bearing garnets, perovskite and possibly Fe^{3+}-enriched ferropericlase. The inverse process, "redox melting", occurs when such mantle domains are entrained by the upwelling mantle and cross the 660-km discontinuity (Figure 10). In this scenario, the destabilization and increased activity of Fe^{3+} will lead to the re-oxidation of diamond to CO_2 (i.e. production of carbonatite melts once again). In account of the redox freezing and melting reactions, a recent study has provided an explanation for the rarity of diamonds originating from the transition zone depths as oppose to the often occurrence of upper-mantle or even lower-mantle-depth diamonds (Figure 11) [34].

Despite the carbonate melt/mineral stability condition due to iron disproportionation-induced redox freezing, local carbonate-rich environments could proceed on their journey through the Earth' interior entering the Earth's lower mantle [53]. This scenario is supported by recent experiments on the stability field of $FeCO_3$, demonstrating that self-redox reactions in Fe-bearing carbonates can preserve carbonates in the Earth's lower mantle [54]. In addition, experiments on the $MgCO_3$ system in the presence of metallic iron (Fe^0) suggest that oxidizing conditions and slow kinetics within the subducting

slab will facilitate the transport of carbonates at the near core-mantle-boundary depths [55]. However, the role of the oxygen fugacity conditions in such experiments remains unclear. This is of high importance, since different experimental works can reach contradictory results, such is the case of experiments by [56], suggesting that $CaCO_3$ will be the stable carbonate phase in the bottom of the mantle as oppose to the conclusions of [54] and [55].
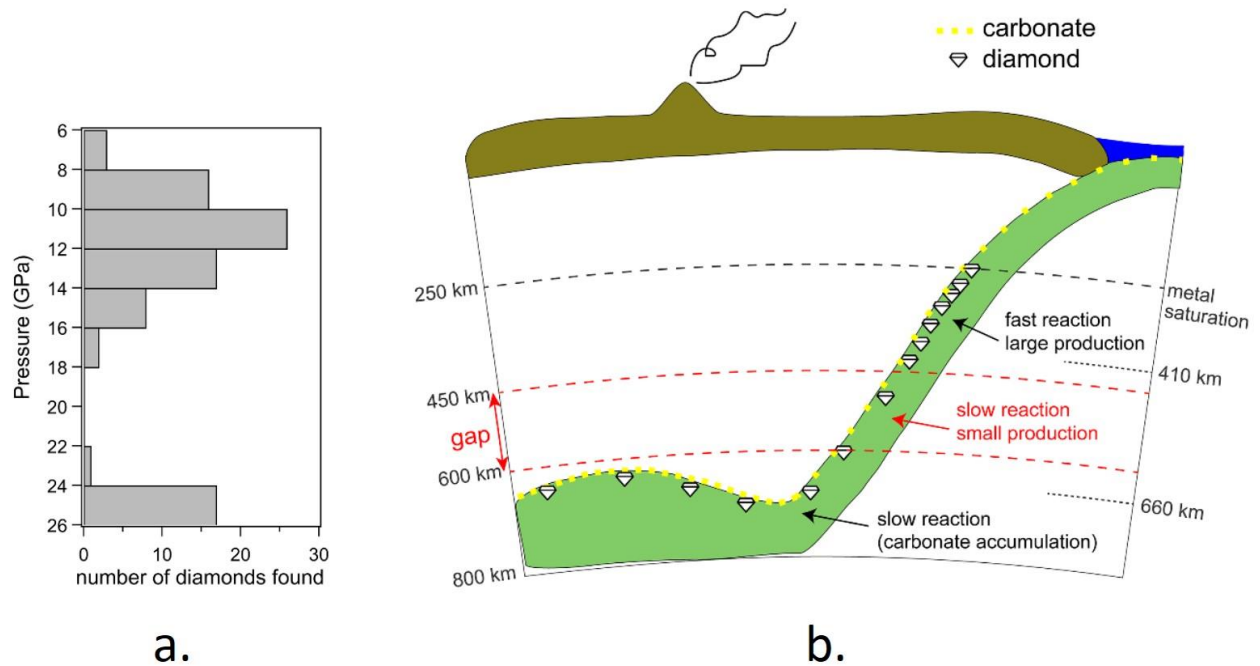
Figure 11. a) The frequency of diamonds formed at different pressure intervals reveals a gap at about 18-22 GPa (~450-600 km). **b)** Schematic illustration of diamond production through metal-carbonate reaction at the slab-mantle interface. Diamonds are produced from reaction between carbonates in the subducting slab (yellow dots) and iron metal in the ambient mantle. The reaction rates are high at depths <450 km. Accumulation of unreacted carbonates in the base of the transition zone increases the diamond production again. Adapted from [34].

1.4. Motivation for this thesis

1.4.1 Crystal chemistry of carbonates at extreme conditions

1.4.1.1. High-pressure sp^2 carbonates

The sp^2–bonding of the carbonate ion CO_3^{2-} defines the carbonate minerals/salts. Years of research on the high-pressure and high-temperature behavior of the rhombohedral carbonate minerals, in particular, represent the challenges of understanding the deep carbon mineralogy. A variety of reversible transitions to denser sp^2 metastable forms have been reported. However, each carbonate mineral has a different story to tell.
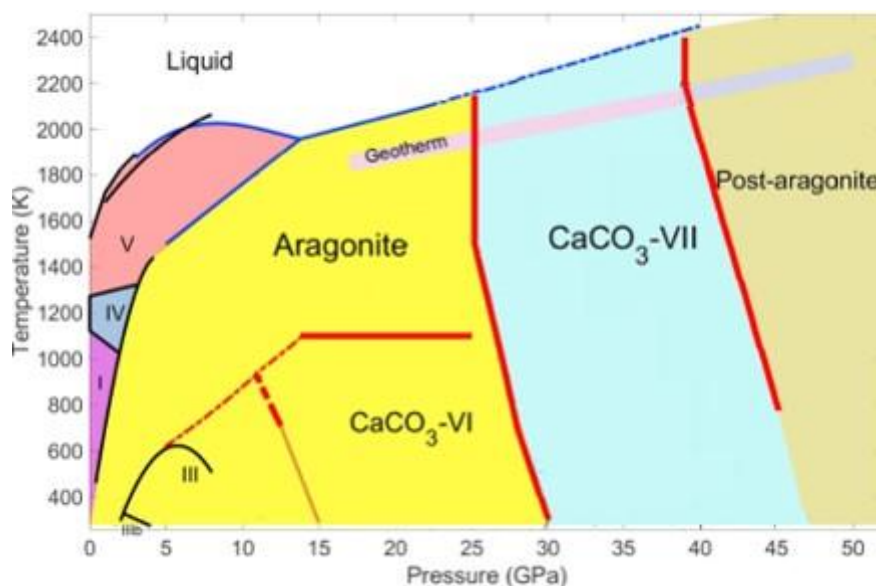
Figure 12. The phase diagram of CaCO₃. The phase stability fields of thermodynamically stable phases are represented by different colours. Simplified after [60].

Calcite (CaCO₃) is one of the earliest test-subjects to demonstrate a phase transformation to a metastable high-pressure carbonate form [57, 58]. Namely, the second order structural transformation of calcite ($R\bar{3}c$) to aragonite ($Pcmn$) at about 800 °C and above 2 GPa is the most popular [57-59]. Since then, a great number of transitions occurring at various pressure and temperature conditions have been reported, and today the complexity of the CaCO₃ phase diagram (Figure 12) [60] nearly reminds us the phase diagram of ice [61]. CaCO₃ transform to the CaCO3-II above 1.7 GPa and at room temperature, which after a lot of debate was found to crystallize in the monoclinic system ($P2_1/c$) using the single-crystal X-ray diffraction (SCXRD) technique [57, 62, 63]. CaCO3-II is stable until 2.5 GPa and above this pressure it transforms to the CaCO3-III and the CaCO₃-IIIb phases. Both phases are indexed with a triclinic space group ($P\bar{1}$), but CaCO₃-IIIb is slightly denser. Once again, following many arguments the structures of CaCO3-III and the CaCO₃-IIIb were untangled using the SCXRD method [63]. The story is repeated for the transition of CaCO3-III to CaCO3-VI above 15 GPa and eventually the crystal structure is solved (indexed in the $P\bar{1}$ space group) by [63]. The new ongoing mystery is the transitions of aragonite to CaCO₃-VII and later to post-aragonite [60, 64]. Although not at high pressures, but at high temperatures instead, the formation of CaCO₃-V and its structure solution is by far the best example of how necessary the use of the SCXRD method is, particularly in the case of low-symmetry systems [e.g. 65-69]. It took nearly a century before the SCXRD method was used and the CaCO₃-V mystery phase was finally solved [69].
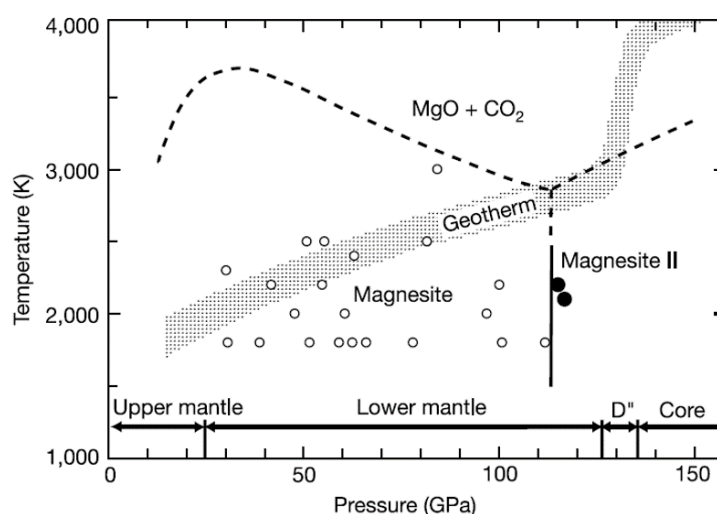
Figure 13. Possible phase relations of $MgCO_3$ in the deep mantle. Adapted from [73]

Magnesite ($MgCO_3$) has received less attention compare to calcite due to its incredible stability nearly in the pressure and temperature conditions of the entire mantle (Figure 13). According to powder X-ray diffraction (PXRD) and IR-spectroscopy experiments and DFT calculations, magnesite remains stable in the $R\bar{3}c$ structure up to at least 115 GPa and ~2500 K [70-76]. As much as all studies agree on the stability of magnesite up to Mbar pressures, they disagree on what happens to magnesite at even higher pressures. Namely, magnesite transforms to magnesite-II (Figure 13), which in a first approximation is believed to contain carbon in tetrahedral coordination with oxygens [74-76]. Several energetically favored space groups have been suggested ($C2/c$, $C2/m$, $C222_1$, $Pbca$...etc) by *ab-initio* calculation studies [74-
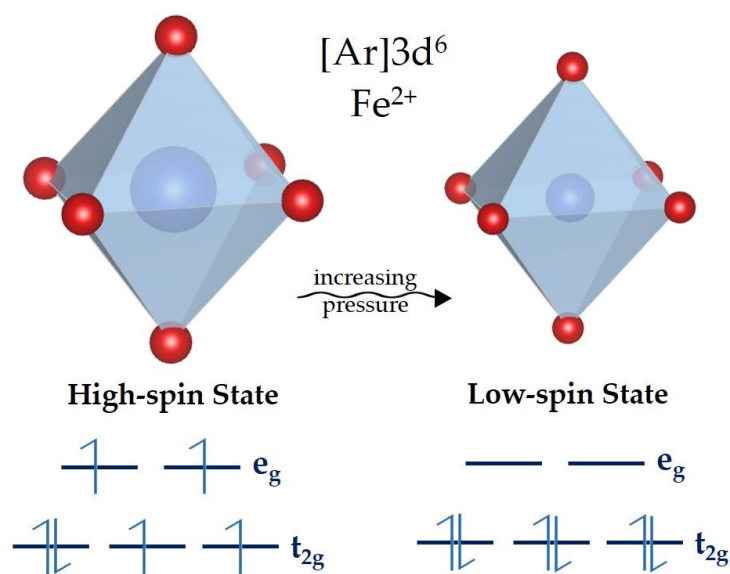
Figure 14. The transition of Fe^{2+} from high spin to low spin state.

28

76] and a few of those can explain most of the powder diffraction peaks observed experimentally. The structure of magnesite-II is an ongoing debate that possibly a SCXRD study could end. This is precisely what we did in **Chapter 8**.

Siderite ($FeCO_3$) is a carbonate that has received a lot of attention mainly due to the spin crossover that it exhibits at high pressures [54, 77-83]. The electronic configuration of Fe^{2+} is $[Ar]3d^6$. According to Hund's rules and since iron occupies octahedral sites in carbonates, the six 3d electrons split in two energy levels (e_g and t_{2g}) in the high-spin (HS) state configuration (left side of Figure 14). When high pressure is applied, it is energetically favorable for the electrons to form pairs and transition to the metastable low-spin (LS) state configuration (i.e. pressure-induced spin transition, right side of Figure 14). The electron pairing of the LS-state is inducing an instant shrink of the iron atom radius, which in turn causes and abrupt volume collapse of the FeO_6 octahedra and of the unit cell in overall (Figure 14). Although the spin transition influences the electromagnetic properties [80, 81-83] and the compressibility of siderite [77-79], it does not induce a structural transformation. The pressure-induced spin transition of Fe^{2+} in Fe-bearing carbonates has been documented by several methods, including Mössbauer spectroscopy [80], X-ray diffraction [77-79], X-ray Raman scattering [82], and Raman spectroscopy [80, 81, 83]. There is much discussion in the literature concerning the exact pressure that the spin transition takes place, whether it is sharp or not, and how impurity elements in a natural sample affect the transition. Despite the arguments, most of the previous studies agree that the spin transition in $FeCO_3$ starts around 40-44 GPa (Figure 15), while the onset of the transition can shift to slightly higher pressures with the addition of Mg. In addition, experiments in laser-heated diamond anvil cells have revealed the decomposition of siderite in several Fe-oxides, such as Fe_2O_3, Fe_3O_4, Fe_5O_7 [54] and Fe_4O_5 [84] at high temperatures (Figure 15), but
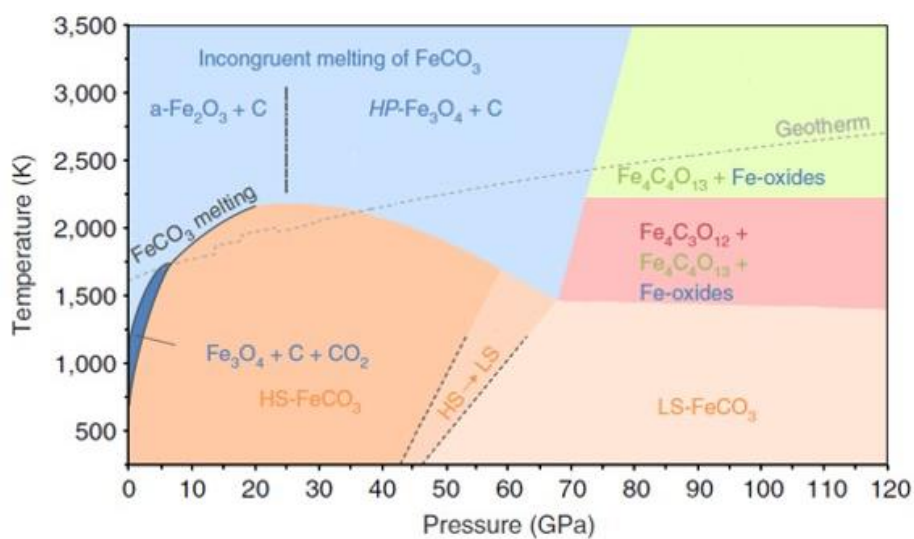
Figure 15. Stability phase diagram of $FeCO_3$ at high pressures and temperatures. Simplified after [54].
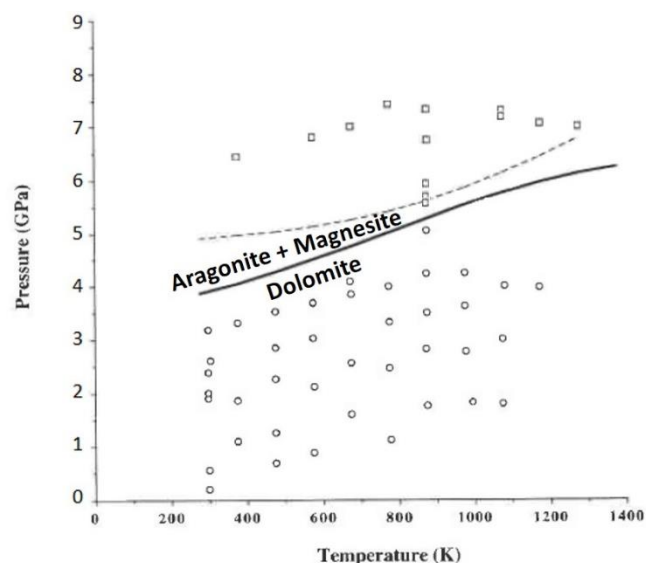
Figure 16. Calculated equilibrium curves for the reaction dolomite / aragonite + magnesite. Modified after [86].
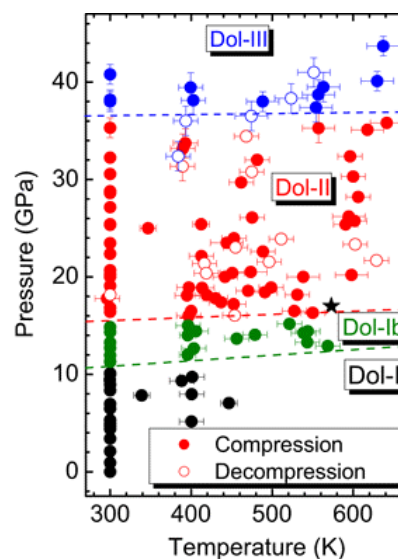
Figure 17. Phase diagram of dolomite at high pressures and temperatures. Adapted from [87].

also the transformation to new high-pressure carbonate polymorphs that contain tetrahedrally coordinated carbon to which we will refer in more details in the next section (1.4.1.2.).

Dolomite [Ca(Mg,Fe)(CO$_3$)$_2$] is consider to be a major constituent of the subducted carbonates [85], however it has drawn little attention due to the early experiments that observed decomposition of dolomite to aragonite (CaCO$_3$) and magnesite (MgCO$_3$) at relative low pressures and temperatures (Figure 16) [86]. Dolomite was revisited several years later to reveal three main second order transitions (Figure 17) to dolomite-II ($P\bar{1}$) at 17 GPa and 300 K, then to dolomite-III ($P\bar{1}$) at 36 GPa and 300 K and finally to dolomite-IV ($Pnma$) at 115 GPa and 2500 K [87-90]. The latter contains tetrahedrally coordinated carbon to which we will refer again in the next section (1.4.1.2.). The transitions dolomite-I to dolomite-Ib and dolomite-III to dolomite-IIIb have also been reported [87, 89].

Rhodochrosite (MnCO$_3$) has been in the spotlight for the past four years [95-99]. Not considered a significant constituent of the carbonate-rock assemblage in subduction zones, early studies mainly investigated the influence of Mn incorporation in the calcite and dolomite structures by means of IR and Raman spectroscopy experiments [91, 93]. In these studies, no peculiar behavior of up to 50 GPa was noticed, apart from its ability to shift the calcite phase transitions to higher pressures (Figure 18) [93]. An early PXRD study suggested formation of an unknown orthorhombic phase at 50 GPa and after laser heating [92]. However, the suggested unit cell or the orthorhombic symmetry was never observed by consequent studies. In addition, a study based on the combination of Raman and X-ray emission spectroscopies and PXRD experiments reported possible electronic transitions at 15 and 30 GPa and

30

suggested a possible change of symmetry at about 50 GPa [94]. More PXRD experiments followed by nearly the same scientific group and were coupled with IR-spectroscopy measurements and additional DFT calculations to reveal a second order transition of $MnCO_3$ to a triclinic structure ($P1$), but this time at 34 GPa [95]. Within a week away from the latter publication, a single-crystal X-ray diffraction study on $MnCO_3$ reported its transformation to MnCO3-II ($P\bar{1}$, isostructural to CaCO3-VI) at 44 GPa by inducing a 5% volume collapse [96]. Nearly a year later, the scientific group that reported the results in [95] agreed that the $MnCO_3$→$MnCO_3$-II transition takes place at ~40

Figure 18. Progressive increase in pressure of the $CaCO_3$-I to $CaCO_3$-II and $CaCO_3$-II to $CaCO_3$-III phase transitions with increase in content of $MnCO_3$. Adapted from [93].

GPa and performed a series of experiments to observe the various decomposition products of $MnCO_3$ using PXRD and X-ray near-edge structure spectroscopy (Figure 19) [97]. The complex PXRD patterns were interpreted largely based on the phase diagram of Mn_2O_3 reported in a previous study [100], while several diffractions peaks remained unexplained. Since then, two more studies on the $MnCO_3$ system were performed [98, 99]. The first study observed the $MnCO_3$→$MnCO_3$-II transition at ~32 GPa using Raman spectroscopy, but argued that their discrepancy in the pressure-range of the transition is due to non-

Figure 19. The figure is slightly modified after [97] and summarizes their experimental results. The phase diagram for Mn_2O_3 as described in [100] was used for comparison.

hydrostatic conditions in their diamond anvil cells [98]. The second study carried out a random structure search for $MnCO_3$ at high pressures using DFT calculations and suggested several potential high-pressure polymorphs, among which a phase based on tetrahedrally coordinated carbon above 65 GPa [99]. The crystal-chemistry of $MnCO_3$ appears complex, like $FeCO_3$, while at high temperatures $MnCO_3$ is associated with the formation of various Mn-oxides that are of high interest in material science [e.g. 100,101]. Thus, further clarification on the stability phase diagram of $MnCO_3$ is required.

The high-pressure and high-temperature behavior of other carbonate minerals is poorly explored. Smithsonite ($ZnCO_3$) was found to be stable in the calcite-type structure ($R\overline{3}c$) up to ~50 GPa [102]. Additional a *ab initio* calculations predicted that $ZnCO_3$ will undergo two phase transitions at 78 GPa ($C2/m$) and at 121 GPa ($P2_12_12_1$) [103], but they were never confirmed experimentally. Otavite ($CdCO_3$) undergoes a structural transformation to an unknown phase above 19 GPa, while above 30 GPa it adopts the aragonite structure [104]. A comparative compressibility study of rhombohedral carbonates, demonstrated, among else, the stability of spherocobaltite ($CoCO_3$) and gaspeite ($NiCO_3$) in the $R\overline{3}c$ structure up to ~8 GPa [105]. Besides trigonal carbonates, malachite's ($Cu_2CO_3(OH)_2$) and azurite's ($Cu_3(CO_3)_2(OH)_2$) compressional behaviors were studied up to 10 and 11 GPa, respectively [106, 107]. Finally, little attention has been paid on aragonite-type carbonates, such as strontianite ($SrCO_3$), cerussite ($PbCO_3$) and witherite ($BaCO_3$) [108-110].

Reviewing the high-pressure behavior of sp^2-carbonates demonstrates how distinct the character of minerals that belong to the same family can be. Conflicting results presented from several authors over the years have made the classification of carbonates at Earth's mantle conditions a difficult (and unnecessarily confusing) task. Important source of discrepancies among studies can arise from differences in the samples such as variations in chemistry (i.e., natural versus synthetic) and/or the presence of significant non-hydrostatic stress (i.e., single crystal versus polycrystalline). In addition, PXRD in combination with theoretical calculations aiming to structure prediction have been the most frequent tool to use among previous studies, but the results were often corrected by means of accurate structure solutions and refinements in single-crystal X-ray diffraction studies. Search for crystallochemical regularities after the careful investigation of the individual behavior of pure synthetic carbonate end-members at extreme conditions is essential. Such a study will help in answering important questions. For instance, why calcite behaves so differently than magnesite? What is the effect of the metal cationic radius on the stability fields of carbonates? Why some trigonal carbonates transform quickly to denser sp^2-polymorphs, while others show incredible sustainability in the $R\overline{3}c$ structure? Will carbonates dissociate in formation of oxides, diamond or other C-bearing fluid phases during subduction or will they endure the

extreme conditions that exist in the deeper parts of our planet? These and many others are key-questions that describe our motivations behind the results presented in **Chapter 5 and 6.**

1.4.1.2. High-pressure sp^3 carbonates

A key concept in understanding the effects of high-pressure on the crystal chemistry of minerals is the tendency of cations to increase their coordination number (CN) with increasing pressure. This is particularly exemplified by most silicate minerals subjected to high pressures (Figure 20a-d) [111-113]. Silicon strongly prefers four-coordinated crystallographic sites due to the sp^3 hybridization. Consequently, silicon is mainly found tetrahedrally coordinated with oxygens in silicate minerals characteristic of the crust and the upper mantle (e.g. α – quartz or enstatite, Figure 20a,c). This low CN along with the mesodesmic nature of Si-O bonds result in a significant structural flexibility (i.e. silicates can easily polymerize to form a number of different configurations, like chains, rings, sheets or 3D frameworks). However, once subjected at pressures relevant to the Earth's lower mantle, hypervalent states are favored and silicon resides in octahedral sites (i.e. six-coordinated with oxygens), leading to more compact, higher-density phases (e.g. stishovite or bridgmanite, Figure 20b, d).
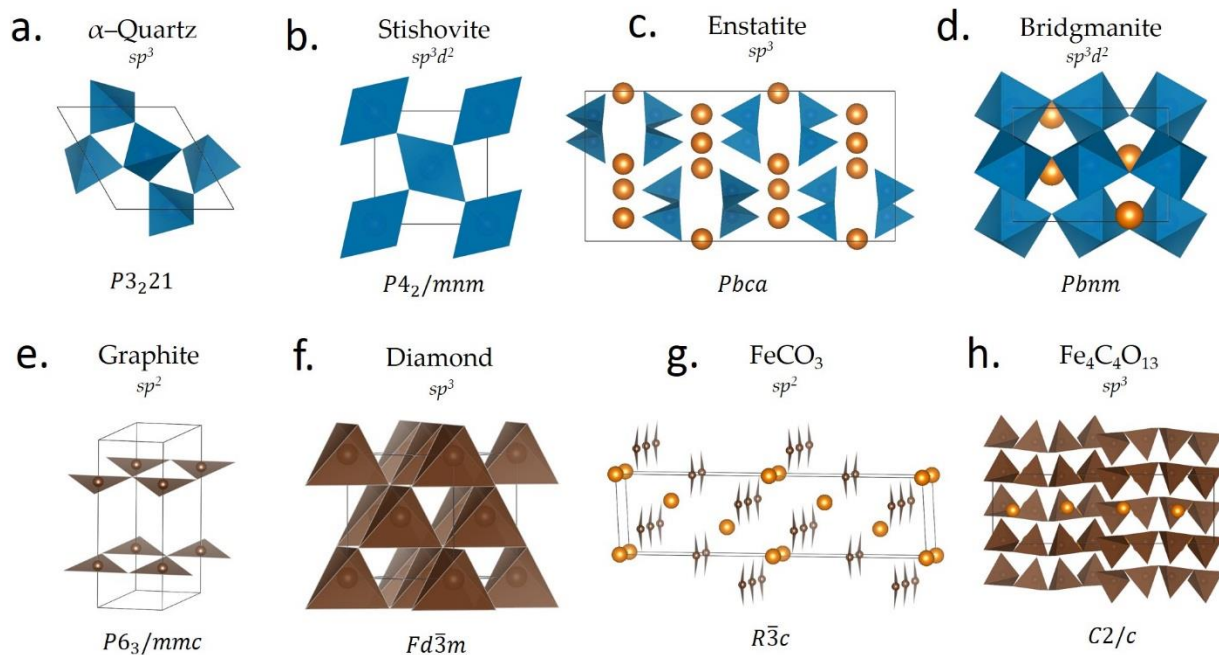
Figure 20. Examples of pressure-induced increase in cations coordination number in silicates (a-d) and in carbon-bearing phases (e-h). **a,c)** SiO$_4$ tetrahedra in α-quartz and enstatite shift to **b,d)** SiO$_6$ octahedra in Stishovite and bridgmanite at high pressures, respectively . Similarly, **e,g)** three coordinated carbon in graphite and siderite transitions to **f,h)** four coordinated carbon in diamond and Fe-tetracarbonate at high pressures, respectively.

According to the Pauling's first rule, cations with smaller radii tend to have smaller coordination numbers at ambient conditions. Therefore, not surprisingly, C^{4+} (0.15 Å) is often found in three-coordinated crystallographic sites (i.e. sp^2 hybridization) as oppose to the Si^{4+} (0.26 Å) atoms [114]. This is true at ambient conditions, however, at high pressures, Pauling's first rule is often lifted due to the repulsion forces developed due to the decrease of interatomic distances. The shift from sp^2 bonding (trigonal coordination) to sp^3 bonding (tetrahedral coordination) in carbon-bearing phases is typically exemplified by the transformation of graphite (Figure 20e) to diamond (Figure 20f) [115]. Apart from carbon allotropes, CO_2 was predicted to adopt an sp^3–based structure at high pressures (~20 GPa) [74]. Later, the new CO_2 phase, otherwise known as CO_2-V (β-cristobalite-type structure, $I\bar{4}2d$), was confirmed experimentally [116]. Given the high-pressure behavior of the aforementioned carbon-bearing systems, it seemed very likely that carbonates, which traditionally involve carbon in trigonal coordination (e.g. $FeCO_3$–siderite, Figure 1g), will eventually transform to new high-pressure phases containing tetrahedrally coordinated carbon (e.g. $Fe_4C_4O_{13}$–tetracarbonate [54], Figure 1h). These new phases are known in the literature as sp^3-carbonates, tetracarbonates or carbonates with tetrahedrally coordinated carbon.

Early studies on this path were mainly based on theoretical predictions [117, 118], which were not always positively confirmed by experiments [73, 119]. However, even in the cases that a suggested structural model was supported by both experimental and theoretical work, it was not necessarily reproducible by later studies, a matter which lead to many debates in the following years [e.g. 74, 75, 120-123]. The main reason for discrepancies in between studies, not only was the different purity of starting materials, the different diamond-anvil-cell-preparations, the different structure-prediction packages or ,simply, the different interpretations by several authors, but it was mostly the lack of a method that would undeniably solve the structure of the novel phases with great accuracy. Such a method is the single-crystal X-ray diffraction and it was implemented by recent studies that revealed the structural complexity and

a. $Fe_4C_3O_{12}$ **b.** $(Mg,Fe)_4C_4O_{13}$ **c.** $Ca(Fe,Mg)_2C_3O_9$

$R3c$ $C2/c$ $Pnma$
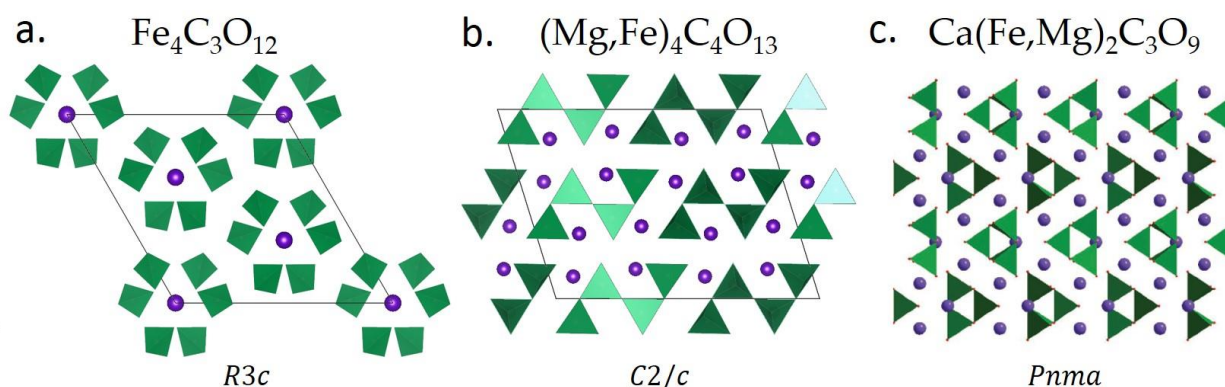
Figure 21. Examples of sp^3–carbonates characterized by single-crystal X-ray diffraction. The CO_4 tetrahedra can appear **a)** isolated [54], **b)** in chains [54, 124]or **c)** in ring-like [89] arrangements.

variability of some sp^3–carbonates (Figure 21) [54, 89, 124]. Allegedly, tetracarbonates polymerize to form a number of different configurations either as isolated $C_3O_{12}^{-12}$ units (Figure 21a), zigzag-shaped $C_4O_{13}^{-10}$ chains, (Figure 21b), $C_3O_9^{-6}$ rings or many others that were predicted [74], but await to be experimentally discovered.

Instinctively, tetracarbonate analogies to silicates are invited, and indeed many authors often try to compare the two [e.g. 54, 73-75, 116-124]. Although provocative, the analogy is yet very limited. The great majority of the sp^3–carbonate structures suggested are very different from the known silicate phases and belong to new structure types. Unlike carbonates, silicates own their enormous diversity of structures, their high compressibility, and easy glass formation to the great flexibility of the intertetrahedral Si-O-Si angle [74] (Figure 22). Inspecting the energy variation as a function of the Si-O-Si angle in the H$_6$Si$_2$O$_7$ model [74, 125] (red dashed line in Figure 22) reveals only a shallow minimum at about 135° (i.e. there is a little variation of energy in a wide range of angles). On the other hand, the C-O-C angle in the H$_6$C$_2$O$_7$ model [74] (black dotted line in Figure 22) displays a deep minimum at about 124° and very sharp energy variations accompanying small changes of the angles. Therefore, it is suggested that carbonates will present limited structural divergence, lower compressibility and lower propensity to amorphization than silicates. Indeed, the C-O-C angles in the experimentally observed tetracarbonates (Figure 21) are in the relative narrow range of 112–120° at Mbar pressures, while none of those phases were reported to be retrievable at ambient conditions (i.e. unstable phases).
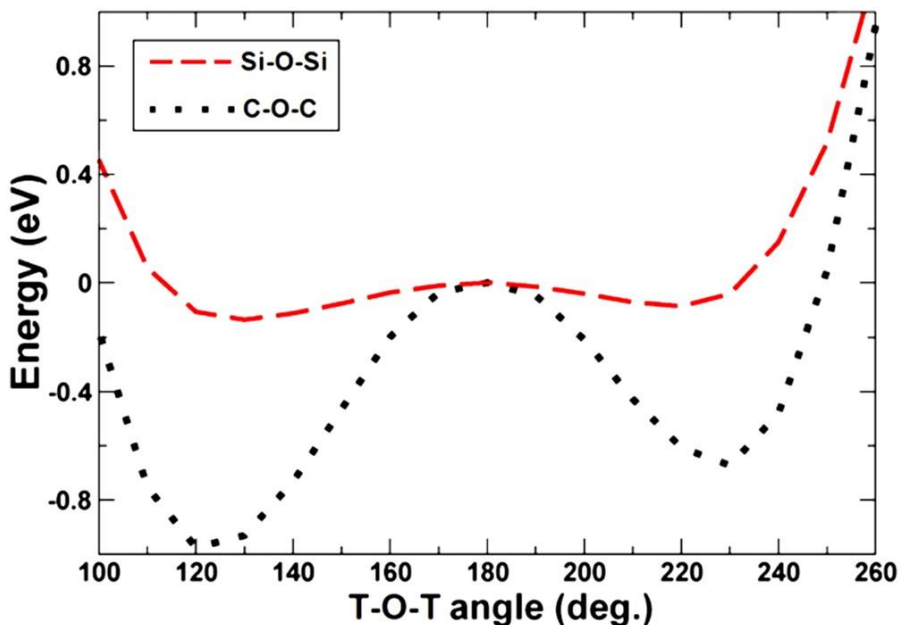
Figure 22. Energy variation as a function of the T-O-T angle in the H$_6$Si$_2$O$_7$ and H$_6$C$_2$O$_7$ models. Optimum angle for C-O-C is nearly 124° and 135° for Si-O-Si. Figure adapted from [74].

It is highly interesting that the novel tetracarbonates (Figure 21) are mainly discoveries in the $(CaCO_3–)MgCO_3–FeCO_3$ solid solution system. Is this because the $CaCO_3–MgCO_3–FeCO_3$ system represents the most realistic carbonate compositions expected in the deep Earth and thus studies were purposely dedicated to this system? The Fe-endmember carbonate ($FeCO_3$), as well as $FeCO_3$-$MgCO_3$ solid solutions have demonstrated through experiments their ability to form sp^3-carbonates [54, 124]. The sp^2–to–sp^3 transformation of $MgCO_3$ has long been predicted with great consistency among studies [74, 75], but never experimentally confirmed. On the other hand, the sp^2 shift of pure $CaCO_3$ to sp^3-type bonding is a subject under a lot of debate, with very contradictory predictions and absent experimental justifications [e.g. 74, 117, 119, 121, 122, 126]. Given the very different sizes of the Ca, Mg, and Fe cations, there might be another reason why Fe and Mg, as oppose to Ca, are preferentially incorporated in the tetracarbonate structures. To date, little knowledge do we have on the formation of tetracarbonates by other metal carbonates or the possible effect of cationic radius size on the stability fields of novel high-pressure carbonate polymorphs. Are there any systematic relations on which carbonates have a probability to form tetracarbonate-structures at high pressures? Are there other CO_4 tetrahedra-configurations that we have not discover yet? Which predicted tetracarbonate-structures have a valid experimental counterpart? These are key-questions that describe our motivations behind the results presented in **Chapter 6 and 8.**

1.4.2. Carbon seismic detectability

As we described in a previous section, samples originating from transition zone and lower mantle depths are extremely rare. Indirect methods to study the Earth's deep interior come from experimental and theoretical studies, but also through geophysical applications. A common geophysical technique used to derive information on a global scale is seismic tomography. According to this imaging method, primary (P), secondary (S) and surface waves can be used for tomographic models of different resolutions based on seismic wavelength, wave source distance, and the seismograph array coverage [127]. The data received at seismic recording stations around the world are used to solve an inverse problem, wherein the locations of reflection and refraction of the wave paths are determined. This solution can be used to create 2D and 3D images of velocity anomalies (perturbation maps) which may be interpreted as structural, thermal, or compositional variations.

Some examples of seismic tomography images near subduction zones are shown in Figure 23 [128]. In this plots, bins faster than average are marked with blue colors to indicate colder regions, while slower bins are marked with red to represent hotter areas. The effect caused by chemical variations are

usually less pronounced than the thermal ones. In areas where subduction takes place, local tomography models reveal areas of higher velocities (Figure 23). Those are interpreted as subducting slabs, which are colder than the surrounding mantle material. The great majority of modern subducting slabs tend to be trapped within the transition zone (410-660 km). However, few subducted slabs have been observed to
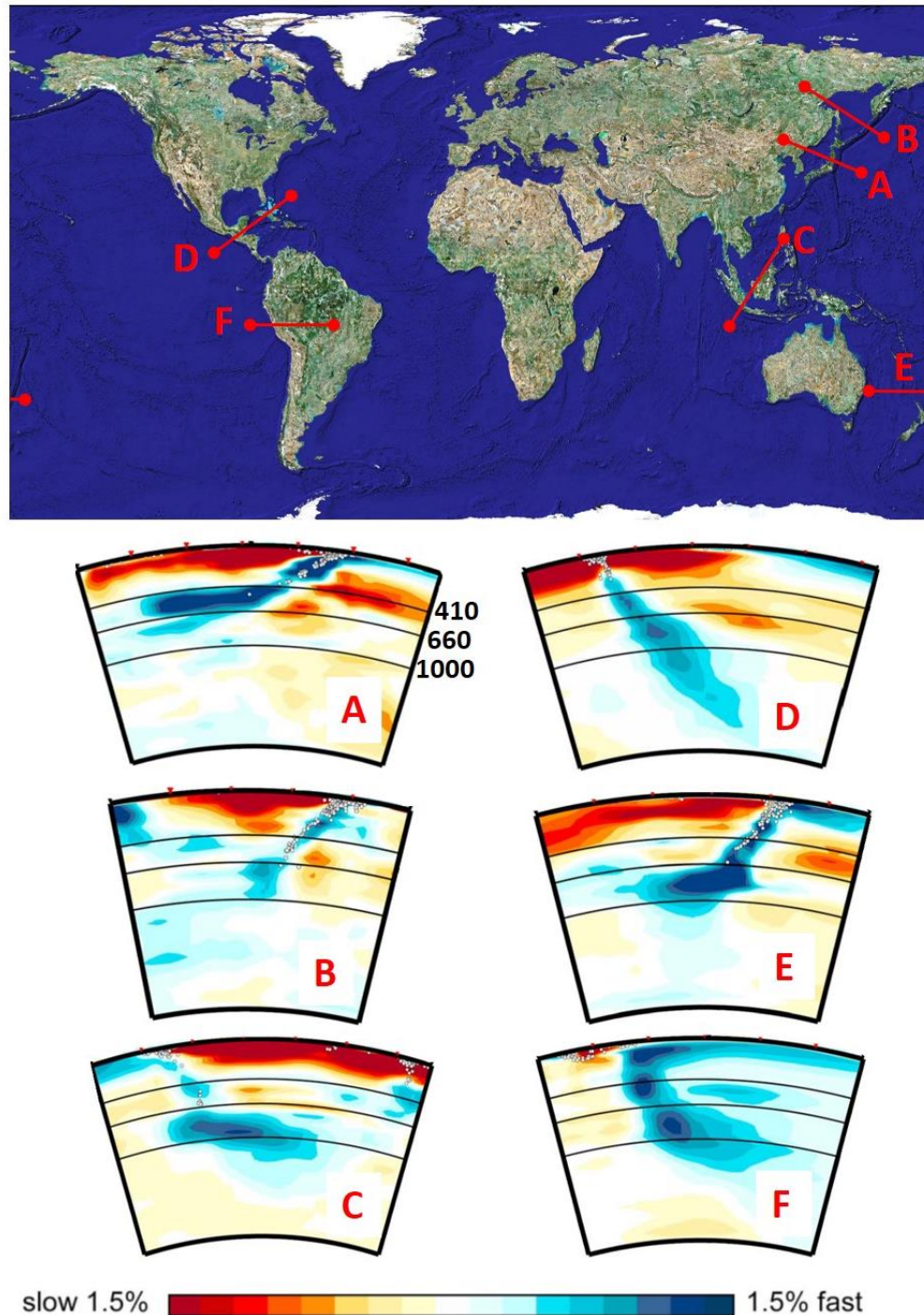
Figure 23. Selected tomography images along famous subduction slabs that stagnate or penetrate the 660 km discontinuity. **A)** Honsu **B)** Kurile **C)** Java **D)** Central America **E)** Tonga-Kermadec and **F)** Northern South America. Tomographic images adapted and slightly modified after [128].

deeply penetrate the 660 km discontinuity, such as the subduction zone in Indonesia (Figure 23C), Central America (Figure 23D), Tonga (Figure 23E) or Northern South America (Figure 23F). The case of the subduction slab in Central America is particularly interesting, since the tomographic images are a snapshot of the remnants Farallon-plate [129]. Farallon is an ancient tectonic plate that used to be active during the Mesozoic and experienced the intense carbonate sedimentation rates of the Cretaceous period (see section 1.2.2.).

The transition zone was traditionally assumed to be seismically isotropic due to lack of evidences supporting the opposite. Increasingly, however, evidence suggests that ordering of material over seismic wavelengths occurs there and at deeper layers, but it is unclear what causes this [130]. Ringwoodite, present between the 520 km deep discontinuity and the 660 km discontinuity is nearly isotropic [131]. Wadsleyite, the dominant mineral between the 410 km discontinuity and the 520, is moderately anisotropic [132], but there is still uncertainty regarding its deformation mechanism and it appears that though it may form a weak lattice preferred orientation (LPO), this decreases with water content [133]. Deeper still, magnesium silicate-perovskite in the uppermost lower mantle is highly anisotropic and may develop a significant LPO if large strains exist near the 660 [134-136]. Slab mineralogy at these depths is
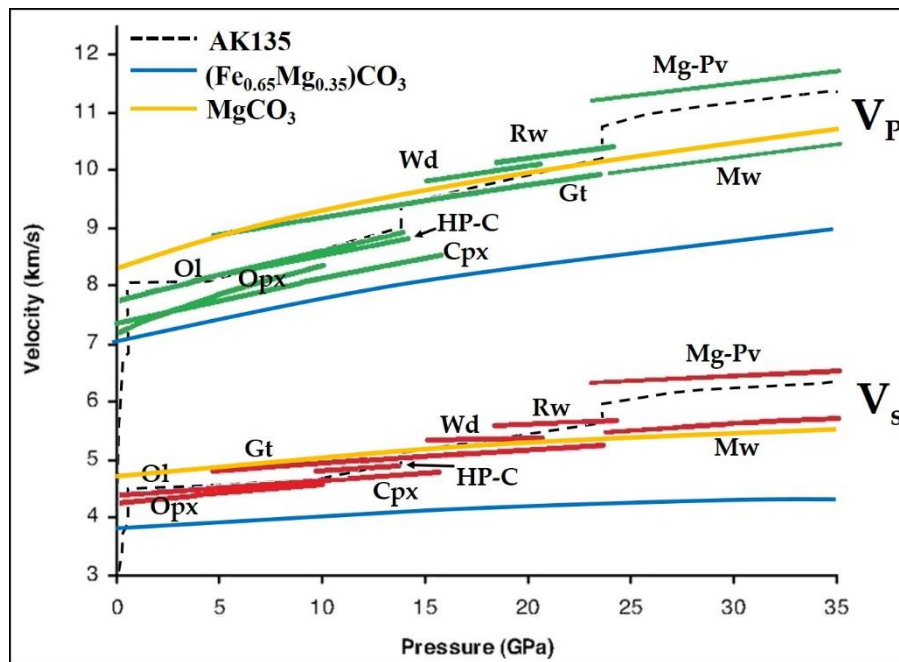
Figure 24. Primary (V_P) and secondary (V_S) wave velocities of major mantle phases (green and red lines) as a function of pressure along a 1600 K adiabatic geotherm, compared with the global seismic model AK135 (dashed black lines) and two different carbonate compositions [142, 143] (yellow and blue lines). (Ol, olivine; OPx, orthopyroxene; CPx, clinopyroxene; HP-C, high-pressure clinopyroxene; Wd, wadsleyite; Rw, ringwoodite; Gt, garnet; Mg-Pv, magnesium silicate perovskite; Mw, magnesiowüstite). Modified after [145].

more uncertain. Olivine may be metastable in narrowing regions of slab cores [137], water may lead to significant amounts of hydrous phases in the subducted lithosphere [138], and akimotoite may exist in the high-pressure, low-temperature slab cores [139].

Carbonates, however, were not really considered as possible candidates to explain the velocity anomalies in the mantle so far. This was mostly due to our lack of knowledge on the elasticity of carbonate minerals at high pressures and temperatures relevant to the Earth's mantle. To date, few studies reported the elasticity of $CaCO_3$ and $MnCO_3$ [140], $MgCO_3$ [141] and the $FeCO_3$-$MgCO_3$ system [142, 143] at high pressures and room temperatures using Brillouin spectroscopy (BS), inelastic X-ray scattering (IXS), ab initio calculations based on density functional theory (DFT) or impulsive stimulated light scattering (ISS). In addition, an early study reported the strong anisotropic character (up to 30%) of ferromagnesian carbonates and its velocity contrast from crustal lithologies (eclogites, peridotites) that commonly host carbonates [144]. When compared with the velocities of major mantle minerals or global seismic models (e.g. AK135, PREM), carbonates stand out, however depending on their chemical composition (Figure 24).

Ferromagnesian carbonates attracted most of the attention due to their most realistic composition, which is expected to persist in the deep Earth (see discussion in sections 1.3.2. and 1.4.1.1.). All previous studies have demonstrated the increase in acoustic velocities with increasing pressure and Mg content (Figure 24 and 25) [141-144]. In addition, their elastic properties are particularly interesting due to the presence of Fe^{2+} that undergoes a spin crossover at about ~44 GPa (see section 1.4.1.1.), and which causes an abrupt increase of velocities at higher pressures and room temperatures (Figure 25). The Fe^{2+} spin crossover affects the physical, optical and elastic
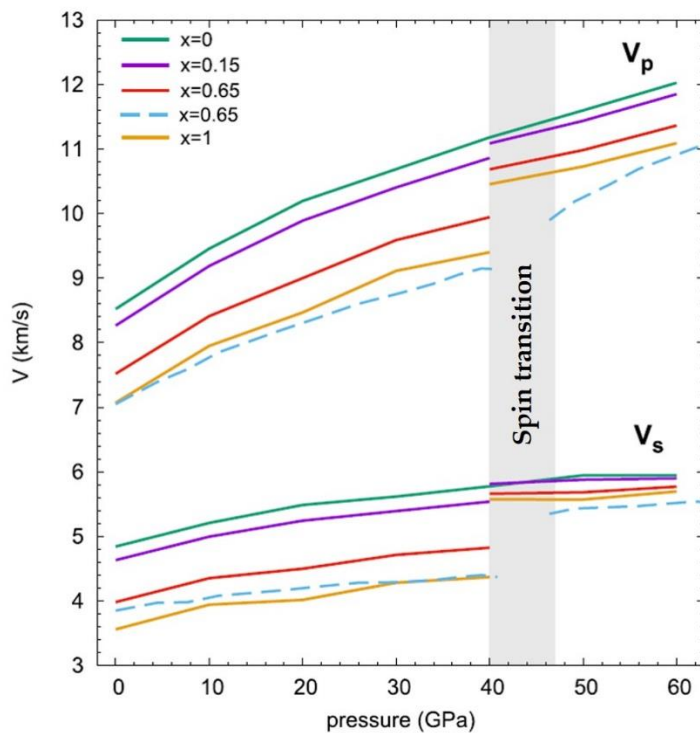
Figure 25. Calculated (solid lines) [143] and experimental (dashed line) [142] sound velocities waves of $Mg_{(1-x)}Fe_xCO_3$ across the spin transition. Note the discrepancies between the experimental and theoretical studies for the composition x=0.65. Velocities vary greatly for different Fe contents and increase substantially after the spin transition of Fe^{2+} (grey shaded area). All velocities shown are at room temperature. Figure is slightly modified after [143]

properties of carbonates [146]. One important consequence of the spin transition is the sample's change of color, from colorless or light orange to intense red [79]. This is a great problem for Brillouin spectroscopy measurements and thus alternative methods to study Fe-bearing carbonates should be explored.

Determining the elastic wave velocities of carbonates, particularly in the $FeCO_3$-$MgCO_3$ system, will not only set carbonates among other candidates that can explain the anisotropic anomalies observed in the mantle, but also possibly allow us to quantify the deep carbon through seismology. This domain is still very poorly explored. Rough estimates suggest that unrealistically high CO_2 contents (~15-20 wt%) must be present in order to observe a contrast above the assumed 2% seismic resolution limit between carbonates and crust lithologies [144]. Other authors argued that at lower mantle depths (~1200 km) where the Fe^{2+} spin crossover takes place, the abnormal elastic behavior of Fe-bearing carbonates would induce a drastic decrease of V_P (~10%), thus increasing the probability to seismically detect such a feature [142]. However, the effect of temperature was never considered previously. Given the perplexing phase stability diagrams that are now known for Fe-bearing carbonates at high pressures and high temperatures [54] and accounting for important geological aspects that were not discussed before, we owe to revise our estimates for the threshold of carbon's seismic detectability in the deep Earth. This is the motivation behind the results presented in **Chapter 7**.

1.5. References

[1] T. Bensby, and S. Feltzing, **(2006)** *The origin and chemical evolution of carbon in the Galactic thin and thick disks.* Monthly Notices of the Royal Astronomical Society, 367, 1181-1193.

[2] B. Marty, C.M.O'D. Alexander, and S.N. Raymond, **(2013)** *Primordial origins of Earth's carbon.* Reviews in Mineralogy and Geochemistry, 75, 149-181.

[3] B.S. Meyer, and E. Zinner, **(2006)** *Nucleosynthesis. In: Meteorites and the Early Solar System II.* University of Arizona Press, Tucson, 69-108.

[4] R. Wilson, **(1997)** *The Stars- their Birth, Life, and Death*. Taylor & Francis, ISBN 9780203212738, p320.

[5] T. Henning and D. Semenov, **(2013)** *Chemistry in protoplanentary disks.* Chemical Reviews, 113, 9016-9042.

[6] R. Dasgupta, **(2013)** *Ingassing, storage, and outgassing of terrestrial carbon through geologic time.* Reviews in Mineralogy and Geochemistry, 75, 183-229.

[7] D.S. Grewal, R. Dasgupta, C. Sun, K. Tsuno, G. Costin, **(2019)** *Delivery of carbon, nitrogen, and sulfur to the silicate Earth by a giant impact.* Science Advances, 5, eaau3669.

[8] B.J. Wood, J. Li, and A. Shahar, **(2013)** *Carbon in the core: Its influence on the properties of core and mantle.* Reviews in Mineralogy and Geochemistry, 75, 231-250.

[9] K. Lodders, **(2003)** *Solar system abundances and condensation temperatures of the elements.* The Astrophysical Journal, 591, 1220-1247.

[10] B. Marty, **(2012)** *The origins and concentrations of water, carbon, nitrogen and noble gases on Earth.* Earth and Planetary Science Letters, 313-314, 56-66.

[11] R. Brett, **(1966)** *Cohenite in meteorites: A proposed origin.* Science, 153, 60-62.

[12] Y. Zhang, and Q-Z. Yin, **(2012)** *Carbon and other light element contents in the Earth's core based on first-principles molecular dynamics.* Proceedings of the National Academy of Science, 109, 19579-19583.

[13] D.C. Rubie, D.J. Frost, U. Mann, Y. Asahara, F. Nimmo, K. Tsuno, P. Kegler, A. Holzheid, and H. Palme, **(2011)** *Heterogeneous accretion, composition and core–mantle differentiation of the Earth.* Earth and Planetary Science Letters, 301, 31-42.

[14] B.A. Buffett, **(2000)** *Earth's core and the geodynamo.* Science, 288, 2007-2012.

[15] R.J. Reeder, **(1983)** *Crystal chemistry of the rhombohedral carbonates.* Reviews in Mineralogy, 11, 1-47.

[16] S.J. Burns, and P.A. Baker, **(1987)** *A geochemical study of dolomite in the Monterey formation, California.* Journal of Sedimentary Petrology, 57, 128-139.

[17] W.H. Berger, **(2016)** *Calcite Compensation Depth (CCD).* Encyclopedia of Marine Geosciences: Encyclopedia of Earth Sciences Series, Springer Netherlands, 71–73.

[18] H.C. Jenkyns, **(1980)** *Cretaceous anoxic events: from continents to oceans.* Journal of the Geological Society of London, 137, 171-188.

[19] B. Campisi, **(1977)** *Le Argille Scagliose di Moio e di Floresta (Sicilia nordorientale)*. Geologica Romana, 16, 113-30.

[20] T. Plank, and C.H. Langmuir, **(1998)** *The chemical composition of subducting sediments and its consequences for the crust and mantle.* Chemical Geology, 145, 325-394.

[21] T. Plank, **(2014)** *The chemical composition of subducting sediments.* Reference Module in Earth Systems and Environmental Sciences: Treatise on Geochemistry (2nd edition), 4, 607-629

[22] R. Dasgupta, and M.M. Hirschmann, **(2010)** *The deep carbon cycle and melting in Earth's interior.* Earth and Planetary Science Letters, 298, 1-13.

[23] P. Allard, J. Carbonnelle, D. Dajlevic, J. Le Bronec, P. Morel, M.C. Robe, J.M. Maurenas, R. Faivre-Pierret, D. Martin, J.C. Sabroux, and P. Zettwoog, **(1991)** *Eruptive and diffuse emissions of CO_2 from Mount Etna.* Nature, 351, 387-391.

[24] P.B. Kelemen, and C.E. Manning **(2015)** *Reevaluating carbon fluxes in subduction zones, what goes down, mostly comes up.* Proceeding of the National Academy of Science, 112, 3997-4006.

[25] F.K.B. Johnston, A.V. Turchyn, and M. Edmonds, **(2011)** *Decarbonation efficiency in subduction zones: Implications for warm Cretaceous climates.* Earth and Planetary Science Letters, 303, 143-152.

[26] P.J. Gorman, D.M. Kerrick, and J.A.D. Connolly, **(2006)** *Modeling open system metamorphic decarbonation of subducting slabs.* Geochemistry Geophysics Geosystems, 7, Q04007.

[27] R. Dasgupta, M.M. Hirschmann, and A.C. Wirthers, **(2004)** *Deep global cycling of carbon constrained by the solidus of anhydrous, carbonated eclogite under upper mantle conditions.* Earth and Planetary Science Letters, 227, 73-85.

[28] A. Ridgwell, **(2005)** *A Mid Mesozoic revolution in the regulation of ocean chemistry.* Marine Geology, 217, 339-357.

[29] C-T.A. Lee, B. Shen, B.S. Slotnick, K. Liao, G.R. Dickens, Y. Yokoyama, A. Lenardic, R. Dasgupta, M. Jellinek, J.S. Lackey, T. Schneider, and M.M. Tice, **(2013)** *Continental arc–island arc fluctuations, growth of crustal carbonates, and long-term climate change.* Geosphere, 9, 21-36.

[30] T. Nakamori, **(2001)** *Global carbonate accumulation rates from Cretaceous to Present and their implications for the carbon cycle model.* The Island Arc, 10, 1-8.

[31] H. Becker, and R. Altherr, **(1992)** *Evidence from ultra-high-pressure marbles for recycling of sediments into the mantle.* Letters to Nature, 358, 745-748.

[32] Y. Liu, D. He, C. Gao, S. Foley, S. Gao, Z. Hu, K. Zong, and H. Chen, **(2015)** First direct evidence of sedimentary carbonate recycling in subduction-related xenoliths. Scientific Reports, 5, 11547.

[33] J.D. Bliss, **(1992)** *Grade-tonnage and other models for diamond kimberlite pipes.* Nonrenewable Resourses, 1, 214–230.

[34] F. Zhu, J. Li, J. Liu, X. Lai, B. Chen, and Y. Meng, **(2018)** *Kinetic control on the depth distribution of superdeep diamonds.* Geophysical Research Letters, doi: 10.1029/2018GL080740.

[35] M.J. Walter, S.C. Kohn, D. Araujo, G.P. Bulanova, C.B. Smith, E. Gaillou, J. Wang, A. Steele, and B. Shirey, **(2011)** *Deep mantle cycling of oceanic crust: Evidence from diamonds and their mineral inclusions.* Science, 334, 54-57.

[36] G.P. Bulanova, M.J. Walter, C.B. Smith, S.C. Kohn, L.S. Armstrong, J. Blundy, and L. Gobbo, **(2010)** *Mineral inclusions in sublithospheric diamonds from Collier 4 kimberlite pipe, Juina, Brazil: Subducted protoliths, carbonated melts and primary kimberlite magmatism.* Contributions to Mineralogy and Petrology, 160, 489-510.

[37] P.C. Hayman, M.G. Kopylova, and F.V. Kaminsky, **(2005)** *Lower mantle diamonds from Rio Soriso (Juina area, Mato Grosso, Brazil).* Contributions to Mineralogy and Petrology, 149, 430-455.

[38] F.V. Kaminsky, I.D. Ryabchikov, and R. Wirth, **(2016)** *A primary natrocarbonatitic association in the 8eep Earth.* Mineralogy and Petrology, 110, 387-398.

[39] F.V. Kaminsky, **(2012)** *Mineralogy of the lower mantle: A review of 'super-deep' mineral inclusions in diamond.* Earth-Science Reviews, 110, 127-147.

[40] F.V. Kaminsky, R. Wirth, and A. Schreiber, **(2013)** *Carbonatitic inclusions in deep mantle diamond from Juina, Brazil: new minerals in the carbonate-halide association.* The Canadian Mineralogist, 51, 669-688.

[41] F.V. Kaminsky, R. Wirth, S. Matsyuk, A. Schreiber, and R. Thomas, **(2009)**. *Nyerereite and nahcolite inclusions in diamond: evidence for lower-mantle carbonatitic magmas.* Mineralogical Magazine, 73, 797–816.

[42] T. Stachel, G.P. Brey, and J.W. Harris, **(2005)** *Inclusions in sublithospheric diamonds: Glimpses of deep Earth.* Elements, 1, 73-78.

[43] P. Cartigny, **(2005)** *Stable isotopes and the origin of diamond.* Elements, 1, 79-84.

[44] A. Rohrbach, and M.W. Schmidt, **(2011)** *Redox freezing and melting in the Earth's deep mantle resulting from carbon-iron redox coupling.* Nature, 472, 209-214.

[45] V. Stagno, D.O. Ojwang, C.A. McCammon, and D.J. Frost, **(2013)** *The oxidation state of the mantle and the extraction of carbon from Earth's interior.* Nature, 493, 84-90.

[46] R.M. Hazen, A.P. Jones, and J.A. Baross, **(2013)** Carbon in Earth. Reviews in Mineralogy and Geochemistry, 75, 680.

[47] R.W. Luth, **(1999)** *Carbon and carbonates in the mantle.* Mantle Petrology: Field Observations and High Pressure Experimentation: A Tribute to Francis R. (Joe) Boyd, 6. The Geochemical Society, 297–316.

[48] S.S. Shcheka, M. Weidenbeck, D.J. Frost, and H. Keppler, **(2006)** *Carbon solubility in mantle minerals.* Earth and Planetary Science Letters, 245, 730-742.

[49] R. Dasgupta, M.M. Hirschmann, and N. Dellas, **(2005)** *The effect of bulk composition on the solidus of carbonated eclogite from partial melting experiments at 3 GPa.* Contributions in Mineralogy and Petrology, 149, 288–305.

[50] C. Biellmann, P. Gillet, F. Guyot, J. Peyronneau, and B. Reynard, **(1993)** *Experimental evidence for carbonate stability in the Earth's lower mantle.* Earth and Planetary Science Letters, 118, 31-41.

[51] A.R. Thomson, M.J. Walter, S.C. Kohn, and R.A. Brooker, **(2016)** *Slab melting as a barrier to deep carbon subduction.* Nature volume 529, 76-79.

[52] D.J. Frost, and C.A. McCammon, **(2008)** *The redox state of Earth's mantle.* Annual Review of Earth and Planetary Sciences, 36, 389-420.

[53] V. Stagno, Y. Tange, N. Miyajima, C.A. McCammon, T. Irifune, and D.J. Frost, **(2011)** *The stability of magnesite in the transition zone and lower mantle as function of oxygen fugacity.* Geophysical Research Letters, 38, L19309.

[54] V. Cerantola, E. Bykova, I. Kupenko, M. Merlini, L. Ismailova, C. McCammon, M. Bykov, A.I. Chumakov, S. Petitgirard, I. Kantor, V. Svitlyk, J. Jacobs, M. Hanfland, M. Mezouar, C. Prescher, R. Rüffer, V.B. Prakapenka, and L. Dubrovinsky, **(2017)** *Stability of iron-bearing carbonates in the deep Earth's interior.* Nature Communications, 8, 15960.

[55] N.S. Martirosyan, K.D. Litasov, S.S. Lobanov, A.F. Goncharov, A. Shatskiy, H. Ohfuji, and V. Prakapenka, **(2018)** *The Mg-carbonate–Fe interaction: Implication for the fate of subducted carbonates and formation of diamond in the lower mantle.* Geoscience Frontiers, https://doi.org/10.1016/j.gsf.2018.10.003.

[56] S.M. Dorfman, J. Badro, F. Nabiei, V.B. Prakapenka, M. Cantoni, and P. Gillet **(2018)** *Carbonates stability in the reduced lower mantle.* Earth and Planetary Science Letters, 489, 84-91.

[57] P.W. Bridgman, **(1939)** *The high-pressure behavior of miscellaneous minerals.* American Journal of Science, 237, 7-18.

[58] D.R. Dasgupta, **(1963)** *The oriented transformation of aragonite into calcite. Mineral Magazine, 33, 924-928.*

[59] K. Suito, J. Namba, T. Horikawa, Y. Taniguchi, N. Sakurai, M. Kobayashi, A. Onodera, O. Shimomura, and T. Kikegawa, **(2001)** *Phase relations of $CaCO_3$ at high pressure and high temperature.* American Mineralogist, 86, 997-1002.

[60] L. Bayarjargal, C-J. Fruhner, N. Schrodt, and B. Winkler, **(2018)** *$CaCO_3$ phase diagram studied with Raman spectroscopy at pressures up to 50 GPa and high temperatures and DFT modeling.* Physics of the Earth and Planetary interiors, 281, 31-45.

[61] M. Akyurt, G. Zaki, B. Habeebullah, **(2002)** *Freezing phenomena in ice–water systems.* Energy Conversion and Management, 43, 1773–1789.

[62] M. Merlini, M. Hanfland, and W.A. Crichton, **(2012)** *CaCO$_3$-III and CaCO$_3$-VI, high-pressure polymorphs of calcite: possible host structures for carbon in the Earth's mantle.* Earth and Planetary Science Letters, 333-334, 265-271.

[63] T. Pippinger, R. Miletich, M. Merlini, P. Lotti, P. Schouwink, T. Yagi, W.A. Crichton, and M. Hanfland, **(2015)** *Puzzling calcite-III dimorphism: crystallography, high-pressure behavior, and pathway of single-crystal transitions.* Physics and Chemistry of Minerals, 42, 29-43.

[64] G.X. Li, Z. Zhang, J-F. Lin, H. Ni, V.B. Prakapenka, and Z. Mao **(2018)** *New High-Pressure Phase of CaCO3 at the Topmost Lower Mantle: Implication for the Deep-Mantle Carbon Transportation.* Geophysical Research Letters.

[65] H.E. Boeke, **(1912)** *Die Schmelzerscheinungen und die umkehrbare Umwandlung des Calciumcarbonats.* Neues Jahrbuch für Mineralogie, 1,91–121.

[66] P.W. Mirwald, **(1976)** *A differential thermal analysis study of the high-temperature polymorphism of calcite at high pressure*. Contributions to Mineralogy and Petrology, 59, 33–40.

[67] E.N. Maslen, V.A. Streltsov, and N.R. Streltsova, **(1993)**. *X-ray study of the electron density in calcite, CaCO$_3$.* Acta Crystallographica Section B, 49, 636–641.

[68] N. Ishizawa, H. Setoguchi, and K. Yanagisawa, **(2013)** *Structural evolution of calcite at high temperatures: phase V unveiled.* Scientific Reports, 3, 2832.

[69] N. Ishizawa, **(2014)** *Calcite V: a hundred-year-old mystery has been solved.* Powder Diffraction, 29, 19-23.

[70] Katsura, T., Tsuchida, Y., Ito, E., Yagi, T., Utsumi, W. and Akimoto, S. (1991). Stability of magnesite under the lower mantle conditions. Proc. Japan Acad., **67** (B), 57-60.

[71] G. Fiquet, F. Guyot, and J. Itié, **(1994)** *High-pressure X-ray diffraction study of carbonates: MgCO3, CaMg(CO3)2 and CaCO3.* American Mineralogist, 79, 15-23.

[72] G. Fiquet, G. Guyot, M. Kunz, J. Matas, D. Andrault, and M. Hanfland, **(2002)** *Structural refinements of magnesite at very high pressure.* American Mineralogist, **87**, 1261-1265.

[73] M. Isshiki, T. Irifune, K. Hirose, S. Ono, Y. Ohishi, T. Watanuki, E. Nishibori, M. Takata, and M. Sakata, **(2004),** *Stability of magnesite and its high-pressure form in the lowermost mantle*. Nature, 427, 60-63.

[74] A.R. Oganov, S. Ono, Y. Ma, C.W. Glass, A. Garcia, **(2008)** *Novel high-pressure structures of MgCO$_3$, CaCO$_3$ and CO$_2$ and their role in Earth's lower mantle.* Earth and Planetary Science Letters, 273, 38-47.

[75] E. Boulard, D. Pan, G. Galli, Z. Liu, and W.L. Mao, **(2015)** *Tetrahedrally coordinated carbonates in Earth's lower mantle.* Nature Communications, 6, 6311.

[76] W.R. Panero, and J.E. Kabbes, **(2008)** *Mantle-wide sequestration of carbon in silicates and the structure of magnesite II.* Geophysical Research Letters, 35, L14307.

[77] B. Lavina, P. Dera, R.T. Downs, V. Prakapenka, M. Rivers, S. Sutton, and M. Nicol, **(2009)** *Siderite at lower mantle conditions and the effects of the pressure-induced spin-pairing transition.* Geophysical Research Letters, 36, L23306.

[78] B. Lavina, P. Dera, R.T. Downs, O. Tschauner, W. Yang, O. Shebanova, and G. Shen, **(2010)** *Effect of dilution on the spin pairing transition in rhombohedral carbonates.* High Pressure Research, 30, 224-229.

[79] B. Lavina, P. Dera, R.T. Downs, W. Yang, S. Sinogeikin, Y. Meng, G. Shenand, and D. Schiferl, **(2010a)** *Structure of siderite $FeCO_3$ to 56 GPa and hysteresis of its spin-pairing transition.* Physical Review B, 82, 064110.

[80] V. Cerantola, C. McCammon, I. Kupenko, I. Kantor, C. Marini, M. Wilke, L. Ismailova, N. Solopova, A.I. Chumakov, S. Pascarelli, and L. Dubrovinsky, **(2015)** *High-pressure spectroscopic study of siderite (FeCO3) with focus on spin crossover.* American Mineralogist, 100, 2670-2681.

[81] J. Müller, S. Speziale, I. Efthimiopoulos, S. Jahn, and M. Koch-Müller, **(2016)** *Raman spectroscopy of siderite at high pressure: Evidence for a sharp spin transition.* American Mineralogy, 101, 2638–2644.

[82] C. Weis, C. Sternemann, V. Cerantola, C.J. Sahle, G. Spiekermann, M. Harder, Y. Forov, A. Kononov, R. Sakrowski, H. Yavas, M. Tolan, and M. Wilke, **(2017)** *Pressure driven spin transition in siderite and magnesiosiderite single crystals.* Scientific Reports, 7, 16526.

[83] J-F. Lin, J. Liu, C. Jacobs, and V.B. Prakapenka **(2012)** *Vibrational and elastic properties of ferromagnesite across the electronic spin-pairing transition of iron.* American Mineralogist, 97, 583-591.

[84] B. Lavina, P. Dera, E. Kim, Y. Meng, R.T. Downs, P.F. Weck, S.R. Sutton, and Y. Zhao, **(2011)** *Discovery of recoverable high-pressure iron oxide Fe_4O_5.* Proceeding of the National Academy of Science, 108, 17281-17285.

[85] Y. Zhu, and Y. Ogasawara, **(2002)** *Carbon recycled into deep Earth: evidence from dolomite dissociation in subduction-zone rocks.* Geology, 30, 947-950.

[86] I. Martinez, J. Zhang, and R.J. Reeder **(1996)** *In situ X-ray diffraction of aragonite and dolomite at high pressure and high temperature: Evidence for dolomite breakdown to aragonite and magnesite.* American Mineralogist, 81, 611-624.

[87] I. Efthimiopoulos, S. Jahn, A. Kuras, U. Schade, and M. Koch-Müller, **(2017)** *Combined high-pressure and high-temperature vibrational studies of dolomite: phase diagram and evidence of a new distorted modification.* Physics and Chemistry of Minerals, 44, 465-476.

[88] Z. Mao, M. Armentrout, E. Rainey, C.E. Manning, P. Dera, V.B. Prakapenka, and A. Kavner, **(2011)** *Dolomite III: A new candidate lower mantle carbonate.* Geophysical Research Letters, 38, L22303.

[89] M. Merlini, V. Cerantola, G.D. Gatta, M. Gemmi, M. Hanfland, I. Kupenko, P. Lotti, H. Müller, and L. Zhang, **(2017)** *Dolomite-IV: Candidate structure for a carbonate in the Earth's lower mantle.* American Mineralogist, 102, 1763-1766.

[90] M. Merlini, W.A. Crichton, M. Hanfland, M. Gemmid, H. Müller, I. Kupenko, and L. Dubrovinsky, **(2012)** *Structures of dolomite at ultrahigh pressure and their influence on the deep carbon cycle. Proceedings of the National Academy of Science, 109, 13509-13514.*

[91] J. Santillán, and Q. Williams, **(2004)** *A high-pressure infrared and X-ray study of FeCO$_3$ and MnCO$_3$: comparison with CaMg(CO$_3$)$_2$ – dolomite.* Physics of Earth and Planetary Interiors, 143-144, 291-304.

[92] S. Ono, **(2007)** *High-pressure phase transformation in MnCO$_3$: a synchrotron XRD study.* Mineralogical Magazine, 71, 105-111.

[93] W. Shi, M. Fleet, and S.R. Shieh **(2012)** *High-pressure phase transitions in Ca-Mn carbonates (Ca,Mn)CO$_3$ studied by Raman spectroscopy.* American Mineralogist, 97, 999-1001.

[94] G.A. Farfan, E. Boulard, S. Wang, and W.L. Mao, **(2013)** *Bonding and electronic changes in rhodochrosite at high pressure.* American Mineralogist, 98, 1817-1823.

[95] E. Boulard, A.F. Goncharov, M. Blanchard, and W.L. Mao, **(2015)**. *Pressure-induced phase transition in MnCO$_3$ and its implications on the deep carbon cycle.* Journal of Geophysical Research: Solid Earth, 120, B011901.

[96] M. Merlini, M. Hanfland, and M. Gemmi, **(2015)**. *The MnCO$_3$-II high pressure polymorph of rhodochrosite.* American Mineralogist, 100, 11-12.

[97] E. Boulard, Y. Liu, A. Koh, M.M. Reagan, J. Stodolna, G. Morard, M. Mezouar, and W.L. Mao, **(2016)** *Transformations and decomposition of MnCO$_3$ at Earth's lower mantle conditions.* Frontiers in Earth Science, 4, 107.

[98] C. Zhao, H. Li, J. Jiang, Y. He, and W. Liang, **(2018)** *Phase Transition and vibration properties of MnCO$_3$ at high pressure and high-temperature by Raman spectroscopy. High Pressure Research, 38, 212-223.*

[99] H-C. Hung, C-R. Hsing, and C-M. Wei, **(2019)** *High-pressure phases of MnCO$_3$ by random structure search.* Physical Review B, 99, 024106.

[100] S.V. Ovsyannikov, A.M. Abakumov, A.A. Tsirlin, W. Schnelle, R. Egoavil, J. Verbeeck, G. Tendeloo, K.V. Glazyrin, M. Hanfland, and L. Dubrovinsky **(2013)** Angewandte Chemie International Edition, 52, 1494-1498.

[101] J.Cong, K. Zhai, Y. Chai, D. Shang, D.D. Khalyavin, R.D. Johnson, D.P. Kozlenko, S.E. Kichanov, A.M. Abakumov, A.A. Tsirlin, L. Dubrovinsky, X. Xu, Z. Sheng, S.V. Ovsyannikov, and Y. Sun, **(2018)** *Spin-induced multiferroicity in the binary perovskite manganite Mn$_2$O$_3$.* Nature Communications, 9, 2996.

[102] J. Gao, F. Zhu, X.J. Lai, R. Huang, S. Qin, D.L. Chen, J. Liu, L.R. Zheng, and X. Wu, **(2014)** *Compressibility of natural smithsonite up to 50 GPa.* High Pressure Research, 34, 89-99.

[103] A. Bouibes, and A. Zaoui, **(2014)** *High-pressure polymorphs of ZnCO$_3$: Evolutionary crystal structure prediction.* Scientific Reports, 4, 5172.

[104] R. Minch, D.H. Seoung, L. Ehm, B. Winkler, K. Knorr, L. Peters, L.A. Borkowski, J.B. Parise, Y. Lee, L. Dubrovinsky, and W. Depmeier **(2010)** *High-pressure behavior of otavite (CdCO$_3$)*. Journal of Alloys and Compounds, 508, 251–257.

[105] J. Zhang, and R.J. Reeder, **(1999)** *Compararative compressibilities of calcite-structure carbonates: Deviations from empirical relations.* American Mineralogist, 84, 861-870

[106] M. Merlini, N. Perchiazzi, M. Hanfland, and A. Bossak, **(2012)** *Phase transition at high pressure in Cu$_2$CO$_3$(OH)$_2$ related to the reduction of the Jahn-Teller effect.* Acta Crystallographica Section B, 68, 266-274

[107] J. Xu, Y. Kuang, B. Zhang, Y. Liu, D. Fan, W. Zhou, and H. Xie, **(2015)** *High‑pressure study of azurite Cu$_3$(CO$_3$)$_2$(OH)$_2$ by synchrotron radiation X‑ray diffraction and Raman spectroscopy.* Physics and Chemistry of Minerals, 42, 805-816.

[108] I. Efthimiopoulos, J. Müller, B. Winkler, C. Otzen, M. Harms, U. Schade, and M. Koch-Müller, **(2019)** *Vibrational response of strontianite at high pressures and high temperatures and construction of P–T phase diagram.* Physics and Chemistry of Minerals, 46, 27-35.

[109] K. Catalli, J. Santillan, and Q. Williams, **(2005)** *A high pressure infrared spectroscopic study of PbCO$_3$-cerussite: constraints on the structure of the post-aragonite phase.* Physics and Chemistry of Minerals, 32, 412-417.

[110] C-C. Lin, and L-G. Liu **(1997)** *High-pressure Raman spectroscopic study of post-aragonite phase transition in witherite (BaCO$_3$).* European Journal of Mineralogy, 9, 785-792.

[111] A.M. Plonka, P. Dera, P. Irmen, M.L. Rivers, L. Ehm, and J.B. Parise, **(2012)** β-*diopside, a new ultrahigh-pressure polymorph of CaMgSi$_2$O$_6$ with six-coordinated silicon.* Geophysical Research Letters, 39, L24307.

[112] Y. Hu, B. Kiefer, C.R. Bina, D. Zhang, and P.K. Dera, **(2017)** *High-pressure γ-CaMgSi$_2$O$_6$: Does penta-coordinated silicon exist in the Earth's mantle?* Geophysical Research Letters, 44, 11340–11348.

[113] R.M. Hazen, and L.W. Finger, **(1978)** *Crystal chemistry of silicon-oxygen bonds at high pressure: Implications for the Earth's mantle mineralogy.* Applied Physics Letters, 37, 288-289.

[114] R.D. Shannon, C.T. Prewitt **(1969)** *Effective ionic radii in oxides and fluorides.* Acta Crystallographica Section B, 25, 925-946.

[115] F.P. Bundy, H.P. Bovenkerkm, H.M. Strong, R.H.Jr. Wentorf, **(1961)** *Diamond-graphite equilibrium line from growth and graphitization of diamond.* Journal of Chemistry and Physics, 35, 383-391.

[116] F. Datchi, B. Mallick, A. Salamat, S. Ninet, **(2012)** *Structure of polymeric carbon dioxide CO$_2$-V.* Physical Review Letters, 108, 125701.

[117] A.R. Oganov, C.W. Glass, and S. Ono, **(2006)** *High-pressure phases of CaCO$_3$: Crystal structure prediction and experiment.* Earth and Planetary Science Letters, 241, 95-103.

[118] N.V. Skorodumova, A.B. Belonoshko, L. Huang, R. Ahuja, and B. Johansson, **(2005)** *Stability of the MgCO$_3$ structures under lower mantle conditions.* American Mineralogist, 90, 1008-1011.

[119] S. Ono, T. Kikegawa, and Y. Ohishi, **(2007)** *High-pressure phase transition of CaCO$_3$ at 40 GPa.* American Mineralogist, 92, 1246-1249.

[120] E. Boulard, A. Gloter, A. Corgne, D. Antonangeli, A-L. Auzende, J-P. Perrillat, F. Guyot, and G. Fiquet, **(2011)** *New host for carbon in the deep Earth.* Proceeding of the National Academy of Science, 108, 5184-5187.

[121] S. Arapan, J. Souza de Almeida, and R. Ahuja, **(2007)** *Formation of sp^{3}hybridized bonds and stability of CaCO$_3$ at very high pressure.* Physical Review Letters, 98, 268501.

[122] X. Yao, C. Xie, X. Dong, A.R. Oganov, and Q. Zeng, **(2018)** *Novel high-pressure calcium carbonates.* Physical Review B, 98, 014108.

[123] J. Liu, J-F. Lin, and V.B. Prakapenka **(2015)** *High-pressure orthorhombic ferromagnesite as a potential deep-mantle carbon carrier.* Scientific Reports, 5, 7640.

[124] M. Merlini, M. Hanfland, A. Salamat, S. Petitgirard, and H. Müller, **(2015)** *The crystal structures of Mg$_2$Fe$_2$C$_4$O$_{13}$, with tetrahedrally coordinated carbon, and Fe$_{13}$O$_{19}$, synthesized at deep mantle conditions.* American Mineralogist, 100, 2001-2004.

[125] A.C. Lasaga and G.V. Gibbs, **(1987)** *Applications of quantum-mechanical potential surfaces to mineral physics calculations.* Physics and Chemistry of Minerals, 14, 107-117.

[126] S. Ono, T. Kikegawa, J. Tsuchiya, **(2007)** *Post-aragonite phase transformation in CaCO$_3$ at 40 GPa.* American Mineralogist, 90, 667-671.

[127] G. Nolet, **(1987)** *Seismic wave propagation and seismic tomography.* Seismic Tomography, Seismology and Exploration Geophysics, 5, ISBN: 978-90-277-2583-7.

[128] Y. Fukao, and M. Obayashi, **(2013)** *Subducted slabs stagnant above, penetrating through, and trapped below the 660 km discontinuity.* Journal of Geophysical Research: Solid Earth, 118, 5920-5938.

[129] L. Liu, S. Spasojevic, and M. Gurnis, **(2008)** *Reconstructing Farallon Plate Subduction Beneath North America Back to the Late Cretaceous.* Science, 322, 934-938.

[130] A. Nowacki, J-M. Kendall, J. Wookey, and A. Pemberton, **(2015)** *Mid-mantle anisotropy in subduction zones and deep water transport.* Geochemistry Geophysics Geosystems, 16, 764–784.

[131] Li, L., D. Weidner, J. P. Brodholt, D. Alfe`, and G. Price **(2006)** *Elasticity of Mg2SiO4 ringwoodite at mantle conditions.* Physics of Earth and Planetary Interiors, 157, 181–187.

[132] Zha, C., T. Duffy, H.-K. Mao, R. Downs, R. Hemley, and D. Weidner **(1997)** *Single-crystal elasticity of b-Mg$_2$SiO$_4$ to the pressure of the 410 km seismic discontinuity in the Earth's mantle.* Earth and Planetary Science Letters, 147, 9–15.

[133] Ohuchi, T., K. Fujino, T. Kawazoe, and T. Irifune **(2014)** *Crystallographic preferred orientation of wadsleyite and ringwoodite: Effects of phase transformation and water on seismic anisotropy in the mantle transition zone.* Earth and Planetary Science Letters, 397, 133–144.

[134] Cordier, P., T. Ungar, L. Zsoldos, and G. Tichy **(2004)** *Dislocation creep in MgSiO3 perovskite at conditions of the Earth's uppermost lower mantle,* Nature, 428, 837–840.

[135] Wenk, H.-R., I. Lonardeli, J. Pehl, J. Devine, V. Prakapenka, G. Shen, and H.-K. Mao **(2004)** *In situ observation of texture development in olivine, ringwoodite, magnesiowüustite and silicate perovskite at high pressure.* Earth and Planetary Science Letters, 226, 507–519.

[136] Mainprice, D. **(2007)** *Seismic anisotropy of the deep earth from a mineral and rock physics perspective.* Treatise on Geophysics, 2, 437–492.

[137] Kirby, S., S. Stein, E. Okal, and D. Rubie **(1996)** *Metastable mantle phase transformations and deep earthquakes in subducting oceanic lithosphere.* Reviews in Geophysics, 34, 261–306.

[138] Ohtani, E. **(2005)** *Water in the mantle.* Elements, 1, 25–30.

[139] Akaogi, M., A. Tanaka, and E. Ito **(2002)** *Garnet—ilmenite—perovskite transitions in the system $Mg_4Si_4O_{12}$—$Mg_3Al_2Si_3O_{12}$ at high pressures and high temperatures: Phase equilibria, calorimetry and implications for mantle structure*. Physics of Earth and Planetary Interiors, 132, 303-324.

[140] C-C. Chen, C-C. Lin, L-G. Liu, S.V. Sinogeikin, and J.D. Bass, **(2001)** *Elasticity of single-crystal calcite and rhodochrosite by Brillouin spectroscopy.* American Mineralogist, 86, 1525-1529.

[141] J. Yang, Z. Mao, J-F. Lin, V.B. Prakapenka, **(2014)** *Single-crystal elasticity of the deep-mantle magnesite at high pressure and temperature.* Earth and Planetary Science Letters, 392, 292–299.

[142] S. Fu, J. Yang, and J-F. Lin, **(2017)** *Abnormal elasticity of single-crystal magnesiosiderite across the spin transition in Earth's lower mantle.* Physical Review Letters, 118, 036402.

[143] M. Stekiel, T. Nguyen-Thanh, S. Chariton, C. McCammon, A. Bosak, W. Morgenroth, V. Milman, K. Refson, and B. Winkler, **(2017)** *High pressure elasticity of $FeCO_3$-$MgCO_3$ carbonates.* Physics of the Earth and Planetary Interiors, 271, 57-63.

[144] C. Sanchez-Valle, S. Ghosh, and A.D. Rosa, **(2011)** *Sound velocities of ferromagnesian carbonates and the seismic detection of carbonates in eclogites and the mantle.* Geophysical Research Letters, 38, L24315.

[145] B. Li, and R.C. Liebermann, **(2007)** *Indoor seismology by probing the Earth's interior by using sound velocity measurements at high pressures and temperatures.* Proceedings of the National Academy of Science, 104, 9145-9150.

[146] H. Shi, W. Luo, B. Johansson, and R. Ahuja, **(2008***) First-principles calculations of the electronic structure and pressure-induced magnetic transition in siderite $FeCO_3$.* Physical Review B, 78, 155119.

Chapter 2

Methods

2.1. Generating extreme conditions

According to the International Union of Geodesy and Geophysics' the average radius of the Earth is about 6731 Km. Humans, however, have never drilled past the Earth's crust; the Kola superdeep borehole is currently holding the record (12.26 km) of the deepest artificial point on Earth [1]. The number of samples that scientists have access to and which are representative of the Earth's deeper inner layers, such as the transition zone (410-660 km), the lower mantle (660-2900 km) or the core (2900-6371 km), become rarer (only individual grain inclusions in diamonds from the lower mantle) or even non-existing (no sample exists from the core) with increasing depth. So, how do we study our planet's deeper parts where no direct access is granted? Our current information comes from studies of the paths and characteristics of earthquake waves travelling through the Earth, as well as from laboratory experiments on surface minerals and rocks at high pressures and temperatures. In the latter case, great technological obstacles were overcome in order to simulate in the laboratory the extreme conditions that feature in the Earth's deep interior.
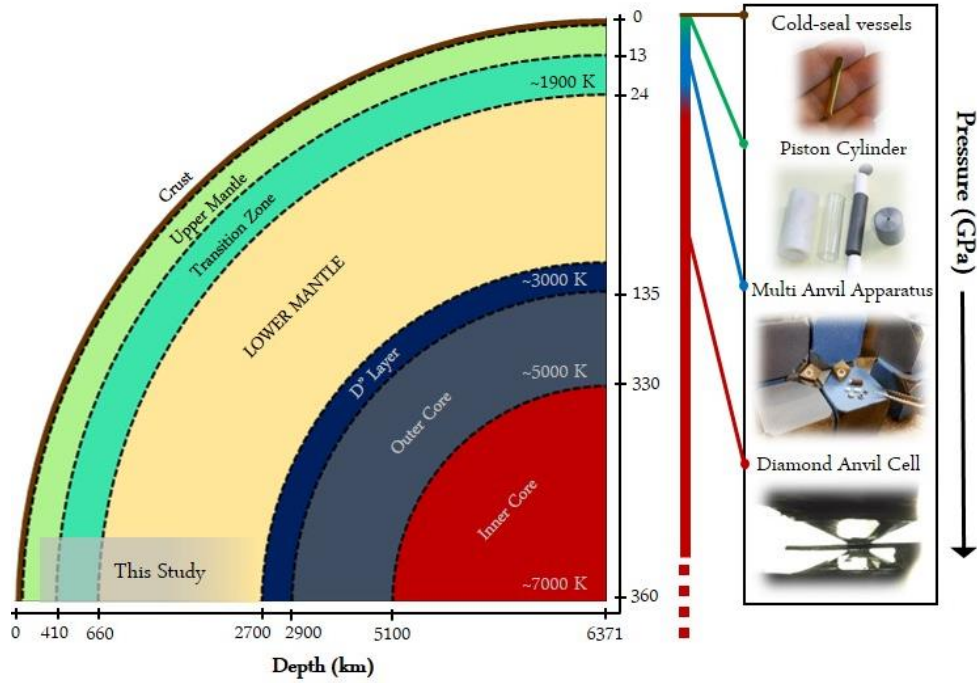
Figure 1. Cross section of the layered structure of Earth's interior along with the pressure and temperature distribution and the most suitable high-pressure techniques commonly used.

The principle of pressure (P) generation is very simple and is expressed by the following formula:

$$P = \frac{F}{A} \qquad\qquad (Eq.\ 1)$$

where F is the force applied to the surface A of an object. To generate high pressure on a sample it is most common to decrease the area to which an external force is applied, rather than increase the magnitude of the force itself. In that manner, various devices were invented over the years, the most common of which are illustrated in Figure 1.

Experiments with **_cold-seal vessels_** are performed on samples of a few centimeters in size (i.e. typically capsules are of about 2-4 cm in length and 2-4 mm in diameter, Figure 2a-i). By pressurizing water in a confined space pressures as high as 2 kbar can be achieved in the cold-seal vessels. Simultaneously, a furnace system can provide external heating up to ~1200 °C. Cold-seal vessels operating in a vertical or horizontal mode were facilitated at BGI for the synthesis of Mn, Co and Fe carbonate powders and the synthesis and growth of Ni and Zn carbonate crystals (Figure 2a-ii, for more details see sections 5.2.1., 6.5.1. and 7.2.1.).

To generate higher pressures (~< 5 GPa) and temperatures (~< 2200 °C) ***piston cylinder*** experiments are performed on samples of a few millimeters to a centimeter size. The experimental assembly is placed in a cylinder (otherwise known as the "bomb") and an underlying piston is advancing to compress the sample. Piston-cylinder experiments have been particularly used in the past to study $CaCO_3$ (calcite/aragonite) phase relations [2], melt mobility [3], or phase solubility in aqueous solutions [4] in uppermost mantle conditions (Figure 1). However, in this thesis we did not use piston cylinder.

Multi-anvil presses are usually employed to generate pressures and temperatures relative to the Earth's deep upper mantle, transition zone and uppermost lower mantle (i.e. <25 GPa and up to ~2500 °C) (Figure 1). The most known design of a multi-anvil apparatus is the Kawai-type. In a Kawai-type press an outer set of 6 steal anvils (3 facing up and 3 facing down) create a void where a secondary set of 8 tungsten carbide cubic anvils is placed. The interior corner of each WC-cube is truncated to fit an octahedral assembly (Figure 2b-iii). The smaller the size of the truncation is the higher are the pressures that one can generate. The sample is usually contained in capsules of a few millimeters, which are embraced by a $LaCrO_3$ or graphite cylinder furnace and then all assembled in an MgO octahedron. The octahedron serves as the pressure medium and ensures that the experiment is under hydrostatic stress. Air pumps are used to pressurize oil that drives the outer set of steal anvils against each other, and thus increasing the pressure on the sample. The furnace can produce considerable heat by electrical heating.
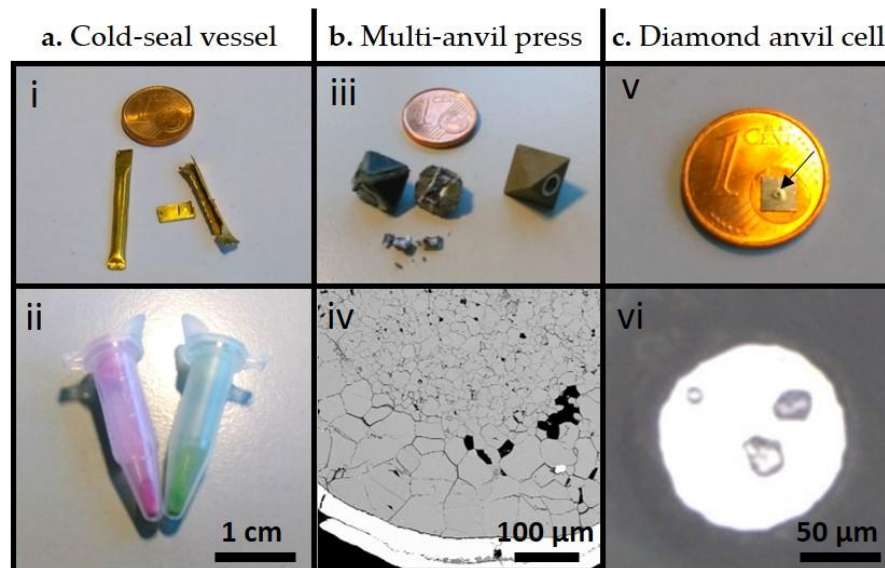
Figure 2. a) A sample retrieved from a cold-seal vessel experiment; ***i.*** a Au capsule before and after cut open to extract ***ii.*** the $CoCO_3$ (pink) powder and the $NiCO_3$ (green) crystals. **b)** A multi-anvil experimental assembly, **iii.** before and after cracked open and **iv.** back-scatter imaging of the $CoCO_3$ crystal-growth inside the Re capsule. **c) v.** The small sample chamber (arrow) on a Re gasket retrieved from a diamond anvil cell experiment, where **vi.** two $MnCO_3$ crystals were loaded together with a ruby sphere.

It is most common that scientists study *ex situ* the recovered products of their multi-anvil experiment. In some cases, and after few equipment modifications, it is possible to perform *in situ* measurements as well, such as conductivity, ultrasonic, X-ray tomography, powder diffraction and other measurements that are often coupled with synchrotron radiation. However, for the purposes of this thesis, multi-anvil experiments were extensively used for the synthesis and crystal-growth of Mn, Co, Fe, and (Fe-Mg) carbonates (Figure 2b-iv, for more details see see sections 5.2.1., 6.5.1. and 7.2.1.).

The ***diamond anvil cell*** was developed to generate the most extreme conditions that persist in the deepest layers of our planet (lower mantle, core) or in those of other planetary bodies, but also for applications in other research fields (e.g. material science). It is a revolutionary and powerful technique mainly due to two very important diamond properties. Firstly, diamond is the hardest (scores 10 in Mohs scale) material on Earth and secondly it is a material optically transparent, as well as transparent to low-energy X-rays, thus allowing us to probe the behavior of materials while in the extreme environment. The flat tips (culets) of two gem-quality diamonds are driven against each other to increase the pressure on a sample that sits in between and which is confined in a small chamber that a hole in a metallic gasket creates (Figure 2v, Figure 3). The smaller the size of the diamond culet is, the higher are the pressures that we can achieve, but at the same time the smaller the size of the sample becomes. For example, we are using diamonds with culets of 250 μm in diameter

Figure 3. The principle of the diamond anvil cell *(not in scale).*

and samples of maximum ~130 x 20 μm (diameter x height) in experiments up to ~70 GPa. On the other hand, we employed diamonds with culets of 80 μm in diameter and samples smaller than 40 x 10 μm (diameter x height) to perform measurements up to ~180 GPa. High temperatures in the diamond anvil cell are generated by either a resistive-wire-furnace encircling the diamond anvils (T<900 K as a rule) or a laser-heating system operating at high powers that can create temperatures as high as those persisting in the center of the Earth (~7000 K). The laser-heated diamond anvil cell is the tool that I employed the most during this PhD thesis to investigate the physical and elastic properties of various carbonate minerals at the Earth's lower mantle pressure and temperature conditions (Figure 1). Thus, the following sections are dedicated in the detailed description of a diamond anvil cell's preparation prior to our Raman spectroscopy, single-crystal X-ray diffraction, and nuclear inelastic X-ray scattering measurements.

2.2. The diamond anvil cell

The first diamond anvil cell (DAC) was designed in the late 1950s and it was capable of generating pressure of a few gigapascals. Since then, several modifications were tested and currently pressures three times greater than those persisting in the center of the Earth are feasible (i.e. ~ 1 TPa) [6]. Despite the many types of DAC designs that exist today (e.g. 7-11), they all share same components. A mainly metallic cell (the "body") contains two aligned diamond anvils placed (glued) on two seats. The two facing anvils indent a gasket and then a hole is drilled in the center to create the sample chamber. The sample is loaded in the chamber with or without a pressure-transmitting medium. Often small chips that act as pressure or temperature indicators are loaded next to the sample. The geometry of the cell and the materials that is made of are designed to serve different purposes and the selection of the correct DAC-type is crucial for the success of the experiment.

2.2.1. The cell design

In the current thesis we choose among the following DAC-types: BX-90 [11], mini BX-90 [11] or ESRF membrane cells [10] for Raman spectroscopy and X-ray diffraction experiments, and long or short panoramic cells (®BGI) for nuclear inelastic scattering measurements (Figure 4). All cells are machined at BGI except for the ESRF cells.
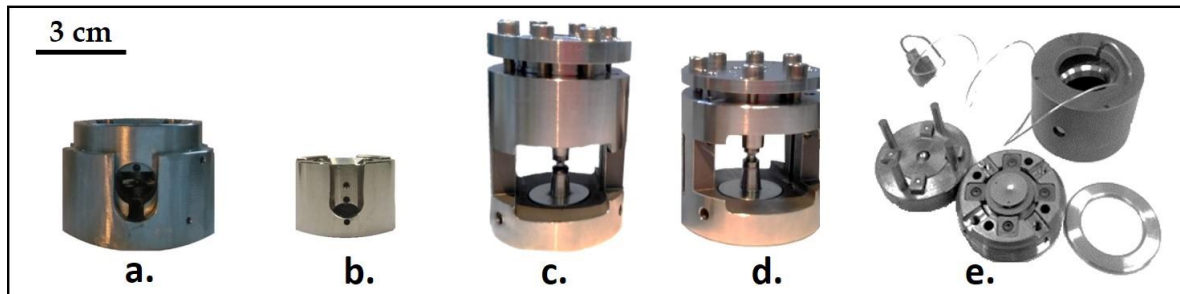
Figure 4. Different diamond anvil cells used in this study. **a)** the BX-90 cell [11], **b)** the mini BX-90 cell [11], **c)** the long panoramic cell, **d)** the short panoramic cell and the **e)** membrane cell provided by ESRF [10].

The features that make the BX-90 cells most suitable for our experiments are the 90° symmetric axial opening and its great stability upon pressurization and heating. If combined with the proper anvils and seats design (i.e. Boehler-Almax), the wide opening of the BX-90 cells allows access to a large part of the reciprocal space in single-crystal XRD measurements (for more details see section 2.4.2.). The pressure in the cell is increased by manually tightening four screws (but also by using membranes). Empirically, the standard-sized BX-90 cells are more reliable (i.e. stable) for experiments in the Mbar range, than the mini BX-90 cells.

While at the ESRF synchrotron facility (France), we conducted sometimes single-crystal XRD experiments using the LeToullec-type DACs provided by ESRF. These cells are membrane driven; an expandable membrane contracts or expands by pumping in or releasing, respectively, a noble gas (usually N_2). The part of the DAC body that is in contact with the membrane is causing increase or decrease of pressure in the sample chamber. The ESRF cells grant stable pressurization and if employed with Boehler-Almax diamond anvils and seats, they provide an opening angle almost as large as the BX-90 cell, which is a desired feature for single-crystal XRD experiments.

Given the special geometry of a NIS experiment (Figure 5, see also sections 2.5.2 and 7.2.1.), the use of the panoramic cell (pDAC) becomes mandatory. Panoramic cells have a large cone opening on the sides, allowing the beam, the detector or other equipment to meet the sample sideways through the gasket. Consequently, the gasket is made of a material that is transparent to X-rays, such as Be. The two versions of the panoramic DAC do not differ substantially (Figure 4c-d). The longer stem of the pDAC provides greater stability during heating sessions and at the same time makes the placement of the pDAC in the holder easier/faster (Figure 5). On the other hand, the preparation of the pDAC with short body is more convenient; it is less heavy and the cell-surface to sample distance is shorter on the one side, which makes the diamond alignment and sample-observation under the optical microscope easier.
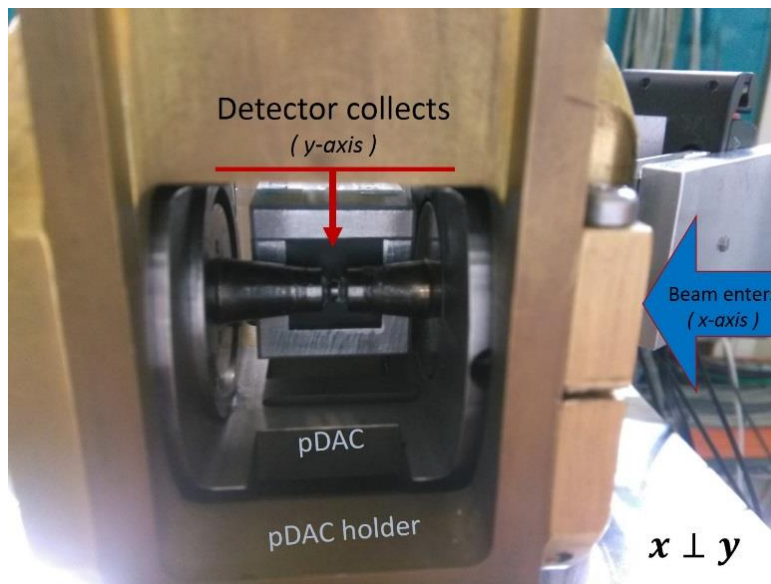
Figure 5. The geometry of a NIS measurement. The panoramic DAC is placed in Cu-holder. The beam meets the sample along the x-axis. The avalanche photodiode detectors are inserted close to the gasket through the side-openings of the pDAC and collect the incoherent nuclear scattering that propagates as a wave along the y-axis.

2.2.2. The diamond anvils and seats

The most essential part of a diamond anvil cell is the diamond itself. There is a great variety of choices on the market mainly based on nitrogen content, cut-designs, and cullet sizes (http://www.almax-easylab.com/DiamondSelectionPage.aspx). For the purposes of this thesis, we used type-Ia Boehler-Almax diamonds with culet size ranging from 300 to 80 μm in diameter for XRD experiments and type-IIa brilliant-cut diamonds with 250 μm culets for spectroscopic/NIS measurements. The selection of culet size strongly depends to the pressures one wants to succeed. For example, the 250 μm (diameter) culet is used for experiments < 70 GPa, while the 120 μm cullet is used for experiments in the Mbar range (~120 GPa). Diamonds that will experience the Mbar range have nearly zero chances to be recovered, while diamonds used for lower pressures (~< 60 GPa) have a high potential to survive decompression and be re-used. Recovered diamonds with damaged culet have a chance to be re-polished prior to a second usage.

The large aperture of the Boehler-Almax diamond anvil and seat (Figure 6a) are crucial for the single-crystal XRD method. In routine experiments, such geometry allows scans of up to ± 38° around the ω-axis (Figure 6a). On the contrary, such a feature is not essential for spectroscopic experiments (Figure 6b), since the DAC remains stationary during the measurement. In Raman spectroscopy experiments a diamond with Raman-low fluorescence is strongly preferred. In NIS experiments, there is no real preference for the type of anvil. In most cases, standard-type anvils were chosen due to their lower cost. The seat on the other hand, is specially designed to fit the long pipe extension of the pDAC (Figure 3c-d, Figure 6c). The pipe has a very small aperture (~10°) that although does not affect the measurement, it makes the cleaning of the diamond surface that is attached to the seat a hard task.

The pair of diamonds of each diamond anvil cell is aligned and then glued in position on the seats. The diamond alignment is a delicate procedure. Even a slight misalignment in the horizontal or vertical axis can be proved fatal for the diamonds and the experiment. Often the Newton rainbow appearing is a
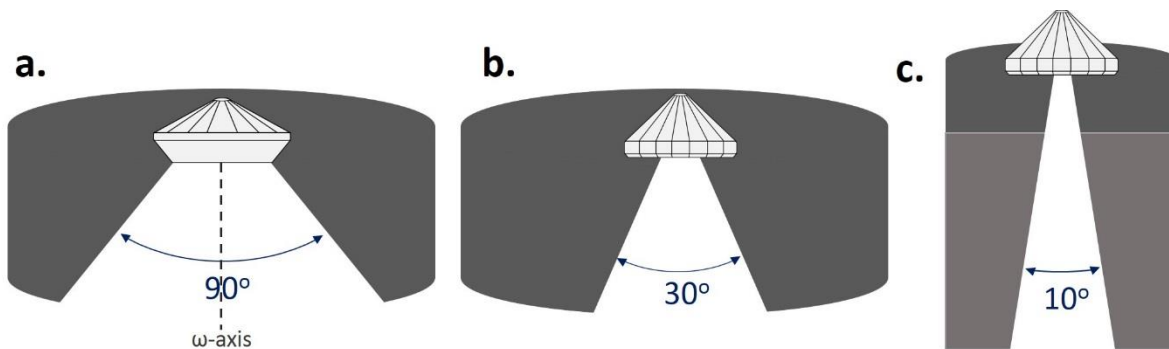
Figure 6. The geometry of diamond anvils and their WC-seats. **a)** Boehler-Almax designed diamond and seat for single-crystal XRD experiments, **b)** standard brilliant-cut diamond and seat for spectroscopic measurements and **c)** WC-seat fitted on the long-steel pipe of the pDAC with a standard diamond anvil for NIS experiments.

useful information about the alignment quality (Appendix Figure A1). Once aligned the diamonds are fixed on the seats by a small amount of glue (cyanoacrylate-based).

2.2.3. The gasket, the sample and the pressure-transmitting medium

The gasket is an important part of the diamond anvil cell assembly; the hole in the gasket provides a chamber for the sample, and prevents it from being crushed by the diamonds or escape during compression (Figure 3). Many materials can be used as a gasket. In routine experiments, gaskets made of Re are employed, which behave exceptionally well under extreme conditions. However, experiments with a special geometry, such as NIS, require gaskets that are transparent to X-rays. Beryllium gaskets can be machined for such purposes. They do contain, however, a very small (about 0.1 wt%) fraction of Fe, which makes them less brittle. This minor Fe-content must be considered during NIS measurements.

In a first step, and independent of the gasket's material choice, the gasket is placed between the two aligned anvils and indented down to a ~30-15 µm thickness (initial gasket thickness is usually ~200 µm). The indentation thickness is smaller for diamonds with smaller culet size that reach the highest pressures. Then, a hole is drilled in the center of the indentation and with half the diameter of the culet size using a powerful laser or a motorized electric discharge machine (EDM-BETSA). After thorough cleaning, the gasket is placed in between the diamonds and the sample chamber is ready for the sample loading.

The sample can be in a single-crystal, polycrystalline or a powder form. If a single-crystal, the sample can be placed in a specific crystallographic orientation flat on the diamond surface or in a random orientation. The sample may be natural or synthetic, and if needed it may be enriched in a desired isotope. Samples qualified for single-crystal XRD measurements in the diamond anvil cell should be excellent or at least, of reasonable diffraction quality (i.e. sharp diffraction peaks, twin absence, low mosaicity, for details see section 2.4), and dimensions to fit the sample chamber alone or share the room with other crystals (e.g. Figure 2-vi). Samples with strong Raman signal of all their vibration bands are ideal for Raman spectroscopy measurements in the DAC. Finally, samples meant for NIS experiments, where Fe atoms are probed, must preferentially be enriched in the ^{57}Fe isotope during their synthesis to enhance the signal and speed up the collection time.

DACs generate uniaxial stress. Therefore, often, transmitting media are used to create homogeneous pressure distribution in the chamber. Many compounds can serve as a pressure transmitting medium (PTM), such as noble gases, halides, oil, alcohol mixtures or sometimes the sample itself in a powder form. Noble gases, such as He, Ne or Ar are either loaded under pressure [12] or
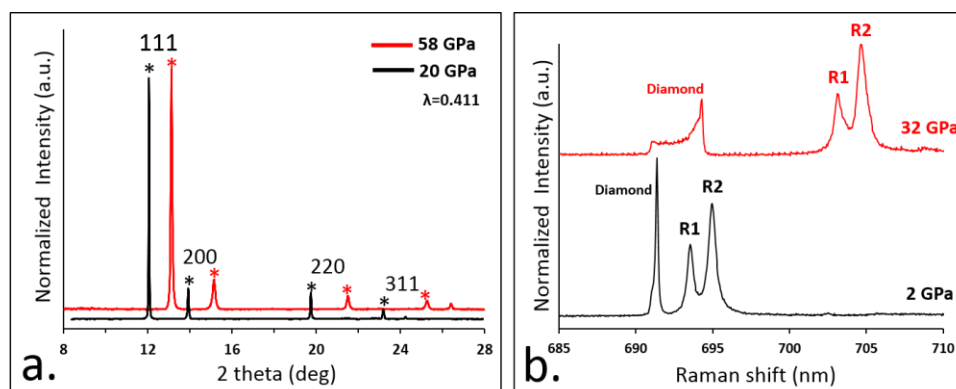
Figure 7. Pressure determination in the diamond anvil cell by **a)** powder X-ray diffraction of solid neon or **b)** Raman spectra of ruby and diamond.

cryogenically [e.g. 13]. Helium gas is the most hydrostatic medium that can be used. However, it can create problems in heating experiments, since the small-sized He atoms can diffuse in the diamond anvils and destroy them. Neon is the most popular PTM in the experiments of this thesis. It assures good quasi-hydrostatic conditions and has a well-studied equation of state (EoS) [14], which helps us to determine the pressure on the sample in XRD experiments. The 2theta ($2\theta^o$) position of the (111) reflection (Figure 7a) of solid neon is usually used for express pressure determination (http://kantor.50webs.com/diffraction.htm). Argon gas was used in few Raman spectroscopy and NIS experiments in this thesis. Argon is not as hydrostatic as neon, but it is easier to load and it is cheaper than Ne. Beside gases, halides such as NaCl, KBr, KCl can serve as PTM. During our NIS heating experiments the samples were loaded together with KCl. The majority of the NIS samples, however, were loaded with silicon oil. This is due to the significant instability of Be gaskets during our efforts to gas load a noble gas, which often led to gasket collapse or even diamond failure.

In cases where the PTM is not Ne, or neon has not crystallized yet (pressures < 7 GPa), or there is no access in a XRD facility during the experiment, the pressure in the sample chamber is determined by other ways. Often a small ruby sphere (Cr-doped Al_2O_3) is loaded next to the sample. The position of most intense peak of a ruby's fluorescence signal (i.e. R2 in Figure 1b) is shifting to higher wavenumbers with increasing pressure. Few calibrations are described in the literature for the hydrostatic or non-hydrostatic behavior of ruby under pressure (http://kantor.50webs.com/diffraction.htm) [15, 16]. A commercial ruby sphere was loaded and used as a pressure determinant in all the DACs and pDACs meant for Raman spectroscopy and NIS experiments. A ruby was loaded also in a few DACs meant for XRD experiments to characterize conditions at low pressures, where neon had not crystallized yet (Figure 2-vi). Other alternatives for pressure estimation include measurements of the Raman shift of the diamond anvil with

increasing pressure (Figure 1b), or determination of lattice parameters of the metals with known EoS, such as W, Pt, Au or the Re (gasket).

2.2.4. Heating in a diamond anvil cell

Studying the Earth's deep interior requires not only high-pressure, but also high-temperature generation (Figure 1). In diamond anvil cell experiments, temperatures as high as ~900 K can be generated by a resistive-wire-furnace placed outside of the DAC or inside and around the gasket. However, at higher temperatures graphitization of the diamond anvils occurs, which alters the unique physical properties that the diamonds offer (i.e. transparency, hardness) and eventually leads to the experiment's failure. To achieve higher temperatures, as is the need in this thesis, laser-heating systems are utilized.

A portable double-sided laser heating system was developed at BGI [17,18] and similar versions are installed at the nuclear resonance beamline, ID18, at ESRF (Grenoble, France) and the extreme conditions beamline, P02.2, at PETRA-III (DESY, Hamburg, Germany). Double-sided laser heating systems allow minimization of radial axial and axial temperature gradients in laser-heated DACs. In properly working laser-heating set-ups, the uncertainty in temperature measurements may be reduced down to about 100 K at ~2500 K. In laser-heating systems, a series of optical components focuses a laser-beam on the sample (Figure 8). The types of laser sources (SPI fiber, ruby, Nd: YAG, CO_2 and others), the maximum output power (50, 100, or 200 W in our work) and the laser operation type (continuous (CW) or pulsed) can vary. Temperature is usually determined by spectroradiometry (i.e. the use of the spectrum of black- or grey-body emission from the sample).

The two laser sides focus a beam on the same part of the sample. High-resolution cameras that are installed on the laser heads, provide an optical image of the sample and the heated area. It is crucial to clean thoroughly the surface of the diamonds attached to the seats before heating. If small dirt particles on the outer surface of the diamond anvils get ignited during heating, they can lead to diamond fracture. Heating periods of several minutes in duration require the use of a running-water cooling system around the DAC. The elevated temperatures warm up the body of the cell and eventually any nearby equipment, which might cause misalignments, melting of delicate parts or other malfunctions. Heating sessions that last a few seconds to a minute can be performed without the use of a cooling system. Dark-colored samples are heated directly by absorbing the incoming laser radiation. Thankfully, the great majority of our samples incorporated transition metals, which give distinct colors to the samples. Due to its full d-

shell, zinc compounds are usually colorless and therefore heating directly $ZnCO_3$ in this thesis was not possible. In such cases, a small amount of absorbing material (in our case, Au) is mixed with the sample ($ZnCO_3$) that serves as an absorber to heat the sample indirectly.
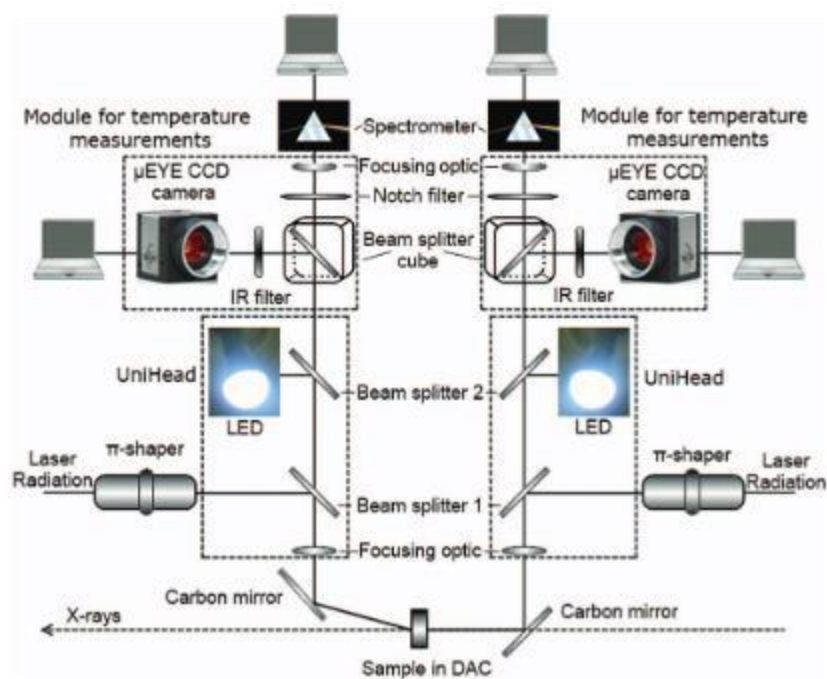
Figure 8. Detailed schematic representation of all components consisting the double-sided laser heating system. The figure is adapted from [17].

2.3. Raman Spectroscopy

2.3.1. Basic principles and instrumentation

Raman spectroscopy is a spectroscopic technique based on the inelastic scattering of monochromatic light from an irradiated sample. The method has an immensely wide field of applications (Earth, life, material, chemical, analytical sciences, etc.) by providing information, among others, on the molecular vibrations and crystal structures. The inelastic scattering of light was predicted theoretically by A. Smekal in 1923, and was experimentally observed a few years later, in 1928, by C.V. Raman after who the method was named.

When light interacts with matter, nearly all of the photons are scattered elastically (Rayleigh scattering) and there is no loss in energy (i.e. $E=E_0$, Figure 9). However, a very small percentage (~10^{-6} %) of the incident light is scattered inelastically and a loss (i.e. $E>E_0$, Stokes Raman scattering) or gain (i.e.

E<E_0, anti-Stokes Raman scattering) of energy occurs (Figure 9). This process is illustrated in Figure 10. In the case of Rayleigh scattering, an incident light of energy E_0 and frequency v_0 , interacts with a molecule and excites the cloud of electrons from the ground level to a "virtual level" (Figure 10a). This state is unstable and, thus the photons return to the original ground level. In
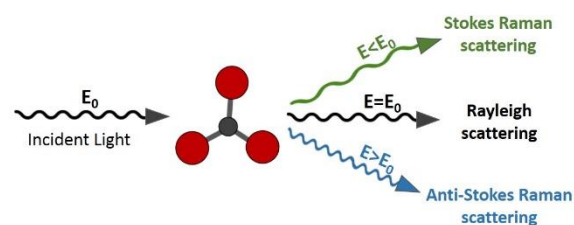
Figure 9. Scattering of light by molecules.

this process no energy is lost, so the Rayleigh scattering has the same energy and frequency (E_0, v_0) as the incident light (i.e. elastic scattering). The Stokes Raman scattering occurs when the electron cloud absorbs part of the incident light and falls back to a vibrational level (i.e. an excited level) instead of the ground level (Figure 10b). In this case, the Stokes Raman scattering has lower energy and frequency (longer wavelength) than the incident light. anti-Stokes Raman scattering occurs when the incident light meets the electron cloud already in a vibrational level (Figure 10c). The cloud is distorted to the "virtual level" and then falls back to the ground level having more energy and higher frequency than the incident light. The probability of the incident light to meet already excited electrons is low at ambient conditions.
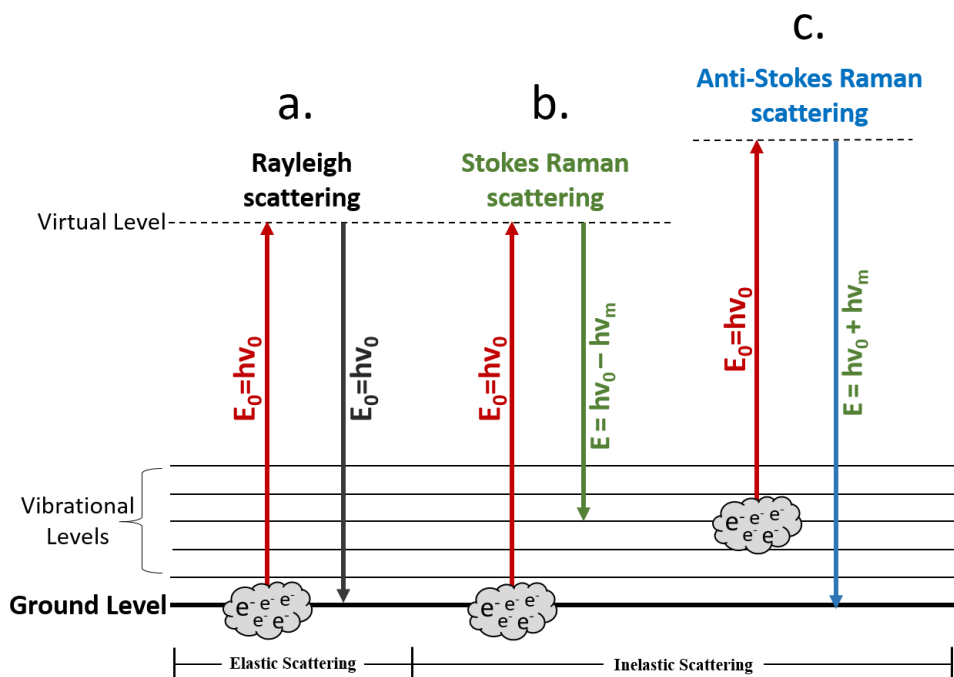
Figure 10. The Rayleigh and Raman scattering processes. **a)** A cloud of electrons is excited from the ground level and fall to the original ground level (Rayleigh). **b)** An electron cloud is excited from the ground level and falls to a vibrational level (Stokes). **c)** An electron cloud is excited from a vibrational level and falls to the ground level (Anti-Stokes). The energy changes are described, where E_0 and v_0 are the energy and frequency of the incident light, respectively, h is the Planck's constant and v_m is the molecular frequency.

Therefore, the Raman signal due to anti-Stokes scattering is weaker than the signal from Stoke scattering. This is the reason that most of the Raman spectroscopy studies in the literature (including this thesis) investigate only the Stokes scattering. The intensity of the anti-Stokes signal increases when the temperature rises and therefore the ratio of the Stokes to anti-Stokes signal can be used to measure the temperature of the sample.

The Raman scattering arises from molecular symmetric or asymmetric stretching and bending vibrations. These vibrations induce a large distortion of the electron cloud around the molecule. More concretely, each peak appearing in the Raman spectrum is derived from a specific molecular or lattice vibration. In calcite-type carbonates ($R\bar{3}c$) there are five Raman-active vibration modes (Figure 11). The position of the five peaks in the frequency scale vary for each carbonate composition, but
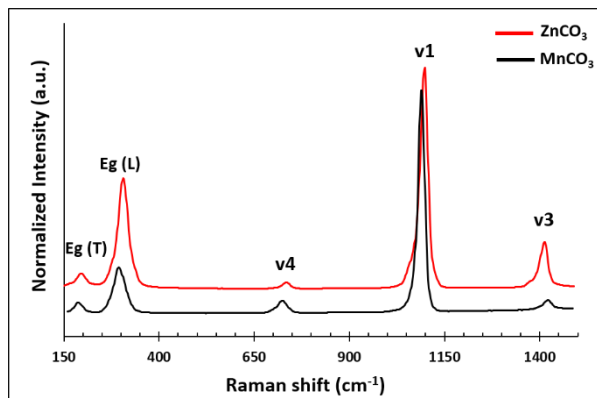
Figure 11. Raman spectra of $ZnCO_3$ and $MnCO_3$ at ambient conditions.

roughly averages to ~200, ~300, ~730, ~1100, and ~1420 cm^{-1}. The first two bands (i.e. with lower wavenumbers) correspond to external modes associated with lattice vibrations, one translational [Eg (T)] (Figure 12a) and one librational [Eg (L)] (Figure 12b), the latter three bands (i.e., with higher wavenumbers) correspond to internal vibrations within the CO$_3$ units, one asymmetric bending (Eg or v4)
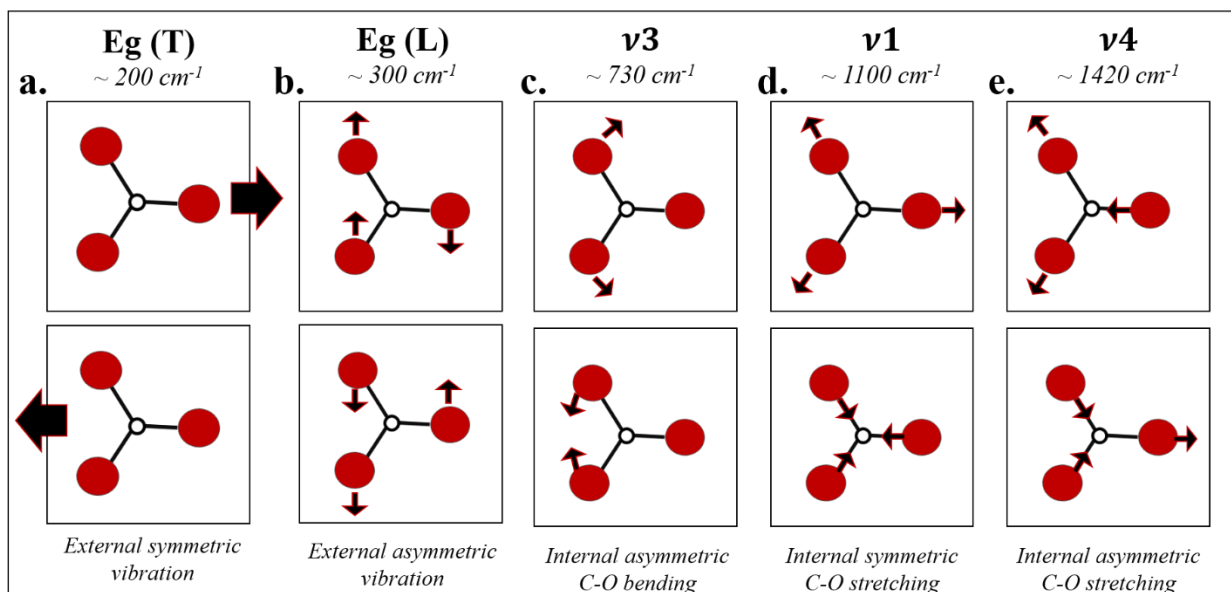
Figure 12. Schematic representation of the five Raman-active vibrational modes of carbonates.

(Figure 12c), one intense symmetric stretching (A1g or v1) (Figure 12d) and one less intense asymmetric stretching mode (Figure 12e) [19].

Many different configurations exist to build a Raman spectrometer. However, all spectrometers have the same basic components: a monochromatic laser source to excite the sample, a microscope/ camera to have optical view of the sample, a filter that separates the Raman signal from the Rayleigh scattering, a diffraction grating to split the Raman light into its constituent colors, a detector (usually a CCD), and a computer to control the operations. For the purposes of this thesis, we employed a Dilor XY spectrometer with 2 cm^{-1} resolution, using a 514 nm (green) line of an Ar$^+$ laser (Figure 13a). In this system, the Raman signal is dispersed by a triple monochromator system. In the cheaper modern spectrometers, double or triple monochromators have been substituted by Notch filter(s) (Figure 13b). In the spectrometer appearing in Figure 13a the detector used to be cooled down to about -75 °C by liquid nitrogen that we regularly filled in. Today the system is modernized by the installation of a Peltier cooled detector.
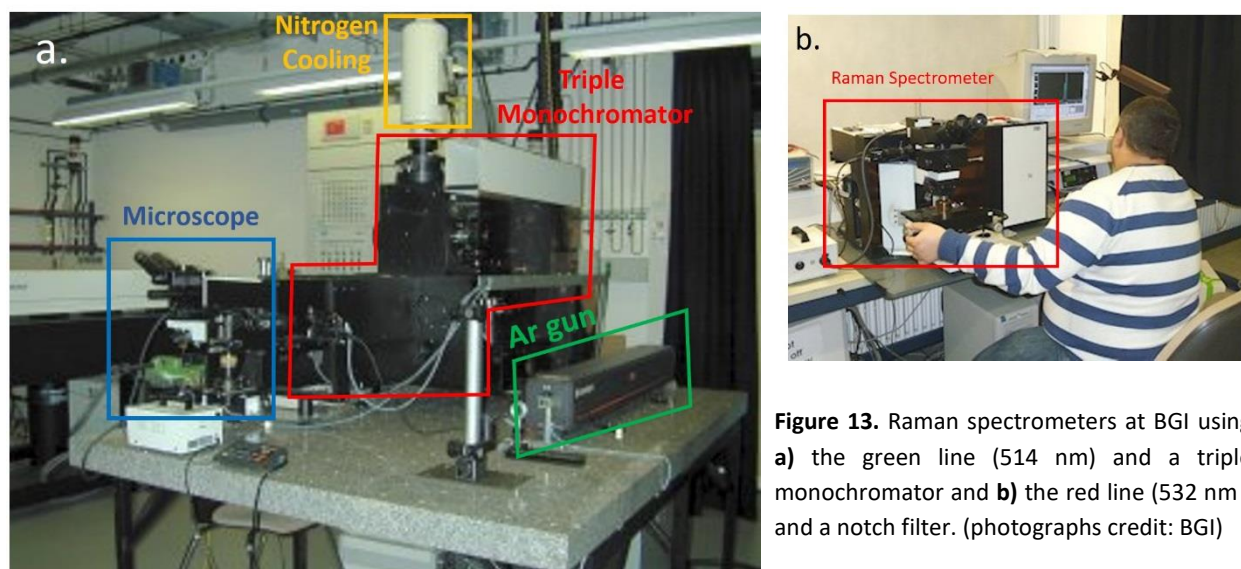
Figure 13. Raman spectrometers at BGI using **a)** the green line (514 nm) and a triple monochromator and **b)** the red line (532 nm) and a notch filter. (photographs credit: BGI)

2.3.2. Data collection and processing

Collection of Raman spectra is a straightforward procedure. The diamond anvil is placed flat on the motorized linear translation stage under the microscope. The proper magnification lens is selected, and the sample chamber is brought in focus. The user edits in the software the range of collection (in cm^{-1} or nm), the exposure time and the number of acquisitions. The light in the room should be turned off prior to collection. A spectrum is collected from the sample-free area of the sample chamber, which will

be used for background subtraction. Then, a spectrum is collected on the sample. The pressure in the cell is increased and is controlled by the ruby's signal (see section 2.2.3.). The user will wait several minutes for the pressure stabilization in the cell before repeating the collection procedure for the new pressure point. In this thesis, we collected Raman spectra over the wavenumber range of 150 to 1300 cm^{-1}. The v3 mode was not monitored due to the overlapping Raman signal of the diamond (1330 cm^{-1}). The spectra were collected for every 3-4 GPa pressure steps. We choose 60 sec exposure time and 5 cycles of acquisition to enhance the signal to noise ratio.

After collection, the background is subtracted from each spectrum. Then, the spectra are normalized with respect to the most intense peak (i.e. v1 mode). The rest of the spectra fitting was carried out using the software package PeakFit (Systat Software) (Figure 14), where the proper baseline is matched and a gaussian function is fitted in every peak. The resulted fitted spectrum is accompanied by the coefficient of determination (i.e. $0 \leq r^2 \leq 1$), which is an indicator of the fitting quality (r^2=1 is the perfect fit) (Figure 14). In all of our spectral fittings r^2 did not range below the 0.9 value.
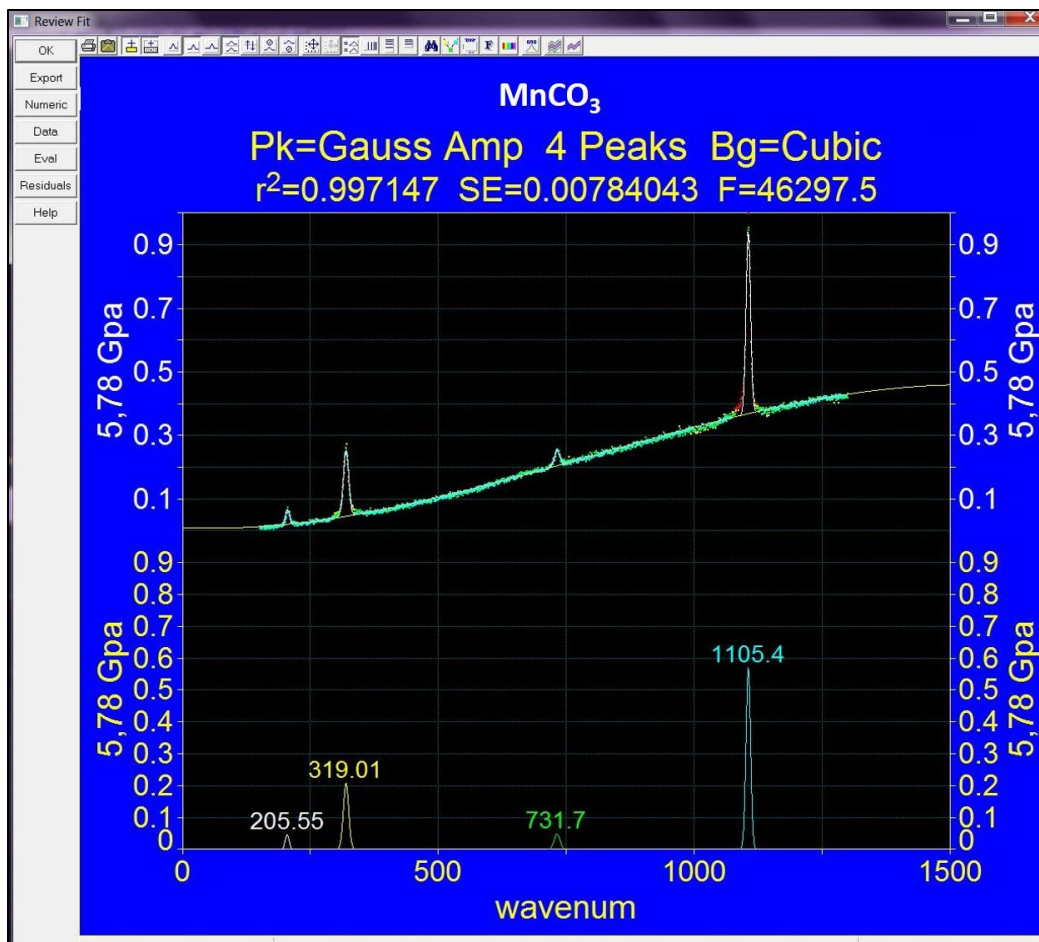
Figure 14. Fitted Raman spectrum of MnCO$_3$ using the Peakfit package.

2.4. X-ray diffraction

2.4.1. Basic principles

X-ray diffraction (XRD) is one of the most widely used non-destructive analytical techniques used to reveal information about the crystal structure, chemical composition, and physical properties of materials in air or under controlled conditions. As the name implies the XRD method benefits from the high energy electromagnetic radiation spectrum (100 eV – 100 keV) known as X-rays or Röntgen rays, after the German scientist W. Röntgen, who discovered them in 1895. Atoms scatter X-ray waves just like a lighthouse scatters an incoming ocean wave and produces secondary spherical waves. This phenomenon is known as elastic scattering, and the electron is known as the scatterer. If a family of scatterers is placed in a regular array, just like atoms do in a crystal structure, then a regular array of spherical waves will be
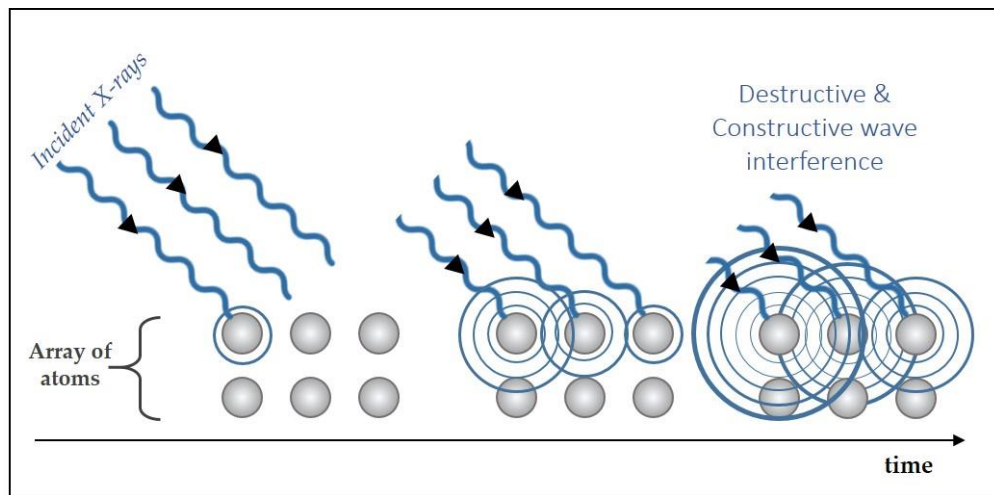
Figure 15. X-rays interact with the atoms in a crystal (sketch is inspired by Wikipedia®).

produced (Figure 15). In most directions, these waves will cancel one another out due to destructive interference. However, in a few specific directions they add constructively. The directions along which constructive interference occurs are determined by the Bragg's law:

$$2d \sin \theta = n\lambda \qquad\qquad (Eq.\ 2)$$

where d is the spacing between diffracting lattice planes, θ is the angle of the incident X-ray, n is an integer number and λ is the wavelength of the beam (Figure 16). A diffraction pattern is obtained by measuring the intensity of scattered waves as a function of scattering angle. Intense peaks, known as Bragg reflections, will form on the diffraction pattern at the theta angles where the Bragg condition is fulfilled. By measuring the angles and the intensities of Bragg reflections, a crystallographer can produce
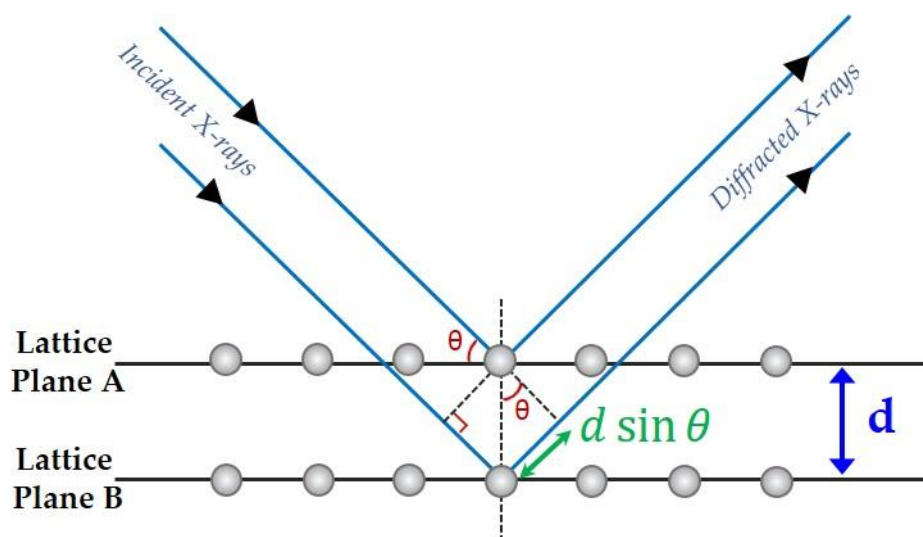
Figure 16. The Bragg's law. Two incident X-rays with identical wavelength, λ, approach two crystal lattice planes and are diffracted by two atoms within. In order for the diffracted waves to interfere constructively, the differences in the travel path must be equal to integer multiples, n, of the wavelength.

a three-dimensional map of the density of electrons within the crystal (Figure 17a). From this electron density map, the mean positions of the atoms in the crystal can be determined (Figure 17b), as well as their chemical bonds, their crystallographic disorder, and various other information.
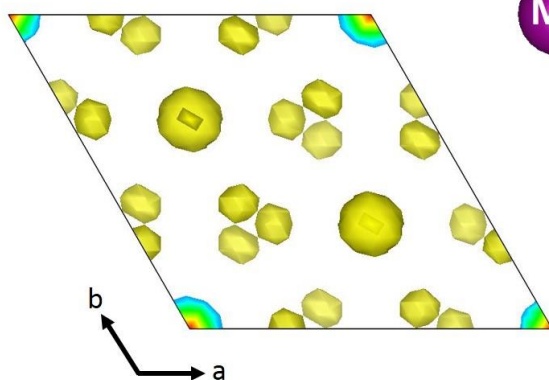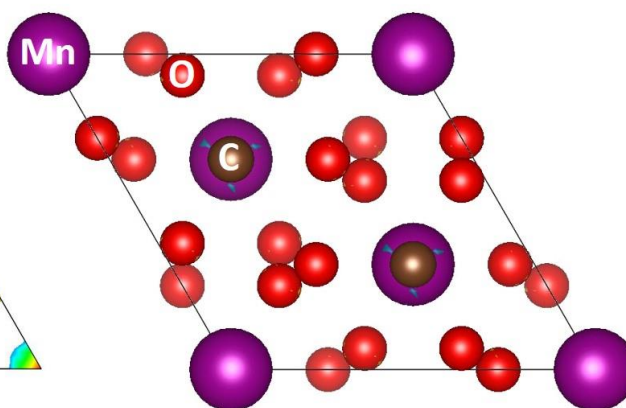
Figure 17. The unit cell of $MnCO_3$ along the c- crystallographic axis. **a)** Using the information of the Bragg reflections (scattering angle and intensities), an electron density map is built. The crystallographer **b)** assigns atoms and tries to eliminate residual electron densities. Note the minor residual density (blue) around the carbon atoms.

2.4.2. Powder versus single-crystal X-ray diffraction

The information that one can retrieve from a powder sample or a single-crystal sample is different. Powder X-ray diffraction (PXRD) is typically used for phase identification and for determining the unit cell parameters. The PXRD method struggles with the characterization of novel compounds and structures. On the other hand, the intensity of the diffraction peaks from a single-crystal sample provides information on the exact content of the unit cell (i.e. the type of atoms (heavy/light) involved, their coordinates in the unit cell, their coordination number and type of polyhedra that they form, their distances from other atoms).

A powder sample consists of countless small crystal grains in random orientations. Therefore, there will always be some crystals having just the right orientation to fulfill the Bragg's law (Eq. 2) and produce diffraction peaks in the form of Debye-Scherrer rings (Figure 18a). The theta-angle or d-spacing positions of the diffraction peaks allow phase identification, since each compound has a unique set of d-spacings, which serves as its fingerprint. In the case of a single-crystal, the XRD pattern consist of many diffraction spots (Bragg reflections) in a certain distance away from each other (Figure 18b). We know that for a given d-spacing and a given wavelength, diffraction peaks will appear only in certain theta angles
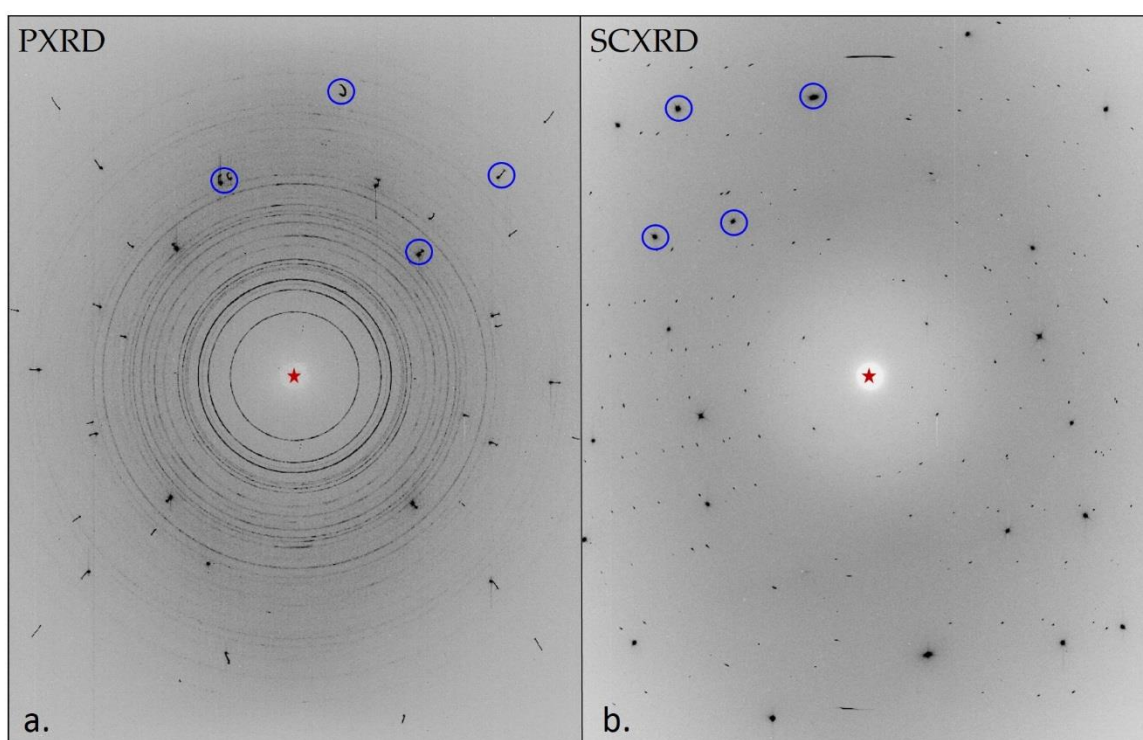
Figure 18. The different XRD patterns produced by **a)** a powder sample ($ZnCO_3$ + Au) and **b)** a single-crystal sample ($CaCO_3$-aragonite on the right) inside a diamond anvil cell. The red star marks the position of the beamstop. The blue circles mark examples of diamond reflections. Theta angles increase as we move from the center (beamstop) to the edge of the frame. Both patterns were collected at ID15b (ESRF).

defined by Bragg's law (Eq. 2). Thus, it is not certain that diffraction will be observed if a fixed crystal is irradiated with an X-ray beam of defined wavelength (Figure 19). To deal with this problem, a crystal's diffraction should be collected at several orientations.
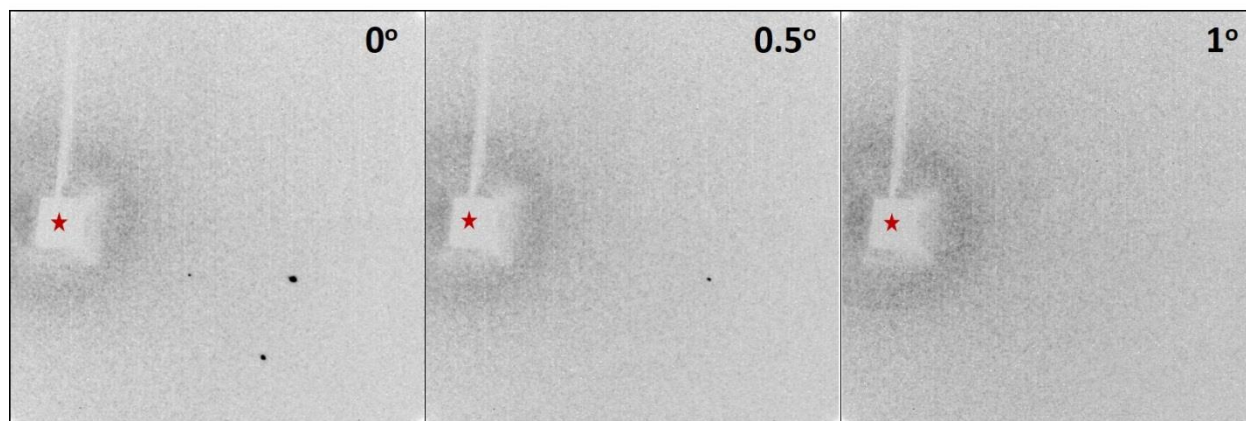
Figure 19. Diffraction patterns of an $FeCO_3$ crystal fixed during rotation. In certain angles, diffraction peaks appear ($0°$), while in others, the Bragg condition is not fulfilled and no diffraction spots are observed ($1°$). The red star marks the position of the beamstop. The patterns were collected at BGI, using a three-circle Brucker diffractometer.

2.4.3. Instrumentation

A typical diffractometer consists of a radiation source, a monochromator to choose the wavelength, a series of slits to adjust the shape of the beam, a sample on a holder and a detector to collect the diffracted waves. Besides the simplicity, many different configurations exist to build an X-ray diffractometer, mainly by altering the wavelength/energy and size of the incident beam, the geometry of the sample's movement with respect to the detector and beam position, and the type of detector used. The geometry of the diffractometer is often different for the purposes of powder (PXRD) or single-crystal (SCXRD) X-ray diffraction.

2.4.3.1. In-house facilities

Common wavelengths of X-rays used in *in-house* diffractometers range between ~1.79 ($\lambda_{K\alpha_1}$ of Co) to 0.56 Å ($\lambda_{K\alpha_1}$ of Ag). For powder diffraction, the Bragg-Brentano geometry is quite common (Figure 20). A thin layer of powder sample is well distributed on a flat disk (~4 cm in diameter) made from an amorphous material. The disk is placed in the diffractometer's holder. During collection, the geometry of the diffractometer is such that the sample rotates in the path of the collimated X-ray beam at an angle θ while the X-ray detector is mounted on an arm to collect the diffracted X-rays and rotates at an angle of
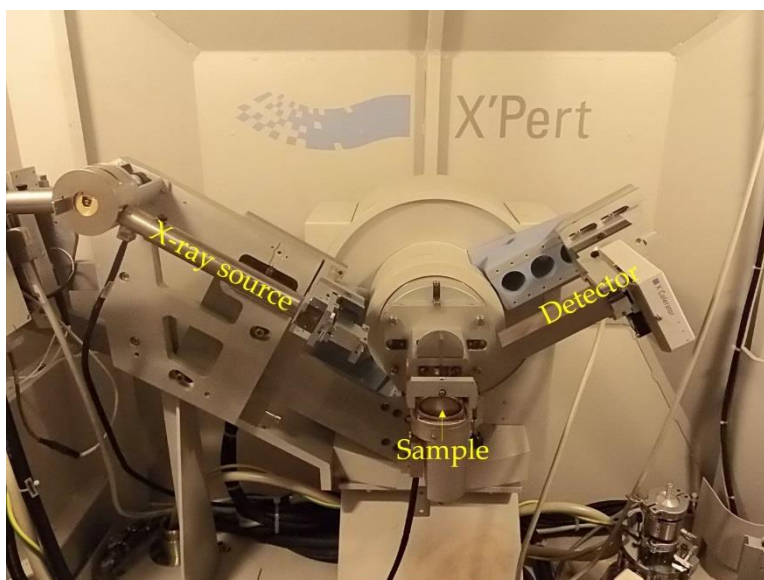
Figure 20. A Bragg-Brentano-type powder diffractometer (Philips X'Pert) at BGI, used for the characterization of the powder products obtained from cold-seal vessel experiments in this thesis.

2θ. At BGI, we employed a Philips X'Pert diffractometer with monochromated Kα1 of Co (λ = 1.788 Å) radiation operating at 40kV and 40 mA (Figure 20) to measure carbonate powders at ambient conditions.

In the case of single-crystal X-ray diffraction, the geometry of the diffractometer becomes more complex. Typically, four or three-circle diffractometers are employed offering the ability of a crystal's rotation along multiple directions during collection (Figure 21). At BGI, we mainly used a three-circle Brucker diffractometer equipped with a SMART APEX CCD detector for carbonate-single-crystal collections at ambient conditions. In the first period of this thesis the diffractometer was operating with a Mo-Kα radiation (Figure 21a). However, in the year 2017, the system was modernized and, among other changes, it now operates with an Ag source (Figure 21b). The crystal is mounted on the top of a glass capillary, which is attached on a goniometer head (Figure 22). The goniometer allows movement along the x,y and z direction, and thus the crystal's center of rotation can be found. This is a very crucial step. The crystal should not move out of the center of rotation or out of the beam during collection, otherwise the diffraction peaks will get broad and correct data integration will not be possible. The crystal is aligned with the help of a camera (Figure 21c, d–2). During collection, the X-ray beam arrives from the source (Figure 21c, d–1) to the sample (Figure 21c,

Figure 22. A goniometer for single-crystal diffraction.

70

d–3). The beamstop (Figure 21c, d–4) will block the intense primary beam that was not diffracted by the sample, and thus it protects the detector which is placed right after (Figure 21c, d–5). Several modes of collection exist by the combination of rotations along several axes in order to cover as bigger part of the reciprocal space as possible (i.e. φ, ω, θ and κ-axis rotations in a four-circle diffractometer, Figure 21c – 6 to 9, and φ, ω and θ-axis rotations in a three-circle diffractometer, Figure 21d – 6 to 8, respectively). Both diffractometers were employed for single-crystal selection of carbonates prior to their loading in the diamond anvil cells.

Figure 21. X-ray diffractometers for SCXRD at BGI. **a)** A three-circle Brucker diffractometer with a Mo-source and **b)** the same system anew using an Ag-source. **c)** A four-circle Oxford Xcalibur diffractometer using a Mo-source and **d)** a magnified photograph of the system in **b** for comparison. In **c** and **d** the same system components appear: 1 – X-ray tube, 2 – camera for samples view, 3 – goniometer with the crystal, 4 – beamstop, 5 – CCD detector, 6 – marks rotation around φ-axis, 7 – marks rotation around ω-axis, 8 – marks rotation around θ-axis, and 9 – marks rotation around the κ-axis only in **c**.

2.4.3.2. Synchrotron facilities

Under certain conditions, it is possible to collect SCXRD patterns under high-pressure in in-house diffractometers. However, data collection is very long (from a couple of hours to a day or more), weakly

scattering samples are not favored, samples much smaller than the beam size (~100 μm) are not ideal, and at high-pressures the constantly decreasing signal of the sample is strongly overpowered by the high-pressure environment's signal. In addition, collection of heated samples is very challenging, since the well heated area often covers only a small portion of the crystal. The problems can be solved with the use of a high-brilliance and high-energy X-ray beam with small divergence, able to focus in an area of just a few μm^2. Such an excellent beam status is provided by synchrotron facilities.

During this thesis, we performed SCXRD experiments at X-ray diffraction beamlines dedicated to extreme conditions, namely, ID15b at ESRF (30 keV, λ≈0.411 Å, ~10x10 μm^2 beam, MAR555 flat-panel detector), P02.2 at PETRA III (42 keV, λ≈0.29 Å, ~2x2 μm^2 beam, PerkinElmer XRD 1621 flat-panel detector), and 13IDD at APS (37 keV, λ≈0.29 Å, ~2x2 μm^2 beam, Pilatus detector). On a historical note, a great portion of our $CoCO_3$ and $MnCO_3$ data was collected at ID09a (ESRF) before the year 2016, and later the beamline was re-located at ID15b. Although each beamline has its own geometry and computer operation window, they have equivalent components and same collection procedures. Below, the ID15b beamline will be described as an example. The primary beam arrives close to the sample (Figure 23-1) to
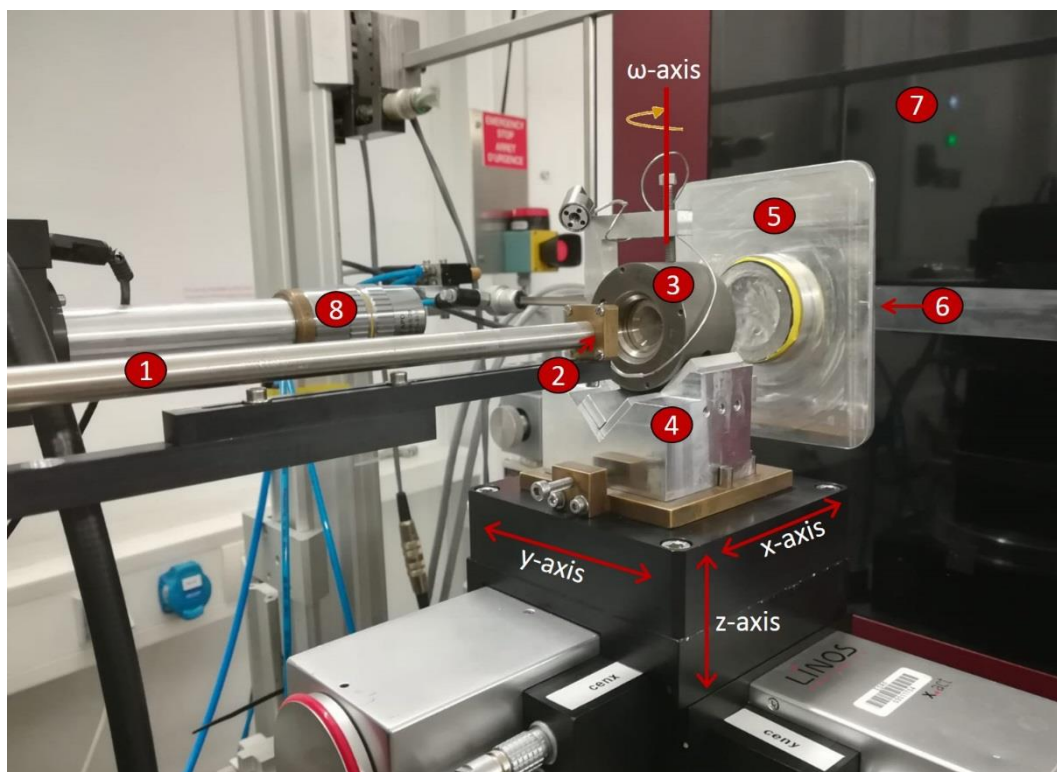
Figure 23. Single-crystal X-ray diffraction at ID15b (ESRF). The following components are depicted: 1 – edge of pipe directing the X-ray beam, 2 – pinhole, 3 – an ESRF membrane cell, 4 – DAC holder, 5 – diode, 6 – the beamstop fixed with tape, 7 – the large area MAR555 flat-panel detector, 8 – camera and PRL system for ruby fluorescence. The DAC stage can move upon command along the y, z and x-axis and rotates around the ω-axis.

the sample having nearly assumed its final form. As a last step the beam tails are reduced by the use of a pinhole (Figure 23-2). The DAC (Figure 23-3) is placed on a special holder (Figure 23-4) right after. A Si-diode (Figure 23-5) can contract and retract on command. The diode servers as a counter during DAC scanning and alignment procedures and must be removed before data collection. Similarly, to in-house SCXRD diffractometers, a beamstop follows to block the intense primary beam (Figure 23-6). A large-area flat-panel detector collects the diffracted reflections (Figure 23-7). The sample chamber can be monitored by a high-resolution camera (Figure 23-8). Many beamlines provide a pressure-by-ruby-luminescence (PRL) system mounted close to the DAC stage (Figure 23-8). During collection the DAC stage can move along the y and z and rotate around the ω-axis. Movement of the DAC stage in the x-axis is not recommended, since in this way the user alters the detector to sample distance.

2.4.4. Data collection in synchrotron

Prior to any data collection powder and single-crystal calibration files must be created. The calibration file contains valuable information for the correct data processing. This information usually is the X-ray wavelength, the sample to detector distance, the x-y position of the primary beam, the pixels size of the detector, the beam polarization, as well as, corrections for the tilting of the detector. To create a calibration file one has to collect PXRD or SCXRD of a material with very well known unit cell parameters (i.e. a standard). Usually different standard materials are used for the calibration of powder and SCXRD patterns. In the case of powder, the most popular choices are CeO_2, Si or LaB_6, while for single-crystal the most popular is enstatite ($MgSiO_3$). Although, we also choose among these standards for calibrations, theoretically, any material with very well characterized lattice parameters (confirmed from more than one diffractometer) that is also chemically stable, not sensitive to the X-ray beam, and easily available can be used as a calibrant.

As soon as the calibration files are ready, the actual data collection of samples can start. We will describe the data collection of one crystal in a diamond anvil cell that has ~78° opening aperture (Figure 6a). The following protocol has been described extensively by Ref. [20].

1) **DAC preparation:** Crystals should be placed as close in the center of the sample chamber as possible, but still few μm away from one another. Crystals placement in the cell should allow for the shrinking hole of the gasket at high pressures. A contact of the gasket with the crystals during the experiment must be
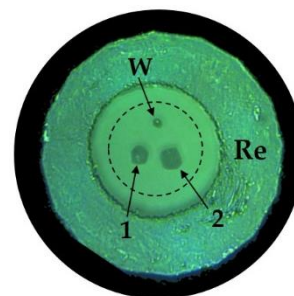
Figure 24. Two $CoCO_3$ crystals and a W chip arranged in the sample chamber. At high-pressures the gasket hole will shrink as indicated by the dashed circle.

avoided. If chosen, pressure determinants (e.g. ruby) or metal absorber chips (e.g. W), should be placed as far as possible from the crystals, but still in a safe position from the gasket (Figure 24). Prior to the DAC placement under the beam, the outer surface of the diamond anvils must be thoroughly cleaned to avoid additional unwanted diffraction. The DAC should be placed on the holder vertically (see Appendix Figure A2), since inclinations can cause problems during cell alignment or lead to collisions with nearby equipment (e.g. pinhole).

2) **DAC and crystal alignment:** The center of the sample chamber is found by scanning the DAC stage along the y and z-axes. The center is found due to difference in X-ray absorbance between the gasket material and the sample chamber (see Appendix Figure A3). If the sample is a strong X-ray absorber (e.g. $FeCO_3$ as opposed to $MgCO_3$) or the cell contains an additional metal absorber chip (e.g. W, Pt or Au, Figure 24), then they are preferentially brought under the center of the beam. This is important for the finding of the center of rotation. The sample must not move out of the center of rotation during collection, thus this procedure is delicate. The cell-position is then corrected and the sample chamber, sample, or metal absorber (depending on which one of those the user decided to center on) is aligned with the beam and the ω-axis. After sample alignment and centering procedure, the user can move the sample under the beam (if not already there) with the help of a camera (Figure 23-8) and start the data collection.

3) **Data collection optimization:** There are three types of scans, the **still-scan** (i.e. the DAC remains stationary while exposed to the beam for a few seconds), the **wide-scan** (i.e. the DAC rotates around the ω-axis continuously from -20° to + 20°, while exposed to the beam for a few seconds) and the **step-scan** (assuming that the DAC has an 90° opening aperture, it rotates around the ω-axis stepwise from -40° to + 40° and is exposed to the beam every 0.5° step for a few seconds). The user should check what is the opening angle of the DAC (i.e. at which angle the X-ray beam is blocked by the seats or body of the cell) before collection by performing and ω-scan. The user gets a first impression of the sample by collecting a still or a wide-image that allows him/her to inspect the crystal's quality and the phases present. If the user decides to collect SCXRD data by performing a step-scan then he/she must adjust the intensity of the reflections by applying filters (in the case of the P02.2 and 13IDD beamlines) or by moving the undulator (IVU20c) that is located in the optics hutch (in the case of the ID15b beamline). It is important the sample is not over or underexposed from the beam. If not so, the data integration and the structure solutions and refinements will be a difficult, if not impossible, task. Following the optimization of the reflections intensity, the user collects step-scan images. The preliminary data processing is strongly advised,

before the user decides to increase pressure, move to another sample or rather repeat the collection under different settings.

4) **Grids:** The sample often powderizes/recrystallizes after heating. Many times the most reacted are is located only in a very small part of the crystal. Thus, the user must map the crystal by collecting still or wide images, before he/she decides in which point(s) to collect step-scans.

2.4.5. Data processing

In the very rare cases during this thesis that powder patterns required processing, the GSAS or JANA software packages were implemented [21, 22]. The powder patterns were fitted using the Rietveld refinement. The Rietveld method uses a least-square approach to refine a theoretical model until it matches the real collection data profile. The following steps are followed:

1) **Data and phases import:** The user inputs the data file and edits necessary information, such as the wavelength used. The lattice parameters and space groups of the expected phases are added along with the atomic coordinates.

2) **Refinements:** The user starts be fitting the background either manually or by using existing functions (e.g. Shifted Chebyschen). Then, the user refines the lattice parameters of each phase, the phase fractions and the Lorentzian and Gaussian profile width until convergence is reached.

A good powder refinement results in small goodness of fit factor (GOF, S^2 or χ^2) close to unity. The difference between calculated model and the observed data must be minimized. All reflection peaks should be fitted, and in the case of a foreign, unfitted, peak, a good explanation must be provided. An example of a powder pattern fitting ($CoCO_3$ and CoO) is shown in section 5.3.3.

Single-crystal X-ray diffraction data processing was extensively performed during this thesis. Integration of the reflection intensities and absorption corrections were performed using the CrysAlis[PRO] software [23]. We choose to carry out structure solutions and refinements using the JANA crystallographic computing system [22]. Other alternative options include the SHELX series-package [24] as implemented in WinGX (or in other software), XSeed, OLEX2 and many others. An extensive tutorial for the data reduction at extreme conditions using CrysAlis[PRO] was provided by Ref. [20]. Therefore, we will restrict ourselves from detailed explanations, and rather briefly review the procedure. The following steps are followed (CrysAlis commands are written in bold and in parentheses):

1) **File conversion:** Synchrotron files are converted in the ESPERANTO format (**dc rit**), which is compatible with the CrysAlis[PRO] software. After file conversion, an experiment is created. The

instrument parameters, as created during the calibration are loaded ($\mathbf{rd\ p}$) and data processing can start.
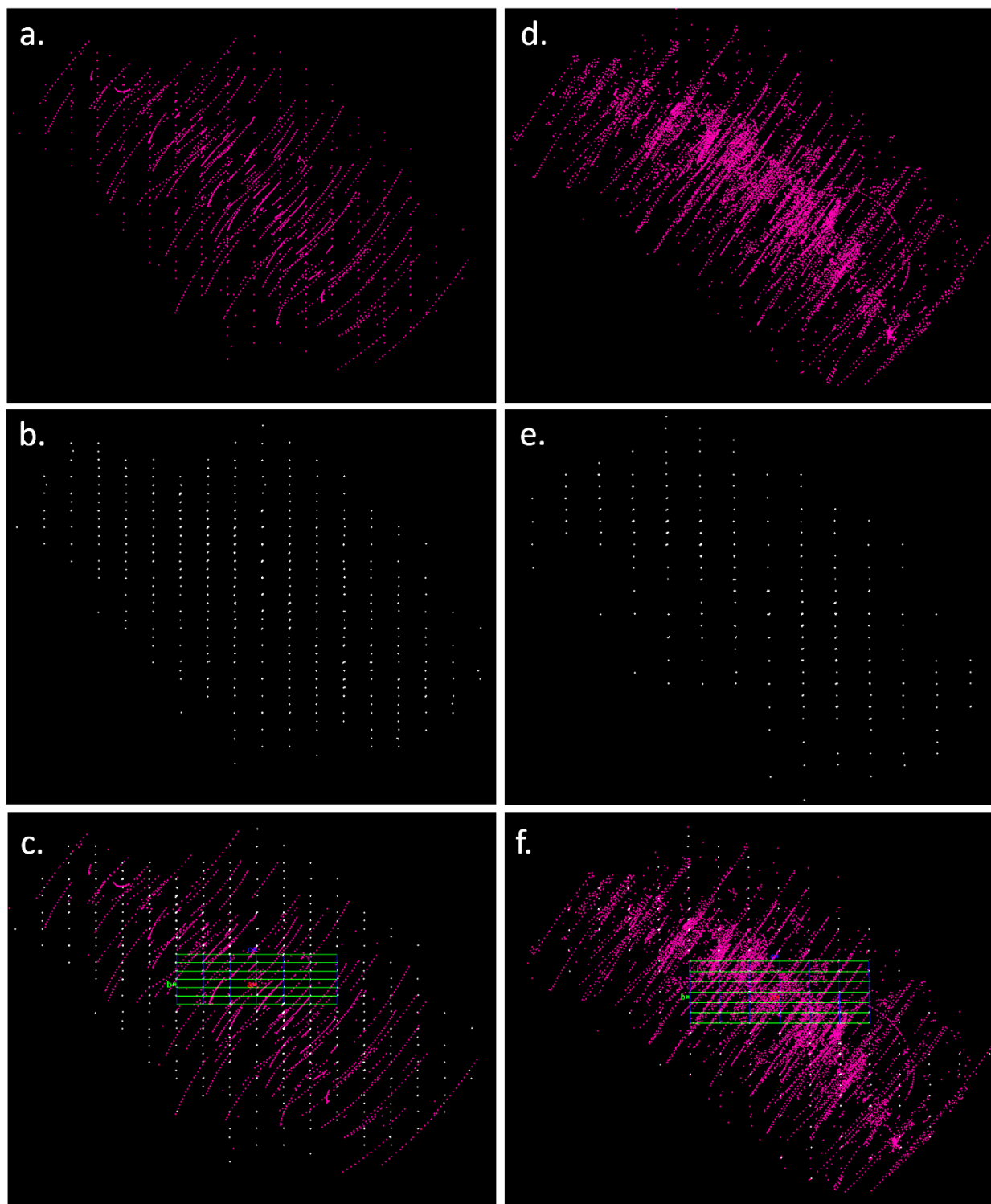
Figure 25. Reflections in the Ewald sphere using CrysAlis[PRO]. Two datasets for $NiCO_3$ SCXRD collection in the diamond cell are depicted along the a*- axis, **a-c)** at 1 bar, and **d-f)** at 62 GPa. Starting from **a** and **d**, the user has to separate the sample reflections (**b** and **e**) from the trash-reflections arising from the high-pressure environment as shown in **c** and **f**.

2) **Peak hunting:** During the peak hunting procedure (**ph s**) the software hunts each frame marking the position of peaks. In the diamond anvil cell, peaks may arise not only from the sample, but also the high pressure environment (e.g. diamonds, pressure-transmitting medium, gasket…) or even dust particles on the anvils. The user can explore all the peaks after hunting in the Ewald sphere (**pt ewald**) (Figure 25).

3)   **Unit cell finding:** As is the case in most DAC experiments, the user has to manually select the peaks that belong to the sample. The user is looking for peaks that form a regular pattern (e.g. Figure 25-b and -e). Once a few points are selected, the software can find the unit cell (**um ttt**) and index the rest of the phase's peaks (**um i**). In the case of heated samples, often many domains of the same phase or different phases appear (Figures 26 and 27), thus making the peak selection for the unit cell indexation a challenging task that requires a patient user.

4) **Data reduction:** During data reduction, the software extracts the reflection intensities and produces a file (.hkl extension) that includes all the hkl reflections observed and their intensities. Other software (e.g. JANA) use this .hkl file for structure solution and refinements. When CrysAlis
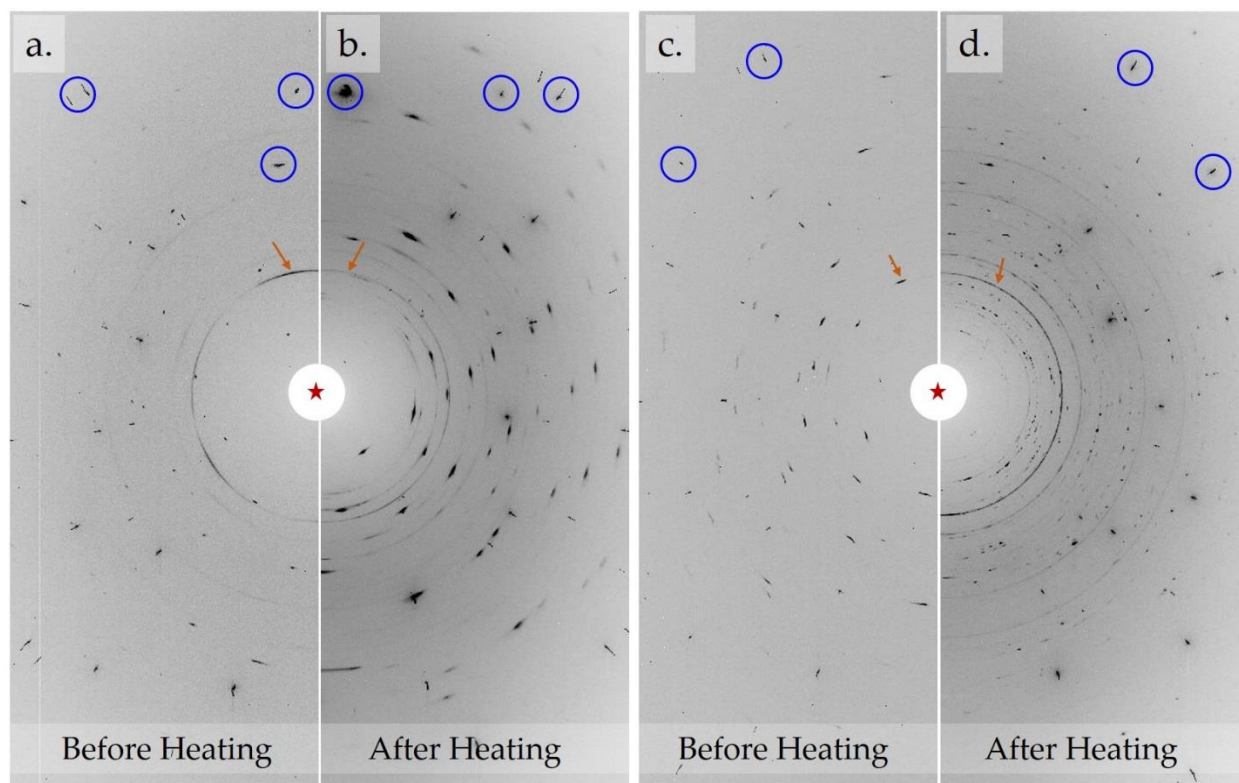
Figure 26. Diffraction patterns of the two $CoCO_3$ crystals in Figure 24 before and after heating. **a,b)** The first $CoCO_3$ crystal is heated at high pressure and low temperature. The sample recrystallizes, but no reaction occurs. **c,d)** The second $CoCO_3$ crystal is heated at low pressures and high temperatures. This time, the sample decomposes to several Co_4O_5 crystallites. The (111) reflection of solid neon is pointed by arrows. Examples of diamond reflections are circled in blue.

performs the data reduction (**dc proffit**) the positions of the reflections based on the UB-matrix that was defined in the previous step (see step 3 above) are predicted. Then, the software extracts the reflection intensities based on their shape and the background level. If asked by the user, a space group is suggested. The user evaluates the quality of the integration with the help of confidence factors, such as R_{int}, and by inspecting the frame scaling curve (Figure 28).

5) **Data finalization:** Once the data reduction is complete, convergence is met and the user is satisfied with the result, the data are finalized (**dc rrp**). This step is actually performed by default following the data reduction. However, the user has access to additional settings by running data
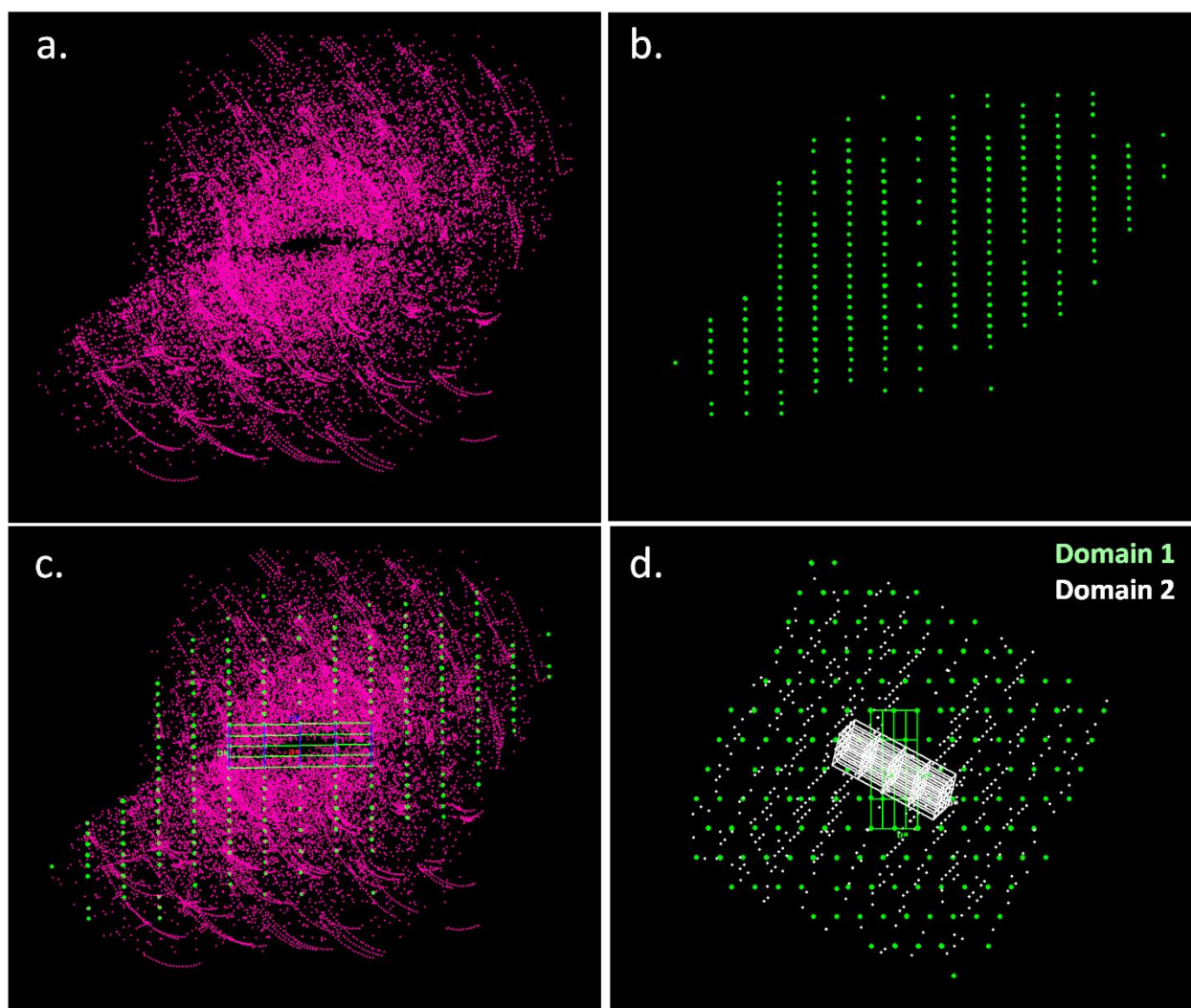
Figure 27. Reflections of a $MnCO_3$ crystal after heating in the Ewald sphere. **a)** Peaks arise from several domains and the high-pressure environment. In **b** and **c,** a $Mn_4C_4O_{13}$ (domain 1 in green) is found and depicted along the a-axis. Many domains belong to the same phase, but have different orientations. For example, in **d**, a second $Mn_4C_4O_{13}$ domain (domain 2 in white) is found together with the first domain, now projected along the c-axis. In this dataset (**a**) we found nine domains of $Mn_4C_4O_{13}$ and two domains of δ-Mn_2O_3, and then we stopped looking for more.

finalization separately, such as advanced choices for absorption corrections, or apply filters (e.g. apply thresholds to remove negative intensities, or to remove R_{int} spikes).

Following this procedure, CrysAlis[PRO] creates various files, among which the most important for the structure-solution software are usually those with the extension type *.hkl*, *.cif-od*, *.cif* and *.ins*. Normally, a good integrated dataset that has R_{int} values less than 15% is eligible for structure solution. However, this does not mean that a dataset with nearly perfect R_{int} values and frame scaling curve will necessarily be a good dataset. This is an often case for phases with low symmetry (i.e. triclinic) or for overexposed data (e.g. Figure 28b).

a. Good Dataset

Statistics vs resolution (taking redundancy into account) – point group symmetry: O-3m1

resolu-tion(Å)	# kept	# theory	# unique	% complete	average redundancy	mean F2	mean F2/sig(F2)	Rint	RsigmaB
inf-1.05	125	45	28	62.2	4.5	304948.54	102.47	0.023	0.008
1.05-0.80	122	43	28	65.1	4.4	158102.58	60.66	0.023	0.011
0.80-0.70	126	44	28	63.6	4.5	100640.19	53.14	0.040	0.015
0.69-0.63	107	38	28	73.7	3.8	70090.45	35.48	0.031	0.016
0.62-0.57	123	50	28	56.0	4.4	60924.10	37.82	0.050	0.018
0.57-0.46	96	182	33	18.1	2.9	29662.97	17.59	0.093	0.031
inf-0.46	699	409	173	42.3	4.0	125792.18	52.99	0.031	0.012
inf-0.80	252	92	58	63.0	4.3	231307.20	81.42	0.023	0.009

b. Over-exposed Dataset

Statistics vs resolution (taking redundancy into account) – point group symmetry: O-3m1

resolu-tion(Å)	# kept	# theory	# unique	% complete	average redundancy	mean F2	mean F2/sig(F2)	Rint	RsigmaB
inf-1.09	66	36	27	75.0	2.4	2294338.77	224.58	0.038	0.004
1.07-0.85	71	34	27	79.4	2.6	2187414.98	194.38	0.038	0.004
0.84-0.72	70	34	27	79.4	2.6	1541155.49	131.00	0.030	0.006
0.72-0.65	72	35	27	77.1	2.7	1666460.77	132.63	0.036	0.006
0.65-0.60	72	32	27	84.4	2.7	1332116.23	89.61	0.037	0.006
0.60-0.55	52	49	27	55.1	1.9	1328984.88	79.97	0.040	0.007
0.54-0.47	39	108	31	28.7	1.3	703417.32	48.78	0.021	0.015
inf-0.47	442	330	193	58.5	2.3	1644913.44	135.42	0.036	0.005
inf-0.80	155	78	61	78.2	2.5	2130029.98	198.13	0.037	0.004

c. Under-exposed Dataset or other problems

Statistics vs resolution (taking redundancy into account) – point group symmetry: Fm-3m

resolu-tion(Å)	# kept	# theory	# unique	% complete	average redundancy	mean F2	mean F2/sig(F2)	Rint	RsigmaB
inf-1.09	159	33	29	87.9	5.5	69.26	13.87	0.138	0.048
1.08-0.82	212	30	29	96.7	7.3	16.15	5.01	0.387	0.135
0.82-0.71	123	30	30	100.0	4.1	6.34	2.11	0.543	0.421
0.70-0.60	70	46	30	65.2	2.3	2.80	0.83	0.693	0.904
inf-0.60	564	139	118	84.9	4.8	27.33	6.36	0.226	0.105
inf-0.80	400	68	63	92.6	6.3	36.27	8.23	0.206	0.070

Figure 28. The user inspects the quality of the data reduction and decides whether to proceed in the structure solution, perform a second data-collection with different settings or change sample. Here are a few examples of: **a)** a good dataset (i.e. R_{int} factor is 3% and the shape of the frame curve scales uniformly around one), **b)** an over-exposed dataset (i.e. the Rint and the shape of the frame scaling curve appear good, but the mean scattering amplitudes are extremely high and do not vary, thus structure solution will be challenging) and **c)** an under-exposed dataset that may harbour other problems (i.e. Rint factor is >15%, the frame scaling curve appears rocky, the scattering amplitudes are extremely low.)

2.4.6. Structure solution and refinements

The atoms, and more specifically the electrons, in the crystal diffract X-rays to form a diffraction pattern. The two are connected to one another through a Fourier transform described by the following formula:

$$\rho_{xyz} = \frac{1}{V}\sum_{hkl} \boldsymbol{F}_{hkl} exp[-2\pi i(hx + ky + lz)] \qquad (Eq.\ 3)$$

where ρ_{xyz} is the electron density in an xyz position inside the unit cell, V is the volume of the unit cell, the sum is over all the crystal lattice planes characterized by Miller indices, hkl, and $\boldsymbol{F}_{hkl}$ is the structure factor, which is a complex number and is given by the formula:

$$\boldsymbol{F}_{hkl} = F_{hkl} exp(i\alpha_{hkl}) = \sum_{j} f_j exp\left[2\pi i\left(hx_j + ky_j + lz_j\right)\right] =$$

$$= \sum_{j} f_j cos\left[2\pi\left(hx_j + ky_j + lz_j\right)\right] + i\sum_{j} f_j sin\left[2\pi\left(hx_j + ky_j + lz_j\right)\right] \qquad (Eq.\ 4)$$

where α_{hkl} is the phase of the diffracted beam, x_j, y_j, z_j and f_j are the atomic coordinates and the scattering factor of the jth atom, respectively. F_{hkl} is the magnitude of the scattering factor known as scattering amplitude and is given by the following formula:

$$F_{hkl}^{\ 2} = \frac{I_{hkl}}{K \cdot Lp \cdot A} \qquad (Eq.\ 5)$$

where I_{hkl} is the reflections intensities, K is the scale factor, Lp is the Lorentz-polarization correction and A is the transmission factor.

In diffraction experiments, we measure the intensities of waves scattered from the lattice planes in the crystal. Therefore, we can calculate the structure amplitudes (Equation 5), but what we are still missing is the phase (α_{hkl}) of the diffracted beam (Equation 4), a problem widely known in crystallography as the "Phase Problem" [25]. The phase carries very important structural information as demonstrated by the famous cat and duck example (Figure 29). In this example, the Fourier transform (i.e. a diffraction pattern) of a cat and a duck are derived. Different colors shown different phases and the brightness of the

color indicates the amplitude. By combining the amplitudes of the duck pattern and the phases of the cat pattern, a new hybrid diffraction is created. When the latter is translated into an image through reverse Fourier transform, the result is a cat. This is an example of how the assignment of the wrong phase can lead to the wrong atom placement in the unit cell. To overcome the phase problem one can determine very simple crystal structures by trial and error methods (i.e. start with a plausible model and calculate
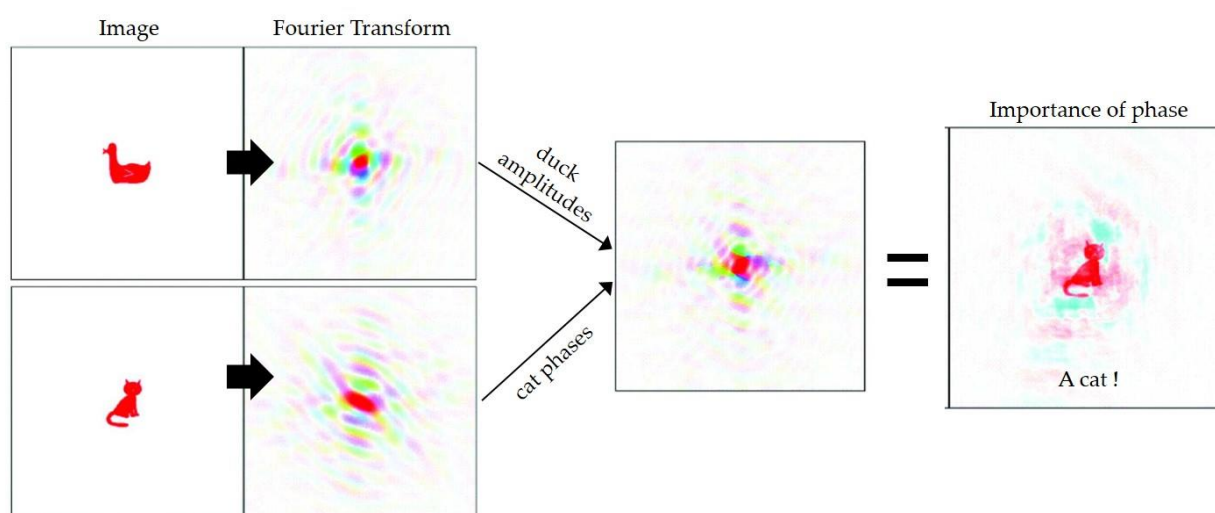
Figure 29. The duck and cat example demonstrating the importance of phases in carrying information. The example is adapted by Kevin Cowtan's Book of Fourier (http://www.ysbl.york.ac.uk/~cowtan/fourier/fourier.html).

the expected intensities and if they match the observed intensities then the structure is solved, if not then another model is calculated until a match is found). Even for simple structures, the trial-and-error method is a diligent approach, and in the case of slightly more complex structures, it may take years before the correct model is found. Overcoming the phase problem is an automated procedure nowadays and many phasing methods are implemented in software, such as the Patterson syntheses, direct methods, heavy-atom methods, charge flipping algorithms and others. Once the phases are somehow derived, atoms are assigned to their xyz coordinates in the unit cell (Figure 30) and the refinements of the atomic coordinates, the site occupancies and the anisotropic displacement parameters (ADP) can start.

The quality of the structural model is determined by the residual R-factors given by the following formulas:

$$R_1 = \frac{\sum ||F_{obs}| - |F_{calc}||}{\sum |F_{obs}|} \qquad\qquad (Eq. \ 6)$$

$$wR_2 = \left[\frac{\sum w |F_{obs}^2 - F_{calc}^2|}{\sum w F_{obs}^2} \right]^{1/2} \qquad\qquad (Eq. \ 7)$$
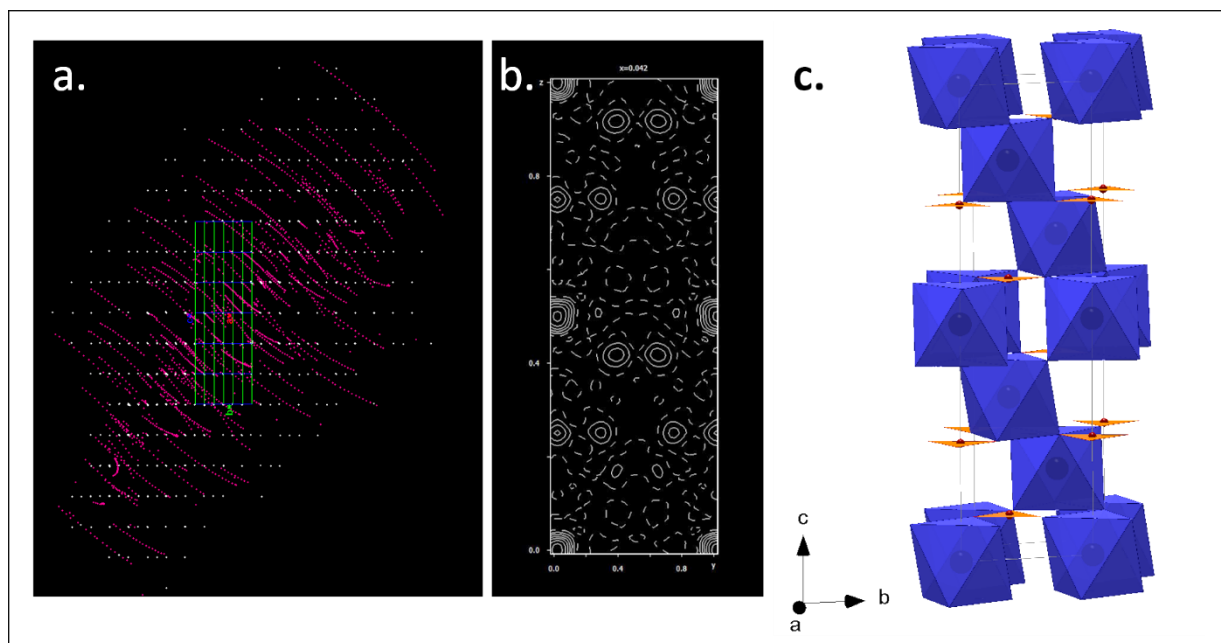
Figure 30. Snapshots of some of the processes involved to solve the structure of a crystal. **a)** Using CrysAlis[PRO], the diffraction peaks that belong to a NiCO$_3$ crystal in the diamond anvil cell are found in the reciprocal space. **b)** A Patterson map of the same dataset is created and points in the position where electron density is high and atoms should be placed. **c)** The calcite-type structure of the NiCO$_3$ crystal is now solved. All images present NiCO$_3$ data along the a-axis.

where F_{obs} is the observed structure factor amplitude, F_{calc} is the calculated structure factor amplitude based on the model and w is the weighting factor individually derived for each measured reflection based on its standard uncertainty. The crystallographer knows that his/her structural model is of good quality if:

1) The R-factors are small (i.e. R1 = 1-2% is excellent, R1= 10% is acceptable, R1>15% indicates serious problems with the data quality or the model solution).

2) The data to refined-parameters ratio is high (i.e. ratio > 10 is excellent, 10 < ratio < 8 is good, 8 < ratio <6 is acceptable if a good reasoning is provided, ratio < 6 is unacceptable).

3) No major positive or negative electron residual densities exist.

4) The model makes sense from crystallographic and chemical point of view.

2.4.7 Equation of state

An equation of state (EoS) is a fundamental characteristic of a material that relates thermodynamic variables, namely the pressure, temperature and the material's density. Most frequently, the isothermal (i.e. T= 300 K, ΔT=0) EoS of minerals at high-pressures are reported. One of the most popular EoS, the Birch-Murnaghan equation of state is defined as follows:

$$P(V) = \frac{3K_0}{2}\left[\left(\frac{V_0}{V}\right)^{\frac{7}{3}} - \left(\frac{V_0}{V}\right)^{\frac{5}{3}}\right]\left\{1 + \frac{3}{4}(K_0' - 4)\left[\left(\frac{V_0}{V}\right)^{\frac{2}{3}} - 1\right]\right\} \qquad (Eq.\ 7)$$

where P is the pressure, K_0 and V_0 are the bulk modulus and volume of the unit cell at zero pressure, respectively, V is the volume at a given pressure and K_0' is the derivative of the bulk modulus with respect to pressure. The bulk modulus describes the how compressible a material is. High bulk modulus values characterize materials that are very hard to compress and vice versa. A second ($K_0' = 4$), third or fourth ($K_0' \neq 4$) order of Birch-Murnaghan EoS may be fitted depending to the degree of linearity that the data show. A discontinuity or divergence from the main EoS curve is an indication of a change in the mineral's structure or the atoms electronic properties (Figure 31).
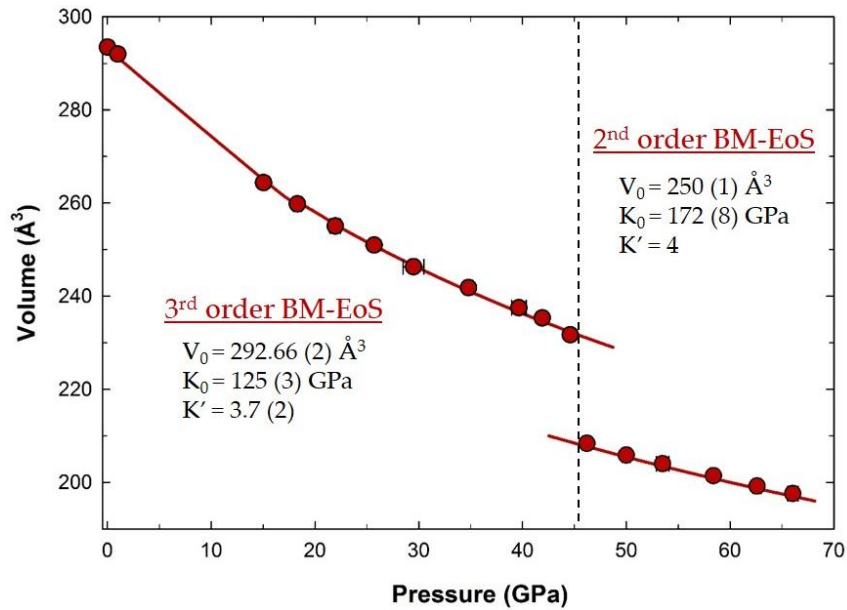

Figure 31. Example of EoS fitting for $FeCO_3$ upon cold compression. A 3rd order Birch-Murnaghan EoS is fitted to the data up to 44 GPa. At higher pressures, an abrupt volume collapse, due to the Fe^{2+} spin crossover, is changing the compressibility of the mineral.

2.5. Nuclear inelastic scattering

2.5.1. History and basic principles

Nuclear inelastic scattering (NIS), also known as Nuclear resonant inelastic X-ray scattering (NRIXS), is a technique based on synchrotron radiation [26, 27]. The method is performed on compounds that contain a nuclear resonant isotope (e.g. ^{57}Fe, ^{119}Sn, ^{61}Ni, ^{161}Dy, and others) and provides valuable information on the lattice dynamics, not available otherwise. Lattice dynamics is the study of the atoms vibrational motion in the crystal lattice. For a long time, this has been the research subject of neutron and X-ray inelastic scattering methods. Nuclear inelastic scattering can provide additional information, such as the direct measurement of the (partial) phonon density of states (DOS), along with thermodynamic properties, such as the vibrational internal heat capacity and entropy.

NIS has many similarities with Mössbauer spectroscopy: they share similar equipment and they are partially based on the same principles. However, Mössbauer spectroscopy focuses on the recoil-free events of the resonant nuclei after γ-ray absorption, whereas NIS focuses on the inelastically scattered phonons after a recoil event. Both methods are isotope-specific; the gamma rays emitted by one nucleus can be resonantly absorbed by a sample containing nuclei of the same isotope. The most popular isotope in nuclear resonance techniques is ^{57}Fe (Figure 32). Typically, the precursor of ^{57}Fe is ^{57}Co with a half-life of 271 days. A small percent of the ^{57}Fe* will decay directly to the ground level with release of γ-rays, while the majority will decay to another excited state with emission of 121.9 keV energy. The lower
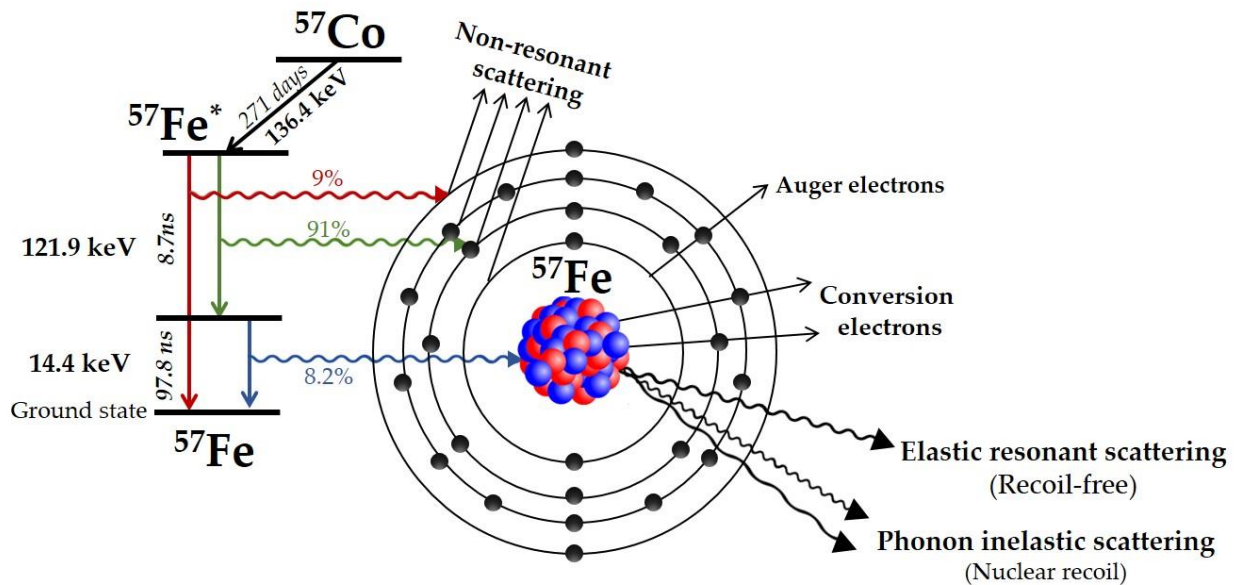
Figure 32. The nuclear decay scheme for ^{57}Co to ^{57}Fe and various backscattering processes for ^{57}Fe that can follow resonant absorption of an incident gamma photon. Modified after [28].

excited state finally decays to the ground state with emission of 14.4 keV and having as short life time as 97.8 ns. When each of the aforementioned emissions probe a sample that contains the ^{57}Fe isotope, several absorption and scattering processes take place, but not all are related to the nucleus (Figure 32). The most important quantum phenomenon in our case is the nuclear recoil. Atomic nuclei releasing or absorbing high-energy waves (e.g. γ-rays) recoil just like a gun kicks back when fired to conserve the momentum. If the transferred momentum of the nuclear recoil is high enough to force lattice vibrations, phonons are generated and are inelastically scattered (Figure 32). This process is where the nuclear inelastic scattering method derives from, as opposed to the Mössbauer effect, which is based on the absorption of high-energy waves without the participation of lattice vibrations (recoil-free) (Figure 30).

Soon after the discovery of the Mössbauer effect (in 1958) and the first applications of the Mössbauer spectroscopy, theoretical calculations predicted the opportunity to observe the phonon density of states (i.e. the number of states per an interval of energy available to be occupied by phonons) through nuclear resonant excitation (in 1960) [29, 30]. Experiments, however, were proven extremely difficult due to the small inelastic absorption cross and the high background of transmitted or electronically scattered radiation (in 1979-1981) [31, 32]. Given the many challenges, the method was soon forgotten, only to revive again nearly 15 years later. In the early 90s, the 3rd generation synchrotron light sources were introduced, offering, among others, an extremely high brilliance beam with pulsed structure [e.g. 33]. An instrumentation breakthrough followed, including the improvement of high-resolution monochromators [26, 34, 35] and the development of the avalanche photo diode detectors (APDs) [33]. All of these technological advances contributed to the reconsideration of the nuclear inelastic scattering method and thus, the first high-quality NIS spectra and DOS functions of α-^{57}Fe foil, Fe alloys and Fe oxides were derived in 1995 [36, 37]. A few years later, measuring a sample's sound velocity with NIS became possible [38]. Since then, NIS experiments have been performed on fluids [34], proteins [39], and nanoparticles [40]. Experiments on single crystals revealed the crystallographic-orientation dependence of the NIS signal [41]. The temperature dependence of NIS was reported [42], and it was only a matter of time, before the first high-pressure experiments in laser-heated diamond anvil cells were performed [e.g. 27, 43].

2.5.2. Instrumentation

Nuclear inelastic scattering can only be performed using synchrotron radiation and special instrumentation. First experimental efforts without the use of synchrotron radiation faced the following problems [26, 31, 32]:

1) In order to scan an energy range of ±100 meV with Doppler shift, one needed a velocity of about 2 km/s. This was not possible by the time of the first pilot experiments.

2) A very intense radiation was required since the energy range of the phonon spectrum is nearly 10^7 times broader than the nuclear line width and the spreading of the probability of inelastic interaction over the ±100 meV range makes the cross section of the inelastic scattering weak.

3) Background originating from the prompt electronic scattering was overpowering the inelastic scattering signal.

Today, all these problems are overcome in Nuclear Resonance beamlines, such as ID18 at ESRF (Grenoble, France), where we also carried out the NIS measurements of this thesis. Following electron acceleration, an initial beam of ~6.04 GeV is created in the storage ring. A series of undulators will tune the initial beam to the desired 14.4 keV energy for the ^{57}Fe applications (Figure 33). The essential part for the NIS experiments is the storage ring mode. Time-resolved experiments are performed when the storage ring
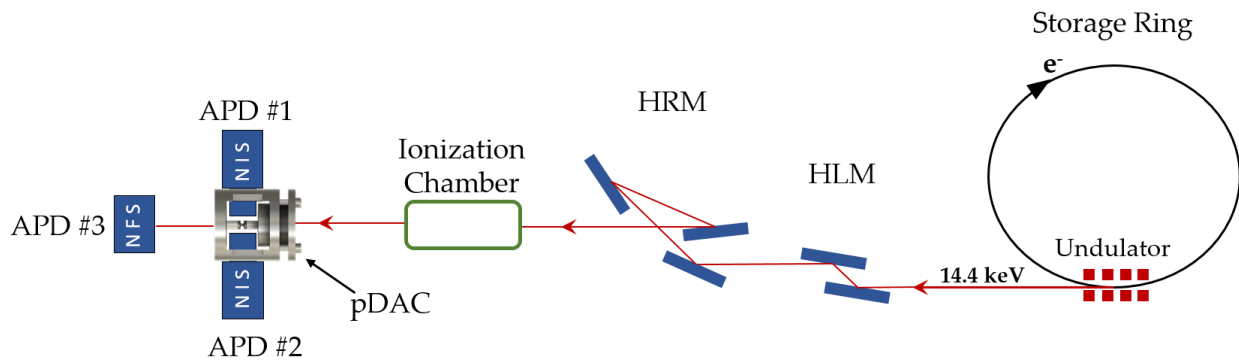
Figure 33. Schematic representation of the experimental set-up for nuclear inelastic scattering measurements. Modified after [26].
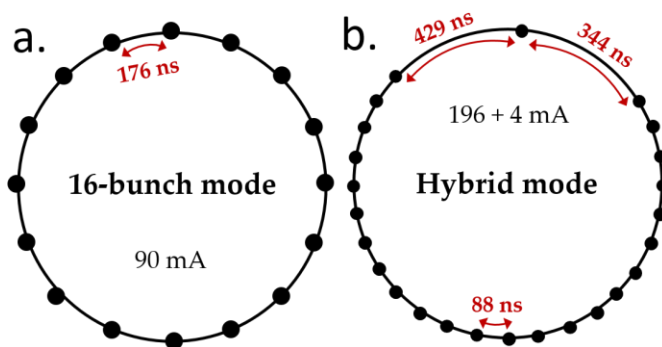
Figure 34. Storage-ring operation modes at ESRF for time-resolved studies, such as NIS. **a)** 16-bunch and **b)** hybrid modes were chosen. .
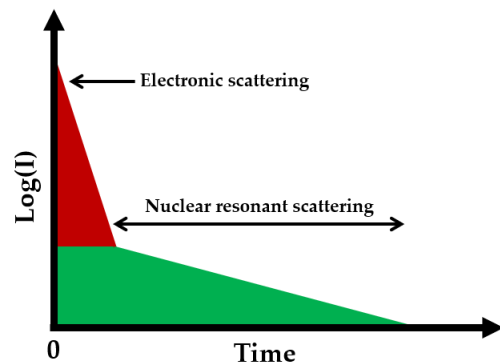
Figure 35. Scattering intensity versus time. Note the promt and short-lived electronic scattering compared to the delayed nuclear response.

operates in a pulsed mode, such as the 16-bunch or the hybrid mode (Figure 34). The 16-bunch mode provides a time window of 176 ns between the electron-bunches (Figure 34a). In the hybrid mode, the ring is divided in 32 buckets, where one clean 4mA single bunch is diametrically opposed to 24 bunches of 196 mA spread over 3/4 of the storage ring circumference (Figure 34b). Each pulse has typically a duration less than 100 ps. Fast electronics are synchronized with the pulsed structure of the beam allowing us to count only the events between the pulses. In this way, the prompt electronic scattering which otherwise would have dominated the spectra, is readily excluded, and thus the user can focus on the delayed nuclear resonant scattering (Figure 35).

Once the modulated beam goes through the undulators, the resulting 14.4 keV energy has a relative large bandwidth (~300 eV), which must be decreased before meeting the sample. Therefore, the beam is further monochromatized, first, by the high heat-load monochromator (HLM), and later, by the high-resolution monochromator (HRM) (Figure 33). The HLM consists of two silicon crystals that must be efficiently cooled down, while they reduce the bandwidth to a few eV. The HRM, which also consists of a series of silicon crystals, reduces the bandwidth to the final size of 0.5 to 2 meV. As a final step before meeting the sample, the beam passes through the ionization chamber (Figure 33) where the flux of the incident radiation is monitored.

When entering the experimental hutch (Figure 36a-1), the beam is directed immediately to the sample (Figure 36a-3) and excites the resonant nuclei. Three avalanche photo diode detectors (APDs) (Figure 33, Figure 36a-7, Figure 36b-3) measure the nuclear inelastic scattering. The two APDs located close (i.e. APD #1 and #2 in Figure 33) to the sample count the photons scattered in a large solid angle. The inelastically scattered quanta have gained a phase shift and, thus they are no longer coherent with the incident radiation. If the phase shift is random the scattering is spatially incoherent over the nuclear ensemble, and the scattered photons may be associated with a particular nucleus. The products of de-excitation are emitted as a spherical wave. Therefore, the two APD detectors close to the sample count the incoherent scattering (i.e. NIS) of radiation by localized resonant nuclei in large solid angle. The third APD detector is placed far away from the sample (i.e. APD #3 in Figure 33), in order to avoid a contribution from the incoherent scattering. In this case, the path of the waves scattered by various nuclei in the forward direction are indistinguishable and, thus they all have the same phase shift and the scattered photons cannot be associated with a particular nucleus. This is an elastic process and hence the third detector is counting the coherent nuclear forward scattering (i.e. NFS).
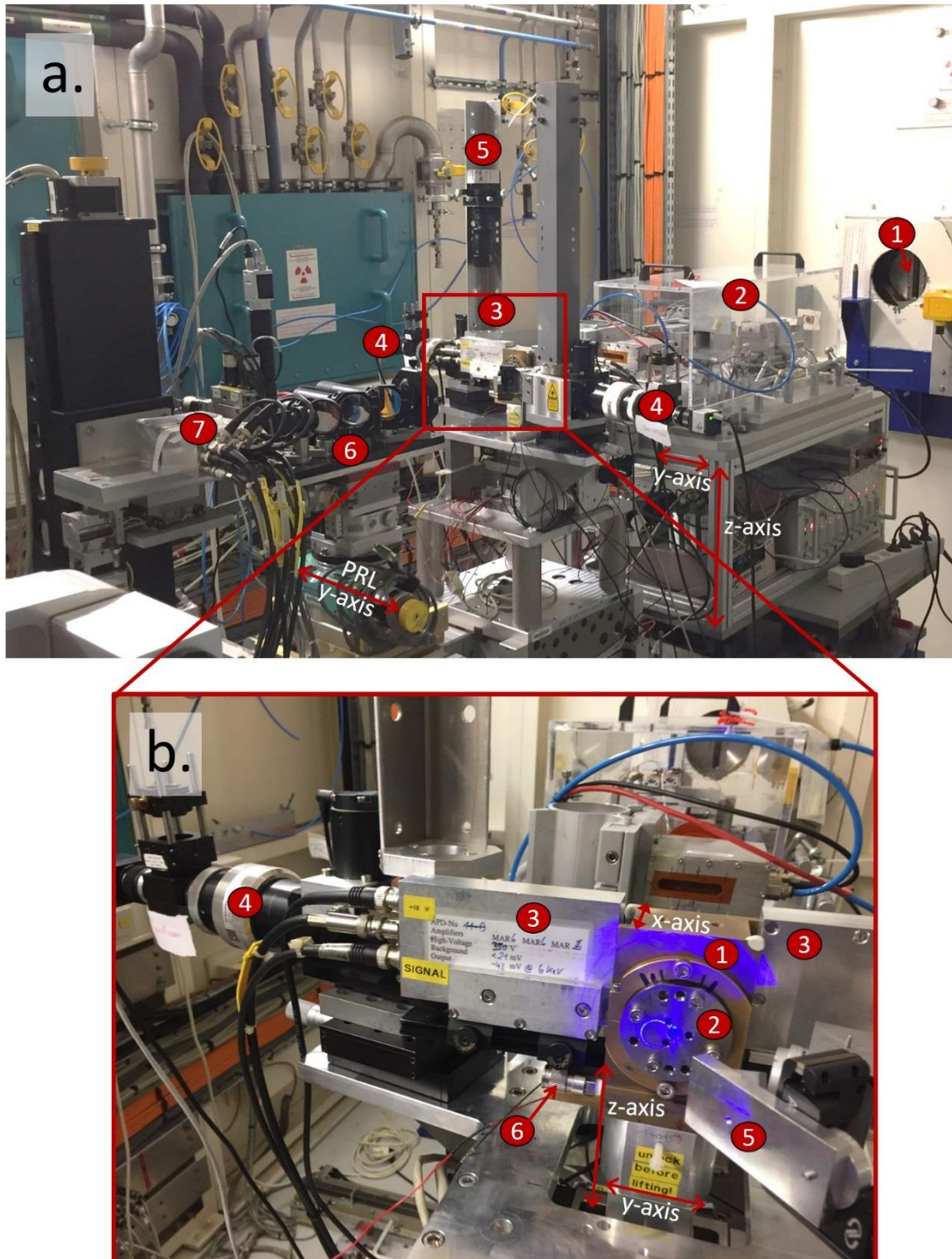
Figure 36. Nuclear inelastic and forward scattering at ID18 (ESRF). **a)** The experimental hutch where the variant components are numbered: 1 – beam entrance from optics hutch, 2 – KB mirror system out of use during NIS, 3 – sample position, 4 – Upstream and downstream laser heads for heating, 5 – high-resolution camera, 6 – PRL system, 7 – APD detector for NFS collection. The table where KB mirrors are placed can move along the y- and z-axis. **b)** Close-up photograph of area #3 in **a**: 1 – pDAC holder, 2 – pDAC placed, 3 – APD detectors for NIS collection, 4 – upstream laser head, 5 – carbon mirror of downstream laser head focusing on the sample, 6 – water connectors on pDAC holder for cooling during heating. The stage, where the pDAC is placed can move along the x-, y- and z-axis. The blue light in **b** comes from the PRL laser.

2.5.3. Data collection

Prior to any data collection, the size of the beam and the energy bandwidth of the beam are optimized by bending the silicon crystals of the high-resolution monochromator. In our experiments, we worked either with the 2 meV or the 0.5 meV energy bandwidth. Typically, the beam has an elliptical shape (horizontal direction being the longer axis) and its size is 13 x 5 μm^2. The next step is to find resonance to assure maximum flux. Normally, the resonance scan is performed on a 0.25 μm thick ^{57}Fe foil, placed in front of the APD#3 detector (Figure 36a-7), while the pDAC is removed. In more rare cases, and only if the ^{57}Fe-enriched is already aligned under the beam, resonance scan can be performed on the sample directly. As a final step, a calibration file pointing at the zero energy position of the elastic peak is created by collecting the NIS spectrum of a standard sample. The calibration sample in ID18 is usually an Fe-bearing cyanide compound, such as $(NH)_4Mg^{57}Fe(CN)_6$ or $K_2Mg^{57}Fe(CN)_6$. The calibration sample must be placed in the sample position (Figure 36a-3) and the APD#1 and #2 detectors must be placed close to it (~1 mm). Subsequently, the data collection in panoramic diamond anvil cells can start following the following protocol:

1) **pDAC preparation:** The sample must preferentially be enriched in ^{57}Fe to speed up the collection time (the natural abundance of ^{57}Fe is ~2%). The NIS method is isotope-specific and thus only the nuclei of the ^{57}Fe isotope will contribute to the signal. The content of Fe in the sample should be at least ~5% to assure a signal. The use of beryllium gaskets is mandatory. The sample placed in the sample chamber should be bigger than the size of the beam and as thick as possible to assure strong signal. If the sample is an oriented single-crystal(s), it should be as thick as possible, but the user must allow for the shrinking gasket hole to avoid sample bridging with the diamond anvils or sample contact with the gasket. Prior to the placement of the pDAC the outer surface of the diamond anvils in contact with the seats must be thoroughly cleaned. Due to the small aperture of the pDACs (Figure 6c) cleaning is a very difficult, but still very crucial procedure, thus the user must persist until the best result is obtained. Small dirt particles on the surface of the diamonds from a Fe-source can contribute to the signal and this must be avoided. The pDAC is placed horizontally inside the holder (Figure 5, 37) in such a way to allow the two APD detectors to slide as close to the gasket as possible (Figure 37b). The cell is secured firmly in position by two metallic rings (Figure 37-3) and if a heating session is planned, then the cooling running-water pipes are connected on the holder (Figure 37-4).

2) **pDAC and sample alignment:** The center of the holes on the seats (~1mm in diameter) is found through X-ray absorption. Then, small scans are performed along the y and the z-axis, while the
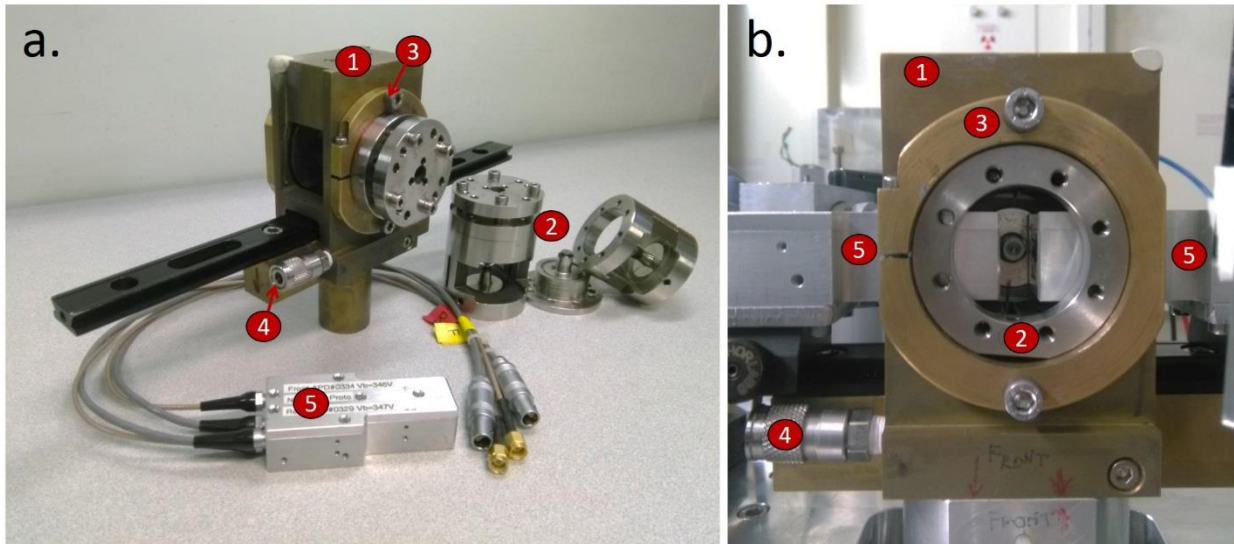
Figure 37. Equipment in the close vicinity of the pDAC. The individual components are depicted numbered as follows: 1 – pDAC holder made of Cu, 2 – pDAC, 3 – Cu rings to secure the pDAC in position, 4 – water connector and 5 – APDs collecting incoherent scattering placed close to the sample.
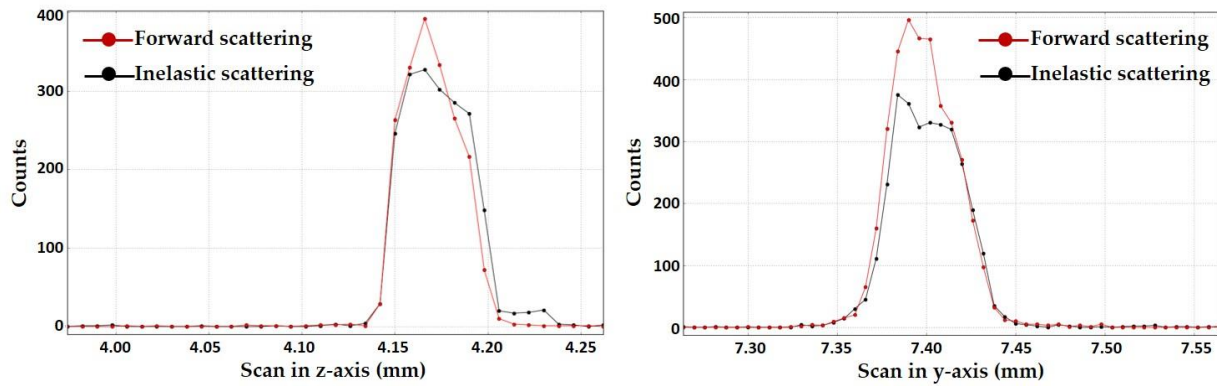
Figure 38. Scanning procedures for locating a ~50 μm $(Mg_{0.74}{}^{57}Fe_{0.26})CO_3$ crystal.

user is looking for increased counts by the APD detectors that will reveal the sample's position (Figure 38). The user can obtain an optical image of the sample by adjusting one or both carbon mirrors (in either side of the pDAC) of the laser heads (Figure 36b-5) that are connected to a camera (Figure 36a-5). The mirrors must not touch the cell or block the beam/signal path.

3) **Data collection:** Once on the sample, a background is collected, typically for 500 sec and at an energy regime far away from resonance (e.g. -200 meV). Then, the NIS scans can start, while on resonance. Depending to the available beamtime and the majority of samples or pressure points that the user wants to measure, the energy range and collection time are adjusted. For room temperatures the scans are usually asymmetric (e.g. -20 to 100 meV), while at high (or low) temperatures the scans must be symmetric (e.g. -100 to 100 meV). Normally, no NIS signal

appears above ± 100 meV. Collection time can vary from 2 up to several seconds. For example, the collection of the calibration sample over the energy range -90 to 90 meV, divided in 360 points and 4 sec exposure in each energy point will last ~1 hr (Figure 39). It is not recommended to increase the statistics of a measurement by increasing the collection time (e.g. > 10 sec). Normally, many scans are collected with small collection time per energy interval (e.g. 2-8 sec) and then are all merged together to increase statistics (Figure 40). In this way the user will not lose valuable beamtime over a long-lasting scan that was eventually disrupted by appearances of spikes, discontinuities, sample misalignment or other misfortunes (e.g. beam loss). At low pressures, usually 5 to 6 NIS scans are adequate for accurate data processing. As we move to higher pressures, the background is increasing and, thus typically the collection of 10 to 12 scans is necessary (Figure 40). The user can set scripts that will collect a NIS scan, stop, optimize the signal and adjust the sample's position due to possible shift of the beam over time, start a new NIS scan, stop all movements in case of beam loss and repeat until terminated by the user himself/herself. In the meantime, the preliminary processing of the data is strongly advised, before deciding to increase pressure or move to another sample. When the user decides to stop the collection, a background must be collected once again. After the collection of a pressure point, the pressure in the cell is increased in position (i.e. the pDAC is not removed from the holder or the stage). The PRL system is moved in front of the cell (Figure 36a-6) and monitors the pressure increase. Once
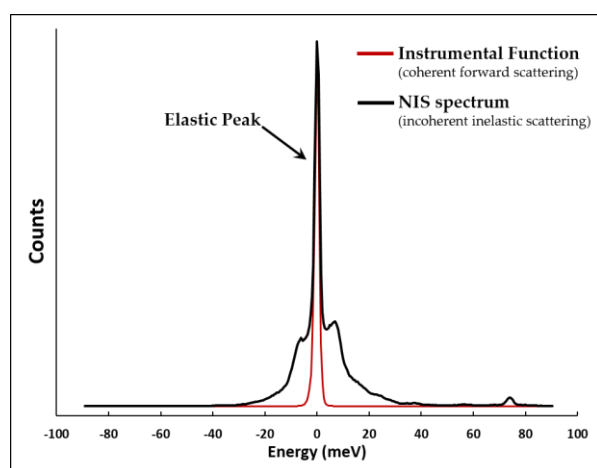
Figure 39. Example of an instrumental function (red) collected by the APD#3 detector and the inelastic scattering collected by the APD#1 and #2 detectors located close to the sample. Note the intense elastic peak at zero energy. The data shown are from the calibration sample that we used at ID18.
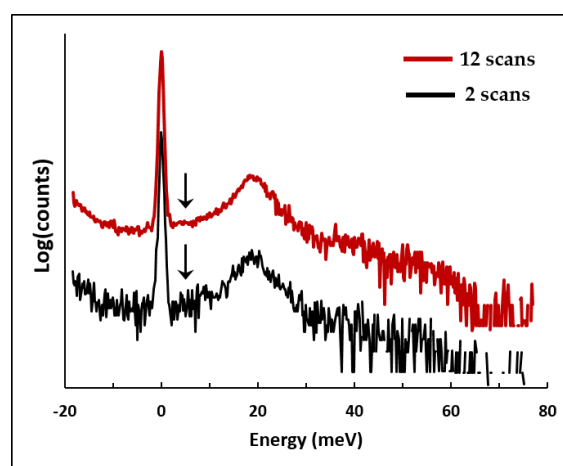
Figure 40. Example of $FeCO_3$ NIS spectra at ~35 GPa after merging only 2 scans (total collection time = 50 min) and after merging 12 scans (total collection time = 5 hr). The use of more scans provides better statistics at the low energy regime (arrows), which is used for the Debye velocity determination.

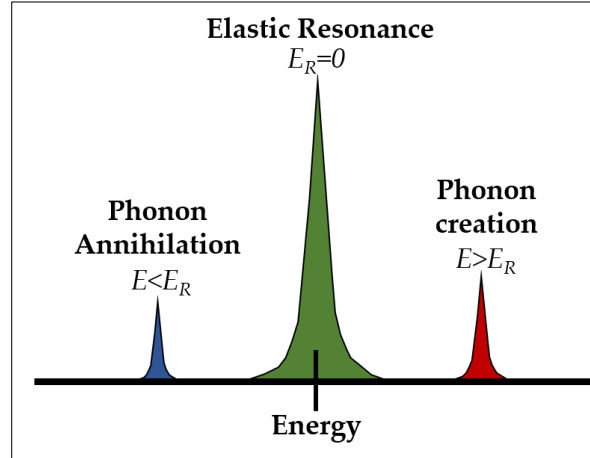the new target pressure is reached, the sample is aligned again (see step 2) and the procedure is repeated.

4) **During heating:** One of the great advantages of the NIS method is that the user can perform in-situ high-pressure and high-temperature NIS collections. The double-sided laser heating system can provide stable heating over long-time periods [17, 18]. During heating the user must be always present in the control room and check regularly the NIS signal. The sample or the cell can move during a heating session and, thus their position under the beam should be constantly corrected. As mentioned above, the energy range of the NIS scan during heating should be symmetric (or at least counts should approach zero from both sides of the elastic line). This is because the ratio of intensities of the inelastic peaks in either side of the elastic peak can be used for temperature determination. In this manner, the NIS spectrum (Figure 39, 41) has many similarities to a Raman spectrum (Figure 9). They both consists of an elastic (Rayeligh) peak, and vibrational modes on lower (Anti-stokes) and higher (Stokes) energies. Similar to Raman, the modes on the left side of the elastic peak (i.e. $E<E_R$) have always lower intensity that the modes located on the right side (i.e. $E>E_R$) at room temperatures. However, during heating (or cooling) the user should expect an increase (or decrease) in the intensity of the modes representing phonon annihilation. The ratio between phonon creation energies (S(E)) and phonon annihilation energies (S(-E)) is given by the Boltzmann factor as follows:

Figure 41. The NIS spectrum consists of the intense elastic resonant peak at zero energy. On the left and right side of the elastic peak vibrational modes appear symmetrically, but with different intensities. Peaks at higher energies represent phonon creation and peaks of lower energies represent phonon annihilation. At high temperatures the intensity ratio of the two peaks approaches the unity.

$$S(E) = e^{\beta E} S(-E) \qquad\qquad (Eq.\ 8)$$

where $\beta = 1/(k_\beta T)$ is the inverse temperature, and k_β the Boltzmann constant. With this equation, we can estimate the sample's temperature using the NIS signal.
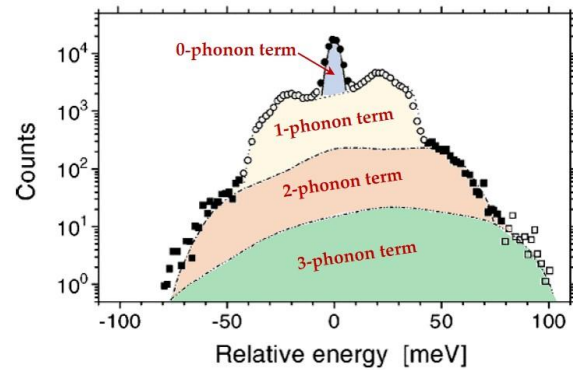
2.5.4. Data processing

The procedure of data analysis has been described in detail by several studies before [26, 37, 44]. Data obtained in this thesis until the year 2016 were processed using a series of FORTRAN scripts which were created and described by [44]. Later, the scripts were implemented in the Python programming language and today a graphical user interface operatable under Windows systems is available [credit to ID18 staff, R. Schadow and 44]. Using NISGUI the user has a good control over the data through constant interaction. By analyzing a NIS spectrum, the user is trying to obtain the (partial) density of phonon states (DOS), but also the values to many other thermodynamic properties. Using the low energy regime of a DOS function, the Debye sound velocities of the sample can be derived, as well (see 2.5.5. and Chapter 7).

A NIS spectrum can break down into a single-phonon and multi-phonon contributions (Figure 42). Normally, for crystals indexed in the cubic system, and polycrystalline samples, which are composed only of resonant atoms, the DOS describes the single-phonon contribution. In the case of more complicated crystal systems and compounds (i.e. the case of carbonates in this thesis), the single-phonon contribution depends on the orientation of the incident beam relative to the crystal lattice [41]. Therefore, the inelastic absorption is not defined by the DOS, but a function that additionally contains a term dependent on the square modulus of the projection of the phonon polarization vector for resonant atoms on the direction

Figure 42. Expansion of the α-^{57}Fe NIS spectrum in multi-phonon terms. Modified after [26].

of the incident beam, otherwise known as projected or partial DOS (i.e. PDOS). To obtain the PDOS the single-phonon contribution must be separated from the multi-phonon contributions (i.e. data deconvolution) by a double Fourier transformation, which is implemented in the NISGUI software.

In practice, the following procedure is followed (Figure 43, 44):

1) **Data summation:** The user sums the data from different scans in order to get a distinctive curve (Figure 43a, 44a). Incomplete scans that do not contain the elastic line, or scan with spikes or other artifacts must be excluded from the summation.

2) **Subtraction of the elastic peak:** First, the user must subtract the background from the NIS spectrum and the instrumental function (Figure 43b). Then, the software offers choices for corrections concerning shifting or broadening of the instrumental function (Figure 44b), and removal of points with negative counts (Figure 44c). The next choice offered is the central peak
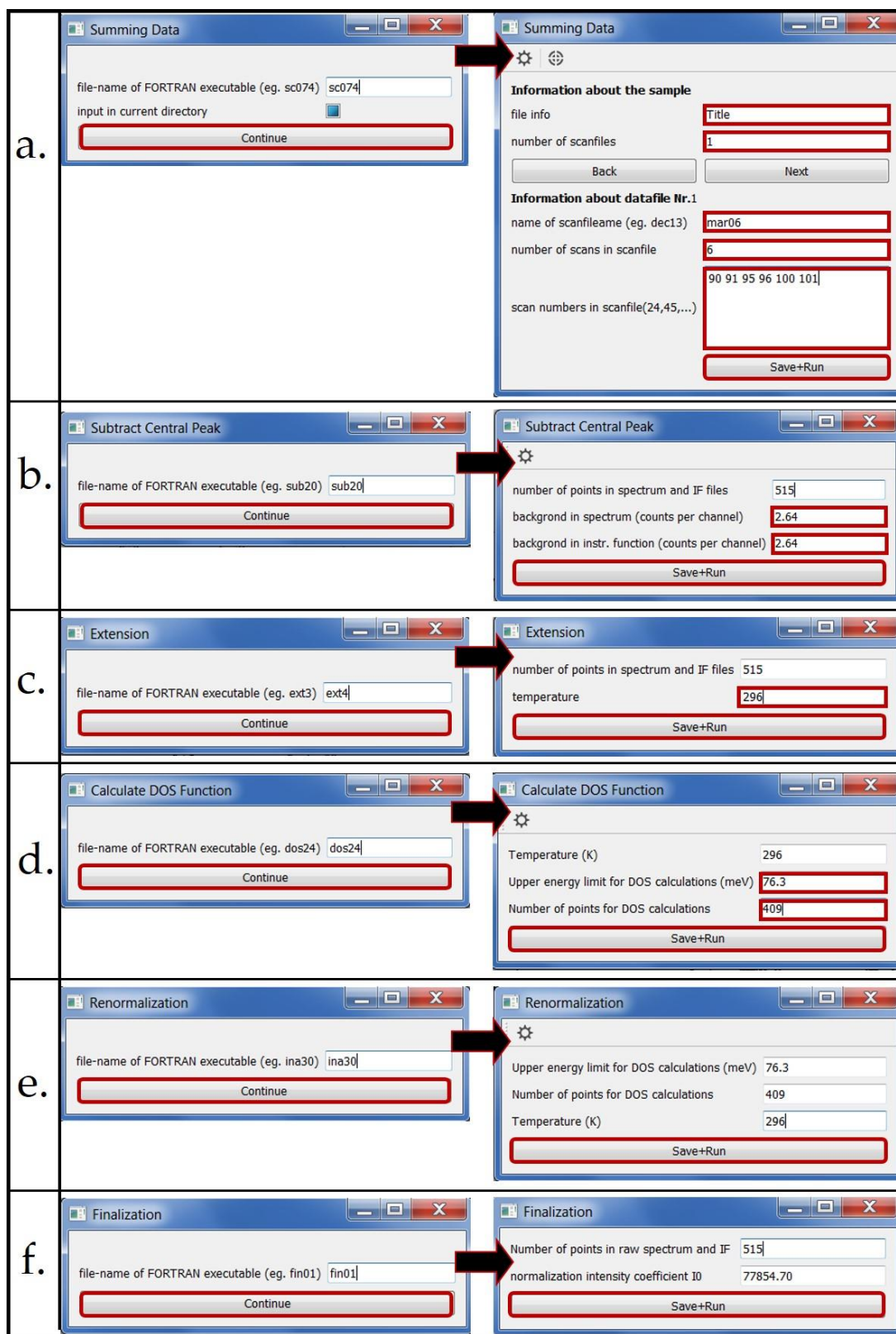
Figure 43. Dialogs appearing during the data analysis with NISGUI. a) Scan summation, b) Subtraction of elastic peak, c) spectrum extension (in case of asymmetric scans), d) DOS calculation, e) data renormalization, and f) data finalization. The red boxes indicate parts of the program that require the user's feedback.
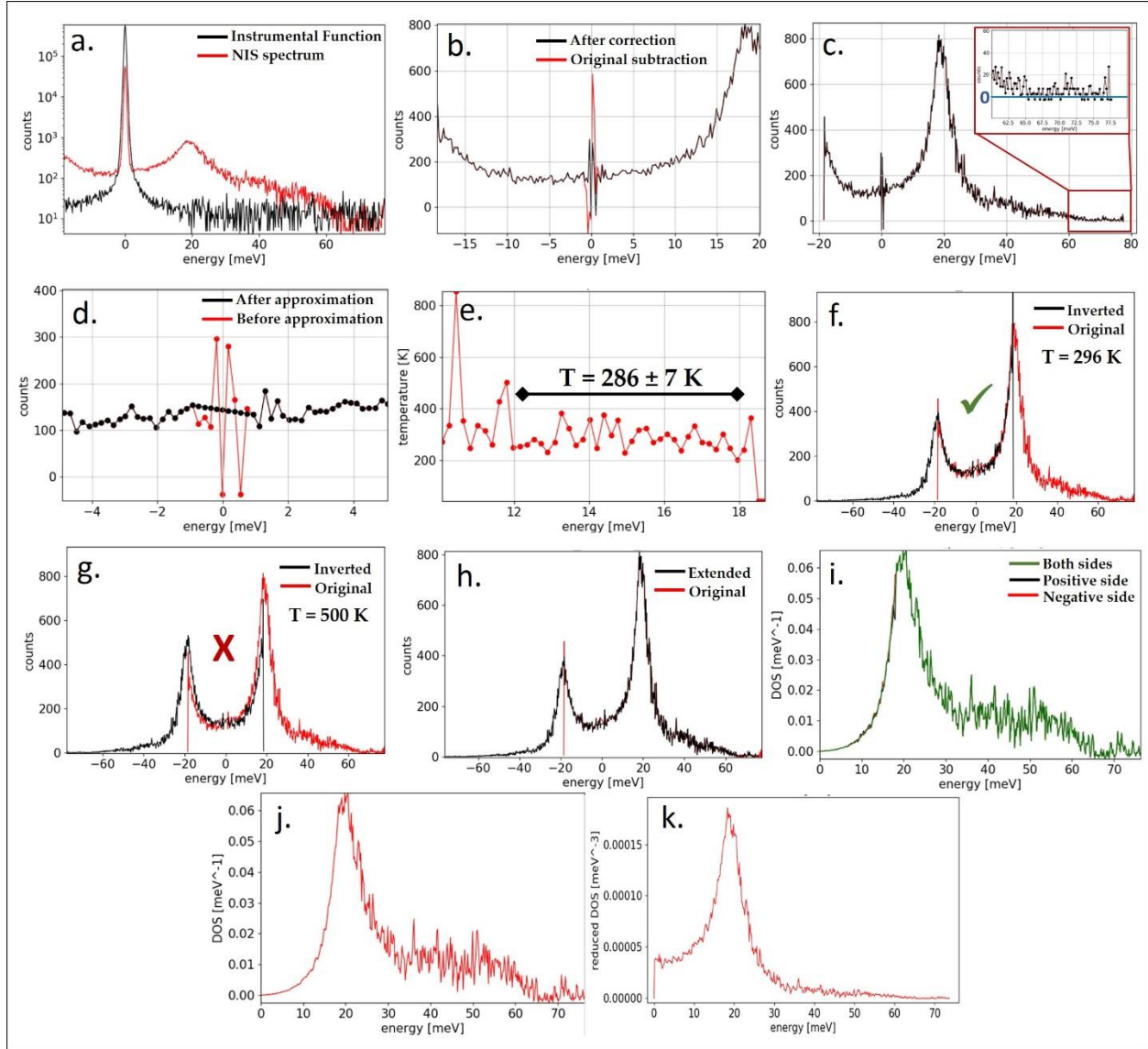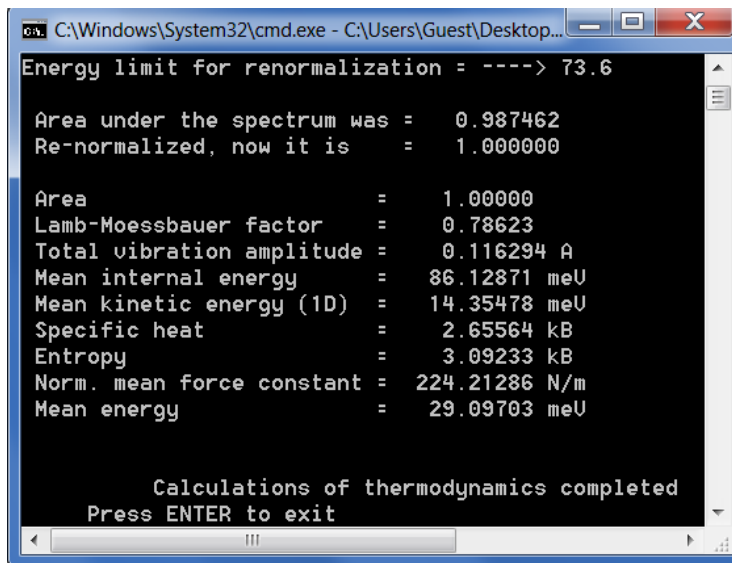
Figure 44. Example of processing steps. This is a $(Fe_{0.26}Mg_{0.74})CO_3$ dataset at 21 GPa and 296 K. The energy bandwidth used is 0.5 meV. **a)** Eight scans are summed together. **b)** Corrections are applied by shifting the instrumental function. **c)** Negative data points can be nullified, but it is not recommended, because this procedure will affected the area calculation under the spectrum. **d)** The central peak is carefully approximated (here the energy regime -1 to 1 meV is subtracted). **e)** The correct energy range is selected for the temperature estimation (here, the energy range from 12 to 18 meV is suggesting T=286 (7) K, which is not far from the real value, i.e. 296 K). **f,g)** The "balance" plot is an indication of how valid the temperature estimation is. **h)** The data are extended to the full range of phonon energies (here, from -76.3 to 76.3 meV). **i)** The DOS function is usually calculated by using data from both sides of the subtracted elastic line. **j)** The normalized DOS, **k)** the reduced DOS (rDOS) and **l)** the finalized NIS spectrum and instrumental function are obtained.

approximation (Figure 44d). The approximation must be done wisely by taking into consideration the energy bandwidth used and the statistics of the dataset. Finally, the user can estimate the sample's temperature (Figure 44 e, Equation 8) or edit a fixed temperature (e.g. room temperature = 296 K) (Figure 44f). The user knows that he/she has choose the correct

temperature by consulting the "balance" plot. Wrong temperature estimation leads to imbalance between the original and inverted scans (Figure 44g). After successful removal of the central peak the Lamb-Mössbauer factor (f_{LM}) can be calculated [37].

3) **Graph extension:** In the case of asymmetric scans, the software proposes extension of the NIS graph to the full range of phonon energies (Figure 43c, 44h). In this step the user can choose to cut few energy points from the edges of the initial spectrum (e.g. red spike and points above 76.3 meV in Figure 44h are removed).

4) **Calculation of DOS:** In this step the user must edit the upper energy limit (in this example it is 76.3 meV) and the number of DOS points (Figure 43d). The latter is easily calculated by opening the "spc_se.dat" file, counting the number of lines (always an odd number), dividing by two and rounding up to the next integer number. Subsequently the software suggest calculation of the DOS function from the positive energy part, the negative energy part only, or both sides (Figure 44i). The difference between the three options is usually small, and in most cases the user selects the DOS calculation from both sides.

5) **Normalization and data finalization:** The data are finally normalized and the final DOS (Figure 44j) and rDOS (i.e. DOS/E^2) (Figure 44k) are obtained along with the corrected NIS spectrum and instrumental function (Figure 44l). In the end of the data analysis, NISGUI can create a logbook with all the crucial parameters of the process and the results (Figure 43f, 45).

Figure 45. Final dialog of NISGUI summarizing the results of the data processing.

2.5.5. Capabilities of the NIS method

In the present thesis, we employed the NIS method for the determination of sound velocities of Fe-bearing carbonate samples and discussed the geophysical implications of the results in the Earth's mantle. Chapter 7 provides a detailed description of the velocity-extraction procedure from a NIS spectrum. In short, it is known that the low-energy part of the (p)DOS function contains information about the dispersion if the acoustic phonons that can be used for the determination of the sample's Debye velocity [27, 39, 45]. The Debye sound velocities (V_D) are derived through the following equation:

$$D(E) = \frac{\widetilde{m}}{m} \cdot \frac{E^2}{2\pi^2 \hbar^3 n V_D} \qquad (Eq.\ 9)$$

where $\widetilde{m}$ is the mass of the nuclear resonant isotope (i.e. ^{57}Fe), m is the average atomic mass, $\hbar$ is Planck's constant and n is the density of atoms. Subsequently, we can calculate the velocities of the primary (V_P) and the secondary (V_S) waves by solving the following three equations:

$$\frac{3}{V_D^3} = \frac{1}{V_P^3} + \frac{2}{V_S^3} \qquad (Eq.\ 10)$$

$$V_P = \sqrt{\frac{K + \frac{4}{3}G}{\rho}} \qquad (Eq.\ 11)$$

$$V_S = \sqrt{\frac{G}{\rho}} \qquad (Eq.\ 12)$$

where K is the adiabatic bulk modulus, G is the shear modulus and ρ is the density. The bulk modulus and density values are obtained by the samples equations of state using the SCXRD method (see section 2.4.7) The shear modulus is derived indirectly, by finding the solution to the following equation:

$$\frac{3}{V_D^3} - \left(\frac{K}{\rho} + \frac{4G}{3\rho}\right)^{-\frac{3}{2}} - 2\left(\frac{G}{\rho}\right)^{-\frac{3}{2}} = 0 \qquad (Eq.\ 13)$$
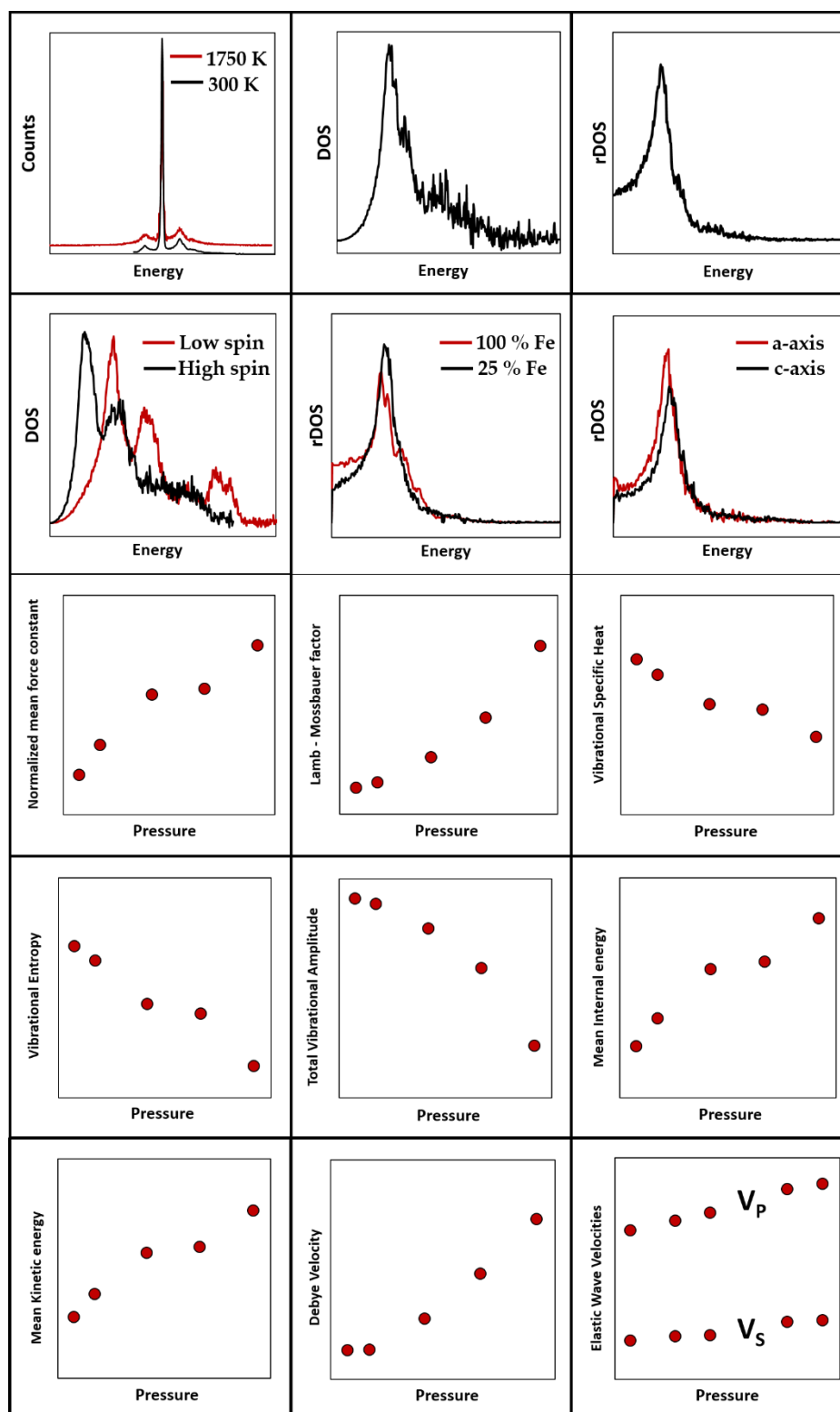
Figure 45. Summary of the type of information that the NIS method can provide.

Compared to other techniques that are capable of sound velocities determination at high pressures and temperatures, the NIS method is competitive. For example, ultrasonic measurements are a reliable method, but are restricted to upper mantle conditions (< 25 GPa). Brillouin spectroscopy has traditionally been used for obtaining accurate velocities at a much wider pressure range (< 100 GPa), but in situ high pressure and temperature experiments are challenging, and the method is restricted by the sample quality (opaque sample cannot be measured). Inelastic X-ray scattering allows the measurement of opaque samples, but the determination of the sample's bulk velocity is more time consuming. Computational methods, such as density functional theory (DFT) calculations, are an interesting alternative, but have their own challenges.

On the positive side, NIS is capable of *in situ* measurements at extreme conditions; measurements in air, at high pressures, at very high temperatures or close to freezing point are all possible. NIS is not restricted by the sample's quality; independent of color, single-crystals, polycrystalline/powders, nanoparticles, thin films, proteins, fluids, and others, are all accepted. Furthermore, NIS can provide very rich information about the lattice dynamics, and the elastic and the thermodynamic properties of materials (Figure 45). In addition, NIS is sensitive to changes in the electronic spin-states, composition and crystal orientation (Figure 45).

On the negative side, NIS is an isotope, and therefore, element specific method; only samples containing a Mössbauer-active element can be probed. NIS is a synchrotron-based method; experiments must be performed within the limited beamtime that was allocated. In the particular case of sound velocity determination, NIS cannot retrieve the full elastic tensor for the accurate determination of V_P and V_S velocities. However, further investigations on complicated materials (complicated by means of lower than cubic symmetry and presenting strong anisotropy, such as carbonates) might reveal new capabilities of the method in the velocity-determination domain.

Besides the disadvantages of the method, Nuclear Inelastic Scattering is expected to rise anew in the upcoming years. Currently (2019), ESRF is undergoing an immense upgrade to the much-promising Extremely Brilliant Source (EBS). The project is expected to be delivered in the year 2020, making ESRF the world's first high-energy, fourth-generation synchrotron light source. Upon completion, many beamlines will be greatly benefited. Among those planned is the nuclear resonance beamline, ID18 (i.e. where the NIS experiments of this thesis were performed), which promises to users an order of magnitude improved energy resolution (50 µeV) (note that the best resolution we have achieved so far is 0.5 meV).

2.6. References

[1] Y.A. Kozlovsky, **(1987)**. *The superdeep well of the Kola Peninsula.* Springer-Verlag Berlin Heidelberg, doi: 10.1007/978-3-642-71137-4.

[2] K. Hagiya, M. Matsui, Y. Kimura, Y. Akahama **(2005)** *The crystal data and stability of calcite III at high pressures based on single-crystal X-ray experiments.* Journal of Mineralogical and Petrological Sciences, 100, 31－36.

[3] W.G. Minarik, **(1998)** *Complications to carbonate melt mobility due to the presence of an immiscible silicate melt.* Journal of Petrology, 39, 1965-1973.

[4] R.C. Newton, C.E. Manning, **(2002)** *Experimental determination of calcite solubility in H2O-NaCl solutions at deep crust/ upper mantle pressures and temperatures: Implications for metasomatic processes in shear zones*. American Mineralogist, 87, 1401-1409.

[6] N. Dubrovinskaia, L. Dubrovinsky, N.A. Solopova, A. Abakumov, S. Turner, M. Hanfland, E. Bykova, M. Bykov, C. Prescher, V.B. Prakapenka, S. Petitgirard, I. Chuvashova, B. Gasharova, Y-M. Mathis, P. Ershov, I. Snigireva, A. Snigirev, **(2016)** *Terapascal static pressure generation with ultrahigh yield strength nanodiamond.* Science Advances, 2, e1600341.

[7] L. Merrill, W.A. Bassett, **(1974)** *Miniature diamond anvil pressure cell for single crystal x-ray diffraction studies.* Review of Scientific Instruments, 45, 290.

[8] H.K. Mao, P.M. Bell, **(1978)** *Design and varieties of the megabar cell.* Carnegie Institution, Washington Yearbook, 77, 904-908.

[10] R. Letoullec, J.P. Pinceaux, P. Loubeyre, **(1988)** *The membrane diamond anvil cell: A new device for generating continuous pressure and temperature variations.* High Pressure Research, 1, 77-90.

[11] I. Kantor, V. Prakapenka, A. Kantor, P. Dera, A. Kurnosov, S. Sinogeikin, N. Dubrovinskaia, L. Dubrovinsky, **(2012)** *BX90: a new diamond anvil cell design for X-ray diffraction and optical measurements.* Review of Scientific Instruments, 83, 125102.

[12] A. Kurnosov, I. Kantor, T. Boffa-Ballaran, S. Lindhardt, L. Dubrovinsky, A. Kuznetsov, B.H. Zehhnder, **(2008)** *A novel gas-loading system for mechanically closing of various types of diamond anvil cells.* Review of Scientific Instruments, 79, 045110.

[13] M. Sekar, N.R. Kumar, P.C. Sahu, N.V. Chandra Sekar, N. Subramanian, **(2008)** *Cryogenic gas loading in a Mao-Bell-type diamond anvil cell for high pressure-high temperature investigations.* Review of Scientific Instruments, 79, 076103.

[14] Y. Fei, A. Ricolleau, M. Frank, K. Mibe, G. Shen, V. Prakapenka, **(2007)** *Toward an internally consistent pressure scale.* Proceedings of the National Academy of Science, 104, 9182-9186.

[15] A. Dewaele, M. Torrent, P. Loubeyre, M. Mezouar, **(2008)** *Title.* Physical Reviews B, 78, 104102

[16] H.K. Mao, J. Xu, P.M. Bell, **(1986)** *Title.* Journal of Geophysical Reasearch, 91, 4673.

[17] I. Kupenko, C. Strohm, C. McCammon, V. Cerantola, K. Glazyrin, S. Petitgirard, D.M. Vasiukov, G. Aprilis, A.I. Chumakov, R. Rüffer, L. Dubrovinsky **(2015)** *Differentiated nuclear resonance spectroscopy coupled with pulsed laser heating in diamond anvil cells.* Review of Scientific Instruments, 86, 114501.

[18] G. Aprilis, C. Strohm, I. Kupenko, S. Linhardt, A. Laskin, D.M. Vasiukov, V. Cerantola, E.G. Koemets, C. McCammon, A. Kurnosov, A.I. Chumakov, R. Rüffer, N. Dubrovinskaia, L. Dubrovinsky, **(2017)** *Portable double-sided pulsed laser heating system for time-resolved geoscience and materials science applications.* Review of Scientific Instruments, 88, 084501.

[19] H.N. Rutt, J.H. Nicola, **(1974)** *Raman spectra of carbonates of calcite type.* Journal of Physics C: Solid State Physics, 7, 4522-4528.

[20] E. Bykova, **(2015)** *Single-crystal X-ray diffraction at extreme conditions in mineral physics and material science.* Doctoral Thesis, EPub – University of Bayreuth, 282.

[21] A.C. Lason, R.B. von Dreele, **(1985)**. *General Structure Analysis System (GSAS).* Los Alamos National Laboratory Report, LAUR B6-748.

[22] V. Petricek, M. Dusek, L. Palatinus, **(2014)** *Crystallographic computing system JANA2006: General features.* Zeitschrift für Kristallographie, 229, 345–352.

[23] Agilent, **(2014)** *CrysAlis PRO.* Agilent Technologies Ltd, Yarnton.

[24] G.M. Sheldrick, **(2008)** *A short history of SHELX.* Acta Crystallographica A, 64, 112–122.

[25] G. Taylor, **(2003)** *The phase problem.* Acta Crystallographica D, 59, 1881-1890.

[26] A. Chumakov, R. Rüffer, **(1998)** *Nuclear inelastic scattering.* Hyperfine Interactions, 113, 59-79.

[27] W. Sturhahn, J.M. Jackson, **(2007)** *Geophysical applications of nuclear resonant spectroscopy.* Advances in High-pressure mineralogy (ed. E. Ohtani), *Geological Society of America,* Special paper 421.

[28] M.D. Dyar, D.G. Agresti, M. Schaefer, C.A. Grant, E.C. Sklute, **(2006)** *Mössbauer spectroscopy of earth and planetary materials.* Annual Reviews of Earth and Planetary Science, 34, 83-125.

[29] W.M. Visscher, **(1960)** *Study of lattice vibrations by resonance absorption of nuclear gamma rays.* Annals of Physics, 9, 194-210.

[30] K.S. Singwi, A. Sjölander, **(1960)** *Resonance absorption of nuclear gamma rays and the dynamics of atomic motions.* Physical Review, 120, 1093.

[31] H. Weiss, H. Langhoff, **(1979)** *Observation of localized models in TbO_x using the Mössbauer effect.* Zeitschrift für Physik B, 33, 365.

[32] G. Endres, F. Strokendl, H. Langhoff, F. Gmelin **(1981)** *Observation of localized modes in TbO_x and $TbAl_2$ by resonance absorption of γ-quanta.* Zeitschrift für Physik B, 44, 253.

[33] R. Rüffer, A.I. Chumakov, **(1996)** *Nuclear resonance beamline at ESRF.* Hyperfine Interactions, 97/98, 589-604.

[34] G. Faigel, D.P. Siddons, J.B. Hastings, P.E. Haustein, J.R. Grover, L.E. Berman, **(1988)** *Observation of the full time evolution of the nuclear collective-decay mode in crystalline Fe_2O_3 excited by synchrotron radiation.* Physical Review Letters, 61, 2794-2796.

[35] T. Ishikawa, Y. Yoda, K. Izumi, C.K. Suzuki, X.W. Zhang, M. Ando, S. Kikuta, **(1992)** *Construction of a precision diffractometer for nuclear Bragg scattering at the Photon Factory.* Review of Scientific Instruments, 63, 1015-1018.

[36] M. Seto, Y. Yoda, S. Kikuta, X.W. Zhang, M. Ando, **(1995)** *Observation of Nuclear Resonant Scattering Accompanied by Phonon Excitation Using Synchrotron Radiation.* Physical Review Letters, 74, 3828-3831.

[37] W. Sturhahn, T.S. Toellner, E.E. Alp. X.W. Zhang, M. Ando, Y. Yoda, S. Kikuta, M. Seto, C.W. Kimball, B. Dabrowski, **(1995)** *Phonon Density of States Measured by Inelastic Nuclear Resonant Scattering.* Physical Review Letters, 74, 3832-3835.

[38] M.Y. Hu, w. Sturhahn, T.S. Toellner, P.D. Mannheim, D.E. Brown, J. Zhao, E.E. Alp, **(2003)** *Measuring velocity of sound with nuclear resonant inelastic X-ray scattering.* Physical Review B, 67, 094304.

[39] K. Achterhold, C. Keppler, A. Ostermann, U. van Bürck, W. Sturhahn, E.E. Alp, F.G. Parak **(2002)** *Vibrational dynamics of myoglobin determined by the phonon-assisted Mössbauer effect.* Physical Review E, 65, 051916.

[40] B. F.ultz, C.C. Ahn, E.E. Alp, W. Sturhahn, T.S. Toellner, **(1997)** *Phonons in Nanocrystalline [57]Fe.* Physical Review Letters, 79, 937-940.

[41] A.I. Chumakov, R. Rüffer, A.Q.R. Baron, H. Grünsteudel, H.F. Grünsteudel, V.G. Kohn, **(1997)** *Anisotropic inelastic nuclear scattering.* Physical Review B, 56, 10758.

[42] A.I. Chumakov, R. Rüffer, A.Q.R. Baron, H. Grünsteudel, H.F. Grünsteudel, **(1996)** *Temperature dependence of nuclear inelastic absorption of synchrotron radiation in α-[57]Fe.* Physical Review B, 54, R9596.

[43] G. Shen, W. Sturhahn, E.E. Alp, J. Zhao, T.S. Toellner, V.B. Prakapenka, Y. Meng, H-R. Mao, **(2004)** *Phonon density of states in iron at high pressures and high temperatures.* Physics and Chemistry of Minerals, 31, 353-359.

[44] V.G. Kohn, A.I. Chumakov, **(2000)** *DOS: Evaluation of phonon density of states from nuclear resonant inelastic absorption.* Hyperfine Interactions, 125, 205-221.

[45] M.Y. Hu, W. Sturhahn, T.S. Toellner, P.D. Mannheim, D.E. Brown, J. Zhao, E.E. Alp, **(2003)** *Measuring velocity of sound with nuclear resonant inelastic x-ray scattering.* Physical Review B, 67, 094304.

Chapter 3

Synopsis

3.1. Summary and linkage of research studies

With the present thesis we aimed to investigate the fate of the calcite-type carbonates following their subduction in to the deep Earth. The determination of the physical and elastic properties of rhombohedral carbonates at extreme conditions has important implications for the deep carbon cycle and the dynamical processes that operate Earth. In addition, such results are important from crystal chemistry point of view, since novel structures and compounds are discovered with unique characteristics that among else highlight the polymerization of carbon.

This part shortly overviews the results presented in Chapters 5 to 8. Each of these chapters is a research article that was either published (Chapter 5), in press (Chapter 7) or prepared for submission to peer-reviewed journals (Chapter 6 and 8). More concretely, Chapter 5 is dedicated to the high-pressure behavior of spherocobaltite ($CoCO_3$) using the Raman spectroscopy and the single-crystal X-ray diffraction (SCXRD) techniques. Using the same methods, in Chapter 6, we investigate the crystal chemistry of other 3d transition-metal carbonates ($MnCO_3$, $NiCO_3$, $ZnCO_3$ and the revisited $CoCO_3$) at extreme conditions and discuss the crystallochemical regularities found in the family of rhombohedral carbonates, but also the deviations from empirical relations. In Chapter 7 we determined the sound velocities of carbonates in the $FeCO_3$-$MgCO_3$ system using the Nuclear Inelastic Scattering (NIS) technique and we discuss the effects of Fe^{2+} spin transition and the chemical composition on the elastic properties of Fe-bearing carbonates at high pressures and temperatures. We then infer the results from our NIS and the additional SCXRD experiments to build a model for the seismic detectability of carbonates in the Earth's mantle. Finally, in Chapter 8 we present the long-debated crystal structure of magnesite-II using the SCXRD method on a slightly Fe-enriched $MgCO_3$ crystal after laser heating at 98 GPa.

Chapter 5 *(published in Physics and Chemistry of Minerals):* To broaden the knowledge of the high pressure crystal chemistry of carbonates we studied spherocobaltite ($CoCO_3$), which contains Co^{2+} with cation radius in between those of Ca^{2+} and Mg^{2+} in calcite and magnesite, respectively. A path for the synthesis of pure and high-quality spherocobaltite single crystals is described here for the first time. The suggested $CoCO_3$ synthesis procedure involves experiments using wet chemistry and cold-sealed vessels. The final crystal growth was performed in multi anvil presses. Subsequently, crystals were loaded in BX90-type diamond anvil cells equipped with either standard brilliant-cut or Boehler-Almax type diamond anvils (culet size of 250 μm) with rhenium gaskets and neon as the pressure transmitting medium. We then performed Raman spectroscopy measurements at BGI and SCXRD experiments at the X-ray diffraction beamline ID09A at ESRF at pressures over 55 GPa. A double-sided laser-heating system was used for heating $CoCO_3$ at high-temperatures (up to 2000 K). Based on single crystal diffraction data we found that the bulk modulus of spherocobaltite is 128(2) GPa and K'=4.28(17). Our Raman spectroscopy (Figure 1) and SCXRD results (Figure 2) suggest that $CoCO_3$ maintains the calcite-type structure up to 56 GPa and 1200 K. At lower mantle temperatures, however, it decomposes, forming cobalt oxide, CoO (Figure 3). The behavior of spherocobaltite upon compression at ambient temperature is different to the behavior of siderite ($FeCO_3$) [1] and rhodochrosite ($MnCO_3$) [2]. Owing to the smaller ionic radius of Co^{2+} (0.745 Å) compared to Fe^{2+} (0.78 Å) and Mn^{2+} (0.83 Å) [3], the behavior of $CoCO_3$ is more similar to that of magnesite ($MgCO_3$), which maintains the $R\bar{3}c$ crystal structure up to 115 GPa and 2000-3000 K [4].
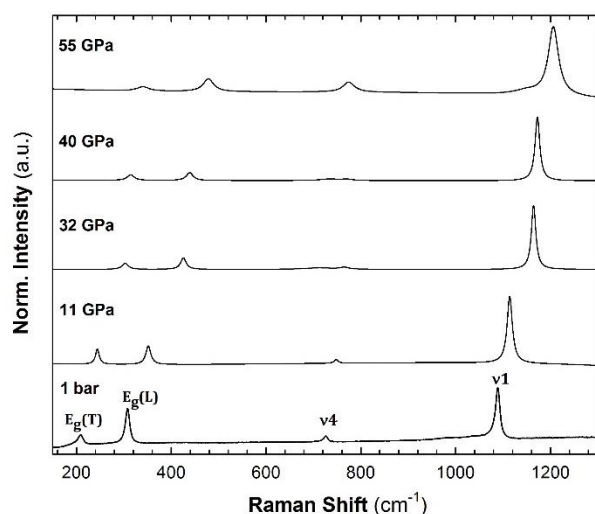
Figure 1. Raman spectra of $CoCO_3$ collected at ambient conditions and at successively higher pressures.
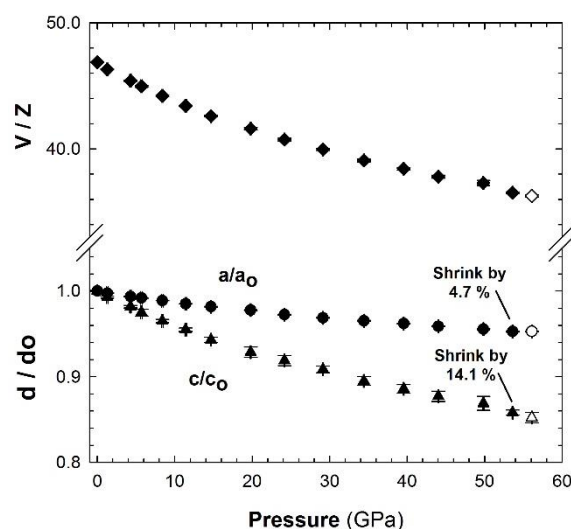

Figure 2. Relative axial compressibilities of a/a_0 (circles) and c/c_0 (triangles) of $CoCO_3$ (lower part of the plot) and volume per formula unit (V/Z) (diamonds) against pressure.
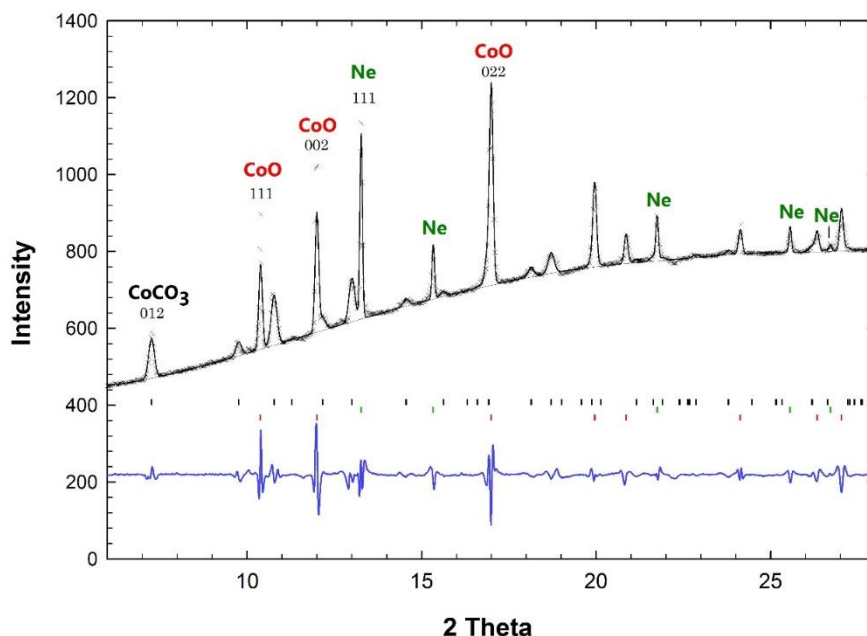
Figure 3. XRD pattern obtained after heating $CoCO_3$ at 2000 K at 57 GPa. Three phases are identified: solid neon, high-pressure $CoCO_3$ and its thermally decomposed product, CoO.

By the time this article was published, our findings on spherocobaltite was one of the few examples of single-crystal diffraction studies of rhombohedral carbonate minerals above 15 GPa, and only the second case when compression above 50 GPa does not lead to a phase transition, first being magnesite. Given $CoCO_3$ high pressure behavior, we may now imply that carbonates can be stable in the calcite-type structure over a wide pressure range that corresponds up to 1400 km depth within the Earth, if the incorporated metal's radius is equal to or lower than that of Co^{2+} (i.e. 0.745 Å). Our study of $CoCO_3$ indicate that high-pressure behavior of calcite-structured carbonates at ambient conditions may be drastically different at high pressures and temperatures (i.e. in comparison with $FeCO_3$ or $CaCO_3$), and thus we were motivated to look at different transition metal carbonates in **Chapter 6**.

Chapter 6 *(for submission to Angewandte Chemie: International Edition):* Although rhombohedral carbonate minerals belong to the same crystallographic family, they can exhibit very distinct behaviors at high pressures and temperatures. The ionic radii of divalent 3d transition metals in octahedral coordination lay between those of Ca^{2+} (1.00 Å) and Mg^{2+} (0.72 Å) [3], thus making transition metal carbonates, such as $(Mn^{2+}, Fe^{2+}, Co^{2+}, Ni^{2+}, Zn^{2+})CO_3$ ideal study cases to reveal crystallochemical regularities. The first step was the synthesis of high-quality endmember crystals of rhodochrosite ($MnCO_3$), gaspeite ($NiCO_3$) and smithsonite ($ZnCO_3$). The synthesis path of spherocobaltite ($CoCO_3$) was
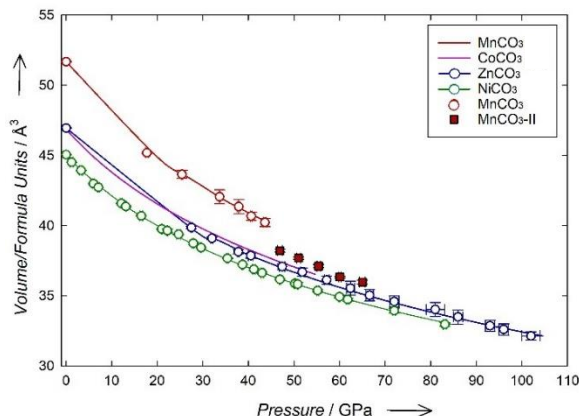
Figure 4. Equations of state of single crystals MnCO₃, NiCO₃, ZnCO₃ and CoCO₃. Note the 5% volume reduction of MnCO₃ when it transforms to MnCO₃-II above 44 GPa.
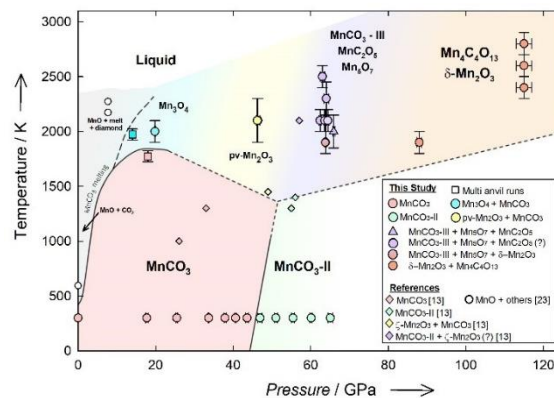
Figure 6. Stability diagram of MnCO₃ at high pressures and temperatures. See Chapter 6 for references.
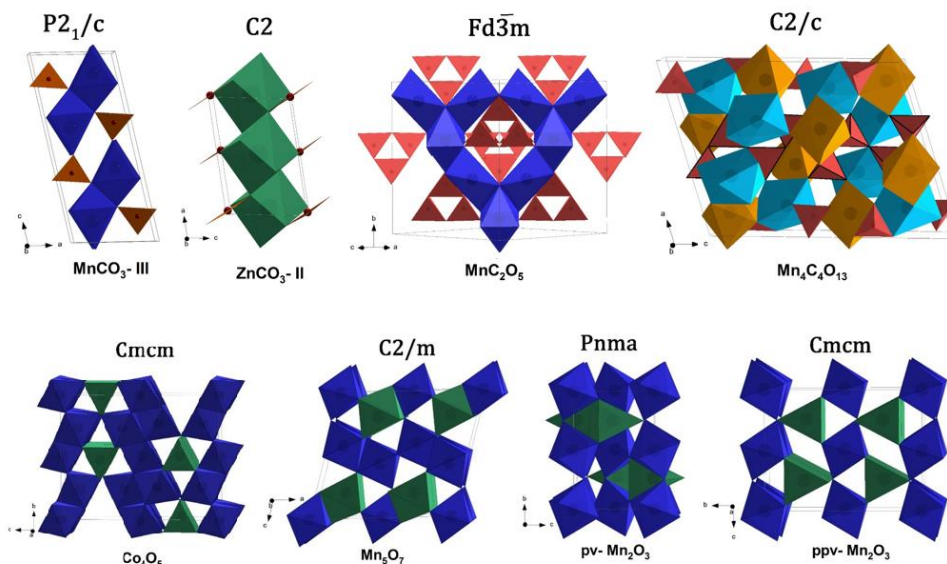
Figure 5. Selected crystal structures of various newly reported carbonate polymorphs and oxides.

described in our previous work (Chapter 5) and thus we followed the same procedure for the synthesis of MnCO₃. However, new synthesis paths had to be developed for NiCO₃ and ZnCO₃, since the previous procedure failed for these two compounds. The synthesis and crystal growth of pure NiCO₃ and ZnCO₃ was for the first time reported in this study and involves wet chemistry and cold-sealed vessel experiments. Following the successful synthesis of all compounds, we performed a long series of high-pressure and high-temperature experiments for each mineral by means of SCXRD measurements at the ID15B (ESRF) and P02.2 (PETRA-III, DESY) diffraction beamlines and complementary Raman spectroscopy measurements at BGI. Doing so, we firstly obtained the equations of state for each mineral and compared them (Figure 4). Among the four studied compositions, only MnCO₃ undergoes several structural

transformations above 44 GPa, while at higher pressures and temperatures it displays complex chemistry with formation of new, high-pressure carbonate polymorphs ($MnCO_3 - II$, $MnCO_3 - III$), but also structures based on CO_4 polymerizable units (MnC_2O_5, $Mn_4C_4O_{13}$), and/or various accompanying Mn-oxides (Mn_3O_4, Mn_5O_7, $pv - Mn_2O_3$, $\delta - Mn_2O_3$) (Figure 5). Apart from the spin transition in siderite [1] and the structural transformation of rhodochrosite [2], both happening at ~44 GPa, $MnCO_3$ (Figure 6)and $FeCO_3$ [5] present many similarities. Although, our results demonstrate a simpler high-pressure behavior for $NiCO_3$, $ZnCO_3$ and $CoCO_3$ more similar to $MgCO_3$, they too present interesting products following thermal treatment at high pressures (NiO, CoO, Co_4O_5, $ZnCO_3$-II) (Figure 5). Having now a better understanding of the crystal-chemical relations of all the endmember representatives of the calcite-type family, we moved forward to the most realistic (Earth-mantle-related) compositions of the $FeCO_3$-$MgCO_3$ system and determined their elastic properties. Our goal in **Chapter 7** was to test whether carbonates can be detected through geophysical methods.

Chapter 7 *(in press in American Mineralogist):* Carbonates play an important role in the transport and storage of carbon in the Earth's mantle. However, the abundance of carbon and carbonates in subduction zones is still an unknown. In order to understand which are the most abundant accessory phases and how they influence the dynamical processes that operate within the Earth, investigations on the vibrational, elastic and thermodynamic properties of these phases are crucial for interpreting the seismological observations. Studies have shown that carbonates in the $FeCO_3$-$MgCO_3$ binary system are among the most expected to persist in the lower mantle. However, measuring *in situ* elastic properties of Fe-bearing samples, which are usually opaque, and while at high pressures and high temperatures relevant to the Earth's lower mantle is a challenge. That is why we explored a new possibility, a synchrotron-based technique called Nuclear Inelastic Scattering (NIS), which only very recently was tested on Fe-bearing geo-materials in laser-heated diamond anvil cells and was proved very promising for the determination of the V_P and V_S [6, 7]. To do so however, we first needed to retrieve the accurate density and bulk modulus values of our samples as a function of pressure. Thus, we performed SCXRD experiments at ID15b (ESRF) and obtained the equations of state for $FeCO_3$ and $(Mg_{0.74}Fe_{0.26})CO_3$ up to ~70 GPa (Figure 7). Subsequently, we performed NIS experiments at the nuclear resonance beamline, ID18 (ESRF) in laser-heated panoramic diamond anvil cells with Be gaskets. In these experiments, we firstly obtained the partial density of state (pDOS) functions with increasing pressure, but also at high temperatures. The low
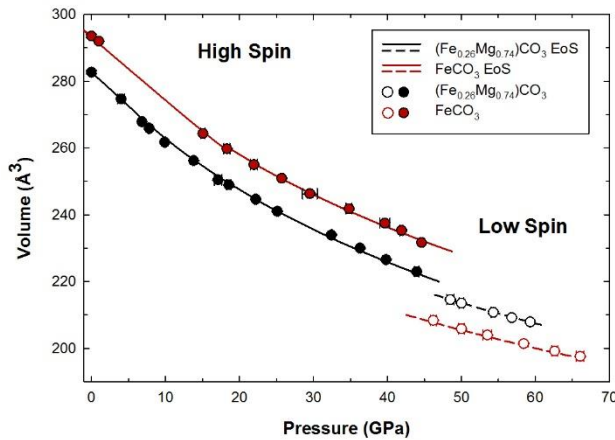
Figure 7. Equations of state (EoS) of single crystal FeCO₃ and (Mg₀.₇₄Fe₀.₂₆)CO₃. Note the sudden volume collapses when Fe²⁺ adopts its low spin state above ~44 GPa.
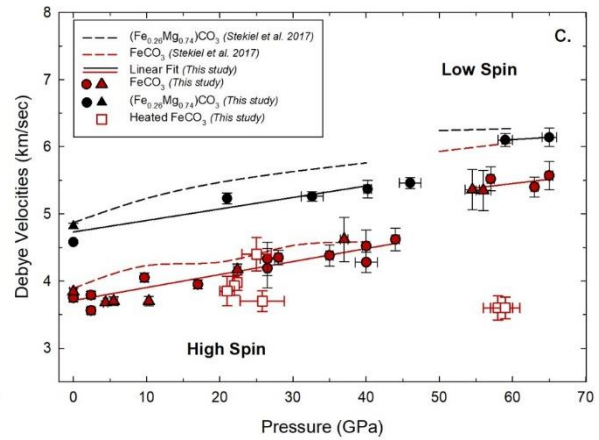
Figure 8. Debye sound velocities of siderite and Fe-bearing magnesite with increasing pressure. Our data are compared to previously reported DFT calculations and show good agreement between studies.

energy regime of the pDOS was used to derive Debye velocities (Figure 8). We concluded that more Mg-rich samples, in this case $(Mg_{0.74}Fe_{0.26})CO_3$, have ~ 19 % higher sound velocities than the pure end-member Fe composition. In addition, we observed a significant velocity increase after the Fe^{2+} spin transition was complete. After laser heating of $FeCO_3$ at lower mantle conditions, we observed a dramatic velocity drop, which is associated with thermal decomposition to another phase. The combined information from our SCXRD (density, bulk modulus) and our NIS (Debye velocity) experiments allowed us to estimate accurately the shear wave velocities (Figure 9). Our results were compared with results obtained by other

methods in previous studies, including Brillouin spectroscopy, inelastic X-ray scattering and DFT calculations, supporting NIS as a reliable alternative method for studying the elastic properties of Fe-bearing systems at high pressures and temperatures. Finally, we discuss the seismic detectability of carbonates, assuming that the dominant carbonate composition of the oceanic sediments that reach the transition zone and the lower mantle is $(Fe_{0.15}Mg_{0.85})CO_3$. Many evidences support this assumption [e.g. 8,
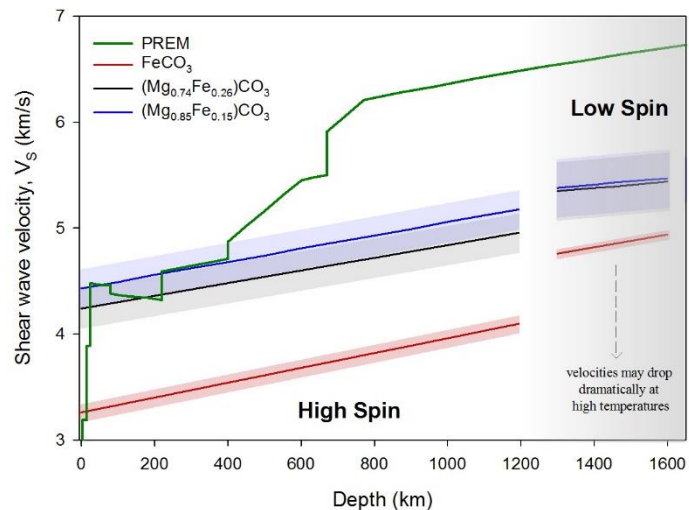
Figure 9. Shear wave velocities (Vₛ) of the PREM model compared to our modeled carbonate compositions as a function of depth. The effect of temperature is not taken into account in this plot (see Chapter 7 for details).

109

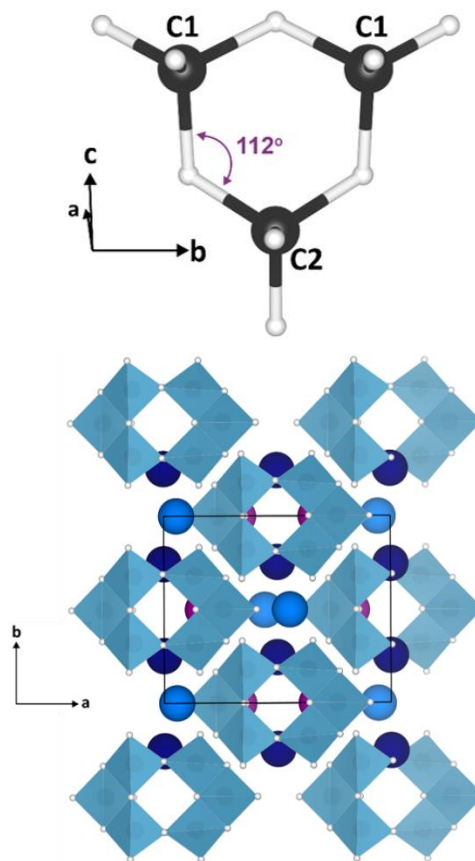9]. Taking into account several factors, such as the annual carbon fluxes, the present-day resolution of seismic imaging and the known phase stability diagrams for $FeCO_3$ [5] and $MgCO_3$ [4], we determine that nearly 22 wt% of CO_2 must be present in the subduction slab in order to detect a 1 % shear wave velocity decrease compared to non-carbonated lithologies at transition zone to lower mantle boundary depths (~600 to <1200 km) (Figure 9). A few subduction trenches exist today that contain such a high amount of CO_2 [10], mostly located in Central America, and they are all well-known examples of subduction slabs that deeply penetrate into the lower mantle [11]. These or similar regions are of high interest for possible future geophysical surveys looking for carbonates in the deep Earth. Nonetheless, it is important to continue our investigations on the stability fields of rhombohedral carbonates, now focused mostly on the Fe-bearing $MgCO_3$ compositions. In this study we observed that in post-spin-transition depths (>1200 km) and following the geotherm, Fe-rich carbonates will most likely decompose and if so then Fe-oxides will play a more important role in the velocity profiles of the deep lower mantle compared to carbonates. But does the same apply for Fe- poor magnesite compositions? This question motivated us to investigate the stability of $(Fe_{0.15}Mg_{0.85})CO_3$ at the pressure and temperature conditions that persist at depths >1200 km and the results are presented in **Chapter 8**.

Chapter 8 *(for submission to Acta Crystallographica: Section E):* Several studies have suggested that the stability of carbonates increases with the addition of Mg^{2+} [e.g. 5, 12]. Early experiments on the pure $MgCO_3$ end-member up to 115 GPa and 2100 K, lead scientists to believe that magnesite is the most stable carbonate in the calcite-type structure and the most likely carbonate candidate to survive subduction nearly in the whole mantle. However, both theoretical calculations and powder diffraction experiments (PXRD) have suggested that magnesite will most likely adopt its sp^3-based form (magnesite-II) close to the basis of the lower mantle (Mbar pressure range). If true, this would have a great impact on the physical and elastic properties of carbonates. It could revise our ideas for the deep carbon cycle; how deep in the Earth does the carbon cycle operate and which C-bearing phases will be dominant; can carbonates be one of them and will they play a prominent role in the mantle processes? However, the precise crystal structure of magnesite-II is still under debate. Several energetically favored structures have been suggested ($C2/c$, $C2/m$, $C222_1$, $Pbca$…etc) as well as several kinds of CO_4 group arrangements within the unit cell [e.g. 13, 14]. Here, we solve this mystery by implementing the SCXRD method. An $(Fe_{0.15}M0g_{0.85})CO_3$ single-crystal was loaded in a BX90 cell equipped with Boehler -Almax diamonds (80 μm culet size). Neon served as a pressure transmitting medium to assure quasi-hydrostatic conditions. The

pressure was increased to 98 GPa and the SCXRD diffraction pattern was collected while at room temperature at the 13IDD diffraction beamline (GSECARS, APS, Chicago, USA). At these conditions we confirmed that $(Fe_{0.15}Mg_{0.85})CO_3$ is still indexed in the calcite-type structure. Subsequently the crystal was laser heated at 2500 K and SCXRD patterns were collected both at 13IDD and ID15B (ESRF) indicating a structural transformation. The symmetry (monoclinic, $C2/m$) and the lattice parameters of this phase matched some of the previous predictions for magnesite-II, and thus we assigned the name. However, using SCXRD data we were now able to solve the structure and describe the CO_4 topology. We found that magnesite-II ($(Fe_{0.4}Mg_{2.6})C_3O_9$) is based on $(C_3O_9)^{6-}$ carbonate rings which alternate with (Fe,Mg) polyhedra perpendicular to the b-axis (Figure 10). The $(C_3O_9)^{6-}$ ring networks have been reported previously for dolomitic compositions [Ca(Fe,Mg)C$_3$O$_9$] using SCXRD [15].

Figure 10. The crystal structure of $(Fe_{0.4}Mg_{2.6})C_3O_9$.

We noted that this phase is not isostructural to $Fe_{0.4}Mg_{2.6}C_3O_9$, possibly due to the presence of Ca^{2+}. Other tetracarbonates were determined by means of SCXRD in the $FeCO_3$ system, such as $Fe_4C_3O_{12}$ (R3m) and $Fe_4C_4O_{13}$ (C2/c) [5]. Thus, we conclude that CO_4 units have the ability to form different varieties of polymerizable networks. We also underline the significance of the SCXRD method in retrieving such valuable information with great precision; here, the nearly 15-year old debate over the magnesite-II crystal structure is finally clarified using SCXRD.

3.2. Brief outlook and perspectives

Natural evidences, theoretical calculation models and experiments at extreme conditions they all support the transportation of carbonates via subduction into the deep Earth. From all carbonates, the rhombohedral family is the protagonist. The depth to which they would travel into the Earth and whether they will survive the reducive mantle intact or decompose in formation of other C-bearing species (diamond, CO_2, carbides etc…) and oxides strongly depends to their chemistry. The present thesis has demonstrated that the presence of some metals (Ca^{2+}, Mn^{2+}, Fe^{2+}), commonly incorporated in

rhombohedral carbonates, grant unique characteristics to the mineral's high-pressure behavior. Therefore, by studying each endmember carbonate separately, we can set constrains on the behavior of the natural compositions and understand the effect of impurity elements, but also explain some of the discrepancies between studies. In addition, this thesis explored the formation of carbonates with tetrahedrally coordinated carbon. Our results show that not all carbonates can form tetracarbonates (at least at the investigated pressure and temperature ranges); it appears that Fe, Mg and Mn play an important role in the polymerization of carbon. Summing up all our knowledge on the high pressure and high temperature behavior of carbonates, we explored the possibilities of their seismic detectability. Our results suggest that this is not very likely, but we have set certain constrains and proposed candidate locations on Earth for further examination.

In order to accurately untangle the complex chemistry of carbonates at extreme conditions and determine the thermoelastic properties of Fe-bearing samples we used the SCXRD and the NIS methods. This thesis is among the few examples that demonstrate the feasibility of SCXRD experiments in laser-heated DACs and highlight the merits of the method. The same holds for the NIS method; it is a very promising technique that deserves more attention in the future.

Although in the time framework of this thesis we answered several questions and proposed the use of specific analytical techniques to solve common problems in the high-pressure research of carbonates, there are still more paths to explore. Dolomitic compositions seem to be on the spotlight today. For long time they received little attention due to their rich chemistry ($Ca(Fe,Mg)(CO_3)_2$). However, using SCXRD in combination with Raman spectroscopy and DFT calculations, new dolomite high pressure polymorphs are ongoing discoveries (e.g. dolomite-V, C2/c, Figure 11) [16]. In addition, the strong velocity anisotropies of Fe-bearing samples needs to be described further. We know that NIS measurements are sensitive to crystal orientations (Figure 12). This is still an ongoing project. Other ongoing projects involve
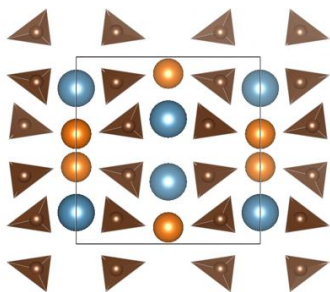
Figure 11. The crystal structure of a new dolomite high-pressure polymorph along the c-axis. (blue Ca forms CaO_{10}; orange Mg forms MgO_6; brown C forms CO_3).
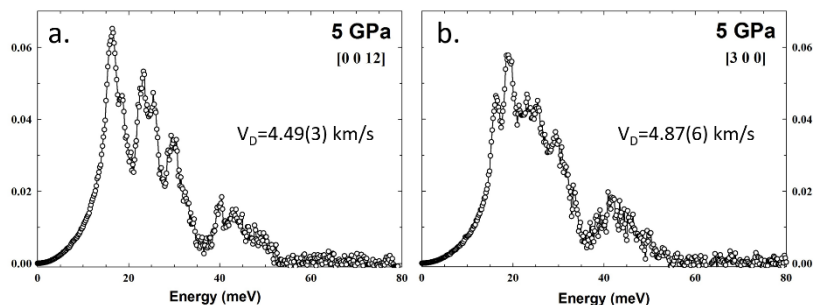
Figure 12. Partial DOS functions of an $FeCO_3$ crystal oriented along **a)** the c-axis and **b)** the a*-axis. The data are derived after NIS measurements at 5 GPa. The different velocities reflect the anisotropic nature of carbonates.

the chemical reactions of carbonates with mantle silicates and the stability fields of carbonates in the $MgCO_3$-$FeCO_3$ system. These and many more are projects that require the expertise of various analytical techniques. In this framework, research units such as CarboPaT (Carbonates at high Pressures and Temperatures) were formed, that invite collaborations between several universities and geo-institutes around Germany (and not only). Thus, many new exciting discoveries for the deep carbon cycle await us in the near future.

3.3. References

[1] V. Cerantola, C. McCammon, I. Kupenko, I. Kantor, C. Marini, M. Wilke, L. Ismailova, N. Solopova, A.I. Chumakov, S. Pascarelli, and L. Dubrovinsky, **(2015)** *High-pressure spectroscopic study of siderite (FeCO3) with focus on spin crossover.* American Mineralogist, 100, 2670-2681.

[2] M. Merlini, M. Hanfland, and M. Gemmi, **(2015)**. *The MnCO$_3$-II high pressure polymorph of rhodochrosite.* American Mineralogist, 100, 11-12.

[3] R.D. Shannon, C.T. Prewitt **(1969)** *Effective ionic radii in oxides and fluorides.* Acta Crystallographica Section B, 25, 925-946.

[4] M. Isshiki, T. Irifune, K. Hirose, S. Ono, Y. Ohishi, T. Watanuki, E. Nishibori, M. Takata, and M. Sakata, **(2004),** *Stability of magnesite and its high-pressure form in the lowermost mantle*. Nature, 427, 60-63.

[5] V. Cerantola, E. Bykova, I. Kupenko, M. Merlini, L. Ismailova, C. McCammon, M. Bykov, A.I. Chumakov, S. Petitgirard, I. Kantor, V. Svitlyk, J. Jacobs, M. Hanfland, M. Mezouar, C. Prescher, R. Rüffer, V.B. Prakapenka, and L. Dubrovinsky, **(2017)** *Stability of iron-bearing carbonates in the deep Earth's interior.* Nature Communications, 8, 15960.

[6] C. McCammon, R. Caracas, K. Glazyrin, V. Potapkin, I. Kantor, R. Sinmyo, C. Prescher, I. Kupenko, A.I. Chumakov, and L. Dubrovinsky, **(2016)** *Sound velocities of bridgmanite from density of states determined by nuclear inelastic scattering and first-principles calculations.* Progress in Earth and Planetary Science, doi:10.1186/s40645-016-0089-2.

[7] D.M. Vasiukov, L. Ismailova, I. Kupenko, V. Cerantola, R. Sinmyo, K. Glazyrin, C. McCammon, A.I. Chumakov, L. Dubrovinsky, and N. Dubrovinskaia, **(2018)** *Sound velocities of skiagite–iron–majorite solid solution to 56 GPa probed by nuclear inelastic scattering.* Physics and Chemistry of Minerals, 45, 397-404.

[8] C. Biellmann, P. Gillet, F. Guyot, J. Peyronneau, and B. Reynard, **(1993)** *Experimental evidence for carbonate stability in the Earth's lower mantle.* Earth and Planetary Science Letters, 118, 31-41.

 [9] R. Dasgupta, M.M. Hirschmann, and A.C. Withers, **(2004***) Deep global cycling of carbon constrained by solidus of anhydrous, carbonated eclogite under upper mantle conditions*. Earth and Planetary Science Letters, 227, 73–85.

 [10] T. Plank, and C.H. Langmuir, **(1998)** *The chemical composition of subducting sediments and its consequences for the crust and mantle.* Chemical Geology, 145, 325-394.

[11] Y. Fukao, and M. Obayashi, **(2013)** *Subducted slabs stagnant above, penetrating through, and trapped below the 660 km discontinuity.* Journal of Geophysical Research: Solid Earth, 118, 5920-5938.

[12] B. Lavina, P. Dera, R.T. Downs, O. Tschauner, W. Yang, O. Shebanova, and G. Shen, **(2010)** *Effect of dilution on the spin pairing transition in rhombohedral carbonates.* High Pressure Research, 30, 224-229.

[13] A.R. Oganov, S. Ono, Y. Ma, C.W. Glass, A. Garcia, **(2008)** *Novel high-pressure structures of $MgCO_3$, $CaCO_3$ and CO_2 and their role in Earth's lower mantle.* Earth and Planetary Science Letters, 273, 38-47.

[14] E. Boulard, D. Pan, G. Galli, Z. Liu, and W.L. Mao, **(2015)** *Tetrahedrally coordinated carbonates in Earth's lower mantle.* Nature Communications, 6, 6311.

[15] M. Merlini, V. Cerantola, G.D. Gatta, M. Gemmi, M. Hanfland, I. Kupenko, P. Lotti, H. Müller, and L. Zhang, **(2017)** *Dolomite-IV: Candidate structure for a carbonate in the Earth's lower mantle.* American Mineralogist, 102, 1763-1766.

[16] J. Binck, S.Chariton, M. Stekiel, L. Bayarjargal, W. Morgenroth, L. Dubrovinsky, and B. Winkler **(2020)** *High-pressure, high-temperature phase stability of iron-poor dolomite and the structures of dolomite-IIIc and dolomite-V.* Physics of the Earth and Planentary Interiors, 299, 106403.

Chapter 4

List of papers and author contributions

[1] Chariton, S. (CS), Cerantola, V. (CV), Ismailova, L. (IL), Bykova, E. (BE), Bykov, M. (BM), Kupenko, I. (KI), McCammon, C. (MC), and Dubrovinsky, L. (DL), **(2018)** The high-pressure behavior of spherocobaltite ($CoCO_3$): a single crystal Raman spectroscopy and XRD study. Physics and Chemistry of Minerals, 45, 59-68.

The study was designed by CS and DL. The samples were synthesized by CS and CV and characterized by CS. Diamond anvil cells were prepared by CS and VC. Single-crystal X-ray diffraction data at synchrotron were collected by CV, IL, BE, BM and KI. Raman spectroscopy measurements were performed by CS. All data were analyzed by CS. CS, MC and LD discussed the results and wrote the manuscript with contributions from all authors. The total contribution of CS is 70 %.

[2] Chariton, S. (CS), McCammon, C. (MC), Vasiukov, D.M. (VDM), Stekiel, M. (SM), Kantor, A. (KA), Cerantola, V. (CV), Kupenko, I. (KI), Fedotenko, T. (FT), Koemets, E. (KE), Hanfland, M. (HM), Chumakov, A.I. (CAI), Dubrovinsky, L. (DL), **(2020)**, Seismic detectability of carbonates in the deep Earth: A nuclear inelastic scattering study. In press in the American Mineralogist.

The study was designed by CS and MC. The samples were synthesized by CS and CV and characterized by CS. Diamond anvil cells were prepared by CS, KI, CV, FT, KE, and DL. The beamline experimental set-ups were prepared by HM and CAI. Nuclear inelastic scattering experiments were performed by CS, MC, VDM, KA, CV and KI and the data were processed by CS and MC. Single-crystal X-ray diffraction experiments were performed by CS, FT and KE and the data were processed by CS. The results were discussed by CS, MC, SM and DL. The manuscript was written by CS, MC and DL with contributions from all authors. The total contribution of CS is 80 %.

[3] Chariton, S. (CS), Bykova, E. (BE), Bykov, M. (BM), Aprilis, G. (GA), Koemets, E. (KE), Fedotenko, T. (FT), Hanfland, M. (HM), McCammon, C. (CM), and Dubrovinsky, L. (DL), **(2019)** Insights in the crystal chemistry of transition metal (Mn, Co, Ni, Zn) carbonates and their oxides at extreme conditions. For submission to Angewandte Chemie International Edition.

The study was designed by SC and DL. The samples were synthesized and characterized by CS. The diamond anvil cells were prepared by CS, BM, KE and FT. The beamline experimental set-ups were prepared by HM and BM. Single-crystal X-ray diffraction experiments were performed by CS, BE, BM, GA, KE, FT and DL. Data from these experiments were analyzed by CS with the help of BE and DL. CS performed and analyzed the data from Raman spectroscopy experiments. CS, MC and DL discussed the results and wrote the manuscript with contributions from all authors. The total contribution of CS is 70 %.

[4] Chariton, S. (CS), Bykov, M. (BM), Bykova, E. (BE), Koemets, E. (KE), Fedotenko, T. (FT), Winkler B. (WB), Hanfland, M. (HM), Prakapenka V.B (PVB), Greenberg E. (GE) McCammon, C. (CM), and Dubrovinsky, L. (DL), (**2019**) Crystal structure of Fe-bearing $MgCO_3$ sp^3-carbonate at 98 GPa using single-crystal X-ray diffraction. For submission to Acta Crystallographica Section E.

The study was designed by CS, DL and MC. The samples were synthesized and characterized by CS. The diamond anvil cell was prepared by CS and DL. The beamline experimental set-ups were prepared by HM, PVB and GE. WB performed the DFT-based model calculations. The diffraction experiments were performed by CS, BM, KE, and FT and the data were analyzed by CS with the help of BE. CS, CM and DL discussed the results and wrote the manuscript with contributions from all authors. The total contribution of CS is 80 %.

Chapter 5

The high-pressure behavior of spherocobaltite (CoCO₃): A single crystal Raman spectroscopy and XRD study

Stella Chariton[1], Valerio Cerantola[1,2], Leyla Ismailova[3], Elena Bykova[1], Maxim Bykov[1], Ilya Kupenko[4], Catherine McCammon[1], Leonid Dubrovinsky[1]

[1] Bayerisches Geoinstitut, Universitat Bayreuth, D-95440 Bayreuth, Germany

[2] European Synchrotron Radiation Facility, 38043 Grenoble, France

[3] Vernadsky Institute of Geochemistry and Analytical Chemistry, Russian Academy of Sciences, 119991 Moscow, Russia

[4] Institute for Mineralogy, Universitat Münster, D-48149 Münster, Germany

Corresponding Author's email:
ORCID iD: 0000-0001-5522-0498
Tel: +49 (0)921 55 3878

ABSTRACT

Magnesite ($MgCO_3$), calcite ($CaCO_3$), dolomite [$(Ca,Mg)CO_3$], and siderite ($FeCO_3$) are among the most well studied carbonate minerals at high pressures and temperatures. Although they all exhibit the calcite-type structure ($R\bar{3}c$) at ambient conditions, they display very different behavior at mantle pressures. To broaden the knowledge of the high pressure crystal chemistry of carbonates we studied spherocobaltite ($CoCO_3$), which contains Co^{2+} with cation radius in between those of Ca^{2+} and Mg^{2+} in calcite and magnesite, respectively. We synthesized single crystals of pure spherocobaltite and studied them using Raman spectroscopy and X-ray diffraction in diamond anvil cells at pressures over 55 GPa. Based on single crystal diffraction data we found that the bulk modulus of spherocobaltite is 128(2) GPa and K'=4.28(17). $CoCO_3$ is stable in the calcite-type structure up to at least 56 GPa and 1200 K. At 57 GPa and after laser heating above 2000 K, $CoCO_3$ partially decomposes and forms CoO. In comparison to previously studied carbonates, our results suggest that at lower mantle conditions carbonates can be stable in the calcite-type structure, if the incorporated metal's radius is equal or lower than that of Co^{2+} (i.e. 0.745 Å).

5.1. Introduction

Spherocobaltite (CoCO$_3$) is a well-known carbonate mineral that has long received an IMA approval (https://www.ima-mineralogy.org/Minlist.htm). It is one of the representative minerals of the calcite-type structure (R$\overline{3}$c) carbonate group (Reeder 1983; Pertlik 1986) and is broadly known due to its impressive magenta color. Although that is a relatively rare mineral, spherocobaltite is often found as a secondary phase in Co-Ni lateritic deposits, Co-bearing deposits or in Cu-bearing hydrothermal ore deposits (Barton et al. 2014). Most of spherocobaltite's physical and optical properties at ambient conditions are well defined, however, our knowledge of its properties and crystal structure as a function of pressure remains severely limited. Until now, there is only one study of CoCO$_3$ up to 8 GPa (Zhang and Reeder 1999). Thus, accomplishing the first goal of the present study, we have extended the pressure range considerably and report here spherocobaltite's behavior at pressures and temperatures relevant to the Earth's mantle (57 GPa and ~2000 K).

Cobalt is a siderophile transition metal cation that in spite of having a low natural abundance (Turekian and Wedepohl 1961; Jagoutz et al. 1979; Veizer 1983; Badro et al. 2015), it is an important model element on the basis of the ionic radius, due to its strong geochemical coherence to Mg^{2+}and Fe^{2+} (Carr and Turekian 1960). Indeed, it is suggested that Co^{2+} often substitutes Mg^{2+}and Fe^{2+} in ferromagnesian silicate minerals, while it has an additional substitution preference of Mn^{2+} sites in minerals of sedimentary origin, such as carbonates (Carr and Turekian 1960; Goldsmith and Northrop 1965). Therefore, in the present study we additionally focus our interest on spherocobaltite, in our effort to systematize the crystal-chemical regularities that have long been observed in the high-pressure behavior of the rhombohedral carbonate mineral group. The three dominant carbonate endmembers, CaCO$_3$-MgCO$_3$-FeCO$_3$, display very different behavior to each other at Earth's mantle conditions (Isshiki et al. 2004; Lavina et al. 2009; Merlini et al. 2012a). At room temperature, calcite (CaCO$_3$) transforms to CaCO3-II already above 1.7 GPa (Bridgman 1939; Vizgirda and Ahrens 1982; Fiquet et al. 1994; Merlini et al. 2012a), while at high temperatures (1073 K) and above 2 GPa, it transforms into aragonite (Pcmn) (Suito et al. 2001). In contrast, magnesite (MgCO$_3$) is stable in the calcite-type structure (i.e. R$\overline{3}$c) up to 115 GPa and at high temperatures (2000-3000 K) (Katsura et al. 1991; Isshiki et al. 2004). Siderite (FeCO$_3$) is consistently reported to show a spin transition between 40-50 GPa at room temperature that is accompanied by ~10% volume collapse (Mattila et al. 2007; Lavina et al. 2009; Lavina et al. 2010a; Boulard et al. 2011; Cerantola et al. 2015) and formation of novel complex structures at higher pressures and temperatures (Boulard et al. 2014). Furthermore, solid solutions of the above components lead to the minerals dolomite [(Mg, Ca)CO$_3$] and ankerite [(Mg, Ca, Fe)CO$_3$], which are close to the expected

composition of the overall carbonated component of the subducting slab in active tectonic margins (Merlini et al. 2012; Mao et al. 2011). Despite their relevance, dolomite and ankerite have not yet been fully studied at relevant to the deep Earth's pressure-temperature conditions, possibly due to their complex crystal chemistry.
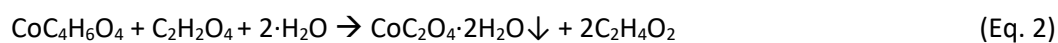
It is well known that at low pressure, the crystallization of carbonates into calcite ($R\bar{3}c$) or aragonite (Pcmn) type structures is controlled by the cation radius (Santillán and Williams 2004). Moreover, changes in the electronic state of transition metal cations (such as Fe^{2+}, Mn^{2+} etc.) may further affect the high pressure behavior of carbonates (Lavina et al. 2010; Shi et al. 2012). Therefore, it is instructive to study transition metal carbonates in order to understand the distinct high-pressure behaviors of the abundant alkaline-earth metal carbonates. Moving forward on this direction, until now, $FeCO_3$ high pressure and high temperature behavior has been well established and many studies have recently focused their interest in rhodochrosite ($MnCO_3$) as well (Ono 2007; Farfan et al. 2013, Boulard et al. 2015; Merlini et al. 2015). Contrary, data on spherocobaltite at pressures above 8 GPa (Zhang and Reeder 1999) are absent and our study is an attempt to fill in this lacuna.

5.2. Methods

Due to previously reported inconsistencies between studies that may arise from differences in the samples, such as variations in chemistry (i.e., natural versus synthetic) and/or the presence of significant non-hydrostatic stress (i.e., single crystal versus polycrystalline) (e.g. Boulard et al. 2015; Merlini et al. 2015), we used chemically pure synthetic single $CoCO_3$ crystals for our study. We studied them by means of Raman spectroscopy and X-ray single crystal and powder diffraction using synchrotron radiation up to 57 GPa and ~ 2000 K.

5.2.1. Synthesis

Pure $CoCO_3$ single crystals were obtained following the same synthesis method used for $FeCO_3$ as described in previous reports (French 1971; Cerantola et al. 2015). Cobalt metal powder reacted with acetic acid (CH_3COOH) (Eq. 1). The solid product of this reaction was cobalt acetate ($Co(CH_3COO)_2$), which was later dissolved into oxalic acid ($C_2H_2O_4$) forming the dihydrated cobalt oxalate ($CoC_2O_4 \cdot 2H_2O$) (Eq. 2).

$Co + 2C_2H_4O_2 \rightarrow CoC_4H_6O_4 + H_2 \uparrow$	(Eq. 1)
$CoC_4H_6O_4 + C_2H_2O_4 + 2 \cdot H_2O \rightarrow CoC_2O_4 \cdot 2H_2O \downarrow + 2C_2H_4O_2$	(Eq. 2)
$CoC_2O_4 + 2 \cdot H_2O = CoCO_3 + CO \uparrow + 2 \cdot H_2O \uparrow$	(Eq. 3

The chemical composition of the solid product described in Eq. 2 was determined by a Philips powder diffractometer with monochromated Kα1 of Co (λ ≈ 1.78897 cm^{-1}) radiation (40kV, 40 mA) at the Bayerisches Geoinstitut (BGI), Bayreuth, Germany. The metal oxalate powder was sealed in a gold capsule and loaded in an externally heated seal cold vessel. The hydrothermal experiment was run at 2 kbar and 633 K for seven days. The product of the latter reaction (Eq. 3) was $CoCO_3$ powder, which was used to grow single crystals using a multi anvil apparatus available at the BGI. A Cr-doped MgO octahedron was used as the pressure medium with a $LaCrO_3$ heater (Frost et al. 2004). A small amount of $CoCO_3$ powder was carefully encapsulated inside a Re capsule. The sample was annealed for 8 minutes at 18 GPa and 1773 ± 323 K. Temperature was monitored by a $W_{75}Re_{25}/W_{97}Re_3$ thermocouple. No correction for the effect of pressure was made on the electromotive force of the thermocouple. The size of the magenta-colored, quite isometric $CoCO_3$ crystals ranged from 10 to 130 μm in diameter (Fig. 1). Chemical analysis of several crystals by wavelength-dispersive X-ray (WDX) micro probe analysis (JEOL JXA-8200; focused beam; 15 keV and beam current 15 nA) and energy-dispersive X-ray spectroscopy (EDXS) confirmed the purity of our $CoCO_3$ crystals. Note that the capsule materials (i.e., Re and the remnants of Au) (Fig. 1) did not chemically interact with the sample.

5.2.2. Diamond anvil cells experiments

We used BX-90 type diamond anvil cells (DACs) (Kantor et al. 2012) with diamonds of 250 μm culet size in this study. For X-ray diffraction (XRD) experiments, Boehler-Almax-type diamonds were used, while for Raman spectroscopy measurements brilliant-cut diamonds and specially selected anvils (Type IIa) were employed. Rhenium gaskets were indented down to about 30 μm thickness and then a hole was drilled with a starting diameter of about 120 μm to produce the sample chamber. Neon gas was loaded under pressure (1.4 kbar) (Kurnosov et al. 2008) as a pressure-transmitting medium in order to achieve
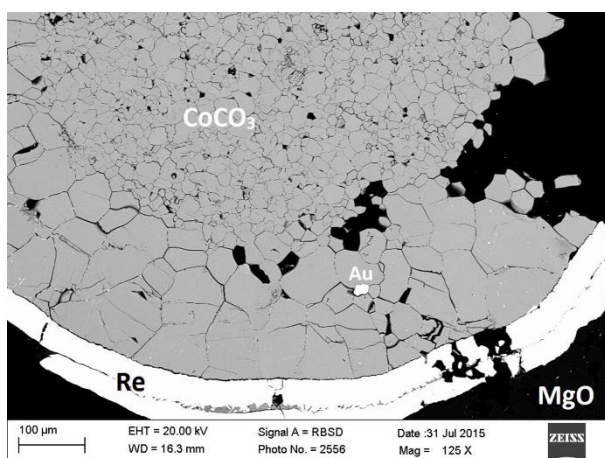
Figure 1. Back scattered electron (BSE) image of a polished section of the multianvil run product showing the $CoCO_3$ microstructure. The image was recorded using a scanning electron microscope (SEM).

quasi-hydrostatic conditions in all of our experiments. In each cell, two $CoCO_3$ single crystals (15-20 μm in diameter, about 10 μm thick) were loaded together with a ruby, which was used for pressure determination (Mao et al. 1986) for the Raman spectroscopy measurements. During our XRD experiments above ~13 GPa, pressure was determined from the Ne equation of state (EoS) (http://kantor.50webs.com/diffraction.htm) (Fei et al. 2007).

5.2.3. Raman spectroscopy

A triple-monochromator DILOR XY spectrometer with 2 cm^{-1} spectral resolution using the 514 nm line of the Ar^+ excitation laser was employed for our Raman measurements. High-pressure Raman spectra were collected in situ over the range 150-1300 cm^{-1}. The Raman active band of $CoCO_3$ at approximately 1400 cm^{-1} was not monitored at high pressure, because it overlaps with the strong Raman signal originating from the diamonds (~1330 cm^{-1}). Raman spectra were collected in steps of 3 - 4 GPa upon compression up to 55 GPa and decompression to ambient conditions. The pressure uncertainty was estimated from the difference in the pressures measured before and after each data point collection and did not exceed 1 GPa. The spectral fitting was carried out using the software package PeakFit (Systat Software).

5.2.4. Synchrotron X-ray Diffraction

Single crystal X-ray diffraction (XRD) patterns of $CoCO_3$ crystals were collected at the ID09A beamline at the European Synchrotron Radiation Facility (ESRF), Grenoble, France (MAR555 flatpanel detector, λ = 0.4150 Å). At each pressure point we collected preliminary XRD wide images (–20 to +20° on omega) used for pressure determination and adjustment of the primary beam intensity. Then data collection experiments were performed by a narrow 0.5° scanning of the –38 to +38° omega range. The $CoCO_3$ crystals were compressed in steps of a few GPa up to about 56 GPa at ambient temperature. Subsequently, a portable double-sided laser-heating system (Kupenko et al. 2012) was employed to first heat directly a crystal to about 1200 K and later another crystal to temperatures above 2000 K. XRD patterns were collected on the temperature-quenched samples.

Integration of the reflection intensities and absorption corrections were performed using CrysAlis^{Pro} software (Agilent 2014). Atomic coordinates of $CoCO_3$ given in Pertlik (1986) were used as a starting mode for the structure refinement. All calculations were performed using the SHELXL software (Sheldrick 2014) as implemented in the WinGX package (Farrugia 2012). All atoms but Co were refined in isotropic approximation giving in total 6 refinable parameters for typically 70 unique reflections

with $F_o > 4\sigma(F_o)$. The final discrepancy factors (R_1) were less than 4% for all pressure points (Table 1). The powder XRD patterns of the laser-heated samples were analyzed using the GSAS software (Rietvield refinement) (Larson and von Dreele 1985).

Table 1. Crystallographic data of $CoCO_3$

| P (GPa)	a (Å)	c (Å)	V (Å³)	O_x	Co-O (Å)	C-O (Å)	R1	R(int)
0.00(0)	4.6582(3)	14.9655(9)	281.23(4)	0.2761(4)	2.1099(10)	1.2861(20)	0.0266	0.036
1.3(1)	4.6469(2)	14.8581(5)	277.86(2)	0.2764(4)	2.1004(8)	1.2846(17)	0.0241	0.019
4.3(1)	4.6280(4)	14.6875(14)	272.44(5)	0.27725(19)	2.0846(4)	1.2831(9)	0.0198	0.024
5.7(1)	4.6209(3)	14.589(4)	269.78(8)	0.2781(4)	2.0757(9)	1.2852(17)	0.0255	0.029
8.4(1)	4.6059(2)	14.440(2)	265.29(4)	0.2783(4)	2.0636(10)	1.2819(20)	0.0280	0.023
11.4(1)	4.5884(2)	14.288(2)	260.51(4)	0.2790(5)	2.0494(10)	1.2803(21)	0.0441	0.036
14.68(5)	4.5733(3)	14.111(3)	255.59(6)	0.2796(4)	2.0351(10)	1.2788(20)	0.0318	0.021
19.80(5)	4.5544(5)	13.895(6)	249.60(12)	0.2803(4)	2.0177(10)	1.2764(19)	0.0296	0.037
24.16(5)	4.5302(5)	13.753(6)	244.43(12)	0.2803(4)	2.0036(10)	1.2700(20)	0.0349	0.033
29.14(5)	4.5127(4)	13.596(4)	239.78(8)	0.2805(4)	1.9904(10)	1.2659(20)	0.0317	0.028
34.42(5)	4.4966(4)	13.393(5)	234.52(10)	0.2814(7)	1.9741(16)	1.2652(31)	0.0346	0.030
39.56(5)	4.4816(3)	13.256(5)	230.57(9)	0.2821(6)	1.9616(15)	1.2641(29)	0.0355	0.030
44.02(5)	4.4664(5)	13.128(6)	226.80(12)	0.2817(6)	1.9520(15)	1.2580(28)	0.0340	0.034
49.84(5)	4.4511(6)	13.003(8)	223.10(15)	0.2822(9)	1.9403(21)	1.2562(41)	0.0374	0.029
53.61(5)	4.4386(6)	12.840(3)	219.07(8)	0.2825(10)	1.9285(23)	1.2540(50)	0.0441	0.041
56.09(5)*	4.4390(6)	12.756(6)	217.68(12)	0.2825(8)	1.9245(18)	1.2542(40)	0.0439	0.025
57.17(5)**	4.421(1)	12.66(1)	214.4(2)	0.2834(4)				

* Single-crystal XRD pattern collected after heating at 1200 K.
** Powder XRD pattern collected after heating at 2000 K. Sample thermally decomposed to $CoCO_3$ + CoO + CO_2

5.3. Results

5.3.1. Raman Spectroscopy

At ambient conditions, spherocobaltite has four active Raman bands in the frequency range that we investigated (i.e., 150-1300 cm^{-1}). Unlike previous reports (Rutt and Nicola 1974), we did not observe decomposition of our synthetic crystals under the laser beam. The Raman spectrum at 1 bar and 300 K presents four main peaks at ~ 194, 302, 725 and 1090 cm^{-1} (Fig. 2). The first two bands (i.e., with lower wavenumbers) correspond to external modes associated with lattice vibrations, one translational (Eg(T)) and one librational (Eg(L)), while the latter two bands (i.e., with higher wavenumbers) correspond to internal vibrations within the $(CO_3)^{2-}$, one asymmetric bending (E_g or v4), which is actually a degenerated mode, and one symmetric stretching (A_{1g} or v1) (Rutt and Nicola 1974).
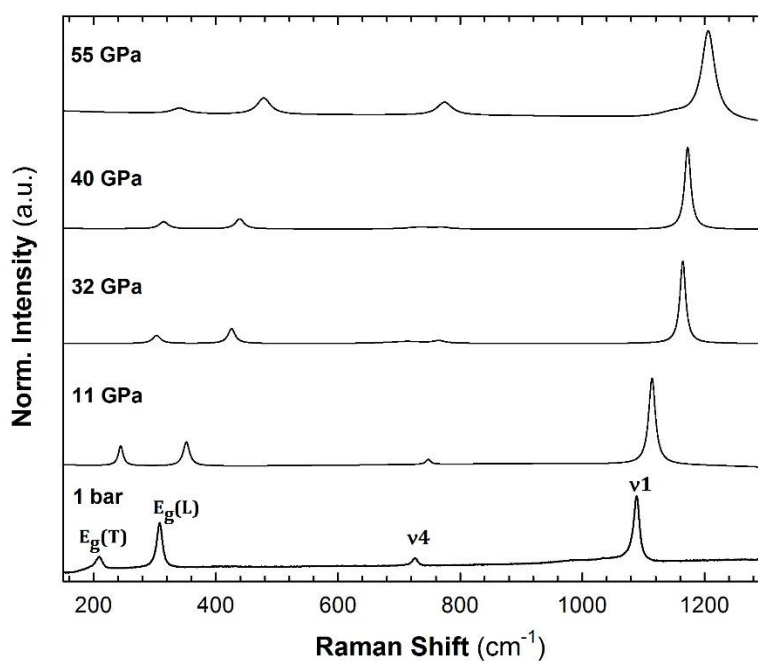
Figure 2. Raman spectra of CoCO$_3$ collected at ambient conditions and at successively higher pressures. Note the broad shape of the v4 mode above 32 GPa.

Spectra collected of a crystal in one DAC during compression and decompression and during compression of a crystal in a second DAC confirm the reproducibility of the collected data. All Raman modes become less intense and broader with increasing pressure as expected, but they still remain resolvable up to 55 GPa. The frequencies of the four Raman bands progressively shift to higher values with increasing pressure (Fig. 2, 3). No splitting of the Raman peaks or new peaks appear. However, above 34 GPa there is a ~12 cm^{-1} red shift of the v4 mode (Fig. 3a) and a further change of the slope with pressure

of the v1 mode (Fig. 3b). Meanwhile, the v4 peak appears broader and less symmetric above 34 GPa (Fig. 2). Keeping in mind that v4 is a degenerate mode, we discuss this interesting feature below, taking into account our XRD results.
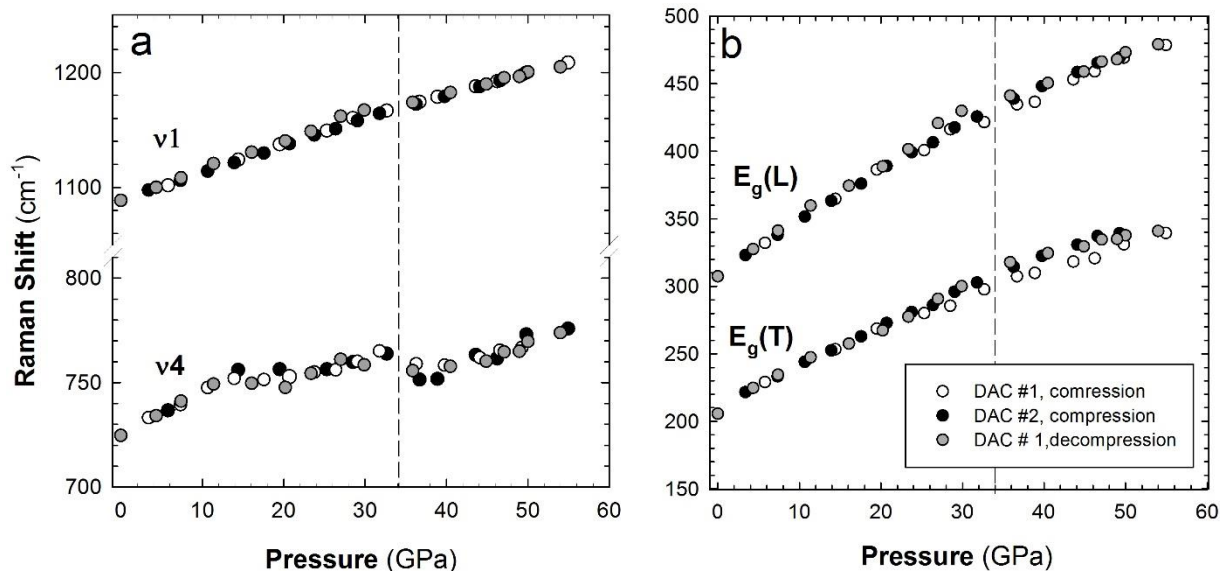

Figure 3. Pressure dependence of the frequency shifts for two experiments, DAC #1 during compression (white circles) and decompression (grey circles) and DAC #2 during compression (black circles), of: **a)** v1 and v4 Raman modes **b)** Eg(T) and Eg(L) Raman modes. The error bars are smaller than the size of the symbols.

Finally, we observed that above ~20 GPa our CoCO$_3$ crystals gradually displayed a color change from intense rose-red to light greenish. At ambient conditions, spherocobaltite has a characteristic intense magenta color attributed to the occupation of Co^{2+} of an octahedral site. Often a color change upon compression is an indication of spin crossover of the respective transition metal cation accompanied by changes in the structural environment, for example for Fe^{2+} in siderite (Lavina et al. 2009). Meanwhile, it has been shown that Raman spectroscopy can detect the occurrence of a spin transition (Cerantola et al. 2015). However, our Raman spectroscopy data do not show any obvious sign of spin crossover up to at least 55 GPa. Thus, we attribute this color change to pressure effects, such as bond shortening and simultaneous increase of the crystal field splitting energy (Δ), which causes a blue shift of the absorption bands (Burns 1993; Taran et al. 2008).

## 5.3.2. X-ray diffraction on compression at ambient temperature

The lattice parameters of the synthetic CoCO$_3$ crystals at ambient conditions are a=4.6582(3) Å, c=14.9655(9) Å, V = 281.23(4) Å^3 and Z=6. These values are in good agreement with a previous report

(Pertlik 1986). With increasing pressure the a- and c-axes gradually decrease (Fig. 4). Up to 54 GPa the a-axis shrinks by ~ 4.7 %, while the c-axis shrinks by ~14.1 %. Similarly, the c/a ratio reduces by about 9.95 % (Fig. 5). As expected for all carbonates with the calcite structure (Zhang and Reeder 1999), the c-axis is nearly three times more compressible than the a-axis, which is due to the planar arrangement of the CO_3 groups parallel to the a-axis. The pressure variation of the volume per formula unit (V/Z) shows the monotonic behavior of $CoCO_3$ up to 54 GPa (Fig. 4). An f-F plot indicates that a 3rd order Birch Murnaghan equation of state is necessary to fit the P-V data of $CoCO_3$. The fitting procedure using EosFit7 GUI software (Angel et al. 2014; Gonzalez-Platas et al. 2016) gave K_0=128(2) GPa, K'=4.28(17), and V_0=281.23(4) Å^3 (Fig. 6).
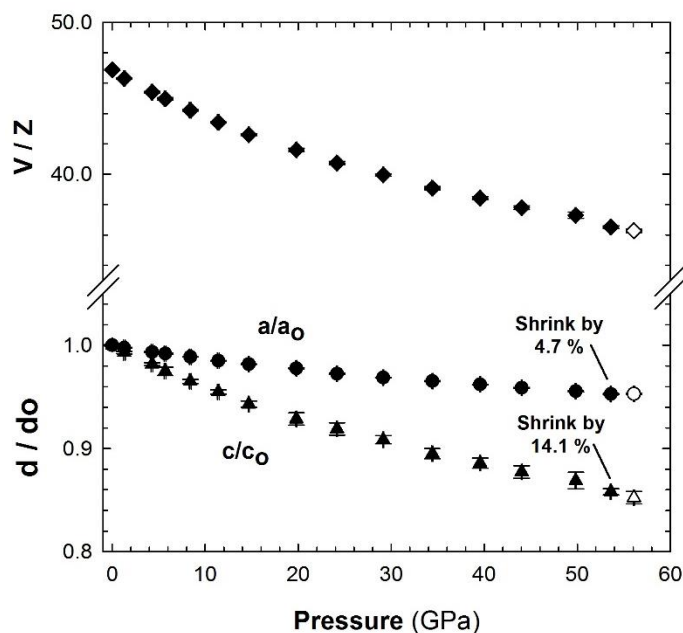
Figure 4. Relative axial compressibilities of a/ao (circles) and c/co (triangles) of $CoCO_3$ (lower part of the plot) and volume per formula unit (V/Z) (diamonds) (upper part of the plot) against pressure. Open symbols are data derived from the temperature quenched sample. Error bars are shown and in some cases are smaller than the size of the symbols.

The bond lengths and angles were determined for each pressure point. The evolution of the carbon-oxygen (C-O) and the cobalt-oxygen (Co-O) bond lengths upon compression is shown in Figure 7. The Co-O bonds are continually shrinking by ~8.6 % up to 54 GPa, while the C-O bonds are only slightly shrinking by ~2.8 %, implying that the CO_3 units are harder to compress. In fact, this observation is characteristic for all carbonate minerals (Zhang and Reeder 1999). There are no any obvious deviations of
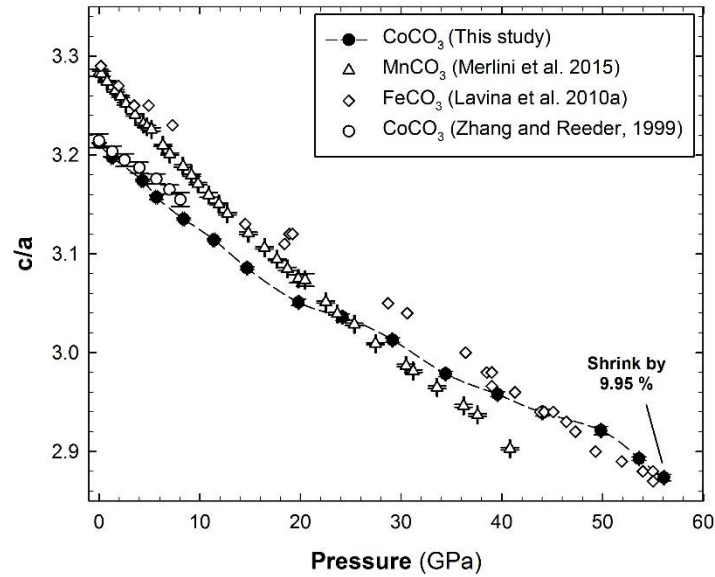
Figure 5. Comparison of the evolution of the c/a ratio on compression for $CoCO_3$ in the present study (solid circles), $CoCO_3$ in Zhang and Reeder (1999) (open circles), $MnCO_3$ (open triangles) (Merlini et al. 2015) and $FeCO_3$ (open diamonds) (Lavina et al. 2010a). The error bars fall within the size of the symbols.
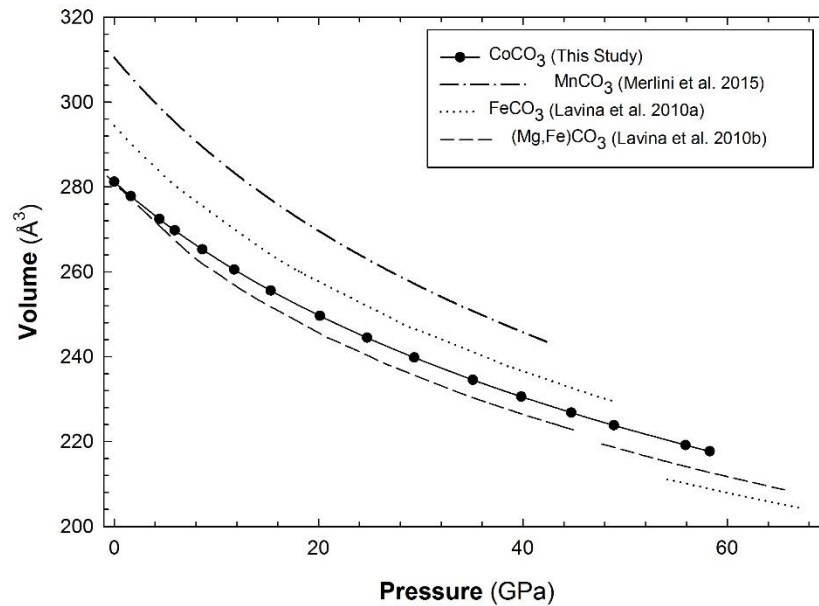
Figure 6. Equation of state (EoS) of $CoCO_3$ (solid line with black circles) compared to the EoS of some calcite-type carbonates, namely $MnCO_3$ (dash-dot line) (Merlini et al. 2015), $FeCO_3$ (dotted line) (Lavina et al. 2010a) and (Mg, Fe)CO_3 (dashed line) (Lavina et al. 2010).

C-O compressibility from a linear relation in the entire studied pressure range (Fig. 7). We recall that the v4 Raman mode is sensitive to changes of the O-O bond lengths in the CO_3 group in such a way that an abrupt decrease of the latter will induce a red shift of the respective mode in the Raman spectrum (Lavina
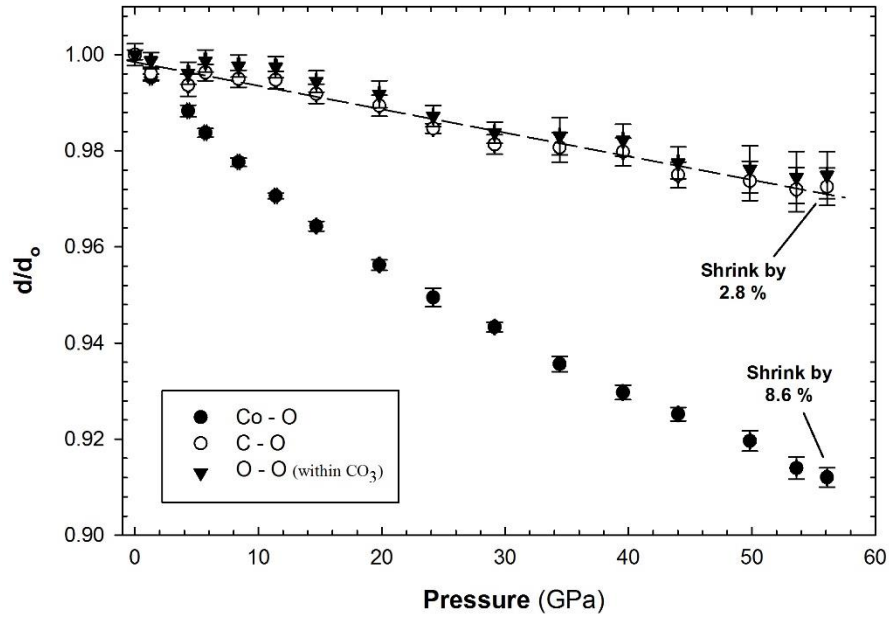
Figure 7. Variation of C-O (open circles), Co-O (solid circles) and O-O (inverse pyramids) bond lengths for CoCO$_3$ with increasing pressure. Note that the O-O bond lengths shown here are within the CO$_3$ unit. The dashed line is a linear fit of the C-O bond lengths. All bond lengths are normalized to unity.
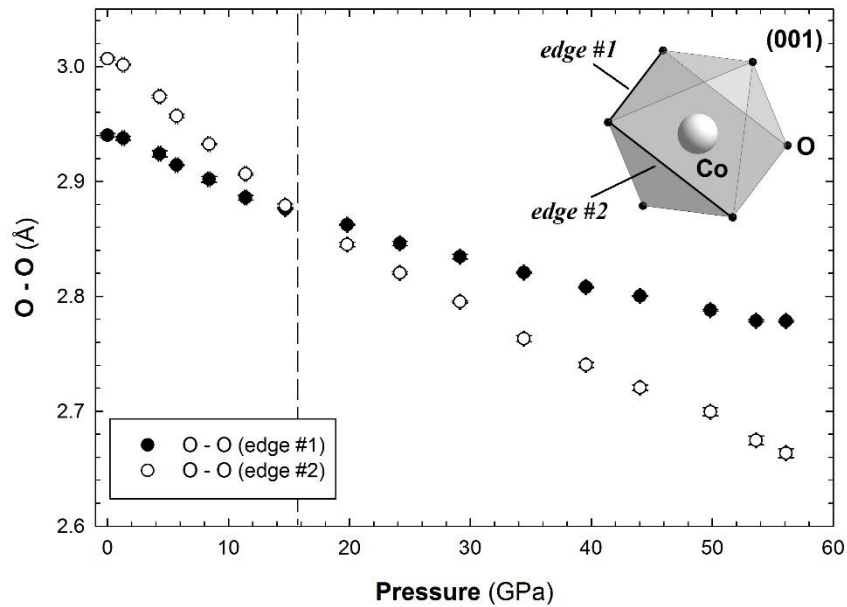
Figure 8. Evolution with pressure of the O-O bond lengths that represent the two octahedra edges, edge #1 (solid circles) and edge #2 (open circles), shown in the depicted schematic representation of the CoO$_6$ octahedron. The viewing direction of the octahedron is towards the (001) plane. The error bars are smaller than the size of the symbols.

et al. 2010a; Cerantola et al. 2015). The absence of any peculiarities in the compressional behavior of O-O contact as implied from single crystal XRD data (Fig. 7) suggest that irregularities in appearance and the
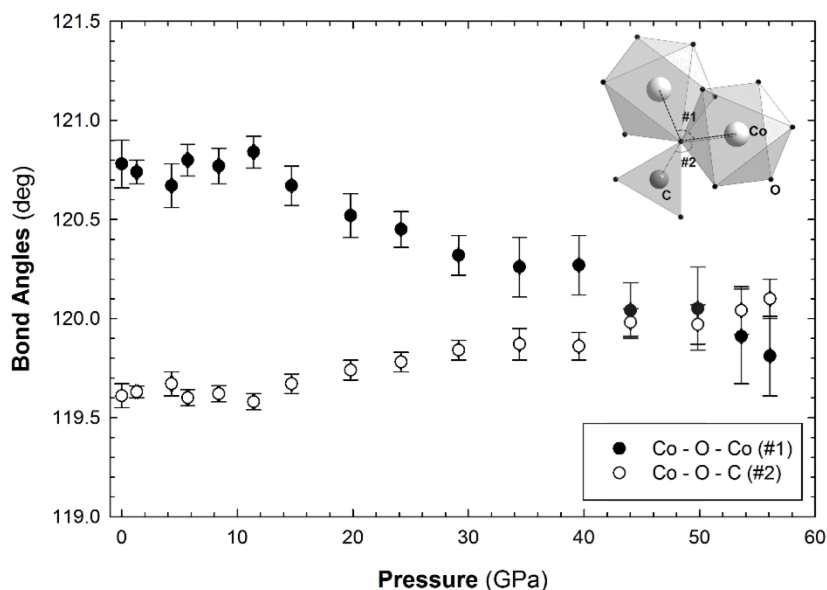
Figure 9. Effect of pressure on the bond angles Co-O-Co (solid circles) and Co-O-C (open circles), indicated as 1 and 2, respectively, in the structure model on the right.

pressure dependence of the v4 mode (Fig. 3a) may be an experimental artefact due to non-hydrostatic stress in the particular sample. Indeed, the behavior of v4 mode is not well reproducible and peculiarities above 34 GPa were observed only on one crystal (black circles in Fig. 3a). More experiments are needed to clarify this issue.

Our XRD results suggest that CoO_6 octahedra are irregular, but not as distorted as octahedra in other calcite-type carbonates at ambient conditions. This finding is in agreement with a previous report, which states that $CoCO_3$ has the least distorted octahedra among all calcite-type carbonates (Effenberger et al. 1981). The two O-O edges of the CoO_6 octahedron are plotted as a function of pressure (Fig. 8). The two bond lengths decrease steadily, but with different rates. At ~16 GPa the two edges as well as the two internal angles of the octahedron become equal, indicating the formation of regular CoO_6 octahedra at this pressure. In addition, the oxygen atomic coordinate (O_x) (Table 1) slightly increases with pressure, which is a result of the uneven evolution of the rigid CO_3 units and the compressible CoO_6 octahedra.

Figure 9 displays the evolution of the cobalt-oxygen-cobalt (Co-O-Co) and the cobalt-oxygen-carbon (Co-O-C) bond angles, which progressively decrease and increase, respectively. However, between 42-50 GPa they are both equal to 120°. This observation suggests that in this pressure range the structure of $CoCO_3$ is "more regular", but there are no indications that this affects the symmetry of the structure as a whole.

5.3.3. X-ray diffraction after laser heating

At about 56 GPa, we heated one of $CoCO_3$ crystals at 1200 K using a laser and subsequently collected an XRD pattern of the temperature-quenched sample. Analysis of the data collected revealed that all diffraction peaks could still be indexed in the rhombohedral $R\bar{3}c$ space group, and thus no structural or chemical transformation occurred in $CoCO_3$ at these conditions (Table 1). A second crystal of $CoCO_3$ crystals was heated in the same DAC at 57 GPa to temperatures of 2000 to 2200 K. The products of the heating were polycrystalline so only a wide scan image was collected and Rietveld analysis using GSAS software was implemented. We found that after about 1 min of heating, $CoCO_3$ partially decomposes to form CoO and presumably CO_2 (Fig. 10). The diffraction peaks of CoO can be indexed in the $Fm\bar{3}m$ space group with a = 3.9708(2) Å and is assigned to the NaCl (B1) structural type.
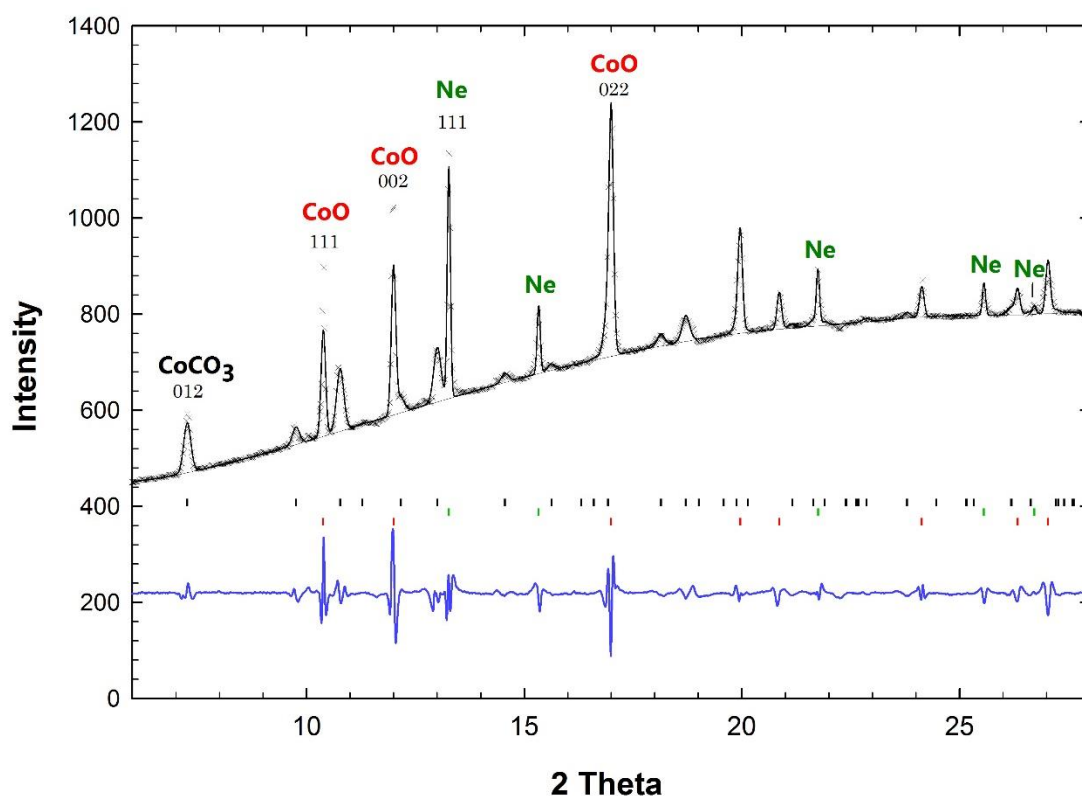
Figure 10. XRD pattern obtained after heating $CoCO_3$ at 2000 K at 57 GPa. Three phases are identified: solid neon, high-pressure $CoCO_3$ and its thermally decomposed product, CoO. Rietveld analysis was performed using the GSAS software package.

5.4. Discussion

The bulk modulus of $CoCO_3$ determined in the present study (K_0=128(2) GPa) is in good agreement with the value reported by Zhang and Reeder (1999) (i.e., K_0=125(1) GPa). $CoCO_3$ is hence slightly less compressible than $FeCO_3$ and $MnCO_3$, where the bulk moduli are 110(2) GPa (Lavina et al. 2010a) and 106.9(11) (Merlini et al. 2015), respectively. The evolution of the carbon-oxygen (C-O) bond lengths with increasing pressure suggests that the CO_3 units in $CoCO_3$ remain nearly rigid (Fig. 7), similar to other calcite-type carbonates (Zhang and Reeder 1999). In addition, our findings indicate that at about 16 GPa the CoO_6 octahedra become regular. This behavior has been reported before in the case of $FeCO_3$ at 23 GPa (Lavina et al. 2010a) and at 15 GPa for $MnCO_3$ (Merlini et al. 2015).

The equations of state of some calcite-type carbonates (Zhang and Reeder 1999; Lavina et al. 2010; Lavina et al. 2010a; Merlini et al. 2015) are plotted together with the EoS of $CoCO_3$ presented in this study (Fig. 6). Rhodochrosite and siderite with Fe^{2+} in its high spin state (i.e., HS-$FeCO_3$) have higher volumes than that of $CoCO_3$. This is an expected pattern, since Co^{2+} has a smaller ionic radius than Mn^{2+} and HS-Fe^{2+}. On the other hand, the volumes of LS-$FeCO_3$ as well as 12 % Fe-doped magnesite in both high and low spin states (i.e., HS or LS-$(Fe,Mg)CO_3$) are smaller than those of $CoCO_3$ (Fig. 6). By summarizing such observations we suggest that with decreasing cation radius the respective carbonate mineral becomes less compressible, forms less distorted octahedra, and is stable in the calcite-type structure over a wider pressure range.

5.5. Implications and concluding remarks

We conducted the first study of spherocobaltite's properties and its crystal structure as a function of pressure above 55 GPa. Our results suggest that $CoCO_3$ maintains the calcite-type structure up to 56 GPa and 1200 K. At lower mantle temperatures, however, it decomposes, forming cobalt oxide, CoO. The regular behavior of spherocobaltite upon compression at ambient temperature is different to the behavior of siderite and rhodochrosite. Owing to the smaller ionic radius of Co^{2+} (0.745 Å) compared to Fe^{2+} (0.78 Å) and Mn^{2+} (0.83 Å) (Shannon and Prewitt 1969), the behavior of $CoCO_3$ is more similar to that of magnesite, which maintains the $R\bar{3}c$ crystal structure up to 115 GPa and 2000-3000 K (Isshiki et al. 2004). More concretely, $CoCO_3$ does not undergo a structural transformation like $MnCO_3$ at about 43 GPa (Merlini et al. 2015). Unlike siderite (Cerantola et al. 2015), Raman spectra and XRD patterns of spherocobaltite, do not give any indication of spin crossover up to 56 GPa.

Until now, our findings on spherocobaltite is one the few examples of single-crystal diffraction studies of rhombohedral carbonate minerals above 15 GPa, and only the second case when compression

above 50 GPa does not lead to a phase transition, first being magnesite. Given $CoCO_3$ high pressure behavior, we may now imply that carbonates can be stable in the calcite-type structure over a wide pressure range that corresponds to <1400 km depth within the Earth, if the incorporated metal's radius is equal or lower than that of Co^{2+} (i.e. 0.745 Å). Such important conclusions are only possible to derive through the systematic studies of the whole row of the individual minerals that represent the carbonate class.

Studies on other transition metal carbonates are needed as they will be considered complementary to spherocobaltite's results. Carbonates such as gaspeite ($NiCO_3$) and smithsonite ($ZnCO_3$) are highly relevant to spherocobaltite due to the similar ionic radii of the metals incorporated. More concretely, both Ni^{2+} (0.69 Å) and Zn^{2+} (0.74 Å) have ionic radii smaller than that of Co^{2+} (0.745 Å) and much closer to Mg^{2+} (0.72 Å) (Shannon and Prewitt 1969) in magnesite. Although additional experiments are required, it is now clear that the discovery of crystal-chemical regularities in the behavior of carbonates at high pressure and high temperature conditions is one demonstration of how mineral physics can help to understand the nature of carbon-related geological processes inside the Earth.

Keywords

Spherocobaltite, $CoCO_3$, high pressure, X-ray diffraction, Raman spectroscopy, transition metal carbonates

5.6. Acknowledgements

5.7. References

Angel JR, Alvaro M, Gonzalez-Platas J (2014) EosFit7c and a Fortran module (library) for equation of state calculations. Z Kristallogr - Cryst Mat 229:405–419

Agilent (2014) CrysAlis PRO. Agilent Technologies Ltd, Yarnton, Oxfordshire, England

Barton I, Yang H, Barton M (2014) The mineralogy, geochemistry and metallurgy of cobalt in the rhombohedral carbonates. Can Mineral 0:1-17

Boulard E, Gloter A, Corgne A, Antonangeli D, Auzende AL, Perrillat JP, Guyot F, Fiquet G (2011) New host for carbon in deep Earth. PNAS 108:5184-5187

Boulard E, Pan D, Galli G, Liu Z, Mao W (2014) Tetrahedrally coordinated carbonates in Earth's lower mantle. Nat Commun. doi:10.1038/ncomms7311

Boulard E, Goncharov AF, Blanchard M, Mao WL (2015) Pressure-induced phase transition in MnCO3 and its implications on the deep carbon cycle. J Geophys Res Solid Earth. doi: 10.1002/2015JB011901

Bridgman PW (1939) The high pressure behavior of miscellaneous minerals. Am J Sci 237:7–18

Burns RG (1993) Mineralogical Applications of Crystal Field Theory, Cambridge University Press, Cambridge

Carr MH, Turekian KK (1960) The geochemistry of cobalt. Geochim Cosmochim Acta 23:9-60

Cerantola V, McCammon C, Kupenko I, Kantor I, Marini C, Wilke M, Ismailova L, Solopova N, Chumakov AI, Pascarelli S, Dubrovinsky L (2015) High-pressure spectroscopic study of siderite (FeCO3) with focus on spin crossover. Am Mineral, 100:2670-2681

Effenberger H, Mereiter K, Zemann J (1981) Crystal structure refinements of magnesite, calcite, rhodochrosite, siderite, smithsonite and dolomite, with discussion of some aspects of the stereochemistry of calcite type carbonates. Z Kristallogr 156:233-243

Farfan GA, Boulard E, Wang S, Mao WL (2013) Bonding and electronic changes in rhodochrosite at high pressure. Am Mineral 98:1817-1823

Farrugia LJ (2012) WinGX and ORTEP for Windows: an update. J Appl Crystallogr 45:849-854

Fei Y, Ricolleau A, Frank M, Mibe K, Shen G, Prakapenka V (2007) Toward an internally consistent pressure scale. PNAS 104:9182–9186

Fiquet G, Guyot F, Itie JP (1994) High-pressure X-ray diffraction study of carbonates—MgCO3, CaMg(CO3)2, and CaCO3. Am Mineral 79:15–23

French BM (1971) Stability relations of siderite (FeCO3) in the system Fe-C-O. Am J Sci 27:37–78

Frost DJ, Poe BT, Tronnes RG, Liebske C, Duba A, Rubie DC (2004) A new large-volume multianvil system. Phys Earth Planet In 143-144:507–514

Goldsmith JR, Northrop DA.(1965) Subsolidus phase relations in the systems $CaCO_3$ – $MgCO_3$ – $CoCO_3$ and $CaCO_3$ – $MgCO_3$ – $NiCO_3$. J Geol 73:817-829

Gonzalez-Platas J, Alvaro M, Nestola F, Angel RJ (2016) EosFit7-GUI: A new GUI tool for equation of state calculations, analyses and teaching. J Appl Crystallogr 49:1377-1382

Isshiki M, Irifune T, Hirose K, Ono S, Ohishi Y, Watanuki T, Nishibori E, Takata M, Sakata M (2004) Stability of magnesite and its high-pressure form in the lowermost mantle. Nature 427:60-63

Jagoutz E, Palme H, Baddenhausen H, Blum K, Cendales M, Dreibus G, Spettel B, Lorenz V, Wänke H (1979) The abundances of major, minor and trace elements in the earth's mantle as derived from primitive ultramafic rocks. Proc Lunar Planet Sci Conf, 10:2031-2050

Kantor I, Prakapenka V, Kantor A, Dera P, Kurnosov A, Sinogeikin S, Dubrovinskaia N, Dubrovinsky L (2012) BX90: A new diamond anvil cell design for X-ray diffraction and optical measurements. Rev Sci Instrum. doi:10.1063/1.4768541

Katsura T, Tsuchida Y, Ito E, Yagi T, Utsumi W, Akimoto S (1991) Stability of magnesite under the lower mantle conditions. Proc Japan Acad Ser B 67:57-60

Kupenko I, Dubrovinsky L, Dubrovinskaia N, McCammon C, Glazyrin K, Bykova E, Boffa-Ballaran T, Sinmyo R, Chumakov A, Potapkin V, Kantor A, Rüffer R, Hanfland M, Crichton W, Merlini M (2012): Portable double-sided laser-heating system for Mössbauer spectroscopy and X-ray diffraction experiments at synchrotron facilities with diamond anvil cells. Rev Sci Instrum. doi:10.1063/1.4772458

Kurnosov A, Kantor I, Boffa-Ballaran T, Lindhardt S, Dubrovisnky L, Kuznetsov A, Zehnder BH (2008) A novel gas-loading system for mechanically closing of various types of diamond anvil cells. Rev Sci Instrum. doi:10.1063/1.2902506

Larson AC, von Dreele RB (1985) General Structure Analysis System (GSAS). Los Alamos National Laboratory Report, LAUR B6-748

Lavina B, Dera P, Downs RT, Prakapenka V, Rivers M, Sutton S, Nicol M (2009) Siderite at lower mantle conditions and the effects of the pressure-induced spin-pairing transition. GRL. doi:10.1029/2009GL039652

Lavina B, Dera P, Downs RT, Tschauner O, Yang W, Shebanova O, Shen G (2010) Effect of dilution on the spin pairing transition in rhombohedral carbonates. High Pressure Res 30:224-229

Lavina B, Dera, P, Downs RT, Yang W, Sinogeikin S, Meng Y, Shenand G, Schiferl D (2010a) Structure of siderite FeCO3 to 56 GPa and hysteresis of its spin-pairing transition. Phys Rev B. doi:10.1103/PhysRevB.82.064110

Mao HK, Xu J, Bell PM (1986) Calibration of the ruby pressure Gauge to 800 kbar under quasi-hydrostatic conditions. J Geophys Res 91:4673-7676

Mao Z, Armentrout M, Rainey E, Manning CE, Dera P, Prakapenka VB, Kavner A (2011) Dolomite III: A new candidate lower mantle carbonate. GRL. doi:10.1029/2011GL049519

Mattila A, Rylkkänen T, Rueff JP, Huotari S, Vankó G, Hanfland M, Lehtinen M, Hämäläinen K (2007) Pressure induced magnetic transition in siderite FeCO3 studied by X-ray emission spectroscopy. J Phys: Condens Matter. doi:10.1088/0953-8984/19/38/386206

Merlini M, Crichton WA, Hanfland M, Gemmi M, Müller H, Kupenko I, Dubrovinsky L (2012) Structures of dolomite at ultrahigh pressure and their influence on the deep carbon cycle. PNAS 109:13509-13514

Merlini M, Hanfland M, Crichton WA (2012a) CaCO3-III and CaCO3-VI, high-pressure polymorphs of calcite: possible host structures for carbon in the Earth's mantle. EPSL 333-334:265-271

Merlini M, Hanfland M, Gemmi M (2015) The MnCO3-II high-pressure polymorph of rhodochrosite. Am Mineral 100:2625-2629

Ono S (2007) High-pressure phase transformation in MnCO3: a synchrotron XRD study. Mineral Mag 71:105-111

Pertlik F (1986) Structures of hydrothermally synthesized cobalt (II) carbonate and nickel (II) carbonate. Acta Cryst C 42:4-5

Reeder RJ (1983) Crystal chemistry of the rhombohedral carbonates. Rev Mineral 11:1-47

Rutt HN, Nicola JH (1974) Raman spectra of carbonates of calcite type. J Phys C: Solid State Phys 7:4522-4528

Santillán J, Williams Q (2004) A high-pressure and X-ray study of FeCO3 and MnCO3: comparison with CaMg(CO3)2 – dolomite. Phys Earth Planet In 143-144:291-304

Shannon RD, Prewitt CT (1969) Effective ionic radii in oxides and fluorides. Acta Cryst B 25:925

Sheldrick GM (2008) A short history of SHELX. Acta Cryst A 64:112-122

Shi W, Fleet M, Shieh SR (2012) High-pressure phase transitions in Ca-Mn carbonates (Ca,Mn)CO$_3$ studied by Raman spectroscopy. Am Mineral 97:999-1001

Suito K, Namba J, Horikawa T, Taniguchi Y, Sakurai N, Kobayashi M, Onodera A, Shimomura O, Kikegawa T (2001) Phase relations of CaCO3 at high pressure and high temperature. Am Mineral 86:997-1002

Taran MN, Langer K, Koch-Mueller M (2008) Pressure dependence of color of natural uvarovite: The barochromic effect. Phys Chem Miner 35:175–177

Turekian KK, Wedepohl KH (1961) Distribution of the elements in some major units of the earth's crust. Geol Soc Am Bull 72:175-182

Vizgirda J, Ahrens TJ (1982) Shock compression of aragonite and implications for the equation of states of carbonates. J Geophys Res 87:4747-4758

Veizer J (1983) Trace elements and isotopes in sedimentary carbonates. Rev Mineral 11:265-299

Zhang J, Reeder RJ (1999) Comparative compressibilities of calcite-structure carbonates: Deviations from empirical relations. Am Mineral 84:861-870

Chapter 6

Insights in the crystal chemistry of transition metal (Mn, Co, Ni, Zn) carbonates and their oxides at extreme conditions

Stella Chariton,*[a] Elena Bykova,[b] Maxim Bykov,[a] Georgios Aprilis,[c] Egor Koemets,[a] Timofey Fedotenko,[c] Michael Hanfland,[d] Catherine McCammon,[a] and Leonid Dubrovinsky[a]

[a] Bayerisches Geoinstitut, Universität Bayreuth, Universitätsstrasse 30, 95447 Bayreuth (Germany)

[b] Deutsches Elektronen-Synchrotron (DESY), Notkestraße 85, 22607 Hamburg, (Germany)

[c] Department of Crystallography, Universität Bayreuth, Universitätsstrasse 30, 95447 Bayreuth (Germany)

[d] European Synchrotron Radiation Facility (ESRF) CS40220 Cedex 9, 38043 Grenoble (France)

Corresponding Author's email: stellachariton@hotmail.com
ORCID iD: 0000-0001-5522-0498
Tel: +49 (0)921 55 3878

(for submission to Angewandte Chemie: International Edition)

ABSTRACT

Carbonates exhibit very distinct behaviors at high pressures and temperatures. Here we explore the effect of cationic-type (Mn^{2+}, Co^{2+}, Ni^{2+}, Zn^{2+}) on the stability fields of the calcite-type ($R\overline{3}c$) carbonates at extreme conditions to expose crystallochemical regularities. Single-crystal X-ray diffraction experiments in laser-heated diamond anvil cells reveal new high-pressure carbonate polymorphs and accompanying metal oxides. Among the four studied compositions, only MnCO$_3$ undergoes several structural transformations above 44 GPa, while at higher pressures and temperatures it displays complex chemistry with formation of CO$_4$ polymerizable units (MnC_2O_5, $Mn_4C_4O_{13}$). Various Mn-oxides (Mn_3O_4, Mn_5O_7, $pv - Mn_2O_3$, $\delta - Mn_2O_3$) coexist with the new carbonate polymorphs. Despite the simpler high-pressure behavior of NiCO$_3$, ZnCO$_3$ and CoCO$_3$ compared to MnCO$_3$, they too present interesting thermal decomposition products (NiO, CoO, Co$_4$O$_5$, ZnCO$_3$-II). Our study demonstrates the complex character that some transition-metals have as oppose to others.

6.1. Main text

Carbonate salts are extremely variant, forming compounds with over 20 alkali, alkali earth or transition metals. The most abundant carbonates found in nature belong in the $CaCO_3$-$MgCO_3$-$FeCO_3$ (calcite-type structure, $R\overline{3}c$) system and they are suspected as the major players of the deep carbon cycle inside the Earth [1]. In addition, carbonates are known to act as solvent-catalysts in the formation of diamond, which has both broad industrial implications and may explain the genesis of natural diamonds [2, 3]. Thus, many studies have been dedicated in the high-pressure and high-temperature behaviour of carbonates demonstrating their structural variability; from carbonates, such as $MgCO_3$, with remarkable phase stability up to 115 GPa and 2100 K [4], to carbonates, such as $CaCO_3$, which undergoes several phase transitions starting at ~2 GPa [5]. The size of the metal-cation incorporated affects strongly the stability field, compressibility and other physical properties of the respective carbonate. The ionic radii of divalent 3d transition metals in octahedral coordination lay between those of Ca^{2+} (1.00 Å) and Mg^{2+} (0.72 Å) [6], thus making transition metal carbonates, such as (Mn^{2+}, Fe^{2+}, Co^{2+}, Ni^{2+}, Zn^{2+})CO_3 ideal study cases to reveal crystallochemical regularities. Furthermore, recent discoveries of novel compounds that consist of tetrahedral CO_4^{-4} units instead of the conventional trigonal CO_3^{-2} groups, suggest that the high-pressure chemistry of carbonates can be far more diverse that we have previously anticipated [7-9]. The new high-pressure carbonate polymorphs are often accompanied by a series of metal-oxides as a result of redox reactions and often diamond formation at extreme conditions [9]. To date, there is an extensive research on $FeCO_3$ behaviour [e.g. 9-11]. However, only few are known for $MnCO_3$ [e.g. 12, 13] and even less for $ZnCO_3$ [14, 15], $CoCO_3$ [16] and $NiCO_3$ [17]. Special is the case of $MnCO_3$, where the existing literature has presented very contradictory results that hinder our understanding of the carbonate or the precise type of manganites that coexist. Here, we employ the synchrotron-based single-crystal X-ray diffraction (SCXRD) method in laser-heated diamond anvil cells (DACs) to describe the complex crystal chemistry of synthetic $MnCO_3$, $CoCO_3$, $NiCO_3$ and $ZnCO_3$ by means of accurate structure solutions and refinements.

Previous powder XRD experiments (PXRD) on natural $ZnCO_3$ suggest that it is stable in the calcite-type structure up to ~50 GPa [14]. *Ab initio* calculations predicted that $ZnCO_3$ will undergo two phase transitions at 78 GPa ($C2/m$) and at 121 GPa ($P2_12_12_1$) [15]. However, our SCXRD experiments show that $ZnCO_3$ remains stable in the $R\overline{3}c$ structure (Figure 2a) at least up to ~102 GPa. The cold compressional behavior of $ZnCO_3$ is very similar to this of $MgCO_3$ [4]. At ambient conditions, the two cations, Zn^{2+} (0.74 Å) and Mg^{2+} (0.72 Å), have very similar ionic radius [6]. Fitting a 3rd order Birch-Murnaghan equation of state (BM EoS) to our data results in V_0= 281.74(3) Å^3, K_0=114(2) GPa and K''=4.6(2) (Figure 1). The bulk modulus value disagrees with previous reported values by Ref. [14] (K_0=126.8(6) GPa), where a 2nd order

BM EoS was fitted. If we fitted a 2nd order BM EoS in our data we would have resulted with K_0=124(1) GPa, as well. However, the fitting is poor, and the F-f plot suggests the necessity for a higher order of EoS. Despite the great stability of $ZnCO_3$ in the calcite-type structure upon cold compression, heating at 2500 K and 57.0 GPa and at 2800 K and 68.8 GPa resulted in a structural transformation to $ZnCO_3$-II (Figure 2d). The novel polymorph crystallizes in the $C2$ space group, with Z=2 (Table S1). The volume difference between $ZnCO_3$ and $ZnCO_3$-II at 57 GPa is nearly zero. $ZnCO_3$-II persists upon decompression to at least 35 GPa before its back-transformation to $ZnCO_3$. We did not observe formation of accompanying Zn-oxides.
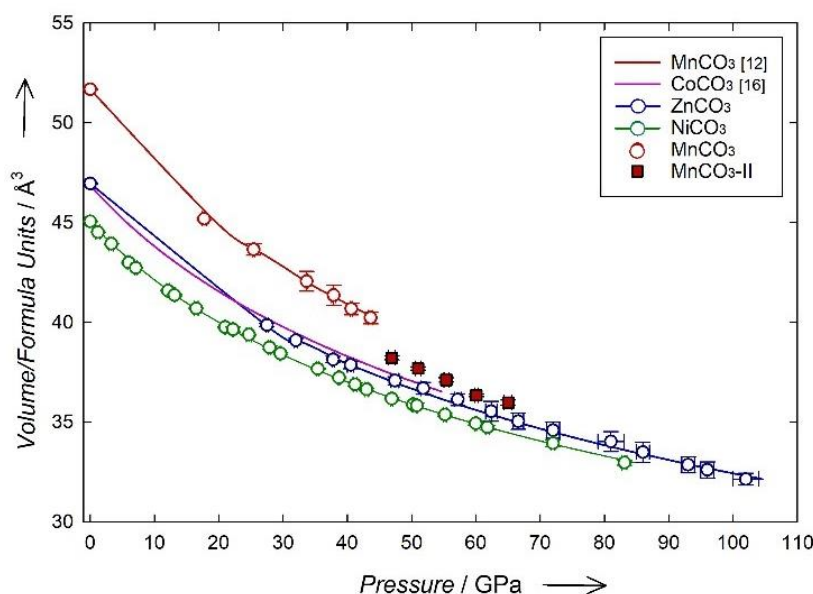
Figure 1. Equations of state of single crystals $MnCO_3$, $NiCO_3$, $ZnCO_3$ and $CoCO_3$ [16]. Note the 5% volume reduction of $MnCO3$ when it transforms to $MnCO_3$-II above 44 GPa.

To date, there is only one compressibility study of powder $NiCO_3$ proposing stability of the phase in the $R\bar{3}c$ structure up to ~8 GPa [17]. Here, we have considerably extent the investigated pressure range. Our SCXRD experiments suggest that $NiCO_3$ remains stable in the calcite-type structure up to at least 83 GPa (Figure 1). At ambient conditions, Ni^{2+} has smaller ionic radius (0.69 Å) than Mg^{2+} and the smallest radius of all divalent six-coordinated 3d transition metals, except Fe^{2+} in low-spin state [6]. Therefore, it is not surprising that $NiCO_3$ behavior upon cold compression is similar to $MgCO_3$ and $ZnCO_3$. However, the smaller size of the Ni cation makes $NiCO_3$ less compressible than $ZnCO_3$. Fitting a 3rd order BM EoS to our $NiCO_3$ data results in V_0= 270.34(2) Å^3, K_0=125(1) GPa and K''=4.9(1) (Figure 1). These values come in relatively good agreement previously reported [17]. Heating of $NiCO_3$ at 2100 K and 2200 K at 59.8 GPa and 83.2 GPa, respectively, result in partial decomposition of $NiCO_3$ and formation of NiO (Figure 3a). We
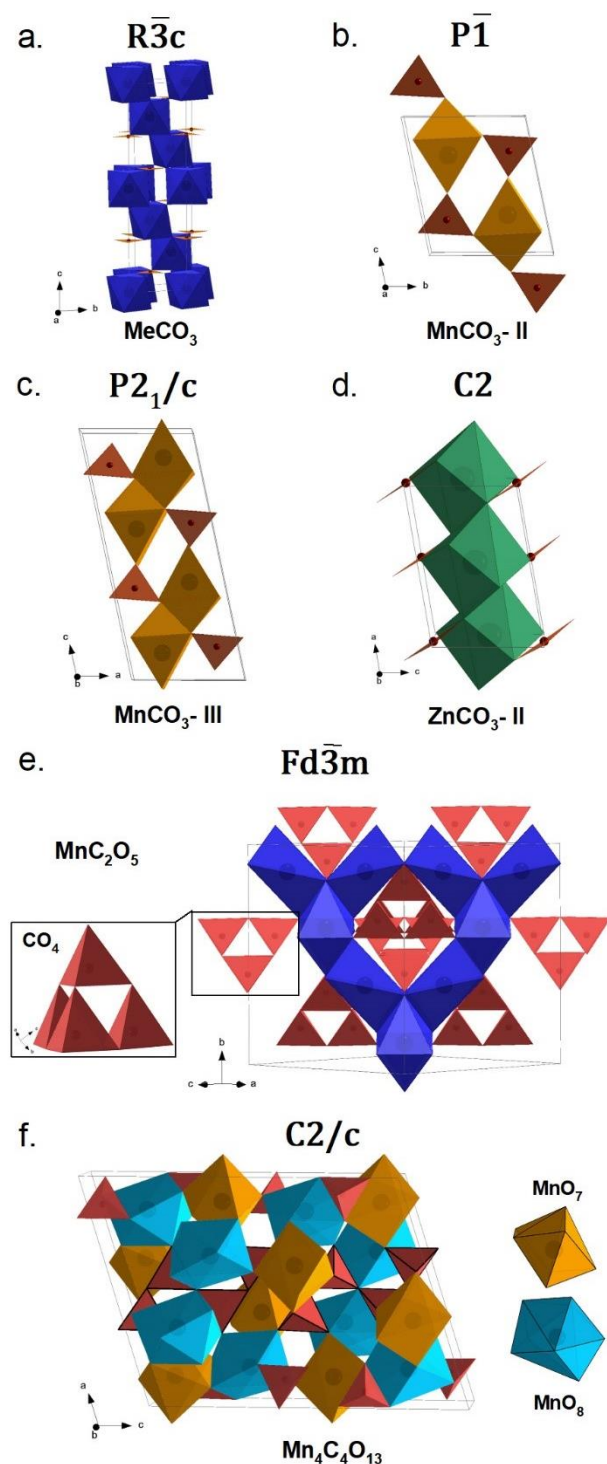
Figure 2. Crystal structures of various high-pressure metal (Me=Mn^{2+}, Co^{2+}, Ni^{2+}, Zn^{2+}) carbonate polymorphs. The calcite-type structure **a)** is built of distorted MeO$_6$ (dark blue) octahedra and CO$_3$ trigonal planar units (brown) in alternating layers. In MnCO$_3$-II **b)** MnO$_7$ monocapped prisms (orange) are connected in a 3D framework by CO$_3$ units (brown) still in planar configuration. MnCO$_3$-III **c)** is similar to MnCO$_3$-II only that the MnO$_7$ prisms (orange) now share edges. In ZnCO$_3$-II **d)** ZnO$_6$ corner-sharing trigonal prisms (green) alternate with parallel CO$_3$ units (brown). The diamond-like structure of MnC$_2$O$_5$ **e)** consists of heavily distorted MnO$_6$ edge-sharing octahedra (dark blue) surrounding the CO$_4$ corner-sharing tetrahedra (red) that build a pyramid. And in Mn$_4$C$_4$O$_{13}$ **f)** MnO$_8$ bicapped prisms (light blue) are connected in a 3D framework by dimers of edge-shared MnO$_7$ monocapped prisms (orange) and zigzag-shaped CO$_4$ tetrahedra (red) in chains.

can index the NiO phase either in the $Fm\bar{3}m$ space group or treat it as a distorted NaCl (B1) structure indexed in the $R\bar{3}m$ space group. Due to our limited data we are not qualified to favor one crystal system over the other (Figure S2). Such a project is beyond the scope of this study.

The compressibility curve of pure synthetic CoCO$_3$ has been previously obtained by means of SCXRD experiments [16]. Partial thermal decomposition of CoCO$_3$ to CoO ($Fm\bar{3}m$) was formerly noticed at 56 GPa and 2000 K [16]. We observed the same reaction after heating at 2200 K and 51.4 GPa. However, heating at moderate pressures, 31.5 GPa and 1900 K, resulted in the formation of Co$_4$O$_5$ ($Cmcm$, Z=4,

Figure 3b). Similar decomposition product (Fe$_4$O$_5$) was previously found after heating of FeCO$_3$ at 10 GPa, which persisted upon compression to at least 30 GPa [18]. We do not know whether Co$_4$O$_5$ is quenchable to ambient conditions, like Fe$_4$O$_5$, due to failure of diamonds that ended the experiment.
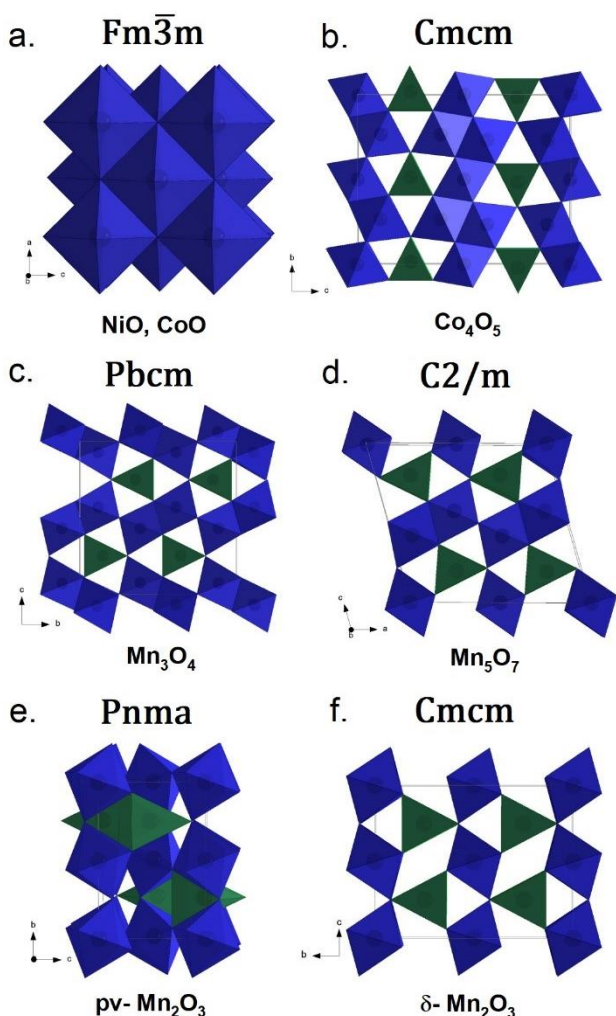
Figure 3. Crystal structures of various metal (Me=Mn^{2+}, Co^{2+}, Ni^{2+}) oxides that are a result of carbonate-decomposition reactions. The NaCl(B1)-type structure of CoO and NiO **a)** consists of MeO_6 octahedra (dark blue) with the maximum number of edge-shared neighbours. In Co_4O_5 **b)** columns of edge-sharing CoO_6 octahedra (dark blue) alternate with CoO_6 isolated trigonal prisms (green). Mn_3O_4 **c)** consists of MnO_6 edge-sharing octahedra dimers (dark blue) that are connected via corners and create voids, which are occupied by MnO_6 trigonal prisms (green). In Mn_5O_7 **d)**, MnO_6 trigonal prisms (green) are connected in a 3D framework by alternate edge-sharing MnO_6 octahedra dimers and monomers (dark blue). In pv-Mn_2O_3 **e)** MnO_6 octahedra (dark blue) connect through common vertices and MnO_6 trigonal prisms (green) share common edges. Note that the depicted MnO_6 prisms can be alternatively seen as heavily distorted MnO_8 cuboctahedra. And δ-Mn_2O_3 **f)** is built of alternating layers of corner-sharing MnO_6 octahedra (dark blue) and isolated MnO_6 trigonal prisms (green).

From our four studied compositions, $MnCO_3$ high-pressure and temperature behavior stands exceptional. $MnCO_3$ is stable in the $R\bar{3}c$ space group up to 44 GPa and 300 K. Our data were fitted in a 3rd order BM EoS (V_0= 310.06(2) Å^3, K_0=110(3) GPa and K''=3.8(2)) proposed by Ref. [12] (Figure 1). Above 44 GPa $MnCO_3$ transforms to $MnCO_3$-II (Figure 2b), which is isostructural to $CaCO_3$-VI [5]. The triclinic symmetry of $MnCO_3$-II ($P\bar{1}$, Z=2) gives rise to many new Raman modes above 44 GPa (Figure S5). Our findings are in excellent agreement with previous studies [12, 19]. The bigger size of Mn^{2+} (0.83 Å) compared to other 3d-metals [6] makes $MnCO_3$ high-pressure behavior more comparable to this of $CaCO_3$ than $MgCO_3$.

Several decomposition reactions have been proposed for $MnCO_3$ at high pressures and temperatures [13, 20] that invite analogies to $FeCO_3$ stability field [9]. However, all preceding results were obtained by means PXRD, and often reported inability to index certain reflections in the diffraction patterns. SCXRD has been previously proved a powerful tool to untangle complex mixtures of phases and to discover novel structures that PXRD experiments failed to identify [9, 21]. Thus, in the present SCXRD study, we were able to uncover the crystal structures of new $MnCO_3$ high-pressure polymorphs and Mn-oxides, which are products of redox reactions at

elevated pressures and temperatures (Figure 4). At 19.8 GPa and temperatures >1800 K MnCO$_3$ partially decomposes to form Mn$_3$O$_4$ ($Pbcm$, Z=4, Table S2, Figure 3c) and was recoverable at ambient conditions. At higher pressures (46.4 GPa) and after annealing at 2000 K, the MnCO$_3$ to MnCO$_3$-II transition is postponed, and MnCO$_3$ decomposes to a GdFeO$_3$-type Mn$_2$O$_3$ phase (perovskite pv-Mn$_2$O$_3$, $Pnma$, Z=4). Alternatively, pv-Mn$_2$O$_3$ can be indexed in the $Pbnm$ in (bca) setting. Note that the crystal structure of perovskite-like Mn$_2$O$_3$ (Figure 3e) was formerly described with the use of an F-centered supercell and was denoted the name ζ-Mn$_2$O$_3$ [22]. Additional experiments are needed to clarify whether pv-Mn$_2$O$_3$ is quenchable at ambient conditions. Heating at 62.4 GPa resulted in the formation of novel Mn$_5$O$_7$ ($C2/m$, Z=2). Interestingly, heating of FeCO$_3$ at the same pressure range results in the formation of Fe$_5$O$_7$ [9]. The mixed-valence manganese oxide (Figure 3d) is preserved on decompression down to at least ~36 GPa. Mn$_5$O$_7$ coexists with the new high-pressure polymorph of MnCO$_3$, the MnCO$_3$-III ($P2_1/c$, Z=2) (Figure 2c). During decompression, MnCO$_3$-III→MnCO$_3$-II transition occurs at ~56 GPa, while MnCO$_3$-II→MnCO$_3$ transition at ~35 GPa. Another phase that coexists with Mn$_5$O$_7$ and MnCO$_3$-III at 66 GPa and after annealing at 2000 K is MnC$_2$O$_5$ ($Fd\bar{3}m$, Z=16), which contains tetrahedrally coordinated CO$_4$ units (Figure 2e). The diamonoid structure was very difficult to crystallize except for one experiment (Figure 4). Few and weak single-crystal reflections were observed in repeated experiments, which confirm the reproducibility of the phase synthesis, but prohibit the structure solution with improved R factors (Table
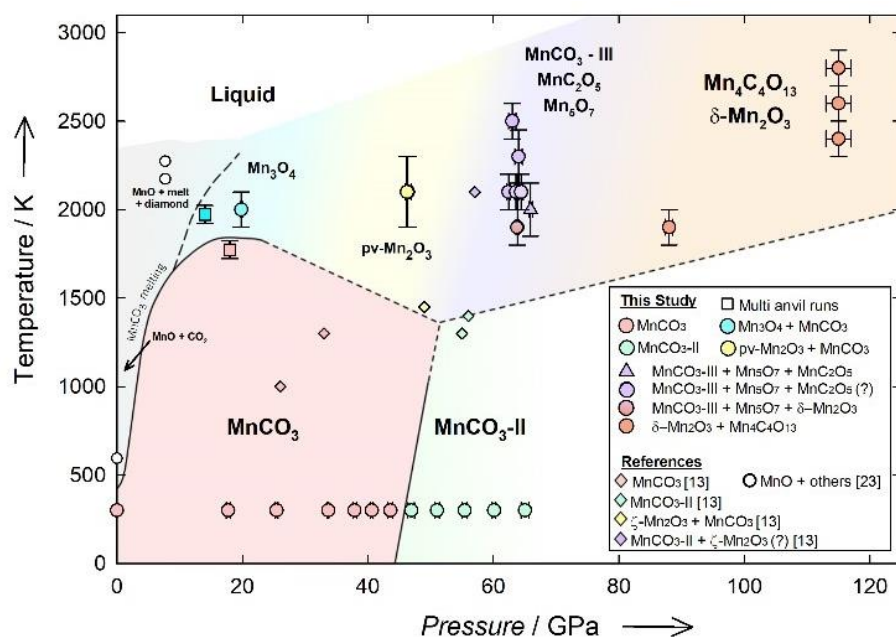
Figure 4. Stability diagram of MnCO3 at high pressures and temperatures. The various phase-assemblages are colour-coded and described in detail on the legend. See the Supporting Information for further discussion.

S2). A different tetracarbonate formed at 88 GPa and after heating at 1900 K, namely Mn₄C₄O₁₃ ($C2/c$, Z=4). The same structure and CO₄ tetrahedra arrangement (Figure 2f) were reported for Fe₄C₄O₁₃ after heating of FeCO₃ at 97 GPa [9]. The mixed-valence manganese carbonate ($Mn_2^{2+}Mn_2^{3+}C_4O_{13}$) coexists with a CaIrO₃-type ($Cmcm$, Z=4) phase ('post-perovskite' δ-Mn₂O₃, Figure 3f). The two phases persist after several heatings at 115 GPa (Figure 4) and remained stable upon compression to 130 GPa, before the diamond anvils failed.

Our study has demonstrated the complexity of MnCO₃ at high pressures and temperatures, which can only be compared to FeCO₃ [9]. The diverse spectrum of Mn-oxides that form can be partly attributed to the many valence states that Mn commonly adopts, like Fe and unlike Zn or even Ni. We did observe, however that CoCO₃ can be associated with the formation of exotic oxides, like Co₄O₅ and thus, it is possible that future experiments at even higher pressures than this study will reveal more carbonate polymorphs and complex oxides. In the case of manganites, which are known for exhibiting unique magnetoresisting properties [22], our discoveries help to motivate future work in this area.

6.2. Experimental section

Pure single crystals of MnCO₃, CoCO₃, NiCO₃ and ZnCO₃ were synthesized at the Bayerisches Geoinstitut (BGI) (Bayreuth, Germany) (see the Supporting Information for details). Pre-selected crystals of all four carbonate compounds were loaded separately in BX90 diamond anvil cells (DACs) equipped with pairs of Boehler-Almax-type diamond anvils of various cullet sizes (i.e. 350, 250, 120, 80 μm) depending on the desired pressure range of the experiment. Neon gas was used as the pressure-transmitting medium in all experiments and its powder diffraction at high pressures served for pressure determination in the DAC [24]. Single-crystal X-ray diffraction experiments were performed at the high-pressure dedicated beamlines ID15b at ESRF (Grenoble, France) and P02.2 at PETRA III (DESY, Hamburg). The wavelengths used were 0.411 Å for ID15b and 0.29 Å for P02.2. Diffraction intensities were collected by a Mar555 flat-panel detector and a PerkinElmer XRD 1621 flat-panel detector for ID15b and P02.2, respectively. Data collection was performed as a series of ω scans with a step of 0.5°. The selection of the omega range depended on the opening angle of the DAC and varied from ±32° to ±38°. Integration of the reflection intensities and absorption corrections were performed using the CrysAlisPRO software [25]. All structure solutions and refinements were performed with the JANA2006 crystallographic computing system [26]. For details of structure refinement, see the Supporting Information. EoSFit7c software was used for fitting the equations of state using a 2nd or 3rd order Birch-Murnaghan (BM) equation [27]. Additional Raman spectroscopy measurements were performed at BGI (see the Supporting Information for details).

Keywords

high-pressure chemistry, transition metal carbonates, X-ray diffraction, tetracarbonates

6.4. References

[1] R. Dasgupta, M.M. Hirschmann, A.C. Withers, *Earth Planet. Sci. Lett.* **2004**, 227, 73–85.

[2] M. Akaishi, H. Kanda, S. Yamaoka, *J. Cryst. Growth*, **1990**, 104, 578-581.

[3] M. Chen, J. Shu, X. Xie, D. Tan, H-K. Mao, *PNAS*, **2018**, 115, 2676-2680.

[4] M. Isshiki, T. Irifune, K. Hirose, S. Ono, Y. Ohishi, T. Watanuki, E. Nishibori, M. Takata, M. Sakata, *Nature*, **2004**, 427, 60-63.

[5] L. Bayarjargal, C-J. Fruhner, N. Schrodt, B. Winkler, *Phys. Earth Planet. Inter.* **2018**, 281, 31-45.

[6] R.D Shannon, C.T. Prewitt, *Acta Crystallogr.* **1969**, B25, 925-946.

[7] A.R. Oganov, S. Ono, Y. Ma, C.W. Glass, A. Garcia, *Earth Planet. Sci. Lett.,* **2008**, 273, 38-47.

[8] E. Boulard, D. Pan, G. Galli, Z. Liu, W.L. Mao, *Nat. Commun.,* **2015**, 6, 6311.

[9] V. Cerantola, E. Bykova, I. Kupenko, M. Merlini, L. Ismailova, C. McCammon, M. Bykov, A.I. Chumakov, S. Petitgirard, I. Kantor, V. Svitlyk, J. Jacobs, M. Hanfland, M. Mezouar, C. Prescher, R. Rüffer, V.B. Prakapenka, L. Dubrovinsky, *Nat. Commun.,* **2017**, 8, 15960.

[10] B. Lavina, P. Dera, R.T. Downs, V. Prakapenka, M. Rivers, S. Sutton, M. Nicol, *Geophys. Res. Lett.,* **2009**, 36, L23306.

[11] V. Cerantola, C. McCammon, I. Kupenko, I. Kantor, C. Marini, M. Wilke, L. Ismailova, N. Solopova, A. Chumakov, S. Pascarelli, L. Dubrovinsky, *Am. Mineral.,* **2015**, 100, 2670-2681.

[12] M. Merlini, M. Hanfland, M. Gemmi, *Am. Mineral.,* **2015**, 100, 2625-2629.

[13] E. Boulard, Y. Liu, A.L. Koh, M.M. Reagan, J. Stodolna, G. Morard, M. Mezouar, W.L. Mao, *Front. Earth Sci.,* **2016**, 4, 107.

[14] J. Gao, F. Zhu, X.J. Lai, R. Huang, S. Qin, D.L. Chen, J. Liu, L.R. Zheng, X. Wu, *High Pressure Res.,* **2014**, 34, 89-99.

[15] A. Bouibes, A. Zaoui, *Sci. Rep.,* **2014**, 4, 5172.

[16] S. Chariton, V. Cerantola, L. Ismailova, E. Bykova, M. Bykov, I. Kupenko, C. McCammon, L. Dubrovinsky, *Phys. Chem. Miner.,* **2018**, 45, 59-68.

[17] J. Zhang, R.J. Reeder, *Am. Mineral.,* **1999**, 84, 861-870.

[18] B. Lavina, P. Dera, E. Kim, Y. Meng, R.T. Downs, P.F. Weck, S.R. Sutton, Y. Zhao, *PNAS, 2018*, 108, 17281-17285.

[19] C. Zhao, H. Li, J. Jiang, Y. He, W. Liang, *High Pressure Res.,* **2018**, 38, 212-223.

[20] S. Ono, *Mineral. Mag., 2007*, 71, 105-111.

[21] M. Merlini, M. Hanfland, A. Salamat, S. Petitgirard, H. Müller, *Am. Mineral., 2015*, 100, 2004-2015.

[22] S.V. Ovsyannikov, A.M. Abakumov, A.A. Tsirlin, W. Schnelle, R. Egoavil, J. Verbeeck, G. Tendeloo, K.V. Glazyrin, M. Hanfland, L. Dubrovinsky *Angew. Chem. Int. Ed., 2013*, 52, 1494-1498.

[23] V. Srikanth, M. Akaishi, S. Yamaoka, H. Yamada, T. Taniguchi, *J. Am. Ceram. Soc., 1997*, 80, 786-790.

[24] Y. Fei, A. Ricolleau, M. Frank, K. Mibe, G. Shen, V. Prakapenka, *PNAS*, **2007**, 104, 9182-9186.

[25] Agilent, *Agilent Technologies Ltd, Yarnton,* **2014**.

[26] V. Petricek, M. Dusek, L. Palatinus, Z. Kristallogr., **2014**, 229, 345–352.

[27] J.R. Angel, M. Alvaro, J. Gonzalez-Platas, *Z. Kristallogr – Cryst. Mat.,* **2014,** 229, 405–419.

References of Supporting Information

[s1] T. Isaacs, Mineralogical Magazine, 1963, 33, 663-678.

[s2] M.C. Hales, R.L. Frost, Polyhedron, 2007, 26, 4955-4962.

[s3] B. Lavina, P. Dera, R.T. Downs, V. Prakapenka, M. Rivers, S. Sutton, M. Nicol, *Geophys. Res. Lett.,* **2009**, 36, l23306.

[s4] H.N. Rutt, J.H. Nicola, *J. Phys. C.: Solid State Phys.,* **1974**, 7, 4522-4528.

[s5] H.K. Mao, J. Xu, P.M. Bell, *J. Geophys. Res.,* **1986**, 91, 4673-4676.

[s6] G.A. Farfan, E. Boulard, S. Wang, W.L. Mao, *Am. Mineral.* **2013**, 98, 1817-1823.

[s7] M.N. Taran, K. Langer, M. Koch-Mueller, *Phys. Chem. Miner.,* **2008**, 35, 175-177.

[s8] N. Kang, M.W. Schmidt, S. Poli, E. Franzolin, J.A.D. Connolly, *Chem. Geology,* **2015**, 400, 34-43.

6.5. Supporting Information
6.5.1. Details of starting material synthesis and crystal growth

We synthesized pure $CoCO_3$ and $MnCO_3$ crystals following the procedure reported by Ref. [11, 16]. For example, in the case of $MnCO_3$, metalic Mn powder first reacted with acetic acid (CH_3COOH) to precipitate manganese acetate ($Mn(CH_3COO)_2$). The latter was then dissolved into oxalic acid ($C_2H_2O_4$), forming dihydrated manganese oxalate ($MnC_2O_4\cdot2H_2O$). We placed this powder product in Au capsules and $MnCO_3$ powder was obtained after a 5 days long experiment at 2 kbar and 365 ºC using a vertical cold seal vessel, available at the Bayerisches Geoinstitut (BGI) (Bayreuth, Germany). Single crystals of 10-80 µm size were obtained after 8-10 min annealing at ~1500 ºC and 18 GPa using a Kawai-type multi anvil apparatus available at BGI. The carbonate powder was carefully encapsulated inside a Re capsule. We used Cr-doped MgO octahedra as the pressure medium, $LaCrO_3$ heaters, and $W_{75}Re_{25}$/ $W_{97}Re_3$ thermocouples to monitor the temperature (Supplementary Figure 1). Alternatively, one could skip the synthesis step of the carbonate powder and use directly commercial powder to grow crystals in the multi anvil apparatus.

We failed to grow single crystals of $ZnCO_3$ and $NiCO_3$ using the above procedure. Such synthesis experiments resulted in the formation of accompanying phases (i.e. often metal oxides). Varying the pressure and temperature conditions of the multi anvil experiment or the capsule material did not favor the carbonate crystal growth. $NiCO_3$ crystals of 5-15 µm size were obtained after a 9 days long experiment at 2 kbar and 360 ºC using a horizontal cold seal vessel at BGI and starting from $Ni(HCO_3)_2$ or $NiC_2O_4\cdot2H_2O$ powders sealed in Au capsules. The use of either starting material lead to comparable quality $NiCO_3$ crystals. For the synthesis of 5-80 µm sized $ZnCO_3$ crystals, we performed a 29 days long experiment at 2 kbar and 275 ºC using a horizontal cold seal vessel at BGI and starting from $Zn(HCO_3)_2$ in Au capsules. Alternative synthesis procedures of $NiCO_3$ and $ZnCO_3$ have been suggested by Ref. [s1] and Ref. [s2], respectively.
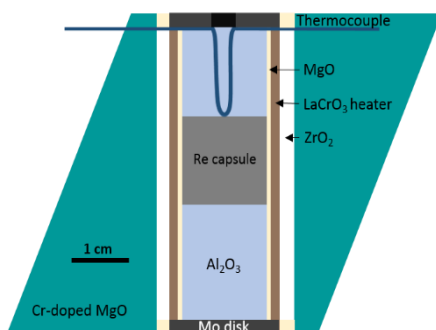
Supplementary Figure S1: Cross section of the multi anvil experimental assembly.

6.5.2. Details of high-pressure single-crystal X-ray diffraction data collection, structure solution and refinement

6.5.2.1. Summary of phases reported

Table S1. Details of crystal structure refinements of various high-pressure carbonate polymorphs. The CIF files of the following structures can be found online (XXXXX).

Phase	ZnCO$_3$-II [a]	MnCO$_3$-II	MnCO$_3$-III	MnC$_2$O$_5$	Mn$_4$C$_4$O$_{13}$
Pressure (GPa)	57.0 (5)	46.2 (2)	63.5 (3)	65.9 (3)	115 (2)
Annealing Temperature (K)	2800 (100)	Not annealed	2200 (100)	2000 (150)	2400 (100)
Space Group	$C2$	$P\bar{1}$	$P2_1/c$	$Fd\bar{3}m$	$C2/c$
a (Å)	4.984 (2)	2.8899 (12)	4.7200 (16)	9.431 (2)	10.0862 (8)
b (Å)	4.3947 (13)	4.8148 (14)	2.8968 (4)	-	3.9783 (3)
c (Å)	3.414 (3)	5.513 (2)	10.6879 (16)	-	13.3538 (11)
α (º)	90	101.08 (3)	90	90	90
β (º)	99.67 (7)	94.53 (3)	102.01 (2)	90	107.678 (9)
γ (º)	90	90.35 (3)	90	90	90
V (Å^3)	73.72 (8)	75.03 (5)	142.93 (6)	838.9 (3)	510.54 (7)
Z	2	2	4	16	4
F(000)	120	110	220	1232	912
ρ (g/cm^3)	5.65	5.09	5.34	5.04	6.19
Theta collection range (º)	2.54 – 17.79	3.23 – 17.85	2.62 – 17.56	3.56 – 21.02	2.61 – 17.20
Completeness to d =0.8 Å, %	35.0	38.2	36.4	87.8	36.1
Redundancy	1.046	1.446	1.564	4.604	1.816
Reflections collected	251	525	912	553	1629
Unique reflections / R$_{int}$	138 / 0.102	228 / 0.022	433 / 0.066	229 / 0.137	744 / 0.032
Unique reflections (I>3σ(I))	135	358	518	86	839
No. of parameters	14	31	36	9	53
R1/wR2 (obs)	0.046 / 0.051	0.078 / 0.087	0.106 / 0.102	0.036 / 0.028	0.037 / 0.045
R1/wR2 (all)	0.049 / 0.051	0.090 / 0.089	0.124 / 0.106	0.091 / 0.035	0.043 / 0.047
Ref. ICSD code					

[a] Heating of ZnCO$_3$ was aided by a few Au particles (~1-2 μm) spread inside the sample chamber.

Table S2. Details of crystal structure refinements of various transition metal oxides that result from the thermal decomposition of carbonates. The CIF files of the following structures can be found online (xxxxx).

Phase	Co_4O_5	NiO	Mn_3O_4	Mn_5O_7	$pv\text{-}Mn_2O_3$	$\delta\text{-}Mn_2O_3$
Pressure (GPa)	31.5 (5)	59.8 (4)	19.8 (2)	62.4 (3)	46.4 (4)	115 (2)
Annealing Temperature (K)	1900 (100)	2100 (100)	2000 (100)	2100 (100)	2000 (200)	2400 (100)
Space Group	$C2/c$	$Fm\bar{3}m$	$Pbcm$ (acb) setting	$C2/m$	$Pnma$ (or $Pbnm$ in (bca) setting)	$Cmcm$
a (Å)	2.7166 (19)	3.9217 (8)	2.9060 (2)	8.927 (3)	5.0206 (10)	2.5728 (9)
b (Å)	9.1787 (14)	-	9.5201 (8)	2.683 (3)	6.853 (3)	8.368 (4)
c (Å)	11.5254 (16)	-	9.3267 (17)	8.079 (4)	4.7038 (10)	6.3805 (15)
α (º)	90	90	90	90	90	90
β (º)	90	90	90	105.83 (4)	90	90
γ (º)	90	90	90	90	90	90
V (Å³)	287.4 (2)	60.31 (2)	258.03 (6)	186.2(2)	161.84 (8)	137.37 (9)
Z	4	4	4	2	4	4
F(000)		144	428	362	296	296
ρ (g/cm³)		8.23	5.89	6.90	6.48	7.63
Theta collection range (º)		3.66 – 16.55	2.9 – 18.08	2.47 – 16.83	2.16 – 16.09	2.61 – 15.71
Completeness to d =0.8 Å, %		100	50	35.9	72.44	54.1
Redundancy	2.09	4.04	2.18	1.74	2.196	2.11
Reflections collected	454	101	1665	663	985	419
Unique reflections / R_{int}		66 / 0.052	618 / 0.057	249 / 0.075	353 / 0.049	219 / 0.023
Unique reflections (I>3σ(I))		23	725	367	419	189
No. of parameters		3	36	27	28	19
R1/wR2 (obs)		0.047 / 0.054	0.055 / 0.056	0.083 / 0.089	0.069 / 0.070	0.041 / 0.05
R1/wR2 (all)		0.047 / 0.054	0.070 / 0.059	0.098 / 0.092	0.088 / 0.075	0.044 / 0.05
Ref. ICSD code						
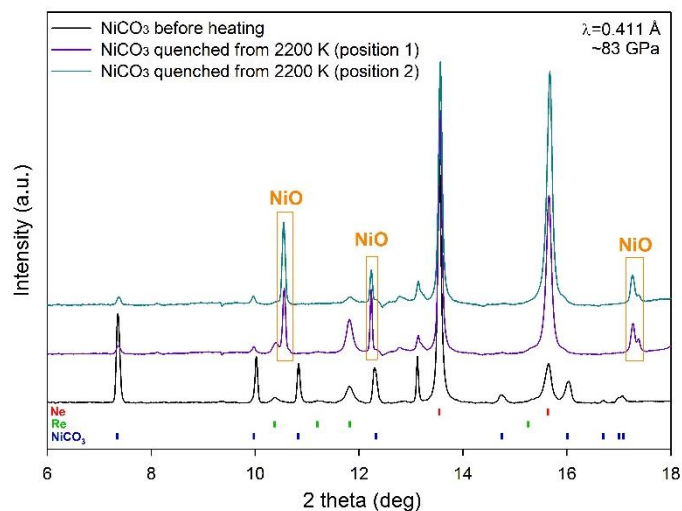
Supplementary Figure S2. Powder X-ray diffraction patterns of NiCO3 at 83 GPa before and after heating at 2200 K. Note the peaks arising from NiO (orange rectangular). Splitting of the first (2θ ≈ 10.6°) and the third (2θ ≈ 10.6°) diffraction peaks would indicate a rhombohedral symmetry for NiO (R3̄m), instead of the rock salt structure ($Fm\overline{3}m$). However, a visual splitting appears only on the third peak. Due to limited number of single-crystal reflections we are unable to properly assign the correct space group.

Table S3. Details of the maximum and minimum size of bonds among various atoms in the phases reported.

Phase	P (GPa)	Atom-Atom	Maximum bond length (Å)	Minimum bond length (Å)
MnCO$_3$-II	46.2 (2)	Mn-O	2.27	2.02
		C-O	1.29	1.20
MnCO$_3$-III	63.5 (3)	Mn-O	2.173	2.026
		C-O	1.264	1.244
ZnCO$_3$-II	57.0 (5)	Mn-O	1.937	1.887
		C-O	1.32	1.272
MnC$_2$O$_5$	65.9 (3)	Mn-O	2.065	2.065
		C-O	1.367	1.293
Mn$_4$C$_4$O$_{13}$	115 (2)	Mn-O	2.374	1.758
		C-O	1.389	1.279
NiO ($Fm\overline{3}m$)	59.8 (4)	Ni-O	1.9609	1.9609
Co$_4$O$_5$	31.5 (5)	Co-O		
Mn$_3$O$_4$	19.8 (2)	Mn-O	2.219	1.856
pv-Mn$_2$O$_3$[a]	46.4 (4)	Mn-O	1.968	1.753
Mn$_5$O$_7$	62.4 (3)	Mn-O	2.150	1.783
δ - Mn$_2$O$_3$	115 (2)	Mn-O	2.194	1.753

[a] If formation of cuboctahedra is considered, then maximum bond distance is 2.194 Å.

6.5.2.2. Equations of state (lattice parameters and bond lengths)

In overall, the CO_3 units appear rigid with increasing pressure compared to the more compressible MeO_6 octahedra (where $Me=Mn^{2+}$, Zn^{2+}, Ni^{2+}). Although initially distorted, MeO_6 octahedra momentarily become regular at different pressures depending to the metal involved. Namely, we noticed regularity in the form of equal O-O bond lengths within the NiO_6, ZnO_6 and MnO_6 octahedra at ~21, ~22, and ~16 GPa, respectively (Tables S4-S6). For comparison, FeO_6 and CoO_6 octahedra in $FeCO_3$ and $CoCO_3$ become regular at ~23 [s3] and ~16 GPa [16].

6.5.2.2.1. ZnCO₃

Table S4. Crystallographic data of ZnCO₃ with increasing pressure and at room temperature. Space group is $R\bar{3}c$. Note the datasets that bond lengths are not provided. This is due to the low quality of data collection that did not allow reliable structure solution and refinement.

P (GPa)	a (Å)	c (Å)	V (Å)	Zn-O (Å)	C-O (Å)	O1-O2 (Å)[a]	O2-O3 (Å)[a]	Crystal
0.0 (0)[b]	4.6539 (2)	15.0204 (16)	281.74 (3)	2.1106 (7)	1.2863 (14)	3.0257 (6)	2.9434 (15)	1
27.5 (2)	4.4950 (6)	13.665 (3)	239.11 (8)	1.9879 (12)	1.262 (3)	2.8004 (9)	2.822 (3)	2
32.0 (3)	4.4759 (10)	13.519 (4)	234.55 (10)	1.9745 (12)	1.258 (3)	2.776 (1)	2.809 (3)	
37.8 (2)	4.4518 (13)	13.329 (8)	228.77 (16)	1.9557 (15)	1.257 (3)	2.7433 (15)	2.788 (3)	
40.5 (5)	4.4418 (15)	13.292 (9)	227.11 (19)	1.9529 (19)	1.250 (4)	2.7376 (18)	2.786 (4)	
47.4 (6)	4.4192 (17)	13.148 (11)	222.4 (2)	1.941 (3)	1.241 (6)	2.714 (3)	2.775 (7)	
51.8 (4)	4.406 (2)	13.093 (16)	220.1 (3)	1.9309 (16)	1.244 (3)	2.7018 (19)	2.759 (3)	
57.2 (5)	4.399 (3)	12.932 (16)	216.7 (3)	1.924 (3)	1.237 (5)	2.6805 (19)	2.760 (5)	
62.4 (9)	4.371 (4)	12.88 (3)	213.2 (5)					
66.6 (8)	4.364 (3)	12.74 (2)	210.2 (4)	1.900 (3)	1.236 (4)	2.644 (5)	2.729 (5)	
72 (1)	4.356 (4)	12.63 (2)	207.5 (4)					
81 (2)	4.336 (4)	12.53 (3)	204.1 (5)	1.883 (3)	1.225 (5)	2.611 (5)	2.714 (5)	
86 (1)	4.327 (4)	12.39 (2)	200.9 (5)					
93 (1)	4.311 (3)	12.247 (19)	197.1 (4)	1.852 (4)	1.239 (6)	2.563 (4)	2.675 (6)	
96 (1)	4.301 (2)	12.21 (1)	195.6 (4)					
102 (2)[b]	4.277 (2)	12.17 (2)	192.8 (3)	1.844 (5)	1.231 (9)	2.549 (4)	2.666 (9)	

[a] See Supplementary Figure 3 for the explanation of notation; [b] ISCD reference files can be found online (######, ######)

6.5.2.2.2. NiCO₃

Table S5. Crystallographic data of NiCO$_3$ with increasing pressure and at room temperature. Space group is $R\overline{3}c$.

P (GPa)	a (Å)	c (Å)	V (Å)	Ni-O (Å)	C-O (Å)	O1-O2 (Å)[a]	O2-O3 (Å)[a]	Crystal
0.0 (0)[b]	4.6004 (2)	14.7497 (4)	270.34 (2)	2.0745 (1)	1.2858 (19)	2.9725 (7)	2.894 (2)	1
1.2 (3)	4.58781 (12)	14.6518 (8)	267.074 (15)	2.0648 (12)	1.285 (3)	2.9557 (8)	2.884 (3)	2
3.3 (3)	4.57476 (14)	14.5437 (8)	263.598 (18)	2.0564 (12)	1.280 (3)	2.9386 (8)	2.877 (3)	3
6.0 (2)	4.5541 (2)	14.3606 (12)	257.93 (3)	2.0369 (16)	1.283 (4)	2.9061 (12)	2.855 (4)	2
7.1 (2)	4.5484 (3)	14.3085 (14)	256.35 (3)	2.0339 (12)	1.279 (3)	2.8987 (10)	2.854 (3)	3
12.1 (2)	4.52331 (19)	14.0809 (9)	249.50 (2)	2.0139 (12)	1.275 (3)	2.8611 (8)	2.835 (3)	3
13.1 (1)	4.5188 (3)	14.0334 (18)	248.17 (4)	2.0097 (14)	1.275 (3)	2.852 (10)	2.832 (3)	2
16.5 (3)	4.50228 (15)	13.9054 (7)	244.106 (17)	1.9975 (12)	1.272 (3)	2.8317 (8)	2.818 (3)	3
21.0 (1)	4.4801 (2)	13.7200 (13)	238.48 (3)	1.9794 (9)	1.2715 (18)	2.7997 (7)	2.799 (2)	3
22.2 (1)	4.4831 (7)	13.662 (6)	237.80 (12)	1.975 (3)	1.277 (6)	2.791 (3)	2.796 (7)	2
24.7 (4)	4.4705 (3)	13.649 (14)	236.24 (3)	1.9722 (9)	1.271 (18)	2.7809 (7)	2.7904 (19)	3
27.9 (2)	4.4665 (4)	13.451 (4)	232.39 (8)	1.9614 (18)	1.27 (4)	2.7598 (14)	2.788 (4)	2
29.6 (1)	4.4518 (3)	13.4338 (17)	230.56 (4)	1.9533 (7)	1.2715 (14)	2.7532 (6)	2.7715 (15)	3
35.4 (2)	4.4343 (4)	13.270 (2)	225.98 (4)	1.9422 (16)	1.263 (4)	2.7278 (18)	2.765 (4)	3
38.7 (1)	4.4224 (4)	13.185 (2)	223.31 (5)	1.9315 (8)	1.2662 (14)	2.7118 (6)	2.7513 (15)	3
41.2 (3)	4.4319 (5)	13.010 (4)	221.30 (9)	1.9304 (16)	1.261 (4)	2.6932 (13)	2.766 (4)	2
43.0 (3)	4.4115 (4)	13.038 (3)	219.76 (6)	1.9227 (9)	1.2651 (18)	2.6889 (7)	2.7489 (19)	3
46.9 (2)	4.4015 (4)	12.931 (2)	216.96 (5)	1.9121 (7)	1.2623 (14)	2.6720 (6)	2.7358 (15)	3
50.2 (1)	4.3960 (4)	12.859 (2)	215.21 (5)	1.9088 (7)	1.2573 (14)	2.6624 (6)	2.7361 (14)	3
50.8 (1)	4.4033 (8)	12.798 (8)	214.90 (15)	1.913 (4)	1.251 (7)	2.659 (3)	2.750 (7)	2
55.2 (1)	4.3857 (6)	12.739 (3)	212.20 (6)	1.8991 (9)	1.2565 (18)	2.6434 (8)	2.7274 (19)	3
60.0 (2)	4.3944 (9)	12.529 (5)	209.53 (11)	1.8912 (9)	1.2543 (18)	2.6270 (8)	2.7213 (19)	2
60.0 (1)	4.3767 (5)	12.630 (3)	209.53 (6)	1.893 (3)	1.258 (5)	2.6177 (19)	2.734 (6)	3
61.8 (3)	4.3757 (8)	12.566 (6)	208.35 (11)	1.8885 (1)	1.2528 (18)	2.6184 (11)	2.7221 (19)	3
72.0 (3)	4.3811 (14)	12.248 (9)	203.59 (18)	1.876 (3)	1.254 (5)	2.578 (3)	2.727 (6)	2
83.1 (4)[b]	4.3571 (11)	12.028 (6)	197.75 (13)	1.857 (3)	1.251 (5)	2.542 (2)	2.707 (5)	2

[a] See Supplementary Figure 3 for the explanation of notation; [b] ISCD reference files can be found online (######, ######)
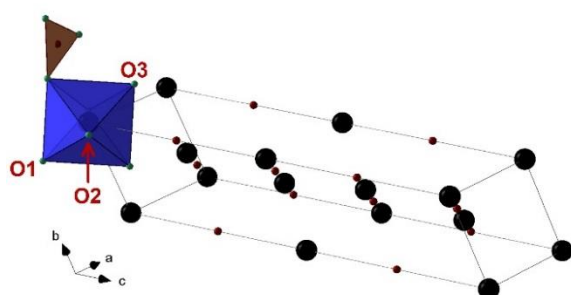
Supplementary Figure S3. Explanatory section of the bond distances between oxygen atoms O1-O2 and O2-O3 that are reported in the supplementary tables 3-5.

6.5.2.2.3. MnCO$_3$

Table S6. Crystallographic data of MnCO$_3$ with increasing pressure and at room temperature. Space group is $R\bar{3}c$.

P (GPa)	a (Å)	c (Å)	V (Å)	Mn-O (Å)	C-O (Å)	O1-O2 (Å)[a]	O2-O3 (Å)[a]	Crystal
0.0 (0)[b]	4.7796 (2)	15.6725 (5)	310.06 (2)	2.1967 (8)	1.2871 (15)	3.1532 (6)	3.0592 (16)	1
17.7 (3)	4.6680 (2)	14.366 (3)	271.10 (7)	2.0911 (15)	1.275 (3)	2.9446 (11)	2.970 (4)	2
25.4 (2)	4.6470 (10)	14.003 (14)	261.9 (3)	2.0679 (17)	1.268 (3)	2.892 (3)	2.957 (4)	
33.7 (1)	4.628 (2)	13.60 (2)	252.3 (5)	2.0435 (19)	1.263 (3)	2.835 (3)	2.944 (4)	
37.9 (3)	4.614 (2)	13.46 (2)	248.1 (5)	2.0316 (19)	1.259 (3)	2.811 (3)	2.934 (4)	
40.6 (2)	4.6028 (15)	13.301 (16)	244.0 (3)	2.0240 (19)	1.252 (4)	2.790 (3)	2.933 (4)	
43.6 (4)	4.6025 (16)	13.152 (17)	241.3 (3)	2.014 (3)	1.257 (6)	2.769 (3)	2.925 (6)	

[a] See Supplementary Figure 2 for the explanation of notation; [b] ISCD reference files can be found online (######, ######)

6.5.2.2.4. MnCO$_3$-II

Table S7. Crystallographic data of MnCO$_3$-II with increasing pressure and at room temperature. Space group is $R\bar{3}c$. The limited amount of reflections in the datasets presented below did not allow reliable structure solutions and refinements. The datasets collected at 46.2 and XX GPa are exceptions.

P (GPa)	a (Å)	b (Å)	c (Å)	V (Å)	α (º)	β (º)	γ (º)	Crystal
46.2 (2)[a]	4.7796 (2)	15.6725 (5)	310.06 (2)	2.1967 (8)	1.2871 (15)	3.1532 (6)	3.0592 (16)	1
46.9 (5)	2.922 (3)	4.8339 (17)	5.543 (4)	76.42 (10)	101.40 (5)	95.21 (7)	90.00 (5)	2[b]
51.0 (4)	2.905 (2)	4.815 (2)	5.510 (4)	75.37 (9)	101.07 (5)	94.79 (6)	90.22 (5)	
55.4 (4)	2.885 (3)	4.801 (2)	5.481 (5)	74.21 (11)	101.27 (5)	94.50 (8)	90.04 (6)	
60.1 (3)	2.864 (3)	4.764 (2)	5.448 (4)	72.67 (6)	101.40 (5)	94.14 (7)	89.96 (6)	
65.0 (6)	2.855 (4)	4.749 (3)	5.427 (5)	71.93 (13)	101.47 (7)	94.01 (9)	89.97 (7)	

[a] ISCD reference files can be found online (######, ######); [b] Crystal No.2 in this table is the same as No. 2 in Supplementary Table 5.

6.5.2.3. Details of the MnCO₃ stability field diagram

Table S8. Lattice parameters of the datasets appearing in Figure 4 of the main text

P (GPa)	Annealing T (K)	Lattice parameters of present phases (Å, °deg, Å³)		
19.8 (2)	2000 (100)	**Mn₃O₄** a=2.9060(2), b=9.5201(8), c=9.3267(17), V=258.03(6)		**MnCO₃** a=4.6555(6), c= 14.2687(14), V=267.82(2)
46.4 (5)	2100 (200)	**pv-Mn₂O₃** a=5.0206(10), b=6.853(3), c=4.7038(10), V=161.84(8)		**MnCO₃** a=4.592(2), c= 13.142(4), V=239.9(3)
65.9 (3)	2000 (150)	**MnCO₃-III** a=4.7154(7), b=2.8986(15), c=10.762(2), β=102.178(16) V=143.79(8)	**Mn₅O₇** a=8.8434(9), b=2.7009(3), c=8.0917(15), β=105.845(16) V=185.93(4)	**MnC₂O₅** a=9.431(2), V=838.9(3)
62.4 (3)	2100 (100)	**MnCO₃-III** a=4.7243(16), b=2.8963(4), c=10.6892(16), β=102.09(2), V=143.02(6)		**Mn₅O₇** a=8.927(3), b=2.683(3), c=8.079(4), β=105.83(4), V=186.2(2)
63.0 (6)	2500 (100)	**MnCO₃-III** a=4.7051(16), b=2.906(4), c=10.735(3), β=102.12(12), V=143.5(2)		**Mn₅O₇** a=8.840(3), b=2.7074(3), c=8.0993(13), β=105.81(3), V=186.50(8)
64.0 (6)	2300 (150)	**MnCO₃-III** a=4.732(6), b=2.891(8), c=10.750(1), β=102.3(2), V=143.7(4)		**Mn₅O₇** a=8.871(10), b=2.7023(5), c=8.081(2), β=105.92(6), V=186.3(2)
64.4 (3)	2100 (100)	**MnCO₃-III** a=4.725(2), b=2.9043(10), c=10.773(3), β=102.23(3), V=144.46(10)		**Mn₅O₇** a=8.855(1), b=2.701(2), c=8.102(1), β=105.8(2), V=186.4(3)
63.8 (2)	2100 (100)	**MnCO₃-III** a=4.733(5), b=2.913(8), c=10.752(8), β=102.40(8), V=144.8(4)		**Mn₅O₇** a=8.869(2), b=2.7053(3), c=8.1108(10), β=106.36(2), V=186.74(5)
63.8 (2)	1900 (100)	**MnCO₃-III** a=4.7326(5), b=2.8918(4), c=10.7901(19), β=101.995(13), V=144.45(4)	**Mn₅O₇** a=8.896(6), b=2.6901(14), c=8.104(3), β=106.04(5), V=186.39(18)	**ppv – Mn₂O₃** a=2.6607(14), b=8.675(2), c=6.650(2), V=153.48(10)
88.0 (6)	1900 (100)	**pv – Mn₂O₃** a=2.6338(5), b=8.5084(5), c=6.5039(5), V=145.75(3)		**Mn₄C₄O₁₃** a=10.2905(17), b=4.0512(7), c=13.521(3), β=107.357(17), V=538.00(18)
115 (2)	2400 (100) 2600 (100) 2800 (100)	**pv – Mn₂O₃** a=2.591(5), b=8.300(3), c=6.364(3), V=136.8(3)		**Mn₄C₄O₁₃** a= 10.0862(8), b=3.9783(3), c=13.3538(11), β=107.678(9), V=510.54(7)
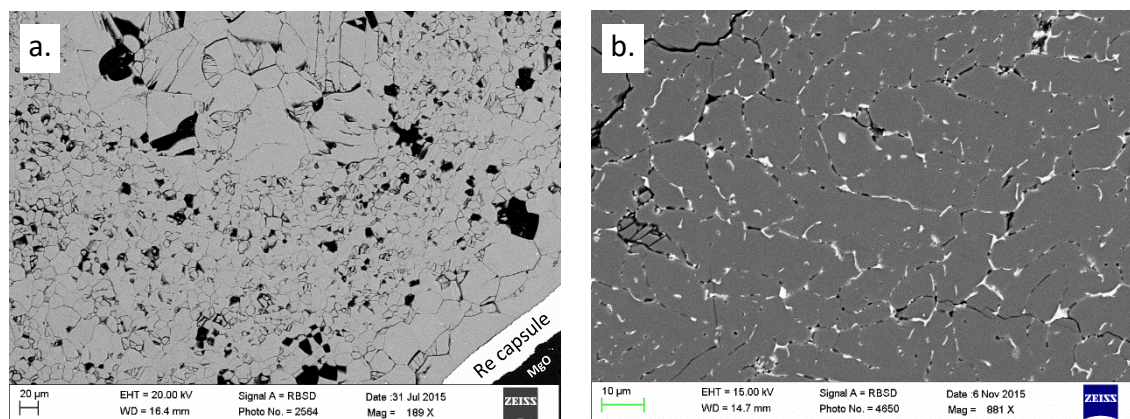
Supplementary Figure S4. Representative back-scattered electron (BSE) images of multi-anvil runs. a) MnCO$_3$ crystal growth experiment at 18 GPa and 1773 K, as described above (Section 1). b) Melt texture of MnCO$_3$ with coexisting Mn-oxides (Mn$_3$O$_4$) along the grain boundaries at 14 GPa and 1973 K. The experimental set-up and results are similar to Ref. [s8]. A small graphite chip was placed in the capsule to ensure internal f_{O_2} close to the CCO buffer.

6.5.3. Raman spectroscopy measurements

At ambient conditions, calcite-type carbonates have four Raman active vibration modes in the frequency range that we investigated (i.e. $150 - 1300\,\text{cm}^{-1}$). The position of the four peaks in the frequency scale vary for each carbonate (MnCO$_3$, ZnCO$_3$, NiCO$_3$), but roughly averages to ~200, ~300, ~750 and ~1100 cm^{-1}. The first two bands (i.e. with lower wavenumbers) correspond to external modes associated with lattice vibrations, one translational [E$_g$ (T)] and one librational [E$_g$ (L)], while the latter two bands (i.e., with higher wavenumbers) correspond to internal vibrations within the (CO$_3$)$^{2-}$, one asymmetric bending (E$_g$ or v4) and one symmetric stretching (A$_{1g}$ or v1) [s4].

Raman spectra were collected by employing a triple-monochromator DILOR XY spectrometer with 2 cm^{-1} spectral resolution using the 514 nm line of the Ar$^+$ excitation laser that is available at BGI. The spectra were collected in steps of 3–4 GPa upon compression up to ~55 GPa. A ruby loaded in the sample chambers was used for pressure determination in the cell [s5]. The pressure uncertainty was estimated from the difference in the pressures measured before and after each data point collection and did not exceed 1 GPa. The spectral fitting was carried out using the software package PeakFit (Systat Software).

The most intense A$_{1g}$ band of all three carbonate compositions shift gradually to higher frequencies with increasing pressure (Supplementary Figure S5) until ~44 GPa, where the first additional peaks appear in MnCO$_3$ (Supplementary Figure S6). Our X-ray diffraction experiments revealed that MnCO$_3$ ($R\bar{3}c$) fully transforms to MnCO$_3$-II ($P\bar{1}$) at ~46 GPa. At 46.2 (5) GPa, we count at least 10 new Raman peaks (14 peaks in total). The appearance of many new vibrational bands is consistent with the lowering of the symmetry

and our results come in excellent agreement with previous studies [12, 19]. An interesting feature however is the overlapping peak close to the A_{1g} mode (~1196 cm^{-1}) at 46.2 (5) GPa (asterisk in Supplementary Figure S5), which nearly disappears at 54.9 (4) GPa. Similar pattern has been observed for $FeCO_3$ at ~43-50 GPa and is attributed to the Fe^{2+} spin transition [11]. It is not clear whether the similar behaviour of A_{1g} mode in $MnCO_3$ or the structural transformation to MnCO3-II are related to a possible spin crossover of Mn^{2+}. X-ray emission spectroscopy measurements (XES) of previous study do not support this scenario though [s6].

No new modes appear for $NiCO_3$ and $ZnCO_3$ upon compression to ~51 GPa, suggesting that no structural or electronic changes occur until that pressure (Supplementary Figure S7). Indeed, our SCXRD experiments show that $NiCO_3$ and $ZnCO_3$ are stable in the $R\overline{3}c$ structure up to ~83 and ~102 GPa, respectively. A worth noting observation, however, is the $NiCO_3$ colour changes with increasing pressure. At ambient conditions, $NiCO_3$ has a light green colour. At ~26 GPa we observed the first colour change to magenta, which gradually changed to a dark yellow-orange colour at ~50 GPa. Given our SCXRD measurements, we attribute this colour change to pressure effects, such as bond shortening and simultaneous increase of the crystal field splitting energy, which causes a blue shift of the absorption bands [s7].
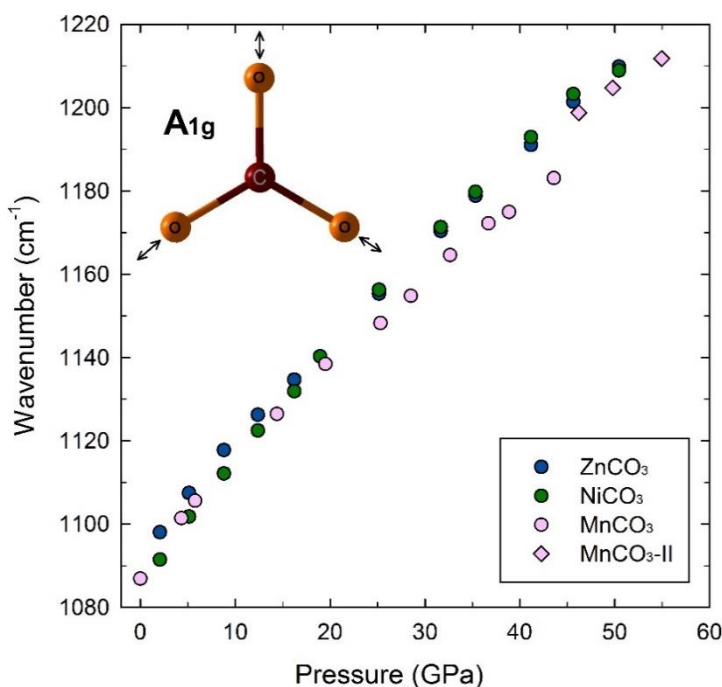
Supplementary Figure S5. Pressure dependence of the most intense v1 (A1g) Raman mode of our three transition-metal carbonates. For all compounds A1g gradually shifts to higher frequencies with increasing pressure except for MnCO3 above 44 GPa, where it transforms to $MnCO_3$-II. The error bars are smaller than the size of the symbols.
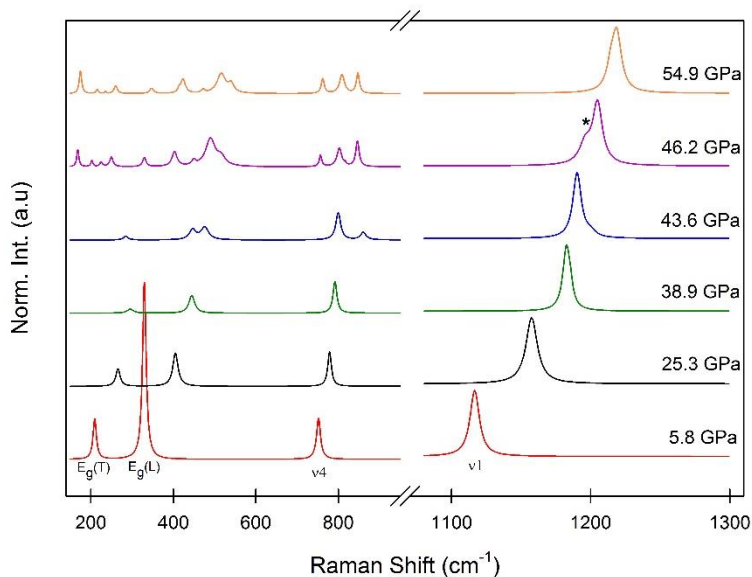
Supplementary Figure S6. Raman spectra of $MnCO_3$ collected at high pressures. Note the new vibration modes of $MnCO_3$-II arising between 43 and 55 GPa.
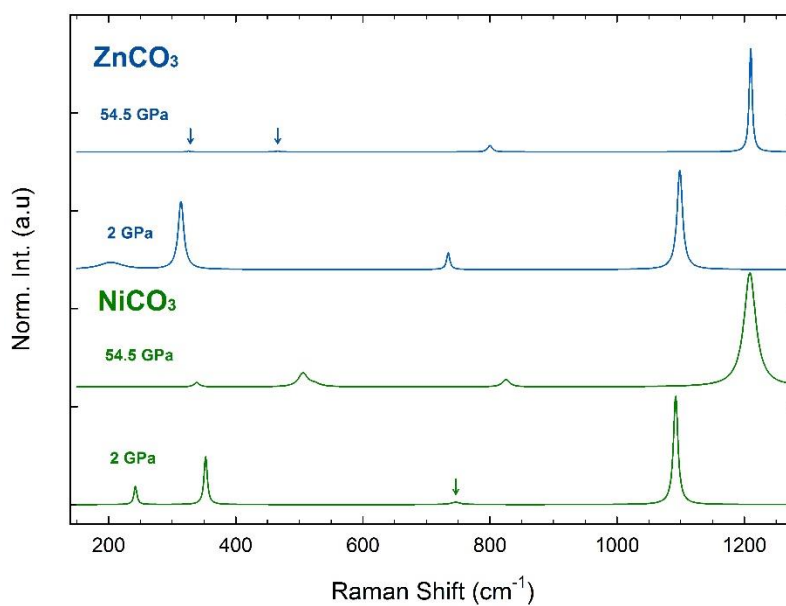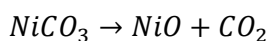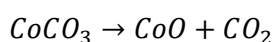

Supplementary Figure S7. Raman spectra of $NiCO_3$ and $ZnCO_3$ at the lowest and highest pressures of our experiment, confirming the stability of the two compounds in the $R\bar{3}c$ space group. The arrows point to the position of peaks with low intensity.
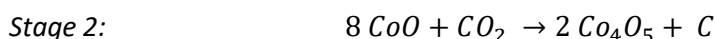
6.5.4. Discussion on the chemical reactions

The formation of $MnCO_3$-II, $MnCO_3$-III and $ZnCO_3$-II are a result of second order structural transitions. Following are some of the possible chemical reactions that lead in the formation of CoO, NiO, Co_4O_5, Mn_3O_4, pv-Mn_2O_3, Mn_5O_7, MnC_2O_5, δ-Mn_2O_3 and $Mn_4C_4O_{13}$. The accompanying exsolution of CO_2 or C (diamond) is suggested, despite the lack of direct evidence in our experiments. CO_2 could not be indexed in the diffraction patterns perhaps due to its non-crystalline form and/or its dissolution in the pressure transmitting medium (i.e. Ne). Detecting diamond formation in diamond anvil cell experiments is challenging as well but has been previously reported [9].

Formation of CoO and NiO

$$CoCO_3 \rightarrow CoO + CO_2$$

$$NiCO_3 \rightarrow NiO + CO_2$$

Formation of Co_4O_5

Stage 1: $\qquad\qquad$ $CoCO_3 \rightarrow CoO + CO_2$

Stage 2: $\qquad\qquad$ $8\,CoO + CO_2 \rightarrow 2\,Co_4O_5 +\ C$

Formation of Mn_3O_4

Stage 1: $\qquad\qquad$ $MnCO_3 \rightarrow MnO + CO_2$

Stage 2: $\qquad\qquad$ $6\,MnO + CO_2 \rightarrow 2\,Mn_3O_4 +\ C$

Formation of pv-Mn_2O_3

Stage 1: $\qquad\qquad$ $MnCO_3 \rightarrow MnO + CO_2$

Stage 2: $\qquad\qquad$ $4\,MnO + CO_2 \rightarrow 2\,Mn_2O_3 +\ C$
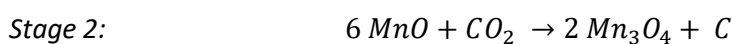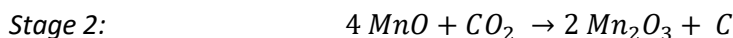
Formation of Mn_5O_7 and MnC_2O_5

Scenario 1: $\qquad\qquad$ $9\,MnCO_3 \rightarrow Mn_5O_7 +\ 4\,MnC_2O_5 +\ C$
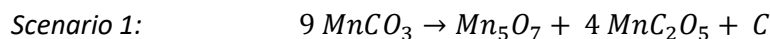
Scenario 2: $\qquad$ *($MnCO_3$ is not exhausted. Release of oxygen promotes MnC_2O_5 formation)*

Stage 1: $\qquad$ $5\,MnCO_3 \rightarrow Mn_5O_7 +\ 4\,O_2 +\ 5\,C$

Stage 2: $\qquad\qquad$ $O_2 +\ C + MnCO_3 \rightarrow MnC_2O_5$

Formation of Mn_5O_7 and δ-Mn_2O_3

Scenario 1: $9\ MnCO_3 \rightarrow Mn_5O_7 +\ 4\ MnC_2O_5 +\ C$
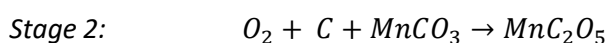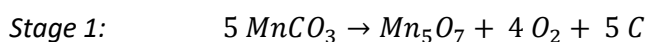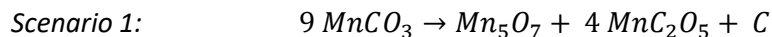
Scenario 2:   *($MnCO_3$ is not exhausted. Reheating after Stage 2 may favour formation of δ-Mn_2O_3)*

  Stage 1: $MnCO_3 \rightarrow MnO + CO_2$

  Stage 2: $5\ MnO + CO_2 \rightarrow Mn_5O_7 + C$

  Stage 3: $Mn_5O_7 + MnCO_3 \rightarrow 8\ Mn_2O_3 + C$
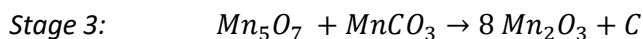
Scenario 3:   *($MnCO_3$ is not exhausted. Firstly δ-Mn_2O_3 forms and promotes the formation of Mn_5O_7 and MnC_2O_5)*

  Stage 1: $MnCO_3 \rightarrow MnO + CO_2$

  Stage 2: $4\ MnO + CO_2 \rightarrow 2\ Mn_2O_3 +\ C$

  Stage 3: $2\ Mn_2O_3 + 2\ MnCO_3 \rightarrow Mn_5O_7 +\ MnC_2O_5$
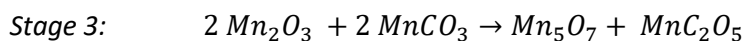
Formation of $Mn_4C_4O_{13}$ and δ-Mn_2O_3

  Scenario 1: $14\ MnCO_3 \rightarrow 3\ Mn_4C_4O_{13} +\ Mn_2O_3 +\ 2C$

  Scenario 2: $37\ MnC_2O_5 +\ 7\ Mn_5O_7 \rightarrow 18\ Mn_4C_4O_{13} +\ 2C$
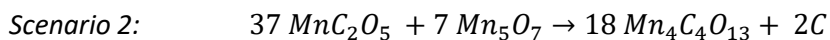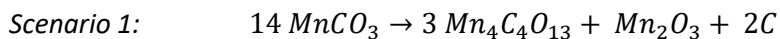
Chapter 7

Seismic detectability of carbonates in the deep Earth: a Nuclear Inelastic Scattering study

Stella Chariton[1], Catherine McCammon[1], Denis M. Vasiukov[2], Michal Stekiel[3], Anastasia Kantor[1,4], Valerio Cerantola[4], Ilya Kupenko[5], Timofey Fedotenko[2], Egor Koemets[1], Michael Hanfland[4], Alexandr I. Chumakov[4] and Leonid Dubrovinsky[1]

[1] Bayerisches Geoinstitut, Universität Bayreuth, 95440 Bayreuth, Germany

[2] Laboratory of Crystallography, Universität Bayreuth, 95440 Bayreuth, Germany

[3] Institute of Geosciences, Goethe Universität, 60438 Frankfurt am Main, Germany

[4] ESRF, The European Synchrotron, CS40220, 38043 Grenoble Cedex 9, France

[5] Institute for Mineralogy, Universität Münster, 48149 Münster, Germany

Corresponding Author's email: stella.chariton@uni-bayreuth.de
ORCID iD: 0000-0001-5522-0498
Tel: +49 (0)921 55 3878

ABSTRACT

Carbonates play an important role in the transport and storage of carbon in the Earth's mantle. However, the abundance of carbon and carbonates in subduction zones is still an unknown quantity. In order to understand which are the most abundant accessory phases and how they influence the dynamical processes that operate within the Earth, investigations on the vibrational, elastic and thermodynamic properties of these phases are crucial for interpreting the seismological observations. Recently, the Nuclear Inelastic Scattering (NIS) method has proved to be a useful tool to access information on the lattice dynamics, as well as to determine Debye sound velocities of Fe-bearing materials. Here we derive the acoustic velocities from two carbonate compositions in the $FeCO_3$-$MgCO_3$ binary system up to ~ 70 GPa using the NIS method. We conclude that more Mg-rich samples, in this case $(Fe_{0.26}Mg_{0.74})CO_3$, have ~ 19 % higher sound velocities than the pure end-member Fe composition. In addition, we observed a

significant velocity increase after the Fe^{2+} spin transition was complete. After laser heating of $FeCO_3$ at lower mantle conditions, we observed a dramatic velocity drop, which is probably associated with thermal decomposition to another phase. Parallel to our NIS experiments, we conducted a single crystal X-ray diffraction (SCXRD) study to derive the equation of states of $FeCO_3$ and $(Fe_{0.26}Mg_{0.74})CO_3$. The combined information from NIS (i.e. Debye velocities) and SCXRD (i.e. densities and bulk moduli) experiments enabled us to derive the primary and shear wave velocities of our samples. Our results are consistent with results obtained by other methods in previous studies, including Brillouin spectroscopy, inelastic X-ray scattering and DFT calculations, supporting NIS as a reliable alternative method for studying the elastic properties of Fe-bearing systems at high pressures and temperatures. Finally, we discuss the seismic detectability of carbonates. We determine that nearly 22 wt% of CO_2 must be present in the subduction slab in order to detect a 1 % shear wave velocity decrease compared to non-carbonated lithologies at transition zone to lower mantle boundary depths.

7.1. Introduction

Over the past two decades, carbonates have been suspected to be one of the main carbon carriers into the Earth's deep interior (Dasgupta and Hirschman 2010). Rare, but indisputable, examples of natural samples in the form of superdeep-diamond inclusions (Kaminsky et al. 2012), exhumed metamorphic rocks and xenoliths (Becker and Altherr 1992; Liu et al. 2015) or carbonate-rich lavas (Fischer et al. 2009) have supported this hypothesis. Samples that carry a mantle signature are extremely rare and thus an experimental approach has been used to investigate such systems. More concretely, the physical properties of various carbonate minerals have been extensively studied at pressures and temperatures of the Earth's mantle to determine their structural and chemical stability at these great depths (e.g. Isshiki et al. 2004; Merlini et al. 2012; Cerantola et al. 2017).

Recent experimental studies on the elastic properties of carbonates at extreme conditions raise questions on whether deep carbon cycling can be detected using seismic methods. Sanchez-Valle et al. (2011) first studied carbonated lithologies (eclogites, peridotites) at ambient conditions with results suggesting that their velocity contrast with non-carbonated mantle may be below the threshold of present seismic resolution unless an unrealistically high carbonate fraction is present. However, it was predicted that under high pressure and particularly through the Fe^{2+} spin crossover, the elastic wave velocities of carbonates will increase substantially (Shi et al. 2008). Later Fu et al. (2017) reported the primary and shear wave velocities of a natural Fe-bearing magnesite crystal at high pressure (70 GPa) with emphasis on the abnormal elasticity that it presents across the Fe spin transition. Finally, Stekiel et al. (2017)

investigated the effect of composition in the binary system $FeCO_3$-$MgCO_3$ on the elastic stiffness coefficients including through the spin transition. All previous studies concluded that carbonates have a strong anisotropic behavior. Nonetheless, they also demonstrated that different velocities can be obtained using different techniques.

Several methods can be used to determine elastic wave velocities. Ultrasonic measurements are a reliable method, but they are mainly restricted to upper mantle conditions (< 25 GPa). Brillouin spectroscopy has traditionally been used for obtaining accurate velocities at a much wider pressure range (< 100 GPa) using a diamond anvil cell. However, in situ high pressure and temperature experiments are challenging, the method is restricted by the sample quality, since non-transparent samples cannot be measured and often the diamond signal blocks the sample signal at very high pressures. The latter problem can be overcome by the combination of Brillouin light scattering (BLS) and the impulsive stimulated light scattering (ISS) techniques. Inelastic X-ray scattering (IXS) is another technique that enables measurement of sound velocities of opaque samples. Sound velocities can be measured along selected directions in the crystal, but the determination of mean velocity can require more time compared to other methods. Computational methods, such as density functional theory (DFT) calculations, are an interesting alternative, but have their own challenges. They require a careful choice of various input parameters and produce results that need to be confirmed experimentally (Winkler and Milman, 2014).

Nuclear inelastic scattering (NIS) is a technique that provides information on the thermoelastic properties of a material by probing lattice vibrations (Chumakov and Rüffer 1998). It is most common to measure the partial density of phonon states (pDOS) of materials using NIS. However, the relationship between the low-energy regime of a reduced DOS (i.e. rDOS = pDOS/Energy^2) function and the Debye sound velocity of the sample was soon recognized (Hu et al. 2003). Since then, NIS has been used to derive accurate Debye velocities from monoatomic solids (Hu et al. 2003) to diatomic solids and solid solution systems (Sturhahn and Jackson 2007; Sinmyo et al. 2014) at ambient conditions. The method was successfully used in high-pressure environments using diamond anvil cells (McCammon et al. 2016; Vasiukov et al. 2018) and also at high temperatures (Shen et al. 2004; Kupenko et al. 2015).

In this work, we use NIS to determine in-situ the sound velocities of Fe-bearing carbonates at pressure and temperature conditions of the Earth's mantle. Siderite ($FeCO_3$) and ferromagnesite $(Fe,Mg)CO_3$ are polyatomic compounds with strong anisotropic behavior, owing to their calcite-type structure ($R\bar{3}c$). We present a parallel high-pressure compressibility study using single-crystal X-ray diffraction (SCXRD) which enables us to derive secondary (Vs) and primary (Vp) wave velocities from the calculated Debye velocities using NIS. The ultimate goal of our study is to investigate the possibility to

detect carbonates using the present seismic technology and provide further insight into the Earth's deep carbon cycle.

7.2. Methods

7.2.1. Sample preparation and NIS measurements

Synthetic samples were prepared in either powder or single crystal form. All Fe-bearing samples were enriched in the ^{57}Fe isotope, in order to enhance the NIS signal and decrease the collection time. Cerantola et al. (2015) described the synthesis procedure in detail, especially for the Fe end-member ($FeCO_3$). Further synthesis of solid solutions in the binary system $FeCO_3$-$MgCO_3$ was carried out with an additional multi anvil experiment. $^{57}FeCO_3$ and $MgCO_3$ powders were well mixed in stoichiometric proportions and placed into a Re capsule. Crystals of 10 – 80 μm in size were obtained after 10 min annealing at 1550 (±50) ^{o}C and 18 GPa. We collected NIS spectra from two different compositions, namely $^{57}FeCO_3$ and $MgCO_3$ with 26 mol% ^{57}Fe. The chemical composition of our samples was determined after structure solution and refinements using the SCXRD method. Our ferromagnesite crystals obtained by multi anvil synthesis had varying compositions with average 26 mol% (± 4 mol%) Fe content.

NIS spectra were collected at the Nuclear Resonance beamline, ID18 (Rüffer and Chumakov, 1996), at the European Synchrotron Radiation Facility (ESRF, Grenoble, France) during timing mode (16-Bunch or Hybrid storage ring mode). High pressure was generated by panoramic diamond anvil cells (pDACs) (Fig. 1), while high temperature was obtained using a double-sided laser heating system, available at ID18 (Kupenko et al. 2012; Aprilis et al. 2017). The use of a beryllium gasket was necessary since the NIS signal is measured perpendicular to the incident beam direction (Fig. 1). Powder samples were loaded
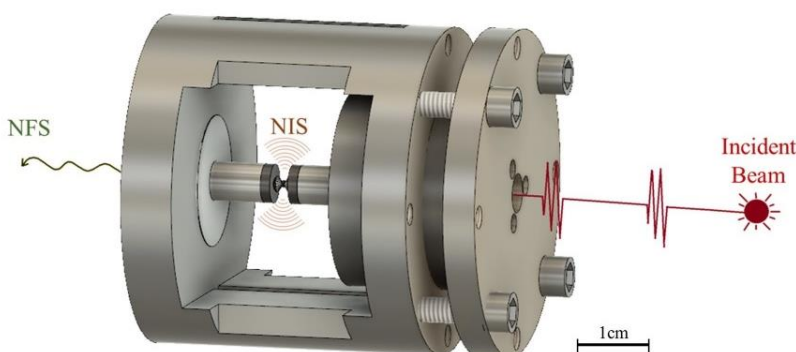
Figure 1. Schematic representation of the panoramic diamond anvil cell (pDAC) created using AutoDesk Fusion 360 (user interactive version: https://a360.co/2NE8RJw). The geometry of the incident beam and NIS and NFS signals are indicated.

inside the pDACs either with KCl as pressure-transmitting medium or with paraffin oil (Table S1). Single crystal samples (~20x15 μm^2, length x thickness) were loaded mostly with paraffin oil. Only a small minority of samples were loaded with Ar gas under pressure (Kurnosov et al. 2008). We recognize the limited hydrostatic conditions that paraffin oil and halides offer during cold compression compared to noble gases, but gas loading was often unsuccessful due to the large instability of beryllium gaskets. Pressure was determined using ruby fluorescence spectra before and after each NIS measurement. Depending on the degree of hydrostatic conditions of each measurement, different calibration references were used (Dewaele et al. 2008; Mao et al. 1986).

The energy dependencies of NIS were collected over a large energy range around the ^{57}Fe nuclear resonance energy of 14.4 keV. We used the range -20 to 100 meV for collections at ambient temperature and the range -100 to 100 meV for collections during heating (Fig. 2). For the majority of our NIS measurements we used a high-resolution monochromator with 2 meV energy bandwidth. The finest energy bandwidth of 0.5 meV was used only for a few sample collections due to limited beamtime. The collection time of one NIS spectrum varied from approximately 15 to 40 min. For each pressure point several scans (3-12) were collected in order to increase statistics and minimize artefacts due to instrument instability. Typically, samples at higher pressures (>50 GPa) required collection of more scans due to the decreasing sample thickness. The experimental set-up at ID18 allowed us to collect nuclear forward
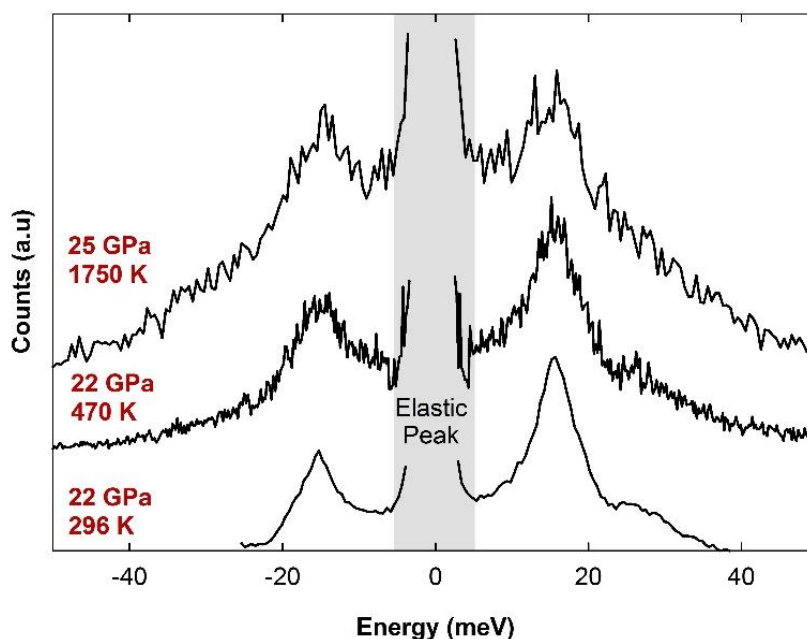
Figure 2. Example of NIS spectra collected from a $FeCO_3$ sample at high pressure and various temperature conditions. The total collection time of each spectrum is ~5 hrs. The shaded grey area indicates the elastic peak that is subtracted during data processing.

scattering spectra (NFS) in parallel with the NIS signal. We used the NFS spectra to distinguish between pressure points where Fe^{2+} was in the high spin (HS) state (Fig. 3a) and the low spin (LS) state (Fig. 3b).
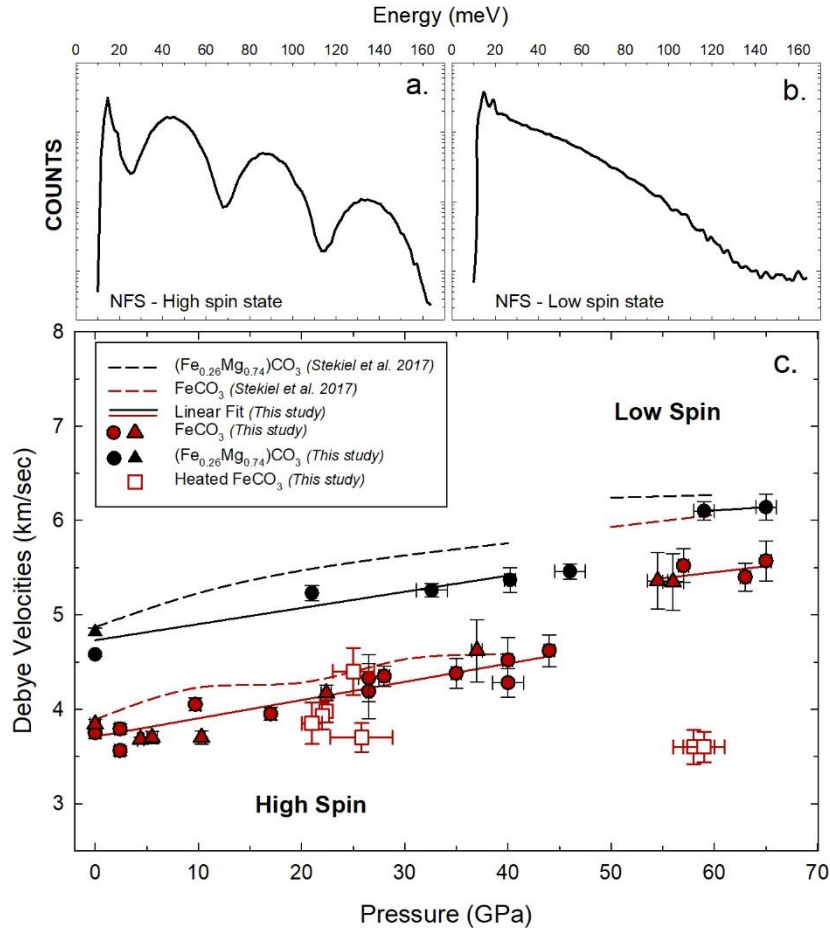
Figure 3. Representative nuclear forward scattering (NFS) spectra for **a)** Fe^{2+} high spin state (<44 GPa) and **b)** Fe^{2+} low spin state (>50 GPa). **c)** Debye sound velocities of siderite and Fe-bearing magnesite with increasing pressure. Triangles refer to powder samples, while circles indicate single crystal samples with random crystallographic orientation. Our data are compared to previously reported DFT calculations (Stekiel et al. 2017) and show good agreement between studies.

7.2.2. Calculation of velocities

The partial DOS and rDOS functions were derived from the initial NIS spectra according to software developed by Kohn and Chumakov (2000). Then, the Debye sound velocities (V_D) were calculated according to the "homogeneous model" as described by Sinmyo et al. (2014) and the following equation (Achterhold et al. 2002; Hu et al. 2003):

$$D(E) = \frac{\widetilde{m}}{m} \cdot \frac{E^2}{2\pi^2 \hbar^3 n V_D^3} , \qquad (1)$$

where $\tilde{m}$ is the mass of the nuclear resonant isotope (i.e. ^{57}Fe), m is the average atomic mass, $\hbar$ is Planck's constant and n is the density of atoms. Only the low energy regime of the rDOS function, typically an interval of 5meV between the energy range 2-10 meV, is used for the determination of the V_D velocities. For each pressure point, we selected the appropriate 5 meV energy range judging from the statistics of the measurement and the energy bandwidth of the high-resolution monochromator that was used. Finally, using the relationship between V_D velocities and the primary and shear wave velocities, the latter can be calculated by solving the following three equations:

$$\frac{3}{V_D^3} = \frac{1}{V_P^3} + \frac{2}{V_S^3} \tag{2}$$

$$V_P = \sqrt{\frac{K + \frac{4}{3}G}{\rho}} \tag{3}$$

$$V_S = \sqrt{\frac{G}{\rho}}\,, \tag{4}$$

where K is the adiabatic bulk modulus, G is the shear modulus and ρ is the density.

7.2.3. Single crystal X-ray Diffraction

In order to determine velocities, it was necessary to obtain accurate ρ and K values of the same sample compositions that we used for NIS experiments. This was possible by obtaining the equations of state (EoS) of FeCO$_3$ and (Mg$_{0.74}$Fe$_{0.26}$)CO$_3$ up to ~66 and 60 GPa, respectively. Two single crystals of each composition were separately loaded inside two BX-90 cells (Kantor et al. 2012) with Boehler-Almax design diamonds and equivalent WC seats. The diamond culet size was 250 µm diameter. We used Re gaskets and Ne as the pressure transmitting medium, where neon under pressure served as a pressure determinant (Fei et al. 2007) (http://kantor.50webs.com/diffraction.htm).

The SCXRD study was carried out at the high-pressure X-ray diffraction beamline, ID15b, at ESRF. We collected XRD patterns during ± 38º omega rotation, with 1 sec exposure time for every 0.5º step. Integration of the reflection intensities and absorption corrections was performed using CrysAlis^{PRO} software (Rigaku 2015). The software package JANA (Petricek et al. 2014) was used for structure solution and refinements. When the number of reflections was sufficiently high, all atoms were refined in the ani-

sotropic approximation, giving in total 10 refinable parameters for typically 80-90 unique reflections with $F_o > 3\sigma$ (F_o). In the few datasets that the reflection to refined parameter ratio was too low, we refined only the anisotropic parameters of the metal cations (Fe, Mg). We used the software package EoSFit7 (Angel et al. 2014; Gonzalez-Platas et al. 2016) to determine equations of state that incorporated weighted fits for both pressure and volume.

7.3. Results

7.3.1. Equations of state

The pressure-induced spin transition of Fe^{2+} in Fe-bearing carbonates has been documented by several methods, including Mössbauer spectroscopy (Cerantola et al. 2015), X-ray diffraction (Lavina et al. 2010a), X-ray Raman scattering (Weis et al. 2017), and Raman spectroscopy (Müller et al. 2016). There is much discussion in the literature concerning the exact pressure that the spin transition takes place, whether it is sharp or not, and how impurity elements in a natural sample affect the transition. Despite the arguments, most of the previous studies agree that the spin transition in $FeCO_3$ starts around 40-44 GPa, while the onset of the transition can shift to slightly higher pressures with the addition of Mg. In this study, we detected the spin transition by NIS, NFS and SCXRD on synthetic samples.

Using SCXRD we observed a dramatic volume drop of ~10% above ~44 GPa for $FeCO_3$ (Fig. 4) as a previous study has suggested (Lavina et al. 2010a). At approximately the same pressure, a less dramatic volumetric effect (~ 3%) was seen in the solid solution $(Mg_{0.74}Fe_{0.26})CO_3$ (Fig. 4). These observations are directly associated with the spin crossover of Fe^{2+}, which induces a reduction of the metal cation radius and thus a volume collapse of FeO_6 octahedra (Fig. S1). At the same time, the rigid triangular CO_3 units slightly expand (Fig. S2).

In the case of $FeCO_3$ with HS Fe^{2+} (i.e. pressure interval 0 – 44 GPa), the volume data were fitted to both a 2nd and 3rd order Birch-Murnaghan (BM) equation of state, resulting in K_0=122.0(6) GPa , $K_0{'}$= 4, V_0= 292.66(2) $Å^3$ and K_0=125(3) GPa, $K_0{'}$= 3.8(2), V_0= 292.66(2) $Å^3$, respectively. The 2nd order BM equation gives a statistically better fit to our data, and $K_0{'}$ does not differ significantly from 4. These values are in relatively good agreement with previous studies (Lavina et al. 2010a, Zhang et al. 1998) (Table S2). For $(Fe_{0.26}Mg_{0.74})CO_3$ with HS Fe^{2+} (i.e. pressure interval 0 – 44 GPa), a 2nd order BM-EoS was used resulting in K_0=115.1(5) GPa , $K_0{'}$= 4 and V_0= 282.69(8) $Å^3$. Alternatively, the parameters become K_0=112(1) GPa and $K_0{'}$=4.3(1) if a 3rd order BM-EoS is used. In Figure 4 we compare the EoS of the two samples when $K_0{'}$=4. We observe that at 44 GPa, pure $FeCO_3$ (K_{44GPa}=284.2(6) GPa, V_{44GPa}=232.2(2) $Å^3$) is less compressible than the $(Mg_{0.74}Fe_{0.26})CO_3$ (K_{44GPa}=273.4(5) GPa, V_{44GPa}=223.0(2) $Å^3$) by ~4%.

Fitting the P-V data after spin crossover to an EoS involves greater uncertainties. Since the K_0' parameter of the above equations of states (i.e. HS-Fe^{2+}) is close to 4, we decided to fit a 2nd order BM EoS for both compositions with LS-Fe^{2+} (Fig. 4). Thus, for LS-siderite (i.e. pressure interval 46 – 66 GPa) the zero pressure volume and bulk modulus become V_0= 250(1) Å^3 and K_0= 172(8) GPa, respectively. In the case of LS-ferromagnesite (i.e. pressure interval 48 – 60 GPa), we obtain V_0= 266(4) Å^3 and K_0= 146(13) GPa. We note that at 48 GPa, pure siderite (K_{48GPa}= 346(8) GPa, V_{48GPa}=207.0(2) Å^3) becomes even less compressible than Fe-bearing MgCO3 (K_{48GPa}= 314(13) GPa, V_{48GPa}=216.0(2) Å^3) by ~10%.
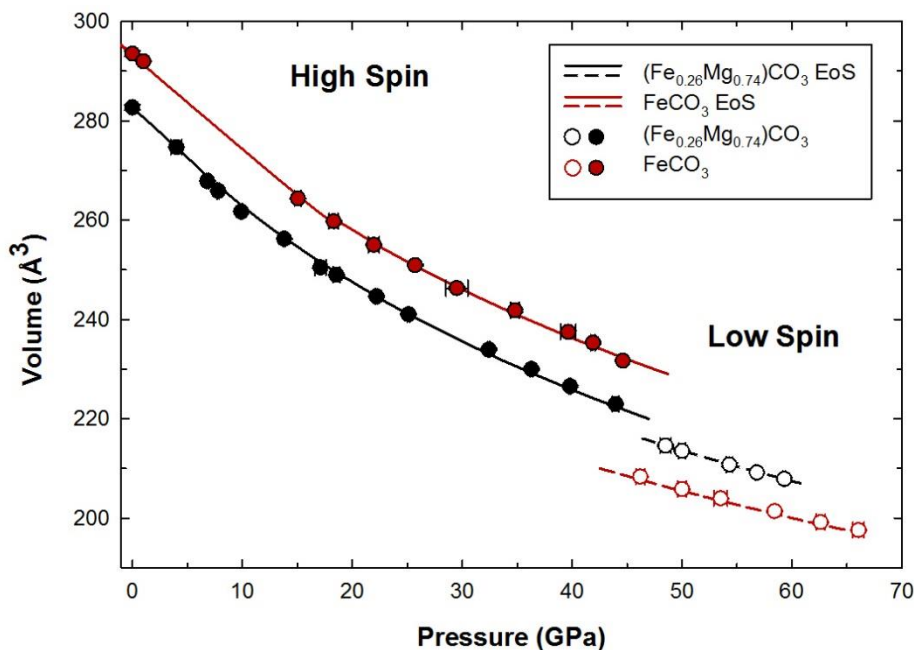
Figure 4. Equations of state (EoS) of single crystal FeCO$_3$ and (Mg$_{0.74}$Fe$_{0.26}$)CO$_3$. The error bars fall within the size of the symbols.

7.3.2. Sound Velocities

7.3.2.1. Cold compression

There are two primary effects detected by NIS in this study. First is the effect of chemical composition on the sound velocities. Equation 1 demonstrates that the Debye velocity of a material is inversely related to its density (via the n parameter). Note that we obtained the density of our two carbonate samples as a function of pressure using SCXRD (Table S1). In addition, V_D velocities are inversely related to both the curvature of the pDOS at low energies (< 10 meV) and the intercept of the rDOS at zero energy (Hu et al. 2003). For example, Figure 5a illustrates the rDOS functions obtained for our two samples at ambient conditions. We observe that (Mg$_{0.74}$Fe$_{0.26}$)CO$_3$ shows clearly a lower zero energy intercept compared to

$FeCO_3$, leading to the result that $(Mg_{0.74}Fe_{0.26})CO_3$ has a ~19% higher sound velocity than pure $FeCO_3$ (Fig. 3c).

The second effect relates to the influence of the Fe^{2+} spin transition on sound velocities. After Fe^{2+} adopts a LS electronic configuration, the V_D velocities increase substantially. For example, Figure 5b demonstrates the pDOS functions of $FeCO_3$ with increasing pressure and along the spin transition. Note that for HS-$FeCO_3$, the pDOS curvature decreases with increasing pressure (35 to 44 GPa) (Fig. 5b), and thus the V_D velocities constantly increase (Fig. 3c). However, above 50 GPa the pDOS curvatures are significantly lowered, resulting in substantially higher (by nearly 19%) V_D velocities. We observe similar but less pronounced behavior (~9%) in the case of $(Mg_{0.74}Fe_{0.26})CO_3$ (Fig. 3c).

We collected NIS data from both powders and single crystals. The crystals were placed in the sample chamber without selecting specific crystallographic orientations. At the same pressure conditions, each crystal gave different pDOS functions and thus different sound velocities outside of experimental error. For example, the V_D velocities of two siderite crystals at ~2.5 GPa differ by ~6% (Fig. 3c; Table S1). Another notable example is the V_D velocities of a single crystal $(Mg_{0.74}Fe_{0.26})CO_3$ and its powdered form, which at 1 bar differ by ~5% (Fig. 3c; Table S1). NIS is sensitive to crystallographic orientation (Chumakov and Rüffer 1998). Similar effects have been previously reported for a $FeBO_3$ single crystal (Chumakov et al. 1997; Parlinski et al. 2001), which is isostructural to the calcite-type carbonates. The different velocities that we observe are likely related to the strong anisotropic nature of carbonates. This interesting phenomenon will be the subject of more careful investigation in the future.
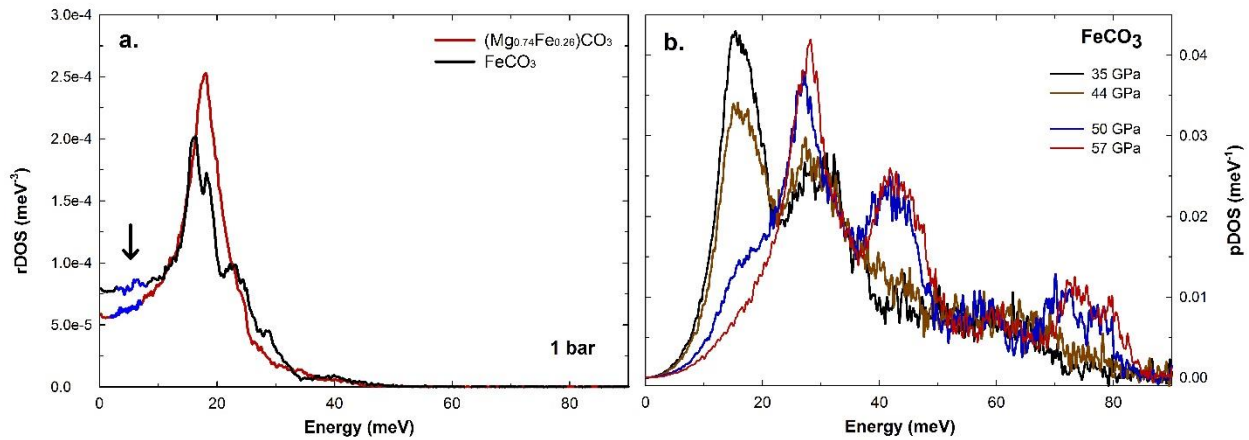
Figure 5. a) Reduced density of state (rDOS) functions of $FeCO_3$ and $(Mg_{0.74}Fe_{0.26})CO_3$ at ambient pressure, demonstrating the effect of composition on the sound velocities. The arrow points at the data points (blue lines) that are considered for the calculation of V_D using Equation 1. The lower intercept of the rDOS curve at zero energy indicates higher velocities. **b)** Partial density of state (pDOS) functions of $FeCO_3$ along the spin transition. The lower curvature of the pDOS curve at low energies (< 10 mev) indicates higher velocities. Note the abrupt peak shifts once the transition is completed.

7.3.2.2. During and after heating

The capability for in situ high pressure and high temperature collection is one of the great advantages of the NIS method. Previous studies have demonstrated the feasibility of such experiments in laser-heated diamond anvil cells (e.g. Shen et al. 2004). In particular, the double-sided laser set-up installed at the ID18 beamline is able to provide a stable laser beam and operate in a continuous or pulsed mode for heating periods as long as ~12 h (Kupenko et al. 2012; Aprilis et al. 2017).

The sample temperature during heating is firstly determined by the thermal radiation signal using spectroradiometry. Additionally, we determine the temperature from the Boltzmann factor using the NIS signal (Chumakov et al. 1996; Shen et al. 2004). For example, Figure 2 shows three NIS spectra of the same sample with increasing temperature. The peak around +16 meV represents phonon creation, while the peak at -16 meV corresponds to phonon annihilation. As temperature increases, the intensity of the two peaks becomes more symmetric and their ratio is given by the Boltzmann factor, which has an exponential relation to the sample temperature (see supplementary material, Eq. S3). Nearly all temperatures shown in Table S3 were calculated from the combination of the two methods. Temperatures below 1000 K could be estimated only from the NIS signal.

We observed that laser heating of siderite at conditions close to the top of the lower mantle decreases the sound velocities slightly (Fig. 3c). Such a result is consistent with the changes of thermal parameters expected when increasing the temperature of the sample (e.g. Yang et al. 2014). However, due to the limited number of data points we cannot provide more definitive results on the temperature dependence of velocities. The slight velocity decrease that we observed is consistent for all data within measurement uncertainty in nearly all cases, except for one point at ~26 GPa (Fig. 3c; Table S3). We postulate that the pressure in the cell dropped from ~37.0(5) to 26(2) GPa during laser heating (~1700 K), because the ruby signal showed non-hydrostatic conditions and one of the diamonds anvils was found to be cracked. Although the lower velocity of this sample might be the result of a pressure gradient, it could also be an indication of a change such as due to a decomposition reaction. Therefore, we consider this measurement to be uncertain.

Heating at lower mantle conditions (>1200 km depth) resulted in an abrupt velocity drop (Fig. 3c). It is likely that the NIS signal collected is not from the original sample which may have thermally decomposed. We were not able to collect XRD patterns of the sample; however, an extensive study on the phase stability of synthetic pure $FeCO_3$ (Cerantola et al. 2017) showed that siderite decomposes to high-pressure Fe_3O_4 (Bbmm) close to the P-T conditions of our measurements. To our knowledge, there are no data in the literature that describe the elasticity of magnetite at pressures above ~20 GPa, so we

are not able to compare the velocities we obtained at 56-60 GPa and 900-1700 K (Table S3). Our hypothesis that siderite decomposition is responsible for the observed velocity decrease does not rule out other possible interpretations of our data. However we have excluded the possibility of a pressure drop in the cell and/or the presence of mixed spin states in the sample (Fig. S4).

7.4. Discussion

It is possible to estimate the primary and secondary elastic wave velocities using NIS (Eq. 2), even though NIS is not able to retrieve a full elastic tensor of the sample. To calculate velocities, it is crucial to have accurate values of the sample density and bulk modulus as a function of pressure. In the present study, we have obtained ρ and K_P (K at pressure) (Table S1) as well as V_D using SCXRD and NIS, respectively. Substitution of equations (3) and (4) in (2) results in equation (5) where G, the shear modulus, is the only unknown parameter:

$$\frac{3}{V_D^3} - \left(\frac{K}{\rho} + \frac{4G}{3\rho}\right)^{-\frac{3}{2}} - 2\left(\frac{G}{\rho}\right)^{-\frac{3}{2}} = 0 \,. \tag{5}$$

We extract the shear modulus by solving equation (5), where the uncertainty in G is estimated through error propagation. Knowing all the necessary parameters, we were able to determine V_P and V_S through equations (3) and (4) (Table S1).

Figure 6 illustrates the elastic wave velocities of $FeCO_3$ and $(Mg_{0.74}Fe_{0.26})CO_3$ determined from our NIS experiments. For comparison, we have plotted the velocity curves derived from fits to experimental IXS data combined with DFT calculations reported by Stekiel et al. (2017). Although our velocities are slightly lower than those from the DFT calculations, we observe that the two datasets follow similar trends (Fig. 6). In particular, the agreement between studies at ambient conditions is remarkable (Sanchez-Valle et al. 2011; Stekiel et al. 2017). The discrepancies at high pressure may be due to several reasons as presented below.

The bulk modulus is important to the calculation of elastic wave velocities, but the uncertainty in K_P is not high enough to explain the discrepancies. For example, the error of ±8 GPa at low spin $FeCO_3$ will induce less than 1% difference in the V_P and V_S calculation. However, Kantor et al. (2008) demonstrated that bulk moduli values obtained for the same sample by XRD and IXS methods may differ up to 20 %. Such an inconsistency may explain why our velocities, with K determined by XRD, are lower than those reported by Stekiel et al. (2017), where K was determined by IXS and DFT calculations (Fig. S3). In order

to consider this further, we compared the Debye velocities obtained from the two studies (Fig. 3c). The calculation of V_D using NIS does not depend on the bulk modulus (Eq. 1). Indeed, the two datasets are in good agreement with the exception of LS-FeCO$_3$, where we observed an ~11% mismatch. Previous studies showed that the velocity jump after the Fe^{2+} spin transition is most pronounced for Fe-rich compositions (Stekiel et al. 2017; Fu et al. 2017). Although, our data follow this trend with increasing Fe content, the case of the pure Fe end-member remains unexplained.

Sinmyo et al. (2014) discussed in detail other reasons for discrepancies between NIS results and other methods, such as the minor effect of impurities and defects or the more considerable effect of Fe clustering in synthetic samples. In Figure 6, we note that V_P velocities obtained by NIS have higher discrepancies with previous studies compared to our V_S values. This is an expected pattern. Primary and secondary velocities in this study are calculated using V_D; however around 90% of the V_D value comes from V_S (Eq. 2). Our estimations of V_S are hence better determined from NIS than those of V_P. Finally, we note that differences may be due to the strongly anisotropic nature of carbonates. Sturhahn and Jackson (2007) showed that the equations used for the estimation of V_P and V_S using NIS hold only approximately for
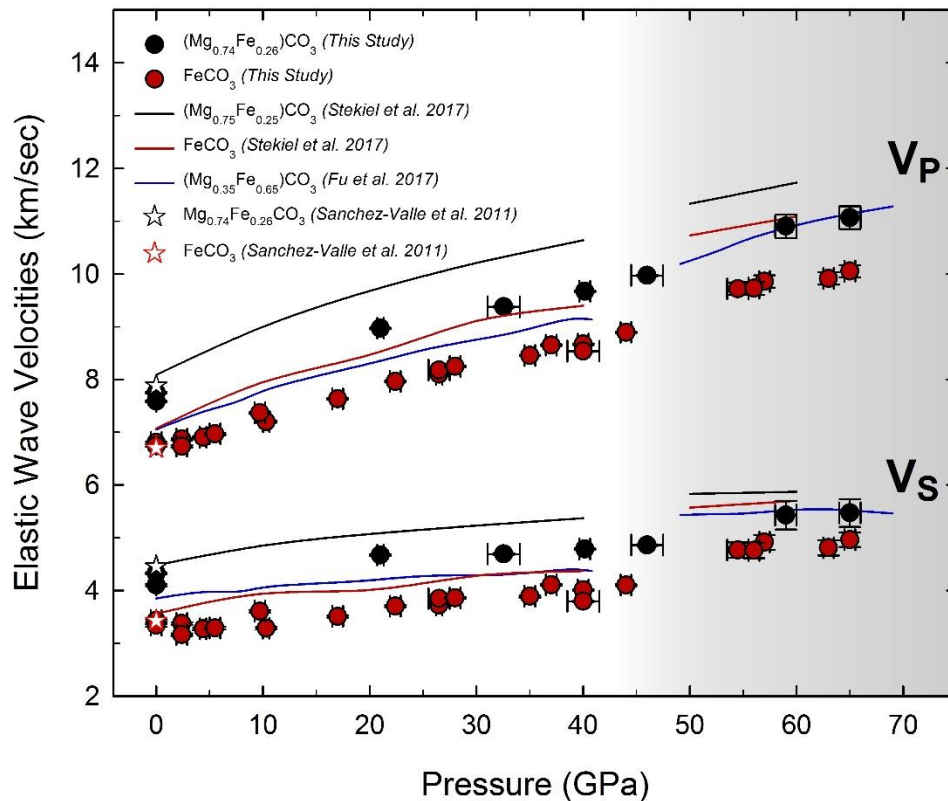
Figure 6. Pressure dependence of the primary (V_P) and secondary (V_S) wave velocities of our two carbonate compositions as derived from the Debye velocities. The errors bars shown are estimated using error propagation (see supplemental information). Our data show similar trends to previous studies. The grey shaded area indicates the Fe^{2+} low spin state.

anisotropic materials and the resulting velocities may deviate from actual values by a few percent or more for strongly anisotropic materials.

7.5. Implications

Previous studies have considered the possibility to detect carbonates in the deep Earth using geophysical methods. Sanchez-Valle et al. (2011) suggested that, depending on composition, an unrealistically high CO_2 content (~15-20 wt%) must be present in order to observe a contrast above the assumed 2% seismic resolution limit between carbonates and crust lithologies. Similarly, Yang et al. (2014) concluded a low probability of detecting ferromagnesian carbonates in the upper mantle where more than 10 wt% pure $MgCO_3$ (~5 wt% CO_2) would be needed to produce a 1% velocity drop. On the other hand, Fu et al. (2017) argued that at lower mantle depths (~1200 km) where the Fe^{2+} spin crossover takes place, the abnormal elastic behavior of Fe-bearing carbonates would induce a drastic decrease of V_P (~10%), thus increasing the probability to seismically detect such a feature. Stekiel et al. (2017) did not observe this abnormal elasticity, likely due to the coarser pressure steps in their experiments and that calculations were performed for pure spin states. However they concluded that the Fe spin transition would induce an observable velocity contrast (~1% Vs decrease) if at least 8-9% $(Fe_{0.15} Mg_{0.85})CO_3$ were present in pyrolitic mantle. Here we elaborate further on the seismic detectability of Fe-bearing carbonates based on the effects of composition, spin transition, and phase stability at Earth's mantle conditions.

Due to the limited constraint on V_P from our NIS measurements as explained above, we consider only V_S for our data comparisons to the PREM model (Dziewonski and Anderson 1981). The AK135 reference model, which differs mostly for upper mantle velocities compared to PREM, could be used instead (Kennett et al. 1995); however our conclusions are not substantially changed. We acknowledge that the use of averaged one-dimensional models (i.e. PREM, AK135) likely sets an upper limit for carbonate detectability, since 2D and 3D models with higher resolution in subduction regions will provide more sensitivity. Modern seismic techniques can offer high-resolution velocity perturbation maps with a scale as fine as 1 % (e.g. Fukao and Obayashi 2013; Chen et al. 2017).

Previous studies agree that the most realistic ferromagnesian carbonate composition expected in deep subducted slabs has approximately ~15 wt% Fe content (McDonough and Sun 1995; Dasgupta et al. 2004). Thus, using our data (see also Eq. S4-S7 in the supplementary material and details therein) and assuming a linear relation we calculated the shear velocities of $(Fe_{0.15}Mg_{0.85})CO_3$ at room temperatures (Fig. 7). Subsequently, we determined the minimum amount of $(Fe_x Mg_{x-1})CO_3$ (where x=1, 0.26 or 0.15)

needed to detect carbonates by geophysical methods. Therefore, we estimated the amount of carbonate necessary to induce a 1% shear velocity drop at various depths within the Earth (Table S4). For example, at uppermost upper mantle depths (~300 km), carbonates of $(Mg_{0.85}Fe_{0.15})CO_3$ composition would be unlikely to be detected (Fig. 7). On the other hand, at the same depths the presence of 4 wt% $FeCO_3$ would be enough to cause a 1% shear velocity decrease. However, the latter scenario is unrealistic since the average composition of subducted carbonates is mostly dolomitic (i.e. Ca- and Mg-rich). Note that as we move to greater depths Ca is preferentially partitioned into silicates and thus Fe-bearing magnesite becomes the dominant carbonate composition that is subducted to the deep Earth (Biellmann et al. 1993). Based on a realistic scenario, our calculations (Table S4) indicate that 9 wt% $(Mg_{0.85}Fe_{0.15})CO_3$ would be required to detect carbonates in the lowermost part of the transition zone (~600 km). The presence of 5 wt% $(Fe_{0.15}Mg_{0.85})CO_3$ well mixed with a lower mantle assemblage will be sufficient to detect carbonates in the uppermost lower mantle (~1000 km). The Fe spin transition that follows at greater depths (~1450 km) would, in contrast, increase the amount of $(Mg_{0.85}Fe_{0.15})CO_3$ (~6 wt%) needed to detect a 1 % V_S drop. Nevertheless, the latter case may be questionable, since the effect of temperature was not considered so far.

In the present study, we demonstrated that the elastic wave velocities of $FeCO_3$ during heating at low pressures are very close to those of the original sample before the thermal treatment (Fig. 3c). On the other hand, at high pressures and after the spin transition, there is a high probability that $FeCO_3$ will decompose (Cerantola et al. 2017) and thus velocities will dramatically drop. Therefore, if we take into consideration the effect of temperature in the above calculations, then the presence of Fe-oxides may play an important role in the velocity profiles of the lower mantle compared to carbonates. This interesting observation motivates further work. Although, $FeCO_3$ appears thermodynamically unstable at lower mantle conditions, the addition of Mg can extend its chemical and structural stability to greater depths (Ishiiki et al. 2004; Cerantola et al. 2017). Hence, any assessment of the amount of $(Fe0.15 Mg_{0.85})CO_3$ needed to produce a 1 % velocity drop at low- spin-state-related depths (>1200 km) will strongly depend on its stability at these conditions.

We have discussed the complications of detecting carbonates at middle lower mantle (>1200 km) and uppermost upper mantle (< 410 km) depths, but detecting carbonates in the transition zone (410 to 660 km) may be challenging as well, due to competition from other phases that could also cause velocity anomalies. Many candidates have been proposed to cause anisotropic anomalies at these depths, such as hydrous wadsleyite, ringwoodite, akimotoite, and other dense hydrous magnesium silicate phases

(Nowacki et al. 2015; Buchen et al. 2018). Nonetheless, owing to their high anisotropy and velocity contrast compared to major mantle mineral assemblages, carbonates are equally plausible candidates.

Further geological aspects are important to consider regarding carbonates. Our calculations demand the presence of at least 9 wt% $(Fe_{0.15}Mg_{0.85})CO_3$ at ~600 km, which means that sediments and the subducted oceanic lithosphere should have at least ~4.4 wt% CO_2 content initially. This is a significant amount of CO_2 that most present-day subduction zones do not have. In addition, a large portion of subducted CO_2 will recycle to the crust or atmosphere mainly via volcanic activities. A precise estimate of CO_2 net flux has been a challenging task and strongly depends on the local geologic setting (Dasgupta and Hirschmann 2010; Kelemen and Manning 2015). Therefore, if we assume that only 20 % of subducted CO_2 will be stored in the deep convecting mantle, this would imply that the initial subducted material would need to contain ~22 wt% CO_2 in order to detect carbonates at the transition zone – lower mantle boundary.
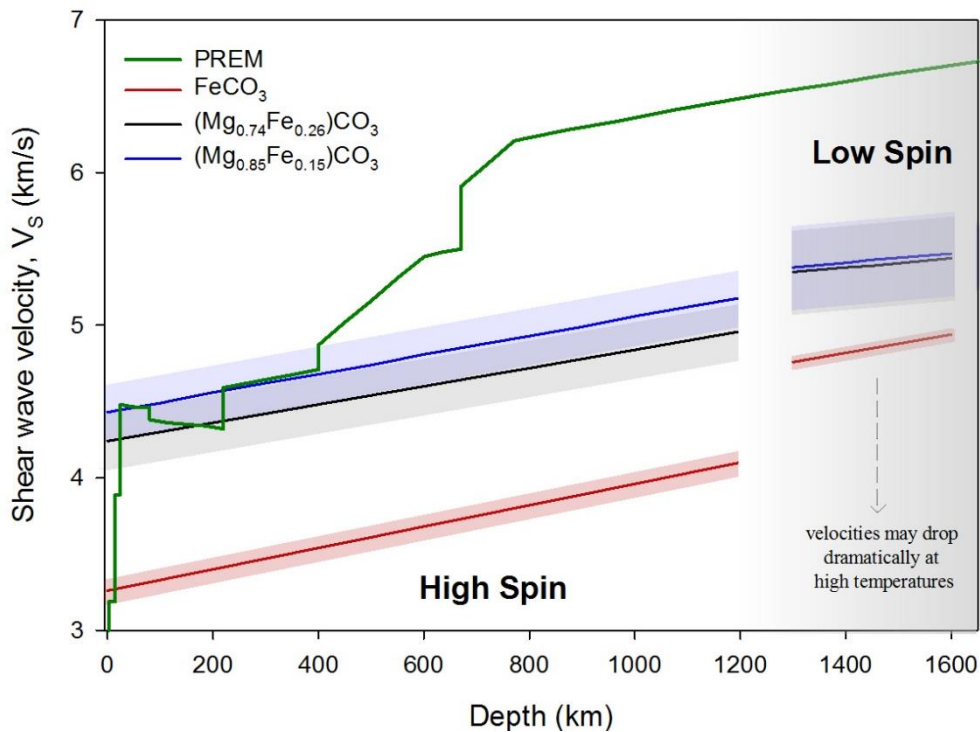
Figure 7. Shear wave velocities (V_S) of the PREM model compared to our modeled carbonate compositions as a function of depth. The effect of temperature is not taken into account in this plot (see text for details).

A few subduction trenches exist today that contain a high amount of CO_2 (Plank and Langmuir 1998), such as the Guatemala (DSDP site 495), Peru (IODP site 321) and Colombian (DSDP site 504) trenches. Interestingly, the subduction zone under Guatemala is a well-known example where a slab

deeply penetrates the lower mantle and is associated with either the subduction of the Cocos plate or with remnants of the Farallon plate (Fukao and Obayashi 2013). Likewise, the Nazca plate subducts under Peru and Colombia with a north-east inclination and the slab is known to penetrate the 660 discontinuity and be trapped in the uppermost lower mantle (Fukao and Obayashi 2013). These are some of the regions that are of high interest for possible future geophysical surveys looking for carbonates in the deep Earth.

There are other influencing parameters that could be considered. For example, the anisotropic behavior of carbonates could affect the threshold limit of carbonate detection as described above. However, this strongly depends on the existence of lattice preferred orientation (LPO) and/or foliation of carbonates, a topic which is poorly examined in the literature so far. In addition, the formation of isolated carbonate-rich reservoirs could give rise to anisotropic anomalies in the mantle. This scenario is highly plausible due to the low solubility of carbon in silicates and the large immiscibility gap between carbonate and silicate melts (Shcheka et al. 2006). Finally, our discussion of carbonate detection is based on present-day carbonate sedimentation rates and plate tectonic activity. However, carbon incorporation in the mantle could have been quite different in the past. These are important topics to be considered, and while they are beyond the scope of the present study, they help to motivate future work in this area.

Keywords

Nuclear Inelastic Scattering; Fe-bearing carbonates; High pressure and temperature; spin transition; elastic wave velocities

7.6. Acknowledgements

7.7. References

Achterhold, K., Keppler, C., Ostermann, A., van Bürck, U., Sturhahn, W., Alp, E.E., and Parak, F.G. (2002) Vibrational dynamics of myoglobin determined by the phonon-assisted Mössbauer effect. Physical Review E, 65, 051916.

Angel, J.R., Alvaro, M., and Gonzalez-Platas, J. (2014) EosFit7c and a Fortran module (library) for equation of state calculations. Zeitschrift für Kristallographie – Crystalline Matters 229, 405–419.

Aprilis, C., Strohm, C., Kupenko, I., Linhardt, S., Laskin, A., Vasiukov, D.M., Cerantola, C., Koemets, E.G., McCammon, C., Kurnosov, A., and others (2017) Portable double-sided pulsed laser heating system for time-resolved geoscience and materials science applications. Review of Scientific Instruments, 88, 084501.

Becker, H., and Altherr, R. (1992) Evidence from ultra-high pressure marbles for recycling of sediments into the mantle. Nature, 358, 745-748.

Biellmann, C., Gillet, P., Guyot, F., Peyronneau, J., and Reynard, B. (1993) Experimental evidence for carbonate stability in the Earth's lower mantle. Earth and Planetary Science Letters, 118, 31-41.

Buchen, J., Marquardt, H., Speziale, S., Kawazoe, T., Boffa-Ballaran, T., and Kurnosov, A. (2018) High-pressure single-crystal elasticity of wadsleyite and the seismic signature of water in the shallow transition zone. Earth and Planetary Science Letters, 498, 77-87.

Cerantola, V., McCammon, C., Kupenko, I., Kantor, I., Marini, C., Wilke, M., Ismailova, L., Solopova, N., Chumakov, A.I., Pascarelli, S., and others (2015) High-pressure spectroscopic study of siderite ($FeCO_3$) with focus on spin crossover. American Mineralogist, 100, 2670-2681.

Cerantola, V., Bykova, E., Kupenko, I., Merlini, M., Ismailova, L., McCammon, C., Bykov, M., Chumakov, A.I., Petitgirard, S., Kantor, I., and others (2017) Stability of iron-bearing carbonates in the deep Earth's interior. Nature Communications, 8, 15960.

Chen, C., Zhao, D., Tian, Y., Wu, S., Hasegawa, A., Lei, J., Park, J-H., and Kang, I-B. (2017) Mantle transition zone, stagnant slab and intraplate volcanism in Northeast Asia. Geophysical Journal International, 209, 68-85.

Chumakov, A.I., Rüffer, R., Baron, A.Q.R, Grünsteudel, H., and Grünsteudel, H.F. (1996) Temperature dependence of nuclear inelastic absorption of synchrotron radiation in a-[57]Fe. Physical Review B, 44, R9599.

Chumakov, A.I., Rüffer, R., Baron, A.Q.R., Grünsteudel, H., Grünsteudel, H.F., and Kohn, V.G. (1997) Anisotropic inelastic nuclear absorption. Physical Review B, 56, 10758.

Chumakov, A.I., and Rüffer, R. (1998) Nuclear inelastic scattering. Hyperfine Interactions, 113, 59-79.

Dasgupta, R., Hirschmann, M.M., and Withers, A.C. (2004), Deep global cycling of carbon constrained by solidus of anhydrous, carbonated eclogite under upper mantle conditions, Earth and Planetary Science Letters, 227, 73–85.

Dasgupta, R., and Hirschmann, M.M. (2010) The deep carbon cycle and melting in Earth's interior. Earth and Planetary Science Letters, 298, 1-13.

Dewaele, A., Datchi, F., Loubeyre, P., and Mezouar, M. (2008) High pressure–high temperature equations of state of neon and diamond. Physical Review B, 77, 094106.

Dziewonski, A.M., and Anderson, D.L. (1981) Preliminary reference Earth model. Physics of the Earth and Planetary Interiors, 25, 297-356.

Fei, Y., Ricolleau, A., Frank, M., Mibe, K., Shen, G., and Prakapenka, V. (2007) Toward an internally consistent pressure scale. Proceedings of the National Academy of Sciences, 104, 9182–9186.

Fischer, T.P., Burnard, P., Marty, B., Hilton, D.R., Füri, E., Palhol, F., Sharp, Z.D., and Mangasini, F. (2009) Upper-mantle volatile chemistry at Oldoinyo Lengai volcano and the origin of carbonatites. Nature Letters, 459, 07977.

Fu, S., Yang, J, and Lin, J-F. (2017) Abnormal elasticity of single-crystal magnesiosiderite across the spin transition in Earth's lower mantle. Physical Review Letters, 118, 036402.

Fukao, Y., and Obayashi, M. (2013) Subducted slabs stagnant above, penetrating through, and trapped below the 660 km discontinuity. Journal of Geophysical Research: Solid Earth, 118, 5920-5938.

Gonzalez-Platas, J., Alvaro, M., Nestola, F., and Angel, R.J. (2016) EosFit7-GUI: A new GUI tool for equation of state calculations, analyses and teaching. Journal of Applied Crystallography, 49, 1377-1382.

Hu, M.Y., Sturhahn, W., Toellner, T.S., Mannheim, P.D., Brown, D.E., Zhao, J., and Alp, E.E. (2003) Measuring velocity of sound with nuclear resonant inelastic x-ray scattering. Physical Review B, 67, 094304.

Isshiki, M., Irifune, T., Hirose, K., Ono, S., Ohishi, Y., Watanuki, T., Nishibori E., Takata, M., and Sakata, M. (2004) Stability of magnesite and its high-pressure form in the lowermost mantle. Nature, 427, 60-63.

Kaminsky, F. (2012) Mineralogy of the lower mantle: A review of 'super-deep' mineral inclusions in diamond. Earth-Science Reviews, 110, 127-147.

Kantor, A., Kantor, I., Kurnosov, A., Dubrovinsky, L., Krisch, M., Bossak, A., and Jacobsen, S. (2008) Anelasticity of Fe_xO at high pressure. Applied Physics Letters, 93, 034106.

Kantor, I., Prakapenka, V., Kantor, A., Dera, P., Kurnosov, A., Sinogeikin, S., Dubrovinskaia, N., and Dubrovinsky, L. (2012) BX90: A new diamond anvil cell design for X-ray diffraction and optical measurements. Review of Scientific Instruments, 83, 125102.

Kelemen, P.B., and Manning, C.E. (2015) Reevaluating carbon fluxes in subduction zones, what goes down, mostly comes up. Proceedings of the National Academy of Sciences, 112, 3997-4006.

Kennett, B.L.N., Engdahl, E.R., and Buland, R. (1995) Constraints on seismic velocities in the earth from travel times Geophysical Journal International, 122, 108-124.

Kohn, V.G., and Chumakov, A.I. (2000) DOS: Evaluation of phonon density of states from nuclear resonant inelastic absorption. Hyperfine Interactions, 125, 205-221.

Kupenko, I., Dubrovinsky, L., Dubrovinskaia, N., McCammon, C., Glazyrin, K., Bykova, E., Boffa-Ballaran, T., Sinmyo, R., Chumakov, A., Potapkin, V., and others (2012): Portable double-sided laser-heating system for Mössbauer spectroscopy and X-ray diffraction experiments at synchrotron facilities with diamond anvil cells. Review of Scientific Instruments, 83, 124501.

Kupenko, I., Strohm, C., McCammon, C., Cerantola, V., Glazyrin, K., Petitgirard, S., Vasiukov, D., Aprilis, G., Chumakov, A.I., Rüffer, R., and L. Dubrovinsky (2015) differentiated nuclear resonance spectroscopy coupled with pulsed laser heating in diamond anvil cells. Review of Scientific Instruments, 86, 114501.

Kurnosov, A., Kantor, I., Boffa-Ballaran, T., Lindhardt, S., Dubrovisnky, L., Kuznetsov, A., and Zehnder, B.H. (2008) A novel gas-loading system for mechanically closing of various types of diamond anvil cells. Review of Scientific Instruments, 79, 045110.

Lavina, B., Dera, P., Downs, R.T., Yang, W., Sinogeikin, S., Meng, Y., Shenand, and G., Schiferl, D. (2010a) Structure of siderite $FeCO_3$ to 56 GPa and hysteresis of its spin-pairing transition. Physical Review B, 82, 064110.

Liu, Y., He, D., Gao, C., Foley, S., Gao, S., Hu, Z., Zong, K., and Chen, H. (2015) First direct evidence of sedimentary carbonate recycling in subduction-related xenoliths. Scientific Reports, 11547.

Mao, H.K., Xu, J., and Bell, P.M. (1986) Calibration of the ruby pressure Gauge to 800 kbar under quasi-hydrostatic conditions. Journal of Geophysical Research, 91, 4673-7676.

McCammon, C., Caracas, R., Glazyrin, K., Potapkin, V., Kantor, A., Sinmyo, R., Prescher, C., Kupenko, I., Chumakov, A.I., and Dubrovinsky, L. (2016) Sound velocities of bridgmanite from density of states determined by nuclear inelastic scattering and first-principles calculations. Progress in Earth and Planetary Science, doi:10.1186/s40645-016-0089-2.

McDonough, W.F., and Sun, S.S. (1995) The composition of the Earth. Chemical Geology, 120, 223-253.

Merlini, M., Crichton, W.A., Hanfland, M., Gemmi, M., Müller, H., Kupenko, I., and Dubrovinsky, L. (2012) Structures of dolomite at ultrahigh pressure and their influence on the deep carbon cycle. Proceedings of the National Academy of Sciences, 109, 13509-13514.

Müller, J., Speziale, S., Efthimiopoulos, I., Jahn, S., and Koch-Müller, M. (2016) Raman spectroscopy of siderite at high pressure: Evidence for a sharp spin transition. American Mineralogy, 101, 2638–2644.

Nowacki, A., Kendall, J-M., Wookey, J., and Pemberton, A. (2015) Mid-mantle anisotropy in subduction zones and deep water transport. Geochemistry Geophysics Geosystems, 16, 764–784.

Parlinski, K., Lażewski, J., Jochym, P.T., Chumakov, A., Rüffer, R., and Kresse, G. (2001) Influence of magnetic interaction on lattice dynamics of $FeBO_3$. Europhysics Letters, 56, 275-281.

Petricek, V., Dusek, M., and Palatinus, L. (2014) Crystallographic Computing System JANA2006: General features. Zeitschrift für Kristallographie - Crystalline Materials, 229, 345–352.

Plank, T., and Langmuir, C.H. (1998) The chemical composition of subducting sediment and its consequences for the crust and mantle. Chemical Geology, 145, 325–394.

Rigaku Oxford Diffraction (2015) CrysAlis[PRO] software system, version 1.171, Rigaku corporation, Oxford, UK.

Rüffer, R., and Chumakov, A.I. (1996) Nuclear Resonance Beamline at ESRF. Hyperfine Interactions, 97/98, 589-604.

Sanchez-Valle, C., Ghosh, S., and Rosa, A.D. (2011) Sound velocities of ferromagnesian carbonates and the seismic detection of carbonates in eclogites and the mantle. Geophysical Research Letters, 38, L24315.

Shcheka, S., Wiedenbeck, M., Frost, D.J., and Keppler, H. (2006) Carbon solubility in mantle minerals. Earth and Planetary Science Letters, 245, 730-742.

Shen, G., Sturhahn, W., Alp, E.E., Zhao, J., Toellner, T.S., Prakapenka, V.B., Meng, Y., and Mao, H-R. (2004) Phonon density of states in iron at high pressures and high temperatures. Physics and Chemistry of Minerals, 31, 353-359.

Shi, H., Luo, W., Johansson, B., and Ahuja, R. (2008) First-principles calculations of the electronic structure and pressure-induced magnetic transition in siderite $FeCO_3$. Physical Review B, 78, 155119.

Sinmyo, R., Glazyrin, K., McCammon, C., Kupenko, I., Kantor, I., Potapkin, V., Chumakov, A.I., Rüffer, R., and Dubrovinsky, L. (2014) The influence of solid solution on elastic wave velocity determination in (Mg,Fe)O using nuclear inelastic scattering. Physics of the Earth and Planetary Interiors, 229, 16-23.

Stekiel, M., Nguyen-Thanh, T., Chariton, S., McCammon, C., Bosak, A., Morgenroth, W., Milman, V., Refson, K., and Winkler, B. (2017) High pressure elasticity of $FeCO_3$-$MgCO_3$ carbonates. Physics of the Earth and Planetary Interiors, 271, 57-63.

Sturhahn, W., and Jackson J.M. (2007) Geophysical applications of nuclear resonant spectroscopy. Geological Society of America, 421, 157-174.

Vasiukov, D.M., Ismailova, L., Kupenko, I., Cerantola, V., Sinmyo, R., Glazyrin, K., McCammon, C., Chumakov, A.I., Dubrovinsky, L., and Dubrovinskaia, N. (2018) Sound velocities of skiagite–iron–majorite solid solution to 56 GPa probed by nuclear inelastic scattering. Physics and Chemistry of Minerals, 45, 397-404.

Weis, C., Sternemann, C., Cerantola, V., Sahle, C.J., Spiekermann, G., Harder, M., Forov, Y., Kononov, A., Sakrowski, R., Yavas, H., and others (2017) Pressure driven spin transition in siderite and magnesiosiderite single crystals. Scientific Reports, 7, 16526.

Winkler, B., and Milman, V. (2014) Density functional theory based calculations for high pressure research. Zeitschrift für Kristallographie, 229, 112–122.

Yang, J., Mao, Z., Lin, J-F., and Prakapenka, V.B. (2014) Single-crystal elasticity of the deep-mantle magnesite at high pressure and temperature. Earth and Planetary Science Letters, 392, 292–299.

Zhang, J., Martinez, I., Guyot, F., and Reeder, R.J. (1998) Effects of Mg-Fe^{2+} substitution in calcite-structure carbonates: Thermoelastic properties. American Mineralogist 83, 280-287.

7.8. Supplementary Material

Table S1. Detailed dataset of all Nuclear Inelastic Scattering experiments at room temperature performed in this study.

Sample	Cell #	Type	PTM$^{\times}$	P (GPa)	ρ (g/cm^3)	K (GPa)	G (GPa)	Vd (km/s)	Vp (km/s)	Vs (km/s)
(Mg$_{0.74}$Fe$_{0.26}$)CO$_3$	1	pwdr*	-	0.00(0)	3.27 (1)	115.1(5)	61.2(5)	4.82(4)	7.75(2)	4.33(2)
	2	rdm cr•	-	0.00(0)	3.27(1)	115.1(5)	55.0(5)	4.58(2)	7.59(2)	4.10(2)
	2	rdm cr	Ar	21.0(3)	3.75(10)	192.9(5)	81.8(5)	5.23(8)	8.97(1)	4.67(1)
	2	rdm cr	Ar	32.6(15)	3.95(18)	231.7(5)	86.9(5)	5.26(7)	9.38(1)	4.69(1)
	2	rdm cr	Ar	40.2(5)	4.07(19)	256.8(5)	93.2(5)	5.37(13)	9.67(1)	4.79(1)
	2	rdm cr	Ar	46.0(15)	4.20(20)	285.6(5)	99.2(5)	5.46(8)	9.97(1)	4.86(1)
	2	rdm cr	Ar	59.0(10)	4.43(20)	353(13)	130(13)	6.10(10)	10.90(22)	5.43(27)
	2	rdm cr	Ar	65.0(10)	4.50(20)	372(13)	134(13)	6.14(14)	11.07(21)	5.47(26)
FeCO$_3$	3	pwdr	Oil$^+$	4.4(3)	4.10(5)	137.0(6)	43.9(6)	3.68(2)	6.90(2)	3.27(2)
	3	pwdr	Oil	10.3(3)	4.27(5)	160.0(6)	46.1(6)	3.70(7)	7.20(2)	3.28(2)
	4	rdm cr1	Ar	26.5(5)	4.66(15)	220.0(6)	64.5(7)	4.19(29)	8.10(1)	3.72(2)
	4	rdm cr2	Ar	26.5 (10)	4.66(15)	220.0(6)	68.9(7)	4.33(25)	8.18(1)	3.85(2)
	4	rdm cr1	Ar	40.0 (5)	4.91(19)	263.9(6)	79.0(7)	4.52(24)	8.67(1)	4.01(2)
	4	rdm cr2	Ar	40.0 (15)	4.91(19)	263.9(6)	70.7(6)	4.28(15)	8.54(1)	3.79(2)
	4	rdm cr1	Ar	54.5(10)	5.73(6)	368(8)	130(8)	5.36(30)	9.72(12)	4.77(15)
	5	pwdr	-	0.00(0)	3.98(6)	121.9(6)	46.8(7)	3.84(5)	6.80(2)	3.43(2)
	6	pwdr	KCl	5.5(5)	4.13(5)	140.9(6)	44.7(6)	3.70(7)	6.96(2)	3.29(2)
	6	pwdr	KCl	22.4(5)	4.58(14)	206.9(6)	62.8(6)	4.17(8)	7.96(1)	3.70(2)

*pwdr = powdered sample; **•rdm cr** = single crystal sample with unknown orientation ; **$^{\times}$PTM** = pressure transmitting medium; $^+$**Oil** = paraffin oil;

Table S1. (Continued…)

Sample	Cell #	Type	PTM$^{\times}$	P (GPa)	ρ (g/cm³)	K (GPa)	G (GPa)	Vd (km/s)	Vp (km/s)	Vs (km/s)
FeCO$_3$	7	rdm cr1•	Oil^{+}	0.00(0)	3.98(6)	121.9(6)	44.4(7)	3.75(6)	6.74(2)	3.34(3)
	7	rdm cr1	Oil	2.4(5)	4.04(1)	129.3(6)	46.0(6)	3.79(6)	6.87(2)	3.37(2)
	7	rdm cr2	Oil	2.4(5)	4.04(1)	129.3(6)	40.4(6)	3.56(5)	6.73(2)	3.16(2)
	7	rdm cr1	Oil	9.7(5)	4.25(5)	157.2(6)	55.2(6)	4.05(7)	7.37(2)	3.60(2)
	7	rdm cr2	Oil	17.0(5)	4.45(9)	186.5(6)	54.8(6)	3.95(7)	7.63(1)	3.51(2)
	7	rdm cr1	Oil	28.0(5)	4.69(18)	226.8(6)	70.0(6)	4.35(11)	8.25(1)	3.86(2)
	7	rdm cr1	Oil	35.0(5)	4.82(20)	247.6(6)	72.9(7)	4.38(16)	8.46(1)	3.89(2)
	7	rdm cr1	Oil	44.0(5)	5.02(20)	284.6(6)	84.4(7)	4.62(17)	8.89(1)	4.10(2)
	7	rdm cr1	Oil	57.0(5)	5.76(6)	375(8)	139(8)	5.52(18)	9.86(12)	4.91(14)
	7	rdm cr1	Oil	63.0(5)	5.85(7)	395(8)	135(8)	5.40(15)	9.91(11)	4.81(14)
	7	rdm cr1	Oil	65.0(5)	5.88(7)	402(8)	145(8)	5.57(21)	10.05(11)	4.96(14)
	8	pwdr*	KCl	37.0(5)	4.86(20)	254.8(6)	81.9(7)	4.62(33)	8.65(1)	4.11(2)
	9	pwdr	KCl	56.0(5)	5.74(6)	370(8)	130(8)	5.35(30)	9.73(12)	4.76(15)

*pwdr = powdered sample; **•rdm cr** = single crystal sample with unknown orientation ; $^{\times}$**PTM** = pressure transmitting medium; $^{+}$**Oil** = paraffin oil;

Table S2. Comparison of the equations of state parameters of ferromagnesite samples between this study and the literature.

	$FeCO_3$ (This study)		$(Fe_{0.72}Mg_{0.24}Mn_{0.03}Ca_{0.01})CO_3$[a] (Lavina et al. 2009,2010a)		$FeCO_3$[a] (Zhang et al. 1998)	$(Fe_{0.60}Mg_{0.38}Mn_{0.02})CO_3$[a] (Zhang et al. 1998)
Sample type	synthetic crystals		natural crystals		natural powder	natural powder
Method	SCXRD[b]		SCXRD		PXRD[c]	PXRD
Spin state	high	low	high	low	high	high
P range (GPa)[d]	0 – 44.6	46.2 – 66	0 – 43.9	46.4 – 56	0 – 8.9	0 – 8.9
V_0 (Å^3)	292.66 (2)[e]	250 (1)[f]	294.4 (3)	263 (3)	292.828 (35)	288.314(133)
K_0 (GPa)	122.0 (6)[g]	172 (8)	110.1(3)	148 (12)	117 (1)	112 (1)
K_0'	4 (fixed)[g]	4 (fixed)	4.6 (2)	5 (fixed)	4 (fixed)	4 (fixed)

	$(Fe_{0.26}Mg_{0.74})CO_3$ (This study)		$(Fe_{0.12}Mg_{0.87}Ca_{0.01})CO_3$[a] (Lavina et al. 2010b)		$(Fe_{0.65}Mg_{0.33}Mn_{0.02})CO_3$[a] (Lin et al. 2012; Fu et al. 2017)	
Sample type	synthetic crystals		natural crystals		natural powder/crystal	
Method	SCXRD		SCXRD		PXRD	
Spin state	high	low	high	low	high	low
P range (GPa)	0 – 44	48.5 – 59.3	0 – 44.1	48.9 – 64.8	0 – 45	45 – 72
V_0 (Å^3)	282.69 (8)[e]	266 (4)[f]	281.0 (5)	-	289.1 (1)	267 (2)
K_0 (GPa)	115.1 (5)[h]	146 (13)	102.8 (3)	-	108 (2)	127 (5)
K_0'	4 (fixed)[h]	4 (fixed)	5.44 (fixed)	-	4.8 (2)	5.1 (2)

	$FeCO_3$ (Stekiel et al. 2017)		$(Fe_{0.25}Mg_{0.75})CO_3$ (Stekiel et al. 2017)		$FeCO_3$[a] (Sanchez-Valle et al. 2014)	$(Mg_{0.33}Fe_{0.65}Mn_{0.02})CO_3$[a] (Sanchez-Valle et al. 2014)
Sample type	-		-		natural crystals	natural crystals
Method	DFT[i]		DFT		BLS[j], SCXRD	BLS, SCXRD
Spin state	low	low	high	low	high	high
Pressure (GPa)	0	59	0	59	1 bar	1 bar
$V_{at\ pressure}$ (Å^3)	310.12	207.54	287.41	208.64	292.58	290.55
$K_{at\ pressure}$ (GPa)	130.80	393.63	112.48	366.71	116 (2)	113 (2)

[a]see reference for more details on sample's chemical composition; [b]single-crystal X-ray diffraction; [c]powder X-ray diffraction; [d]pressure interval of the experiment/calculation; [e]volume measurement at ambient conditions using SCXRD; [f]estimated volume at ambient conditions; [g]alternatively K_0 = 125 (3) and K_0' = 3.8 (2); [h]alternatively K_0 = 112 (1) and K_0' = 4.3 (1); [i] density functional theory calculations; [j]Brillouin spectroscopy

The following equations were used for the calculation of V_P and V_S uncertainty:

$$\sigma_{V_S} = \frac{1}{2}\rho^{-1}(G\rho^{-1})^{-1/2}\sigma_G \qquad\qquad \text{(Eq. S1)}$$

$$\sigma_{V_P} = \left[\rho^{-2}V_P^{-2}\left(\frac{4}{9}\sigma_G{}^2 + \frac{1}{4}\sigma_K{}^2\right)\right]^{1/2} \qquad\qquad \text{(Eq. S2)} \quad,$$

where ρ is density, G is bulk modulus, σ_G is the standard deviation in shear modulus and σ_K is the standard deviation in bulk modulus.

The ratio between phonon creation energies (S(E)) and phonon annihilation energies (S(-E)) is given by the Boltzmann factor as follows:

$$S(E) = e^{\beta E}S(-E) \qquad\qquad \text{(Eq. S3)} \quad,$$

where $\beta = 1/(k_\beta T)$ is the inverse temperature, and k_β the Boltzmann constant. With these equations, we can estimate the sample temperature using the NIS signal.

The following equations describe the linear relation (see also Figure 6) of depth (d in km) with the averaged elastic wave velocity values (V_S and V_P in km/s) that we obtained from our $FeCO_3$ and $(Mg_{0.74}Fe_{0.26})CO_3$ samples using the NIS method:

High spin – $(Mg_{0.74}Fe_{0.26})CO_3$:

$$V_S = 0.0006 \cdot d + 4.2(2) \text{ and } V_P = 0.002 \cdot d + 7.7(4) \qquad\qquad \text{(Eq. S4)}$$

Low spin – $(Mg_{0.74}Fe_{0.26})CO_3$:

$$V_S = 0.0003 \cdot d + 5.0(3) \text{ and } V_P = 0.0012 \cdot d + 9.1(7) \qquad\qquad \text{(Eq. S5)}$$

High spin – $FeCO_3$:

$$V_S = 0.0007 \cdot d + 3.2(1) \text{ and } V_P = 0.002 \cdot d + 6.66(8) \qquad\qquad \text{(Eq. S6)}$$

Low spin – $FeCO_3$:

$$V_S = 0.0005 \cdot d + 4.09(6) \text{ and } V_P = 0.0013 \cdot d + 8.01(5) \qquad\qquad \text{(Eq. S7)}$$

Data points from both powder and crystal samples were considered in the averaging procedure. In the case of $FeCO_3$, data points from powder and single-crystal measurements are uniformly scattered (Figure 3c and 6), thus we can assume that the bulk shear wave velocity can be described by equation (S4). In the case of $(Mg_{0.74}Fe_{0.26})CO_3$, nearly all velocities are represented by measurements on a single crystal with unknown orientation (see Cell#2 in Table S1). Given the sensitivity of the NIS method to crystal orientation we recognize that a systematic error may be introduced in our further modeling calculations of other ferromagnesian compositions. However,

at ambient conditions the Debye and shear wave velocities between a powder sample and our single crystal differ only by 5.1% and 5.5%, respectively, which is comparable to the uniform scattering that is observed for the $FeCO_3$ sample. Therefore, all data points of the $(Mg_{0.74}Fe_{0.26})CO_3$ were considered in the averaging procedure. All equations reported above include the data resolution error. In addition, the errors in equations S4 and S5 account for the systematic error that may be introduced when using single crystal data points. Finally, a linear relation and Vegard's law were assumed for the modeling of the $(Mg_{0.85}Fe_{0.15})CO_3$ shear wave velocities that appear in Figure 7.

Table S3. Detailed dataset of heated samples in this study.

Sample	Cell #	Type	PTM[a]	P (GPa)	T (K)	ρ (g/cm³)	Vd (km/s)
$FeCO_3$	6	pwdr[b]	KCl	22.4(5)	470(50)	4.58(14)	3.98(12)
	6	pwdr	KCl	22.0(5)	296(2)[c]	4.57(14)	3.93(14)
	6	pwdr	KCl	25(2)	1750(100)	4.63(15)	4.40(25)
	8	pwdr	KCl	21(1)	296(2)[c]	4.55(14)	3.85(22)
	8	pwdr	KCl	26(2)	1700(100)	4.64(15)	3.70(15)
	9	pwdr	KCl	58(2)	1100(100)	5.78(6)[d]	3.60(18)
	9	pwdr	KCl	59(2)	1700(100)	5.80(7)[d]	3.60(16)

[a] pressure transmitting medium; [b] powdered sample; [c] measurement on the temperature quenched sample, [d] sample treated as Fe_3O_4 (Bbmm)

Table S4. Calculated minimal amount of carbonate needed to be present at various depths in order to detect seismically a 1 % drop in shear velocities. Note that the composition $(Mg_{0.85}Fe_{0.15})CO_3$ is considered to be the most realistic for the mantle.

Depth (km)	$FeCO_3$	$(Mg_{0.74}Fe_{0.26})CO_3$	$(Mg_{0.85}Fe_{0.15})CO_3$
300	4 wt %	21 wt %	undetectable
600	3 wt %	7 wt %	9 wt %
1000	3 wt %	4 wt %	5 wt %
1450	4 wt %	6 wt %	6 wt %

Supplementary Figures

**Figure S1:** Variation of Fe–O and (Mg,Fe)-O bond lengths for $FeCO_3$ and $(Mg_{0.74}Fe_{0.26})CO_3$ with increasing pressure, respectively. Error bars are shown, and in some cases, are smaller than the size of the symbols.

Figure S1
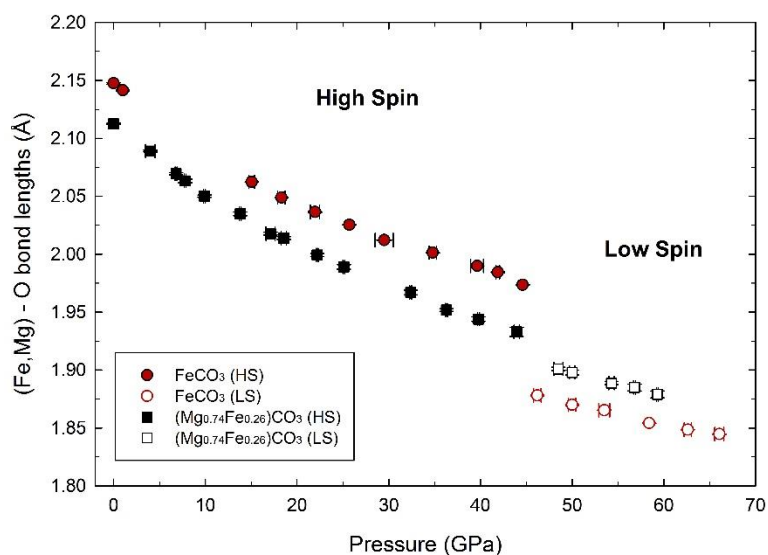
Figure S2: Variation of C–O bond lengths within the CO_3 unit for $FeCO_3$ and $(Mg_{0.74}Fe_{0.26})CO_3$ with increasing pressure.

Figure S2
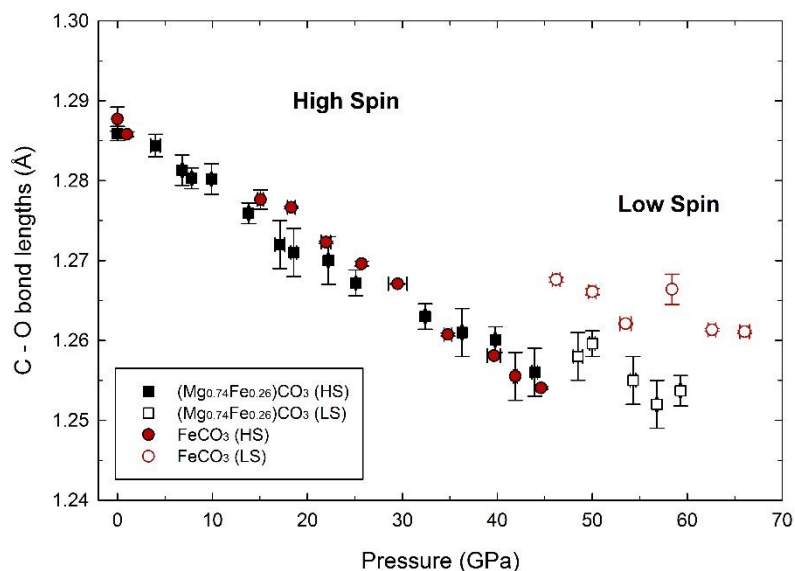
Figure S3: Effect of 20 % increase in bulk modulus on the calculation of V_P. The new values (dashed lines) of this study are compared to the previous study by Stekiel et al. (2017) (bold lines). Although we note that the nature of the samples used in this study and the one of Stekiel et al. (2017) is not the same, the graph illustrates the strong influence of the choice of bulk modulus on V_P.
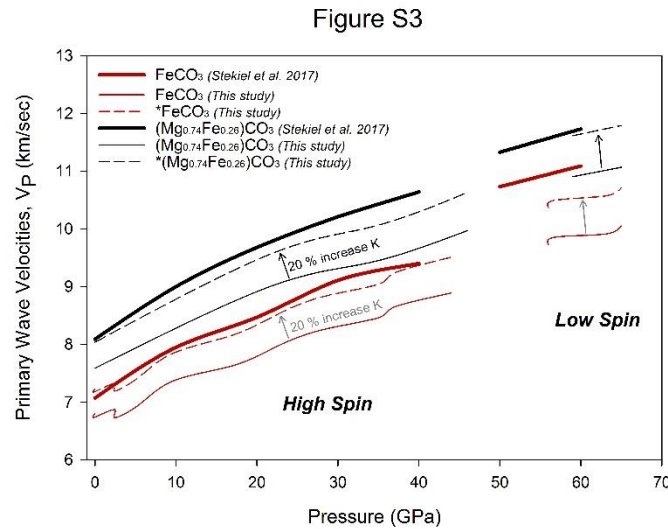
Figure S4: Modeling the effect of mixed Fe spin state compared to Debye velocities of heated $FeCO_3$ at high pressure. Reduced values account for a ~60% drop of primary wave velocities according to Fu et al. (2017) and Equation 2 (main text). The reduced values are not low enough to explain the Debye velocity drop that we observed using NIS. Pressure determination using ruby fluorescence before and after laser heating confirmed that the sample remained under high pressure. The grey dashed line is a guide to the eye showing V_D of $FeCO_3$ at ambient conditions. The heated data (red squares) fall below this line, further suggesting that the two measurements do not correspond to $FeCO_3$ at 1 bar.
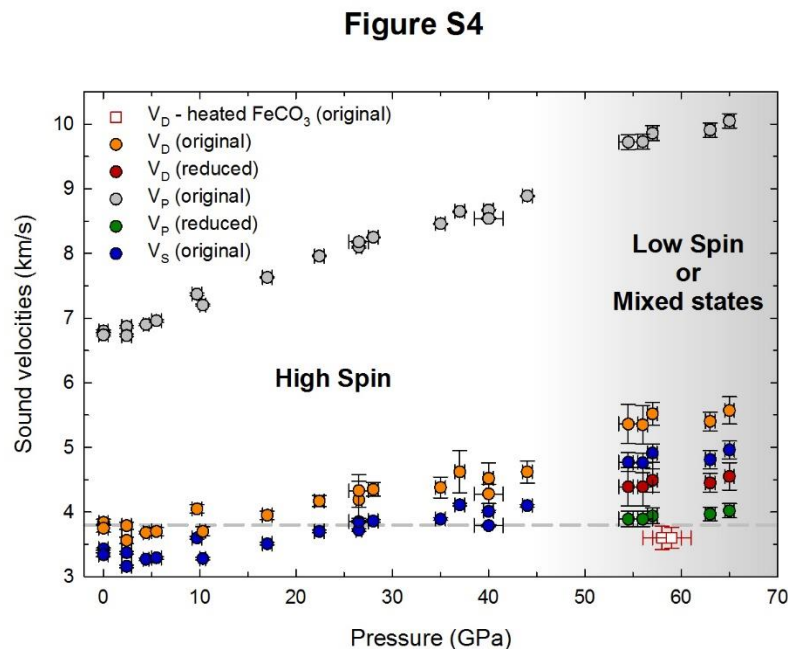
Additional References:

Lin, J-F., Liu, J., Jacobs, C., and Prakapenka, V.B. (2012) Vibrational and elastic properties of ferromagnesite across the electronic spin-pairing transition of iron. American Mineralogist, 97, 583-591.

Lavina, B., Dera, P., Downs, R.T., Prakapenka, V., Rivers, M., Sutton, S., and Nicol, M. (2009) Siderite at lower mantle conditions and the effects of the pressure-induced spin-pairing transition. Geophysical Research Letters, 36, L23306.

Lavina, B., Dera, P., Downs, R.T., Tschauner, O., Yang, W., Shebanova, O., and Shen, G. (2010b) Effect of dilution on the spin pairing transition in rhombohedral carbonates. High Pressure Research, 30, 224-229.

Chapter 8

Crystal structure of Fe-bearing MgCO$_3$ sp^3-carbonate at 98 GPa using single-crystal X-ray diffraction

Stella Chariton[1], Maxim Bykov[1], Elena Bykova[2], Egor Koemets[1], Timofey Fedotenko[3], Björn Winkler[4], Michael Hanfland[5], Vitali B. Prakapenka[6], Eran Greenberg[6], Catherine McCammon[1], and Leonid Dubrovinsky[1]

[1] *Bayerisches Geoinstitut, University of Bayreuth, 95440 Bayreuth, Germany*

[2] *Deutsches Elektronen-Synchrotron (DESY), 22607 Hamburg, Germany*

[3] *Laboratory of Crystallography, University of Bayreuth, 95440 Bayreuth, Germany*

[4] *Institute of Geosciences, Goethe University, 60438 Frankfurt am Main, Germany*

[5] *ESRF, The European Synchrotron, 38043 Grenoble Cedex 9, France*

[6] *GeoSoilEnviroCARS, University of Chicago, 60637 Chicago, Illinois, USA*

Corresponding Author's email: stellachariton@hotmail.com
ORCID iD: 0000-0001-5522-0498

ABSTRACT

The structure of MgCO$_3$-II has long been discussed in the literature where DFT-based model calculations predict a pressure-induced transition of carbon from sp^2 to sp^3-type bonding. We have determined the crystal structure of MgCO$_3$-II based on single-crystal X-ray diffraction measurements using synchrotron radiation. We laser heated a synthetic (Fe$_{0.15}$Mg$_{0.85}$)CO$_3$ single-crystal at 2500 K and 98 GPa and observed the formation of a monoclinic (Fe$_{0.4}$Mg$_{2.6}$)C$_3$O$_9$ phase with space group $C2/m$ that contains tetrahedrally-coordinated carbon, where tetrahedra form three-membered rings linked by corner-shared oxygen atoms. The reported tetracarbonate phase crystallizes in a new structure type. In comparison with

previous structure-prediction calculations and powder X-ray diffraction data, our structural data provide reliable information from experiments regarding atomic positions, bond lengths, and bond angles.

8.1. Chemical context

Carbonates and their high-pressure behavior have attracted significant interest due to their potential role as carbon-bearing phases in the deep Earth. Recent discoveries of novel compounds that contain tetrahedral CO_4^{4-} units (e.g., Merlini et al. 2015, Cerantola et al. 2017) increase the relevance of such studies, as the new high-pressure phases may be stable at conditions prevalent in the deep part of Earth's lower mantle. In addition, theoretical modelling predictions imply potential structural analogues of CO_4-bearing carbonates and silicates, and thus tetracarbonates may be important to understanding the complex geochemistry of Earth's mantle.

Tetrahedrally-coordinated carbonates are not well characterized, despite their potential significance, as structural studies have to be carried out at high pressure and are therefore challenging. A reliable structural characterization is, however, a prerequisite for determining phase stabilities and to understand, for example, why the p,T-phase diagram of $MgCO_3$ is relatively simple compared to the dense phase diagram of $CaCO_3$ (see summary in Bayarjargal et al., 2018).

It is generally accepted that magnesite transforms to $MgCO_3$-II at $80 - 115$ GPa (Isshiki et al., 2004, Boulard et al., 2011, 2015, Maeda et al., 2017). Models based on density functional theory (DFT) (Oganov et al. 2008) and interpretation of X-ray diffraction data and IR spectra imply that magnesite-II contains carbon in tetrahedral coordination (Boulard et al. 2011, 2015). While structure-prediction techniques are undoubtedly useful for preliminary surveys of phase stabilities, they provide a range of possible new phases, derived under constraints such as unit cell contents. Powder diffraction data obtained at pressures around 100 GPa generally do not yield accurate structure determinations and typically do not allow unambiguous assignment of the space group or site occupancies. In contrast, single-crystal X-ray diffraction is a powerful and unique tool that can provide accurate structure refinements (Boffa Ballaran et al. 2013). Well-established statistical parameters allow an assessment of the reliability of the structural model. Other tetracarbonate structures at extreme conditions have been previously reported using this method, such as the novel $Fe_4C_3O_{12}$ ($R3c$), $(Mg,Fe)_4C_4O_{13}$ ($C2/c$) (Cerantola et al. 2017) and $Ca(Fe,Mg)_2C_3O_9$ (Merlini et al. 2017) phases. These results lead to two conclusions. Firstly, the stability fields of carbonates strongly depend on their composition. Secondly, CO_4^{4-} units have the ability to form polymerized networks, and thus are potential analogues to silicates.

8.2. Structural commentary

At ambient conditions $(Fe_{0.15}Mg_{0.85})CO_3$ crystallizes in the calcite-type structure with space group $R\bar{3}c$. Iron and magnesium share the same crystallographic site and are coordinated by six oxygen atoms, while CO_3^{2-} units form planar equilateral triangles. After compression to 98(2) GPa at ambient temperature, X-ray diffraction data of $(Fe_{0.15}Mg_{0.85})CO_3$ can still be indexed in the $R\bar{3}c$ space group (Table 1). However, the unit cell volume is decreased by nearly 32 % compared to ambient conditions. This result challenges a recent suggestion based on DFT-based calculations that predicted a structural transformation of $MgCO_3$ to a triclinic phase at 85-101 GPa and 300 K (Pickard and Needs, 2015). After annealing at 2500 K and 98 GPa, we observed a phase transition to a polymorph in which carbon is tetrahedrally coordinated
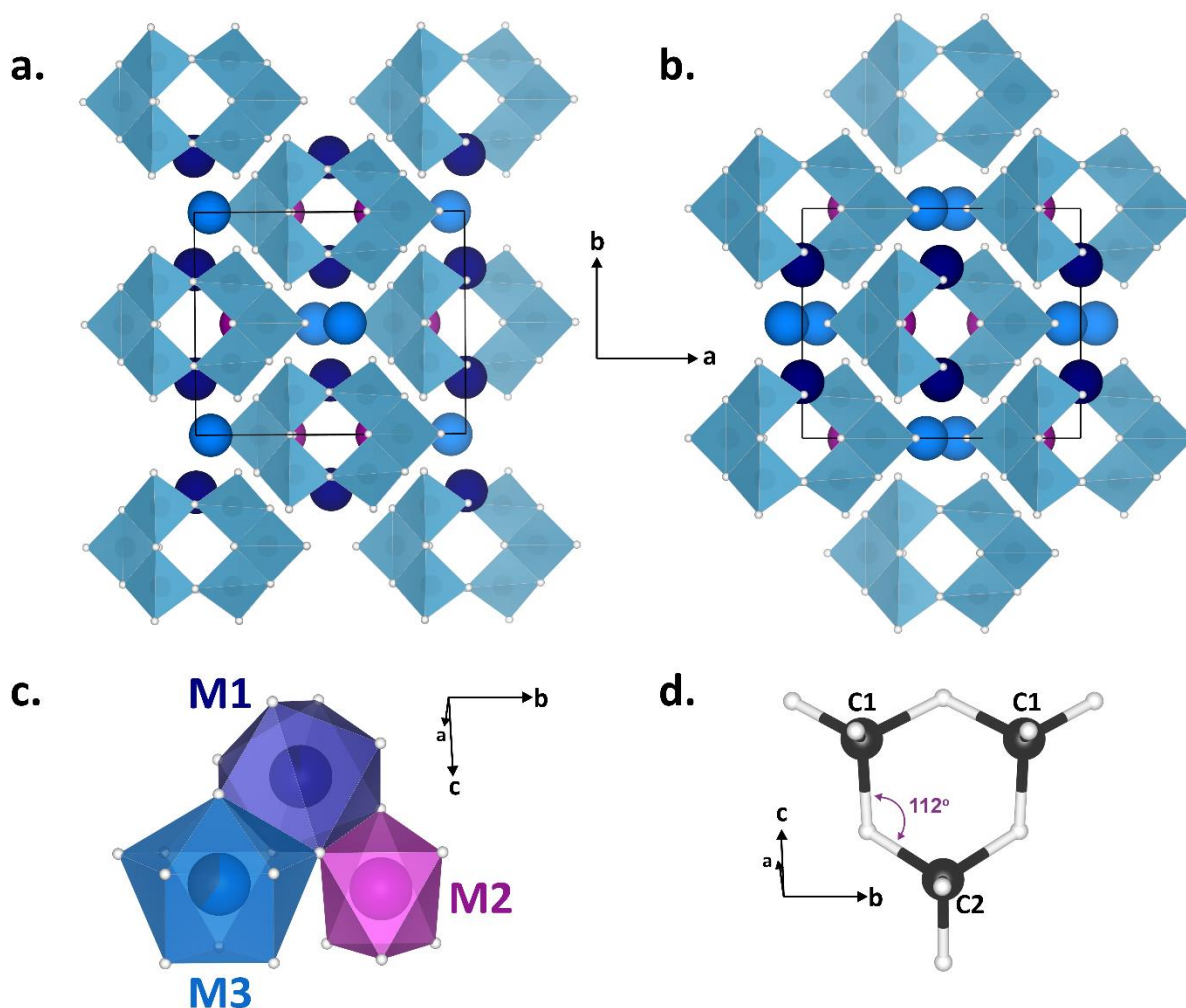

Figure 1. Crystal structure of $(Mg_{2.6}Fe_{0.4})C_3O_9$ according to **a)** this study and **b)** Oganov et al. (2008). The three cation sites that host Mg/Fe atoms are shown in **c. d)** $C_3O_9{}^{6-}$ rings are formed from three edge-shared CO_4 tetrahedra. Atomic positions are shaded according to colors in **c** and oxygen atoms appear as small white spheres.

by oxygen. The newly formed phase with chemical formula $(Fe_{0.4}Mg_{2.6})C_3O_9$ (as determined from structural refinements, see below) has monoclinic symmetry and the diffraction pattern indicates space group $C2/m$ (Figure 1 , Table 1).

We identify this phase as the $MgCO_3$-II structure that was previously predicted (Oganov et al. 2008; Boulard et al. 2015). In contrast to earlier studies, we provide an accurate structure solution and refinement. The atomic coordinates obtained from our structure solution are presented in Table 2. The structure consists of three-membered $C_3O_9^{6-}$ rings formed by corner-sharing CO_4 tetrahedra (Figure 1d) that alternate with (Fe,Mg) polyhedra perpendicular to the *b*-axis. We can distinguish three crystallographic cation positions (Figure 1c): 1) M1 site occupied by Fe and Mg in a 0.11 Fe/Mg ratio surrounded by eight oxygen atoms forming distorted square antiprisms (dark blue), 2) M3 with 0.66 Fe/Mg ratio and coordination number 10 (blue; can be described as half cuboctahedra merged through hexagonal based faces with hexagonal pyramids), and 3) M2 fully occupied by Mg in MgO_6 octahedra (magenta). The maximum and minimum bond distances of each cation from its neighboring oxygen atoms are shown in Table 3. At 98 GPa the C-O bond varies from 1.28-1.41 Å and the C-O-C inter-tetrahedral angle is ~112° (Figure 1d, Table 3).

From all proposed structural models for magnesite-II over the last two decades, only one appears to be comparable to the structure solution model that we report here. On the basis of PXRD experiments and variable-cell simulations, Oganov et al. (2008) suggested several energetically favorable structural models for $MgCO_3$-II, one of which with space group $C2/m$. This model has many similarities to the one proposed here using the single-crystal X-ray diffraction (SCXRD) method (Figure 1a-b). Both models suggest similar lattice parameters and the same space group. Further comparisons revealed that both models explain equally well our SCXRD patterns, resulting in R1 ~ 8.4% (this study) or R1 = 8.7% (Oganov et al. 2008) for the same Fe distribution in M1 and M3 sites. In order to test if one model is more preferable than the other, we performed additional DFT-based model calculations using the plane wave/pseudopotential CASTEP package (Clark et al., 2005). Pseudopotentials were generated "on the fly" using the parameters provided with the CASTEP distribution. These pseudopotentials have extensively been tested for accuracy and transferability (Lejaeghere et al., 2016). The pseudopotentials were employed in conjunction with plane waves up to a kinetic-energy cutoff of 1020 eV. The calculations were carried out with the PBE exchange-correlation function (Perdew et al., 1996). For simplicity we assumed that all three M1, M2 and M3 positions are fully occupied by Mg^{2+}. The calculations revealed that the energies of our structural model and that of Oganov et al. (2008) are identical. Indeed, shifting the origin of the unit cell by (0 , ½ , ½) for all (x, y, z) atomic coordinates of our model (Figure 1a) reproduces the

Oganov et al. (2008) model (Figure 1b) and *vice versa*. The DFT calculations gave C-O distances in good agreement with experimental data. Each carbon atom is coordinated by two oxygen atoms that are each shared with another tetrahedrally coordinated carbon, and two that are not shared. The C-O distances for the latter are significantly shorter (1.29 Å < d(C-O) < 1.32 Å) than the former (1.33 Å < d(C-O) < 1.41 Å).
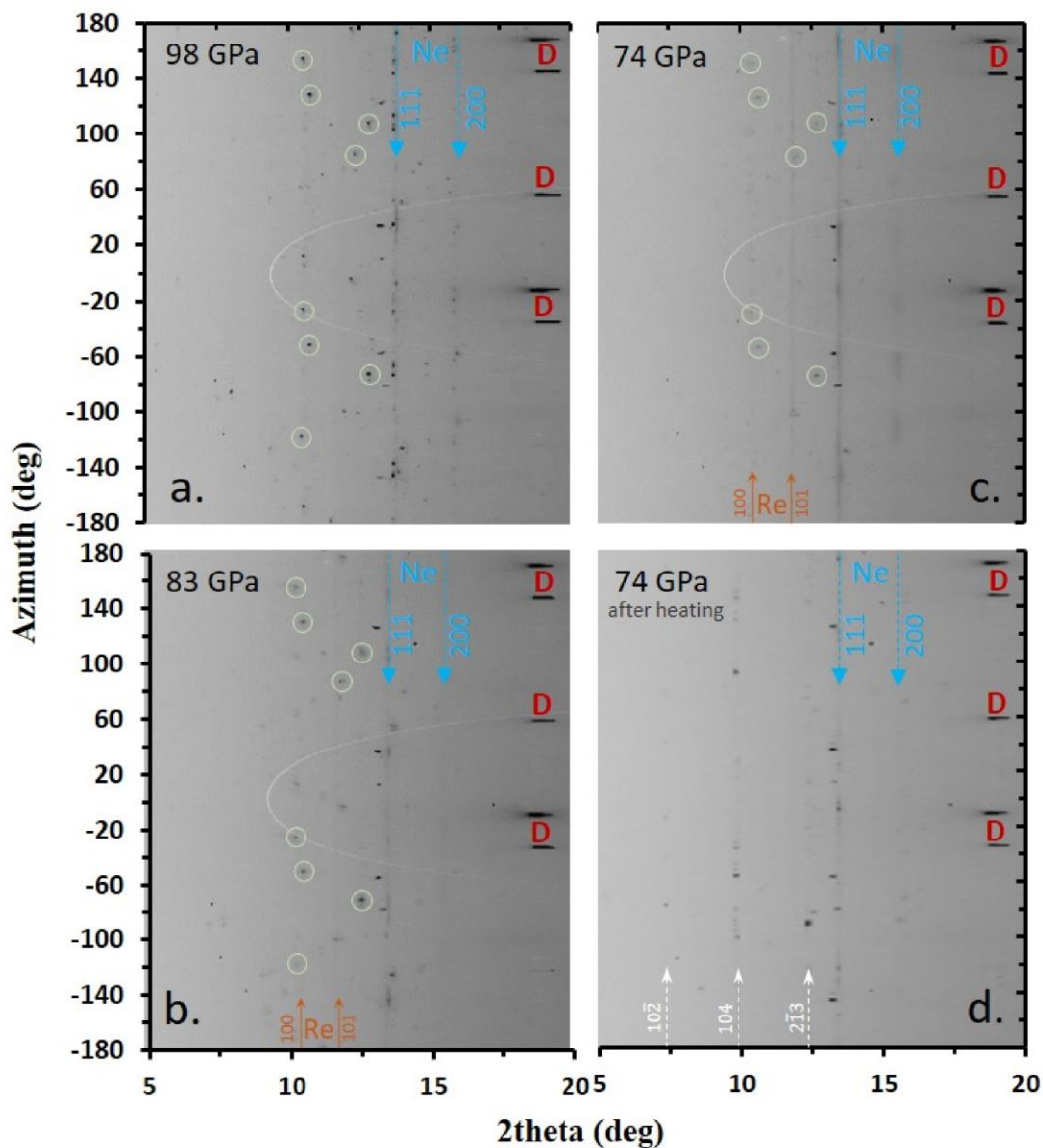
Figure 2. Unrolled X-ray diffraction images collected at room temperature (λ=0.411 Å). a) Sharp and intense reflections of $(Mg_{2.6}Fe_{0.4})C_3O_9$ appear after laser heating of the starting material at 98 GPa and 2500 K. b) The crystal phase gradually deteriorates during decompression and c) nearly disappears at ~74 GPa. d) Consequent laser heating treatment results in the formation of the initial carbonate structure. Green circles mark a few of the characteristic reflections of $(Mg_{2.6}Fe_{0.4})C_3O_9$, the position of Ne reflections and in some cases Re reflections are marked with blue and orange arrows, respectively. The 2theta positions of three characteristic carbonate ($R\bar{3}c$) reflections are indicated with white arrows. Diamond reflections are marked in red.

A Mulliken bond population analysis shows that for the long C-O bonds there is a significant bond population of ~0.5 e/Å^3. This is less than the value for the short bonds, where the bond population is ~0.9 e/Å^3, but this still is a predominantly covalent bond, and justifies the description as a tetrahedrally coordinated carbon atom. The formation of $(C_3O_9)^{6-}$ carbonate rings was previously observed in $Ca(Fe,Mg)C_3O_9$ (dolomite-IV) after laser heating of $Ca(Fe,Mg)CO_3$ at 115 GPa (Merlini et al. 2017). However, dolomite-IV is topologically different from the magnesite-II structure that we report here. Unlike $(Fe_{0.4}Mg_{2.6})C_3O_9$, $Ca(Fe,Mg)C_3O_9$ crystallizes in the orthorhombic system (space group *Pnma*), thus highlighting the significance of the metal cations that are involved in the carbonate.

Upon decompression at ambient temperature, $(Fe_{0.4}Mg_{2.6})C_3O_9$ reflections become broad and weak, and almost disappear at about 74 GPa (Figure 2a-c). This may be an indication of either amorphization or sluggish back-transformation to a carbonate with trigonal symmetry. Anticipating that further heating would aid re-crystallization, we laser-heated the sample at 74 GPa and 2000(150) K for a few seconds. Powder X-ray diffraction patterns collected on the temperature-quenched sample indicated the formation of the calcite structure-type carbonate (Figure 2d).

8.3. Synthesis and crystallization

Magnesium carbonate crystals with 15 (±4) mol% Fe were synthesized following the procedure reported by Chariton et al. (2020). The average composition of the starting material was characterized by single-crystal X-ray diffraction at ambient conditions. A single crystal of about 7 μm size in all dimensions was loaded inside a sample chamber of a BX90-type diamond anvil cell equipped with beveled Boehler-Almax type diamonds (culet diameter 80 μm). Rhenium and neon were used as gasket material and pressure transmitting medium, respectively. The sample was compressed up to 98 GPa and laser heated from both sides up to 2500 (150) K for a few seconds and then quenched to room temperature. The pressure was determined using the equation of state (EoS) of solid Ne (Fei et al. 2007). Consequently, we performed a 5x5 grid of still image collection with 2 μm step and 1 s exposure time around the center of the sample. This strategy is used to locate the most heated area of the crystal and the best spot to collect SCXRD patterns during rotation of the cell. Single-crystal data collection was performed as a series of ω scans over the range ±38° with a step of 0.5°.

8.4. Refinement

Details of the data collection, structure solution and refinement are summarized in Table 1. The crystal structure of $(Fe_{0.4}Mg_{2.6})C_3O_9$ solved at 98 GPa was used for the structure refinements of the data of the same phase collected during decompression. Due to the limited angular range caused by the laser-heated DAC, the resolution of the data set was not sufficient to refine the anisotropic displacement parameters. Therefore, all atoms were refined with the isotropic approximation.

Keywords: carbonates, magnesite-II, sp^3-carbonates, crystal structure, high-pressure single-crystal X-ray diffraction

8.5. Acknowledgments

8.6. References

Bayarjargal, L., Fruhner, C-J., Schrodt, N. & Winkler, B. (2018) PEPI **281**, 31-45.

Boffa Ballaran, T., Kurnosov, A. & Trots, D. (2013). High Press. Res. **33**, 453-456.

Boulard, E., Pan, D., Galli, G., Liu, Z. & Mao, W. (2015). *Nat. Commun.* **6**, 6311.

Cerantola, V., Bykova, E., Kupenko, I., Merlini, M., Ismailova, L., McCammon, C., Bykov, M., Chumakov, A.I., Petitgirard, S., Kantor, I., Svitlyk, V., Jacobs, J., Hanfland, M., Mezouar, M., Prescher, C., Rüffer, R., Prakapenka, V. B. & Dubrovinsky, L. (2017). *Nat. Commun.* **8**, 15960.

Chariton, S., McCammon, C., Vasiukov, D.M., Stekiel, M., Kantor, A., Cerantola, V., Kupenko, I., Fedotenko, T., Koemets, E., Hanfland, M., Chumakov, A.I., Dubrovinsky, L., (2020). Am. Miner. **105***, (in press).*

Clark, S. J., Segall, M. D., Pickard, C. J., Hasnip, P. J., Probert, M. J., Refson, K. & Payne, M. C. (2005). *Z. Krist.* **220**, 567-570.

Fei, Y., Ricolleau, A., Frank, M., Mibe, K., Shen, G. & Prakapenka, V. B. (2007). *PNAS* **104**, 9182–9186.

Isshiki, M., Irifune, T., Hirose, K., Ono, S., Ohishi, Y., Watanuki, T., Nishibori, E., Takata, M. & Sakata, M. (2004) *Nature* **427**, 60-63.

Lejaeghere, K., Bihlmayer, G., Björkman, T., Blaha, P., Blügel, S., Blum, V., Caliste, D., Castelli, I. E., Clark, S., Dal Corso, A., de Gironcoli, S., Deutsch, T., Dewhurst, J. K., Di Marco, I., Draxl, C., Dułak, M., Eriksson, O., Flores-Livas, J. A., Garrity, K. F., Genovese, L., Giannozzi, P., Giantomassi, M., Goedecker, S., Gonze, X., Grånäs, O., Gross, E. K., Gulans, A., Gygi, F., Hamann, D. R., Hasnip, P. J., Holzwarth, N. A., Iuşan, D., Jochym, D.B., Jollet, F., Jones, D., Kresse, G., Koepernik, K., Küçükbenli, E., Kvashnin, Y.O., Locht I. L., Lubeck, S., Marsman, M., Marzari, N., Nitzsche, U., Nordström, L., Ozaki, T., Paulatto, L., Pickard, C. J., Poelmans, W., Probert, M. I., Refson, K., Richter, M., Rignanese, G. M., Saha, S., Scheffler, M., Schlipf, M., Schwarz, K., Sharma, S., Tavazza, F., Thunström, P., Tkatchenko, A., Torrent, M., Vanderbilt, D., van Setten, M.J., Van Speybroeck, V., Wills, J. M., Yates, J. R., Zhang, G. X. & Cottenier, S. (2016). *Science*, **351**, aad3000.

Merlini, M., Cerantola, V., Gatta, G.D., Gemmi, M., Hanfland, M., Kupenko, I., P.Lotti, Müller, H. & Zhang, L. (2017). *Am. Miner.* **102**, 1763-1766.

Merlini, M., Hanfland, M., Salamat, A., Petitgirard, S. & Müller, H. (2015). *Am. Miner.* **100**, 2001-2004.

Oganov, A.R., Ono, S., Ma, Y., Glass, C.W. & Garcia, A. (2008) *Earth Planet. Sci. Lett.,* 273, 38-47.

Perdew, J. P., Burke, K., & Ernzerhof, M. (1996). *Phys. Rev. Lett.* **77**, 3865-3868.
Petricek, V., Dusek, M., & Palatinus, L. (2014). Zeit. Kristallogr. Crystal. Mater. **229**, 345–352.

Pickard, C. J. & Needs, R. J. (2015). Phys. Rev. B 91, 104101.

Rigaku OD (2019). CrysAlisPRO software system, ver. 1.171. Rigaku Corporation, Oxford, U.K.

Table 1. Experimental Details [a]

	$(Fe_{0.15} Mg_{0.85})CO_3$	$(Fe_{0.4} Mg_{2.6})C_3O_9$
Chemical Formula	$(Fe_{0.15} Mg_{0.85})CO_3$	$(Fe_{0.4} Mg_{2.6})C_3O_9$
M_r	89	265.6
Crystal system, space group	Trigonal, $R\bar{3}c$	Monoclinic, $C2/m$
Pressure (GPa)	98 (1)	98 (2)
Annealing temperature (K)[b]	300 K (no heating)	2500 (150)
a, b, c (Å)	4.281(7), 4.281(7), 12.115(16)	8.238(3), 6.5774(12), 6.974 (5)
α, β, γ (°)	90, 90, 120	90, 104.40(6), 90
V (Å^3)	192.3(5)	366.0(3)
Z	6	4
ρ (g/cm^3)	4.61	4.82
μ (mm^{-1})	0.25	0.523
Crystal size (mm)	0.007 x 0.007 x 0.007	
Radiation type, wavelength (Å)	Synchrotron, 0.295	Synchrotron, 0.411
Diffractometer	13IDD @ APS	ID15b @ ESRF
Theta collection range (°)	2.68 – 15.4	2.32 – 20.71
Index ranges	-6 < h < 6 -7 < k < 5 -18 < l <18	-11 < h < 12 -8 < k < 8 -7 < l < 9
Refinement method	Full matrix least squares on F^2	
F(000)	265	530
Completeness to d =0.8 Å, %	87.5	50.7
Redundancy	3.3	3.57
No. of collected, independent and [I>3σ(I)] reflections	214, 65, 60	522, 146, 297
R_{int}	0.054	0.020
No. of parameters	5	39
R[F^2 > 3(F^2)], wR(F^2)	0.10, 0.081	0.083, 0.086
Δρ$_{max}$, Δρ$_{min}$ (e Å^{-3})		1.76 / -1.21

[a] Computer programs: CrysAlis[PRO] (Rigaku OD, 2019), JANA2006 (Petricek et al. 2014)

[b] Data collection was performed on the temperature-quenched sample.

Table 2. Fractional atomic coordinates and isotropic displacement parameters of $(Fe_{0.4}Mg_{2.6})C_3O_9$ at 98 GPa.

| Atom Label	x	y	z	Site Symmetry	Ui_{sxo}[a]	Occupancy
Mg1	0.5	-0.2457(6)	-0.5	4h	0.0117(13)	0.917(17)
Fe1	0.5	-0.2457(6)	-0.5	4h	0.0117(13)	0.083(17)
Mg2	0.6712(7)	0	-0.1854(12)	4i	0.0086(11)	1
Mg3	0.9441(6)	0	0.1503(9)	4i	0.0177(11)	0.61(2)
Fe3	0.9441(6)	0	0.1503(9)	4i	0.0177(11)	0.39(2)
O1	0.3605(17)	0	-0.544(3)	4i	0.020(2)	1
O2	0.2736(13)	-0.3338(9)	-0.653(2)	8j	0.0179(17)	1
O3	0.8442(12)	0.1683(9)	-0.0782(18)	8j	0.0157(15)	1
O4	1.0903(18)	0	0.395(3)	4i	0.021(2)	1
O5	0.6487(16)	0	0.075(3)	4i	0.016(2)	1
O6	0.5062(12)	0.1898(9)	-0.2298(19)	8j	0.0159(17)	1
C1	0.3653(19)	0.1774(13)	-0.183(3)	8j	0.017(2)	1
C2	1.235(3)	0	0.536(4)	4i	0.024(3)	1

[a] All atomic displacement parameters were refined in the isotropic approximation

**Table 3.** Geometric parameters of $(Fe_{0.4}Mg_{2.6})C_3O_9$ at 98 GPa.

Group	Bond distances		Polyhedron Volume ($Å^3$)	Distortion index [a]
	Max (Å)	Min (Å)		
CO_4 (C1-O)	1.409(19)	1.287(18)	1.25	0.045
CO_4 (C2-O)	1.38(3)	1.29(4)	1.25	0.022
MgO_6	1.87(3)	1.813(10)	7.78	0.010
$Mg_{0.9}Fe_{0.1}O_8$	2.039(13)	1.908(14)	13.24	0.020
$Mg_{0.6}Fe_{0.4}O_8$	2.358(14)[b]	1.828(19)	14.59	0.068

[a] as defined in W. H. Baur, Acta Crystallogr., Sect. B: Struct. Sci., 30, 1195 (1974); [b] alternatively, maximal distance is 2.451(14) Å, polyhedral volume is 20.58($Å^3$) and distortion index is 0.080
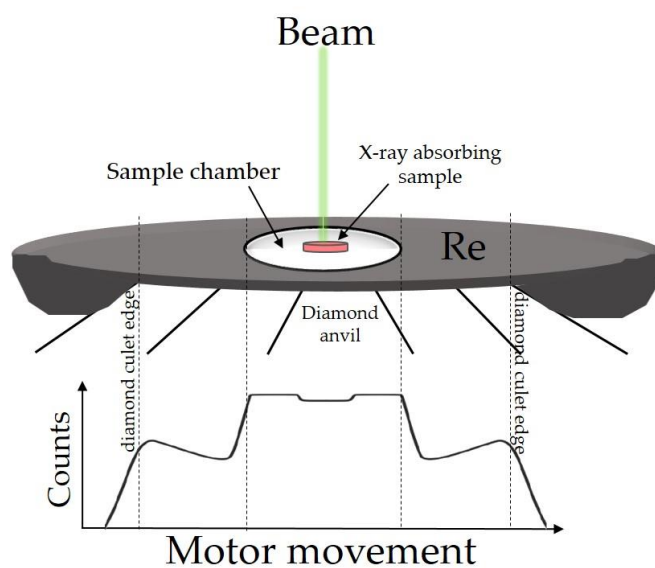
Appendix
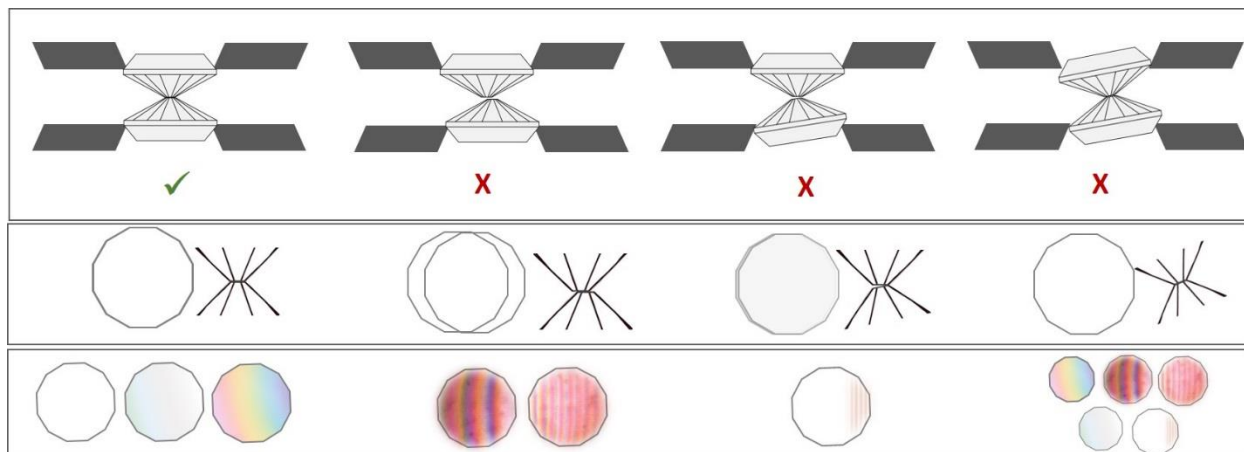
Appendix Figure A1. Four examples of good and bad diamond alignments. Top frame shows side-view. Middle frame shows the magnified side-view of the diamond culets and their appearance under the microscope. Bottom frame shows the type of Newton rings that one can observe in every case.
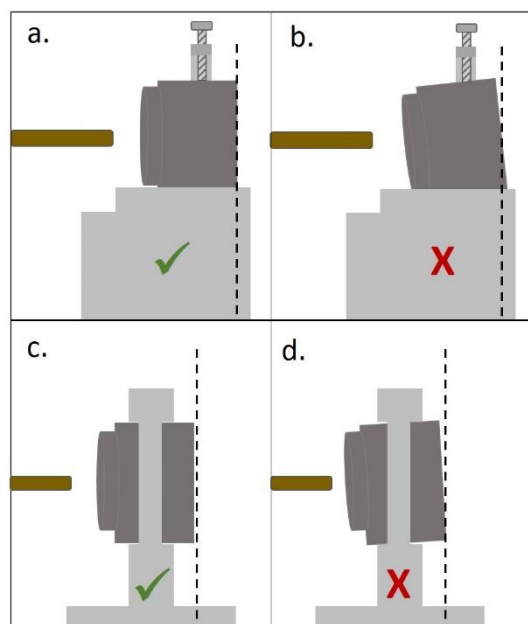
Appendix Figure A2. Examples of correct and wrong placement of the DAC on beamline holders: **a,b**) at ID15b, **c,d)** at P02.2 and IDD13.

Appendix Figure A3. Characteristic profile of an absorption curve recorded by Si-diode when the X-ray beam passes through a DAC.

Abbreviations & Nomenclature

Acronym	Definition
APD	Avalanche Photodiode detector
APS	Advanced Photon Source
BGI	Bayerisches Geoinstitut
BS	Brillouin Spectroscopy
CarboPaT	Carbonates at high Pressures and Temperatures
CN	Coordination Number
DAC	Diamond Anvil Cell
DCO	Deep Carbon Observatory
DESY	Deutsches Elektronen-Synchrotron
DFT	Density Functional Theory
DOS	Density of State
EoS	Equation of State
ESRF	European Synchrotron Radiation Facility
HLM	High-heat Load Monochromator
HRM	High Resolution Monochromator
HS	High spin state
ISS	Impulsive Stimulated Scattering
IXS	Inelastic X-ray Scattering
LPO	Lattice Preferred Orientation
LS	Low spin state
NFS	Nuclear Forward Scattering
NIS	Nuclear Inelastic Scattering
pDAC	panoramic Diamond Anvil Cell
pDOS	Projected or partial Density of State
PREM	Preliminary Reference Earth Model
PTM	Pressure transmitting medium
PXRD	Powder X-ray Diffraction
rDOS	reduced Density of State
SCXRD	Single-crystal X-ray Diffraction
XRD	X-ray Diffraction

Name	Definition	Often expressed as:
a, b, c	Lattice parameters (length)	Å
d	d-spacing	Å
$\mathbf{F}_{hkl}$	Structure factor	-
F_{hkl}	Structure amplitude	-
G	Shear modulus	GPa
hkl	Miller indices	-
I	Intensity	-
K	Bulk modulus	GPa
P	pressure	bar, GPa
r^2	Coefficient of determination	$0 \leq r^2 \leq 1$
Rint,R1,wR2	Confidence factors	%
T	temperature	K, °C
V	Volume (unit cell)	$Å^3$
V_D	Debye velocity	km/s
V_P	Primary velocity	km/s
V_S	Secondary velocity	km/s
Z	Formula units	-
α, β, γ	Lattice parameters (angles)	deg
$\delta^{13}C$	delta ^{13}C, isotopic signature	‰
E	energy	eV, meV, keV…
θ	Theta angle	deg
λ	wavelength	nm, Å
μ	Absorption coefficient	mm^{-1}
M_r	Molecular weight	kg
v	wavenumber	cm^{-1}
ρ	density	g/cm^3

(Eidesstattliche) Versicherungen und Erklärungen

(§ 9 Satz 2 Nr. 3 PromO BayNAT)

Hiermit versichere ich eidesstattlich, dass ich die Arbeit selbstständig verfasst und keine anderen als die von mir angegebenen Quellen und Hilfsmittel benutzt habe (vgl. Art. 64 Abs. 1 Satz 6 BayHSchG).

(§ 9 Satz 2 Nr. 3 PromO BayNAT)

Hiermit erkläre ich, dass ich die Dissertation nicht bereits zur Erlangung eines akademischen Grades eingereicht habe und dass ich nicht bereits diese oder eine gleichartige Doktorprüfung endgültig nicht bestanden habe.

(§ 9 Satz 2 Nr. 4 PromO BayNAT)

Hiermit erkläre ich, dass ich Hilfe von gewerblichen Promotionsberatern bzw. -vermittlern oder ähnlichen Dienstleistern weder bisher in Anspruch genommen habe noch künftig in Anspruch nehmen werde.

(§ 9 Satz 2 Nr. 7 PromO BayNAT)

Hiermit erkläre ich mein Einverständnis, dass die elektronische Fassung meiner Dissertation unter Wahrung meiner Urheberrechte und des Datenschutzes einer gesonderten Überprüfung unterzogen werden kann.

(§ 9 Satz 2 Nr. 8 PromO BayNAT)

Hiermit erkläre ich mein Einverständnis, dass bei Verdacht wissenschaftlichen Fehlverhaltens Ermittlungen durch universitätsinterne Organe der wissenschaftlichen Selbstkontrolle stattfinden können.

_____

Ort, Datum, Unterschrift